Vibrational dynamics of solute in hydrogen-bonding liquid studied by nonlinear infrared spectroscopy

Okuda, Masaki

(Degree)
博士（理学）

(Date of Degree)
2017-03-25

(Date of Publication)
2020-03-25

(Resource Type)
doctoral thesis

(Report Number)
甲第6850号

(URL)
https://hdl.handle.net/20.500.14094/D1006850

Doctoral Dissertation

Vibrational Dynamics of Solute in Hydrogen-bonding Liquid Studied by Nonlinear Infrared Spectroscopy

非線形赤外分光法による水素結合性溶媒中における溶質分子の

振動ダイナミクスに関する研究

January 2017

Graduate School of Science, Kobe University

MASAKI OKUDA (奥田 真紀)

Contents

CHAPTER 1. General Introduction

1.1. Molecular Dynamics in Hydrogen-bonding Liquids 2

1.2. Vibrational Spectroscopy: Nonlinear Infrared Spectroscopy 2

1.3. Outline of this Thesis: Vibrational Dynamics of Non-ionic Vibrational Probe Molecules in Hydrogen-bond Liquids 5

CHAPTER 2. Theoretical Background of Multi-pulse Experiments

2.1. Introduction 16

2.2. Equation Motion for Solute under Solute-solvent Interaction 17

2.3. Formalism of Absorption Spectrum of Solute 21

2.3.1. Nonlinear Response Function and Signal Field 22

2.3.2. Line Broadening Function: Vibrational Energy Relaxation 25

2.3.3. Line Broadening Function: Rotational Relaxation 26

2.3.4. Line Broadening Function: Frequency Fluctuations 28

2.4. Theoretical Background of 2D-IR Spectroscopy 31

2.4.1 Double-side Feynman Diagram 31

2.4.2. Third-order Nonlinear Response Function 33

2.4.3. Line Broadening Function of 2D-IR Spectrum 36

2.5. Summary 39

References 40

Figures 43

CHAPTER 3. Experimental Setup: Two-dimensional Infrared Spectroscopy

3.1. Introduction 48

3.2. Generation of Mid-IR pulses: OPA and DFG Processes 48

3.3. Compact Implementation of Two-dimensional Infrared Spectroscopy 50

3.3.1. Mach-Zehnder Interferometer 50

3.3.2. 2D-IR Data Collection: Pump-probe Geometry 51
3.4. Coherence Time Delay Calibration: Quadrate Fringe Counting Method with He-Ne Interferences 53
3.5. Improvement of Signal to Noise Ratio 55
3.6. Summary 56
References 57
Figures 58
Appendix 3.A. Auto-correlation Measurement of Mid-IR Pulse with $AgGaS_2$ Nonlinear Crystal 64
Appendix 3.B. 2D-IR Measurement for $[RuCl_5(NO)]^{2-}$ in D_2O 67

CHAPTER 4. Frequency Fluctuations of Non-ionic Vibrational Probe Molecule in Aqueous Solution: Experimental Study by Two-dimensional Infrared Spectroscopy

4.1. Introduction 72
4.2. Materials and Methods 74
4.3. Results and Discussions 76
4.3.1. IR Absorption Spectra 76
4.3.2. Polarization-controlled IR Pump-probe Experiments 77
4.3.3 2D-IR Experiments 80
4.4. Conclusion 83
References 84
Figures and Tables 88
Appendix 4.A. Correction Scheme for 2D-IR Signals 102
Appendix 4.B. IR Spectrum of SCN^- in DMSO and the Detailed Analysis of the IR Pump-probe Signals of SCN^- in Water 104

CHAPTER 5. Frequency Fluctuations of Non-ionic Vibrational Probe Molecule in Aqueous Solution: Theoretical Study by Molecular Dynamics Simulation

5.1. Introduction 110

5.2. Computational Details 112
5.2.1. Quantum Chemical Calculations 112
5.2.2. Molecular Dynamics Simulations 113
5.3. Results and Discussions 113
5.3.1. Multi-site Interaction Model for SCN Vibrational Frequency Shift 114
5.3.2. Hydration Structure around SCN Group 116
5.3.3. Water Dynamics around SCN Group 117
5.3.4. Theoretical Analysis for Vibrational Frequency Fluctuations 118
5.4. Conclusion 123
References 125
Figures and Tables 128
Appendix 5.A. Angle-resolved Pair-radial Distribution Functions for SCN Groups of NTBA and SCN^- 145
Appendix 5.B. Pair-radial Distribution Functions for Hydrogen Bond Sites of NTBA and SCN^- 146
Appendix 5.C. Hydrogen Bond Correlation Functions for Hydrogen Bond Sites of NTBA and SCN^- 147
Appendix 5.D. Dipole Moment Reorientational Correlation Functions for Water Molecules around Hydrogen Bond Sites of NTBA and SCN^- 149
Appendix 5.E. Spacitally-resolved Frequecny-frequecny Time Correlation Functions for NTBA/water and SCN^-/water Systems 150
Appendix 5.F. SCN Vibrational Frequecny Fluctuations Indeced by Electrostatic Interactions from Hydrogen Bonded Water Molcules 151

CHAPTER 6. Vibrational Dynamics of N_3-derivatized Amino Acids in Aqueous Solutions Studied by Nonlinear Infrared Spectroscopy

6.1. Introduction 154
6.2. Materials and Methods 155
6.3. Results and Discussions 156
6.3.1. IR Absorption Spectra 156
6.3.2. Vibrational Energy Relaxation 157

6.3.3. Rotational Relaxation 159
6.3.4. Spectral Diffusion 161
6.4. Conclusion 163
References 164
Figures and Tables 167
Appendix 6.A. Numerical Calculation for Multi-component Absorption Spectrum 178

CHAPTER 7. Rotational Dynamics of Solutes with Multiple-bond Axes in 1-alcohol Solutions Studied by Infrared Pump-probe Spectroscopy

7.1. Introduction 188
7.2. Materials and Methods 189
7.3. Results and Discussions 190
7.3.1. IR Absorption Spectra 190
7.3.2. Vibrational Energy Relaxation 191
7.3.3. Solvent- and Temperature-dependent Anisotropy Decays 192
7.4. Conclusion 197
References 199
Figures and Tables 202
Appendix 7.A. Solvent- and Temperature-dependent IR Absorption Spectra 219
Appendix 7.B. Solvent- and Temperature-dependent Isotropic IR Pump-probe Signals 221
Appendix 7.C. Anisotropy Measurements for N_3-Ala and N_3-Nle in DMSO Solutions 223
Appendix 7.D. Extension of the Wobbling-in-a-cone Orientational Correlation Function to Multiple-restricted Angular Motion 224
Appendix 7.E. Solvent-dependent Anisotropy Decays of N_3-Phe in 1-alcohol Solutions 226

CHAPTER 8. Hydrogen-bond Dynamics of 9-fluorenone Derivatives in Aqueous Solutions Studied by Two-dimensional Infrared Spectroscopy

8.1. Introduction 230
8.2. Materials and Methods 231
8.3. Results and Discussions 232
8.3.1. IR Absorption Spectra 232

8.3.2 IR Pump-probe Experiments 233
8.3.3. 2D-IR Experiment for 9FL-2-COO^- in D_2O 234
8.3.4. 2D-IR Experiments for 9FL-4-COO^- in D_2O 237
8.4. Conclusion 240
References 241
Figures and Table 244
Appendix 8.A. IR Absorption Measurements for 9FL-2-COO^- in D_2O at Different Temperature and in THF 254
Appendix 8.B. 2D-IR Measurements for Acetone in D_2O 256
Appendix 8.C. Radial-dependence of Collective Reorientatioanl Motions of Water Molecules 260

Concluding Remarks 263
Publication List 267
Acknowledgements 269

CHAPTER 1.

General Introduction

1.1. Molecular Dynamics in Hydrogen-bonding Liquids

From living cells to test tubes, a huge number of chemical reactions occur in solution. In solution, a solute is continuously affected by various interactions, for instance, collision between solute and solvent and electrostatic interaction from the surrounding solvents. However, the strength of solute-solvent interaction is changing in time due to different motions, namely, translational, rotational, and vibrational motions of solute and solvent molecules. Compared to other molecular liquids, water and alcohols form organized structures with intermolecular hydrogen bonds (HBs), which is so-called a HB network structure [1]. Since a HB is an intrinsically weak interaction, formation and breaking of HBs takes place on an order of picosecond (10^{-12} s), which is different from those of covalent bonds. Due to this rearrangement, the HB network structure is not static but continuously evolving in time. The structural change induces large amplitude of fluctuation in the solute-solvent interaction [2], which strongly affects the static and dynamic properties of a solute (*e.g.* free energy surface, structural dynamics, and so on) [3-6]. Therefore, knowledge on solute-solvent interaction and molecular dynamics is indispensable for understanding chemical reactions in solution from a microscopic viewpoint.

1.2 Vibrational Spectroscopy: Nonlinear Infrared Spectroscopy

It is well known that vibrational spectroscopy provides insight into solute-solvent interaction and molecular dynamics in solution [7-25]. The vibrational frequency of a solute is determined by its chemical properties, that is, bond strength and mass of the vibrating atoms. Therefore, since dynamical solute-solvent interaction causes temporal change in the bond strength (*i.e.* vibrational frequency), the position and lineshape of the IR absorption spectrum of a solute reflects rich information on solute-solvent interaction and molecular dynamics in solution. For example, while the IR absorption spectrum of the OH stretching mode of phenol in CCl_4 exhibits a sharp peak at 3610 cm^{-1}, by adding benzonitrile to the solution, phenol exhibits a new broader IR absorption band at 3450 cm^{-1} (see Fig.1 in Ref. 26). The frequency shift of the IR absorption spectrum of phenol/benzonitrile in CCl_4 is attributed to the formation of a HB between phenol and benzonitrile, and its broader bandwidth reflects a distribution of the HB strength resulting from different conformations of the hydrogen-bonding complexes. However, because molecular motion in solution takes place on an ultrafast time scale, usually within nanosecond (10^{-9} s), molecular information obtained from linear IR spectra is time-averaged over this time scale. Therefore, it is

almost impossible to disentangle all the underlying molecular information based on linear IR absorption spectra, and real-time investigation on molecular vibrational dynamics is required for deeper understandings of solute-solvent interactions and molecular dynamics in solution.

Because of the developments of an ultrafast Ti:sapphire laser system [27-29] and intense short-pulse generation method in mid-IR frequency region [30-32], femtosecond nonlinear IR spectroscopy has been a powerful tool to address the underlying ultrafast molecular dynamics in solution, which is obscured in linear spectroscopy [33-35]. Generally, vibrational dynamics is characterized by the following three relaxation processes: (i) vibrational energy relaxation (VER), (ii) rotational relaxation, and (iii) spectral diffusion. We can examine the first two vibrational dynamics by IR pump-probe spectroscopy [36-65]. For IR pump-probe measurement, the pump pulse creates a non-equilibrium population (hole) in the vibrational excited (ground) state of a solute, and its relaxation back to thermal equilibrium is observed by the probe pulse with a given time delay. During the population relaxation, the excess energy in the excited state dissipates into the surrounding solvents through solute-solvent interactions. In previous works, several groups found that VERs of the solutes are enhanced when they form the intermolecular HBs with the neighboring solvents [38, 55, 57]. Therefore, VER processes should be sensitive to local solute-solvent interactions in solution. Moreover, by using appropriately polarized IR pulses, we can monitor rotational relaxation processes of solutes in solution exclusively. In solution, due to intermolecular interactions (*e.g.* collisions), a solute is continuously changing its direction in time. Hence, similar to VER processes, the time evolution of the direction of the vibrational transition dipole moment, that is, rotational diffusion of a solute reflects local solute-solvent interaction in solution [63, 65]. Furthermore, because vibrational transition dipole moments are localized in solutes, rotational relaxation can provide insight into local structural changes of solutes [55, 62].

We can investigate the third vibrational dynamics, *i.e.*, spectral diffusion by three-pulse IR photon echo (IR-3PE) method or two-dimensional IR (2D-IR) spectroscopy [66-103]. As mentioned above, solute-solvent interactions cause the vibrational frequency shift of a solute. Note that, in actual situation, the surrounding environment (*i.e.* solvation structure) of each solute is different. As a result, each solute has a slightly different vibrational frequency so that there is so-called an inhomogeneous distribution of vibrational frequencies. However, since the solvation structure is not static but fluctuating on a picosecond (10^{-12} s) time scale, the vibrational frequency of the solute and the associated inhomogeneous distribution is also evolving in time. This process

is called spectral diffusion. Here, at each instant of time, the vibrational frequency of a molecule ($\omega(T)$) is defined as:

$$\omega(T) = \Delta\omega(T) + \langle\omega\rangle \tag{1.1}$$

where $<\omega>$ and $\Delta\omega(T)$ are the time-averaged vibrational frequency and the deviation of frequency from the average value at time T, respectively (see Figure 1.1(a)). Therefore, $\Delta\omega(T)$ reflects dynamical information on solute-solvent interaction and solvation structure in the vicinity of the solute. Commonly, $\Delta\omega(T)$ is characterized by its time-correlation function (*i.e.* frequency-frequency time-correlation function, FFTCF, $C_\omega(T)$,):

$$C_\omega(T) = \langle\Delta\omega(T)\Delta\omega(0)\rangle \tag{1.2}$$

where $<\cdots>$ denotes the ensemble average. At sufficiently short time T, since the solvation structure around a solute does not change from its initial structure so much, a correlation exists between initial and final vibrational frequency shifts. On the other hand, at longer time T, the correlation is lost due to the change of the solvation structure. Therefore, $C_\omega(T)$ decays as a function of time T (see Figure 1.1(b)), and the decaying time scale reflects the solvation dynamics in the solution. IR-3PE method and 2D-IR spectroscopy can monitor the correlation function of vibrational frequency fluctuation, *i.e.*, $C_\omega(T)$ for the investigated molecular systems [66, 98]. For instance, Figure 1.2 gives an intuitive explanation for the time-dependence of a 2D-IR spectrum. For a molecular system with an inhomogeneous frequency distribution, at short time T, two vibrational frequencies (denoted as ω_1 and ω_3) are correlated and the 2D-IR lineshape is elongated along the diagonal axis (*i.e.* axis where $\omega_1 = \omega_3$, see Figure 1.2(a)). However, when time T becomes longer than a characteristic time for the solvation dynamics in the system (τ_C), the initial correlation between the frequencies ω_1 and ω_3 is lost and the 2D-IR lineshape is getting round (see Figure 1.2(b)). Finally, when the correlation between the frequencies ω_1 and ω_3 is completely lost, the 2D-IR lineshape becomes round (see Figure 1.2(c)). Hence, we can determine the time scale of the solvation dynamics from the time-dependence of the 2D-IR lineshape.

Before closing this section, it should be noted that a molecular dynamics (MD) simulation is also a powerful tool to investigate the vibrational frequency fluctuation of a solute in solution. By using an appropriate model to describe the vibrational frequency fluctuation of the solute in solution, we can theoretically calculate the corresponding $C_\omega(T)$ with MD simulations [104-117]. Furthermore, since MD simulation can provide molecular-level insight into the

temporal evolution of the solvation structure around a solute, which cannot be directly obtained from IR-3PE and 2D-IR experiments. Consequently, by combining experimental and theoretical studies, we can obtain deep understanding for microscopic mechanism of the vibrational frequency fluctuations of solutes in solutions.

1.3. Outline of this Thesis: Vibrational Dynamics of Non-ionic Vibrational Probe Molecules in Hydrogen-bond Liquids

In this thesis, I investigated vibrational dynamics of solutes in hydrogen-bonding liquids investigated by IR pump-probe and 2D-IR spectroscopies. Especially, in terms of properties of a solute (*e.g.* charge distributions, hydrophobic and hydrophilic groups, structural degrees of freedom *etc.*), I compared the observed vibrational dynamics among different vibrational probe molecules.

This thesis is composed as follows. In Chapter 2, for theoretical and experimental backgrounds of 2D-IR spectroscopy, I derived the mathematical expression of 2D-IR spectra by using the time-dependent perturbation theory. In Chapter 3, I summarized ultrashort mid-IR pulse generation and optical setup for 2D-IR measurements.

In Chapter 4, by using 2D-IR spectroscopy, I experimentally investigated the vibrational frequency fluctuations of 2-nitro-5-thiocyanate benzoic acid (abbreviated as NTBA) and thiocyanate anion (abbreviated as SCN^-) in H_2O. Different from SCN^-, the vibrational probe of an SCN group of NTBA is electrically neutral in part. Furthermore, the SCN group of NTBA connects to a hydrophobic group of aromatic ring. Therefore, since hydration structure and its dynamics around the SCN group of NTBA are likely to be different from those around SCN^-, we can expect that different behaviors of frequency fluctuations of the solutes are observed in 2D-IR measurements. In Chapter 5, in order to obtain microscopic information on water structure and its dynamics around the SCN vibrational probe, I performed classical MD simulations and related theoretical analyses for the NTBA/water and SCN^-/water systems. To obtain deeper information on local environment around NTBA and SCN^- in H_2O, I investigated hydration water structure around the SCN vibrational probe, solute-solvent HB dynamics, and single/collective reorientational motion of hydrated water molecules. Moreover, based on the theoretical framework developed by Cho group [113], I theoretically calculated the SCN vibrational frequency fluctuations of NTBA and SCN^- in H_2O from the MD simulations. By calculating the

radial-dependence of FFTCF and electrostatic potential for NTBA/water and SCN^-/water systems, finally, I established molecular-level pictures for the vibrational frequency fluctuations of NTBA and SCN^- in H_2O experimentally observed by 2D-IR spectroscopy.

In Chapter 6, I examined the vibrational dynamics of non-ionic and ionic N_3 groups in H_2O. For non-ionic vibrational probe molecules, I used Boc-3-azide-Ala-OH (dicyclohexylammonium) salt (abbreviated as N_3-Ala) and *N*-Boc-cis-4-azide-L-proline **(**dicyclohexylammonium**)** salt (abbreviated as N_3-Pro). Same as Chapter 4, from the comparison of the experimental results for N_3-labeled unnatural amino acids and azide anion, I studied the dependence of the vibrational dynamics on the electrical properties of the vibrational probe. Furthermore, while the N_3 group of N_3-Ala connects to an alkyl chain, that of N_3-Pro connects to a pyrrolidine ring. Consequently, I discussed the difference in the vibrational dynamics of N_3-Ala and N_3-Pro from the viewpoint of the structural degrees of freedom around the vibrational probe. In Chapter 7, in order to obtain deeper understanding on the effects of the structural degrees of freedom around a vibrational probe on the rotational relaxation process of a solute, I performed polarization-controlled IR pump-probe measurements for three different N_3-derivatized unnatural amino acids in primary 1-alcohol solutions. By comparing the viscosity- and temperature-dependence of the rotational relaxation dynamics of them in 1-alcohol solutions, I discussed the relationship between the N_3 rotational motion and the other internal rotational motions.

In Chapter 8, I examined the vibrational frequency fluctuations of the CO stretching modes of two different 9-FL derivatives (*i.e.* 9-fluorenone-2-carboxylic acid (abbreviated as 9-FL-2-COO^-) and 9-oxofluorene-4-carboxylic acid (abbreviated as 9-FL-4-COO^-)) in water by 2D-IR spectroscopy. The molecular structures around the vibrational probes are different between 9-FL-2-COO^- and 9-FL-4-COO^-: 9-FL-2-COO^- possesses a COO^- group closer to the vibrational probe than 9-FL-4-COO^-. Therefore, due to the strong electrostatic interactions between the negatively charged COO^- group and surrounding water molecules, water structure and its dynamics around the vibrational probe of 9-FL-2-COO^- may be affected more strongly than that of 9-FL-4-COO^-. Therefore, from the viewpoint of the structural difference in the position of the COO^- group, I discussed the difference in the vibrational frequency fluctuations of 9-FL-2-COO^- and 9-FL-4-COO^- in water. Furthermore, compared to the vibrational probe of NTBA, N_3-Ala and N_3-Pro, those of the two 9-FL derivatives are neighboring to large size of a hydrophobic group (*i.e.* fluorene ring). Therefore, I discussed the hydrophobic effect of the fluorene ring on

the vibrational frequency fluctuations of the solutes in water.

References

1. B. Bagchi, "*Water in Biological and Chemical Processes*", New York, Cambridge University Press (2013).

2. I. Ohmine and H. Tanaka, *Chem. Rev.*, **93**, 2545 (1993).

3. B. J. Gertner, K. R. Wilson, and J. T. Hynes, *J. Chem. Phys.*, **90**, 3537 (1989).

4. M. Yamakawa and R. Noyori, *J. Am. Chem. Soc.*, **117**, 6327 (1995).

5. A. J. Orr-Ewing, *Annu. Rev. Phys. Chem.*, **66**, 119 (2015).

6. C. G. Elles and F. F. Crim, *Annu. Rev. Phys. Chem.*, **57**, 273 (2006).

7. D. W. Oxtoby, *Annu. Rev. Phys. Chem.*, **32**, 77 (1981).

8. C. B. Harris, D. E. Smith, and D. J. Russell, *Chem. Rev.*, **90**, 481 (1990).

9. J. C. Owrutsky, D. Raftery, and R. M. Hochstrasser, *Annu. Rev. Phys. Chem.*, **45**, 519 (1994).

10. G. U. Bublitz and S. G. Boxer, *Annu. Rev. Phys. Chem*. **48**, 213 (1997).

11. S. Mukamel, *Annu. Rev. Phys. Chem.*, **51**, 691 (2000).

12. M. D. Fayer, *Annu. Rev. Phys. Chem.*, **52**, 315 (2001).

13. B. Bagchi, *Chem. Rev.*, **105**, 3197 (2003).

14. E. T. J. Nibbering and T. Elsaesser, *Chem. Rev.*, **104**, 1887 (2004).

15. R. R. Klaus, B. Møller, and J. T. Hynes, *Chem. Rev.*, **104**, 1915 (2004).

16. S. Mukamel and D. Abramavicius, *Chem. Rev.*, **104**, 2073 (2004).

17. E. T. J. Nibbering, H. Fidder, and E. Pines, *Annu. Rev. Phys. Chem.*, **56**, 337 (2005).

18. M. Cho, *Chem. Rev.*, **108**, 1331 (2008).

19. H. J. Bakker, *Chem. Rev.*, **108**, 1456 (2008).

20. M. D. Fayer, *Annu. Rev. Phys. Chem.*, **60**, 21 (2009).

21. H. J. Bakker and J. L. Skinner, *Chem. Rev.*, **110**, 1498 (2010).

22. H. Kim and M. Cho, *Chem. Rev.*, **113**, 5817 (2013).

23. T. Yagasaki and S. Saito, *Annu. Rev. Phys. Chem.*, **64**, 55 (2013).

24. N. F. A. van der Vegt, K. Haldrup, S. Roke, J. Zheng, M. Lund, H. J. Bakker, *Chem. Rev.*, **116**, 7626 (2016).

25. F. Perakis, L. D. Marco, A. Shalit, F. Fujie, T. Zachary, R. Kann, T. D. Kühne, R. Torre, M. Bonn, and Y. Nagata, *Chem. Rev.*, **116**, 7590 (2016).

26. K. Ohta and K. Tominaga, *Chem. Phys.*, **341**, 310 (2007).

27. P. F. Moluten, *J. Opt. Soc. Am. B.*, **3**, 125 (1986).

28. J. Goodberlet, J. Wang, J. G. Fujimoto, and P. A. Schulz, *Opt. Lett.*, **14**, 1125 (1989).

29. M. Ramaswamy, M. Ulman, J. Paye, and J. G. Fujimoto, *Opt. Lett.*, **18**, 1822 (1993).

30. R. A. Kaindl, M. Wurm, K. Reimann, P. Hamm, A. M. Weiner, and M. Woerner, *J. Opt. Soc. Am. B.*, **17**, 2086 (2000).

31. F. Seifert, V. Petrov, and M. Woerner, *Opt. Lett.*, **19**, 2009 (1994).

32. F. Rotermund, V. Petrov, and F. Noack, *Opt. Commu.*, **185**, 177 (2000).

33. D. M. Jonas, *Annu. Rev. Phys. Chem.*, **54**, 397 (2003).

34. S. Mukamel, *Ann. Rev. Phys. Chem.*, **51**, 691 (2000).

35. J. T. Fourkas, *Annu. Rev. Phys. Chem.*, **53**, 17 (2002).

36. D. Levesque, J. -J. Weis, and D. W. Oxtoby, *J. Chem. Phys.*, **79**, 917 (1983).

37. M. Li, J. Owrutsky, M. Sarisky, J. P. Culver, A. Yodh, and R. M. Hochstrasser, *J. Chem. Phys.*, **98**, 5499 (1993).

38. W. T. Grubbs, T. P. Dougherty, and E. J. Heilweil, *J. Phys. Chem.*, **99**, 10716 (1995).

39. R. Rey and J. T. Hynes, *J. Chem. Phys.*, **104**, 2356 (1996).

40. S. A. Egorov and J. L. Skinner, *J. Chem. Phys.*, **105,** 7047 (1996).

41. P. Hamm, M. Lim, and R. M. Hochstrasser, *J. Chem. Phys.*, **107**, 10523 (1997).

42. S. Woutersen, U. Emmerichs, H.-K. Nienhuys, and H. J. Bakker, *Phys. Rev. Lett.*, **81**, 1106 (1998).

43. A. Morita and S. Kato, *J. Chem. Phys.*, **109**, 5511 (1998).

44. R. Laenen, C. Rauscher, and A. Laubereau, *Phys. Rev. Lett.*, **80**, 2622 (1998).

45. R. Laenen, C. Rauscher, and A. Laubereau, *J. Phys. Chem. B*, **102**, 9304 (1998).

46. H.-K. Nienhuys, S. Woutersen, R. A. van Santen, and H. J. Bakker, *J. Chem. Phys.*, **111**, 1494 (1999).

47. S. Woutersen and H. J. Bakker, *Nature*, **402**, 507 (1999).

48. G. M. Gale, G. Gallot, F. Hache, N. Lascoux, S. Bratos, and J.-Cl. Leicknam, *Phys. Rev. Lett.*, **82**, 1068 (1999).

49. G. M. Gale, G. Gallot, and N. Lascoux, *Chem. Phys. Lett.*, **311**, 123 (1999).

50. J. C. Deàk, S. T. Rhea, L. K. Iwaki, and D. D. Dlott, *J. Phys. Chem. A*, **104**, 4866 (2000).

51. M. F. Kropman, H. -K. Nienhuys, S. Woutersen, and H. J. Bakker, *J. Phys. Chem. A*, **105**, 4622 (2001).

52. C. P. Lawrence and J. L. Skinner, *J. Chem. Phys.*, **117**, 5827 (2002).

53. Q. Zhong, A. P. Baronavski, and J. C. Owrutsky, *J. Chem. Phys.*, **119**, 9171 (2003).

54. G. M. Sando, Q. Zhong, and J. C. Owrutsky, *J. Chem. Phys.*, **121**, 2158 (2004).

55. Y. L. Rezus, D. Madson, and H. J. Bakker, *J. Chem. Phys.*, **121**, 10599 (2004).

56. M. Banno, S. Sato, K. Iwata, H. Hamaguchi, *Chem. Phys. Lett*, **412**, 464 (2005).

57. K. Ohta and K. Tominaga, *Chem. Phys. Lett*., **429**, 136 (2006).

58. S. Li, J. R. Schmidt, and J. L. Skinner, *J. Chem. Phys.*, **125**, 244507 (2006).

59. L. Piatkowski, K. B. Eisenthal, and H. J. Bakker, *Phys. Chem. Chem. Phys.*, **11**, 9033 (2009).

60. T. Yagasaki, J. Ono, and S. Saito, *J. Chem. Phys.*, **131**, 164511 (2009).

61. M. Yang, F. Li, and J. L. Skinner, *J. Chem. Phys.*, **135**, 164505 (2011).

62. K. -K. Lee, K. -H. Park, C. Joo, H. -J. Kwon, H. Han, J. -H. Ha, S. Park, and M. Cho, *Chem. Phys.*, **396**, 23 (2012).

63. H. Son, Y. Kwon, J. Kim, and S. Park, *J. Phys. Chem. B*, **117**, 2748 (2013).

64. S. Imoto, S. S. Xantheas, and S. Saito, *J. Phys. Chem. B*, **119**, 11068 (2015).

65. C. Lee, H. Son, and S. Park, *J. Phys. Chem. B*, **120**, 9723 (2016).

66. P. Hamm, M. Lim, and R. M. Hochstrasser, *Phys. Rev. Lett.*, **81**, 5326 (1998).

67. P. Hamm, M. Lim, W. F. DeGrado, and R. M. Hochstrasser, *J. Phys. Chem. A*, **103**, 10049 (1999).

68. M. T. Zanni, M. C. Asplund, and R. M. Hochstrasser, *J. Chem. Phys*., **114**, 5479 (2001).

69. S. Woutersen, R. Pfistrer, P. Hamm, Y. Mu, D. S. Kosov, and G. Stock, *J. Chem. Phys*., **117**, 6833 (2002).

70. N. -H. Ge, M. T. Zanni, and R. M. Hochstrasser, *J. Phys. Chem. A*, **106**, 962 (2002).

71. M. Kozinski, S. Garrett-Roe, and P. Hamm, *Chem. Phys.*, **341**, 5 (2007).

72. K. Ohta, H. Maekawa, S. Saito, and K. Tominaga, *J. Phys. Chem. A*, **107**, 5645 (2003).

73. J. B. Asbury, T. Steinel, K. Kwak, S. A. Corcelli, C. P. Lawrence, J. L. Skinner, and M. D. Fayer, *J. Chem. Phys.*, **121**, 12431 (2004).

74. K. Ohta, H. Maekawa, and K. Tominaga, *Chem. Phys. Lett.*, **386**, 32 (2004).

75. K. Ohta, H. Maekawa, and K. Tominaga, *J. Phys. Chem. A*, **108**, 1333 (2004).

76. H. Maekawa, K. Ohta, and K. Tominaga, *Res. Chem. Intermed.*, **31**, 703 (2005).

77. C. J. Fecko, J. J. Loparo, S. T. Loberts, and A. Tokmakoff, *J. Chem. Phys.*, **122**, 054506 (2005).

78. J. J. Loparo, S. T. Roberts, and A. Tokmakoff, *J. Chem. Phys.*, **125**, 194521 (2006).

79. K. Kwak, S. Park, I. J. Finkelstein, and M. D. Fayer, *J. Chem. Phys.*, **127**, 124503 (2007).

80. J. Tayama, M. Banno, K. Ohta, and K. Tominaga, *Sci. China: Phys., Mech. Astron.*, **53**, 1013 (2010).

81. J. Tayama, A. Ishihara, M. Banno, K. Ohta, S. Saito, and K. Tominag, *J. Chem. Phys*., **133**, 014505 (2010).

82. D. C. Urbanek, D. Y. Vorobyev, A. L. Serrano, F. Gai, and R. M. Hochstrasser, *J. Phys. Chem. Lett.*, **1**, 3311 (2010).

83. M. J. Tucker, X. S. Gai, E. E. Fenlon, S. H. Brewer, and R. M. Hochstrasser, *Phys. Chem. Chem. Phys.*, **13**, 2237 (2011).

84. J. K. Chung, C. Thielges, and M. D. Fayer, *Proc. Natl. Acad. Sci. U. S. A.*, **108**, 3578 (2011).

85. M. C. Thielges, J. Y. Axup, D.Wong, H. S. Lee, J. K. Chung, P. G. Schultz, and M. D. Fayer, *J. Phys. Chem. B*, **115**, 11294 (2011).

86. S. Dutta, W. Rock, R. J. Cook, A.Kohen, and C. M. Cheatum, *J. Phys. Chem.*, **135**, 055106 (2011).

87. S. Dutta, Y.-L. Li, W. Rock, J. C. D. Houtman, A.Kohen, and C. M. Cheatum, *J. Phys. Chem. B*, **116**, 542 (2012).

88. R. Bloem, K. Koziol, S. A. Waldauer, B. Buchli, R. Walser, B. Samatanga, I. Jesarov, and P. Hamm, *J. Phys. Chem. B*, **116**, 13705 (2012).

89. K. Ohta, J. Tayama, and K. Tominaga, *Phys. Chem. Chem. Phys.*, **14**, 10455 (2012).

90. J. Tayama, K. Ohta, and K. Tominaga, *Chem. Lett.*, **41**, 366 (2012).

91. K. Ohta, J. Tayama, S. Saito, and K. Tominaga, *Acc. Chem. Res.*, **45**, 1982 (2012).

92. D. Czurlok, M. von Domaros, M. Thomas, J. Gleim, J. Lindner, B. Kirchner, and P. Vohringer, *Phys. Chem. Chem. Phys.*, **17**, 29776 (2015).

93. R. Yuan, C. Yan, A. Tamimi, and M. D. Fayer, *J. Phys. Chem. B*, **119**, 13407 (2015).

94. S. Dutta, Z. Ren, T. Brinzer, and S. Garrett-Roe, *Phys. Chem. Chem. Phys.*, **17**, 26575 (2015).

95. D. Shaw, K. Adamczyk, P. W. J. M. Frederix, N. Simpson, K. Robb, G. M. 113. Greetham, M. Towrie, A. W. Parker, P. A. Hoskisson, and N. Hunt, *J. Chem. Phys.*, **142**, 212401 (2015).

96. R. Costard, T. Tyborski, B. P. Fingerhut, and T. Elsaesser, *J. Chem. Phys.*, **142**, 212406 (2015).

97. K. Inoue, S. Nihonyanagi, P. C. Singh, S. Yamaguchi, and T. Tahara, *J. Chem. Phys.*, **142**, 212432 (2015).

98. Q. Guo, P. Pagano, Y. -L. Li, A. Kohen, and C. M. Cheatum, *J. Chem. Phys.*, **142**, 212427 (2015).

99. T. Li, Y. Cui, J. Mathaga, R. Kumar, and D. G. Kuroda, *J. Chem. Phys.*, **142**, 212438 (2015).

100. J. P. Kraack, D. Lotti, and P. Hamm, *J. Chem. Phys.*, **142**, 212413 (2015).

101. K. Shinokita, A. V. Cunha, T. L. C. Jansen, and M. S. Pshenichnikov, *J. Chem. Phys.*, **142**, 212450 (2015).

102. K. M. Slenkamp, M. S. Lynch, J. F. Brookes, C. C. Bannan, S. L. Daifuku, and M. Khalil, *Struct. Dyn.*, **3**, 023609 (2016).

103. B. Guchhait, Y. Liu, T. Siebert, and T. Elsaesser, *Struct. Dyn.*, **3**, 043202 (2016).

104. K. F. Everitt, E. Geva, and J. L. Skinner, *J. Chem. Phys.*, **114**, 1326 (2001).

105. A. Piryatinski and J. L. Skinner, *J. Phys. Chem. B*, **106**, 8055 (2002).

106. K. Kwac and M. Cho, *J. Chem. Phys.*, **119**, 2247 (2003).

107. C. P. Lawrence and J. L. Skinner, *J. Chem. Phys.*, **118**, 264 (2003).

108. K. Kwac, H. Lee, and M. Cho, *J. Chem. Phys.*, **120**, 1477 (2004).

109. S. A. Corcelli, C. P. Lawrence, J. B. Asbury, T. Steinel, M. D. Fayer, and J. L. Skinner, *J. Chem. Phys.*, **121**, 8897 (2004).

110. S. A. Corcelli, C. P. Lawrence, and J. L. Skinner, *J. Chem. Phys.*, **120**, 8107 (2004).

111. J. D. Eaves, A. Tokmakoff, and P. L. Geissler, *J. Phys. Chem. A*, **109**, 9424 (2005).

112. B. Auer, R. Kumar, R. Schmidt, and J. L. Skinner, *Proc. Natl. Acad. Sci. U. S. A.* **104**, 14215 (2007).

113. K. -I. Oh, J.-H. Choi, J. -H. Lee, J. -B. Han, H. Lee, and M. Cho, *J. Chem. Phys.*, **128**, 154504 (2008).

114. J. -H Choi, K. -I Oh, and M. Cho, *J. Chem. Phys.*, **129**, 174512 (2012).

115. J. Jeon and M. Cho, *J. Phys. Chem. B*, **118**, 8148 (2014).

116. G. Prampolini, P. Yu, S. Pizzanelli, I. Cacelli, F. Yang, J. Zhao, and J.Wang, *J. Phys. Chem. B*, **118**, 14899 (2014).

117. B. P. Fingerhut, R. Costard, and T. Elsaesser, *J. Chem. Phys.*, **145**, 115101 (2016).

Figures

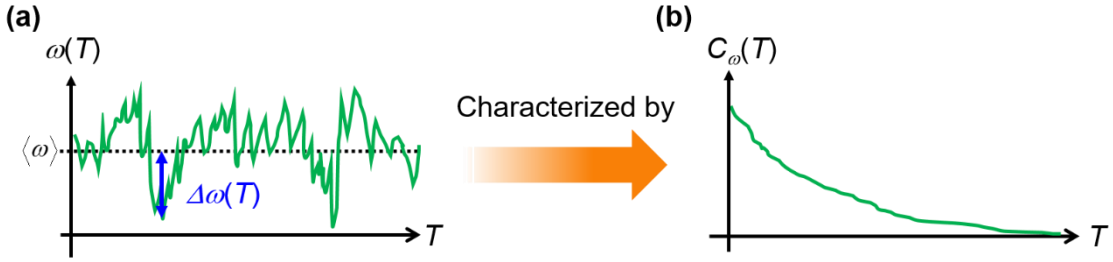

Figure 1.1. Schematic illustration of (a) time-dependent frequency fluctuation and (b) its time correlation function.

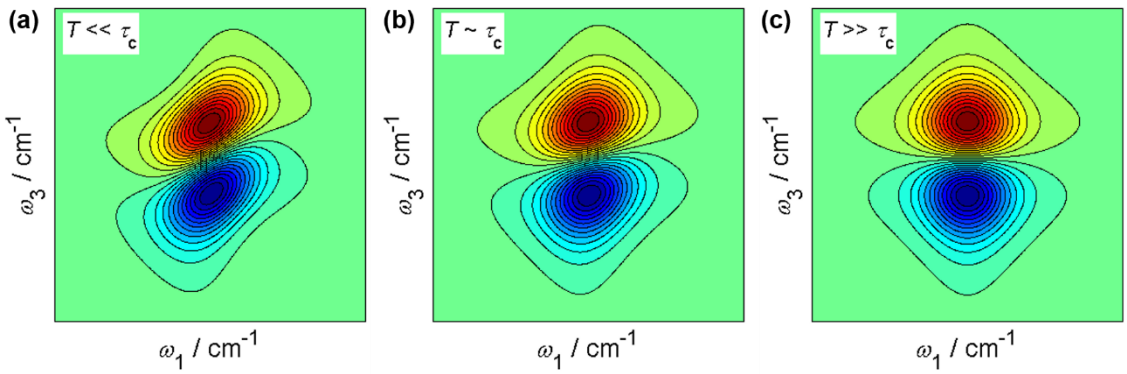

Figure 1.2. Schematic illustration of a 2D-IR spectrum at three different times T: (a) $T << \tau_c$, (b) $T \sim \tau_c$, (c) $T >> \tau_c$. The red and blue regions represent the positive and negative contributions of the 2D-IR spectrum, respectively. As time T increases, the lineshape of the 2D-IR spectrum changes from elliptic to round shapes, which reflects the loss of the correlation between the initial and final frequencies (ω_1 and ω_3, respectively).

CHAPTER 2.

Theoretical Background of Multi-pulse Experiments

2.1. Introduction

Since vibrational transitions are sensitive reporters of the local environment around the molecules, vibrational frequency fluctuations can be used to probe the molecular dynamics and interactions in condensed phase. Nonlinear infrared (IR) spectroscopy is a powerful tool to measure frequency fluctuations on a femtosecond time scale. So far, using nonlinear IR spectroscopy, numerous number of experimental [1-20] and theoretical [21-36] studies have been conducted to investigate the frequency fluctuations of vibrational probe molecules in liquids. In a nonlinear IR experiment, through the multiple matter-field interactions, we can track the temporal evolution of the coherence and/or population states in specific vibrational transitions, which are initially excited by the matter-field interaction. By controlling time delays between subsequent matter-field interactions, one can monitor the vibrational dynamics of interested systems. To understand the details of the solute-solvent interaction and solvation dynamics, it is necessary to quantify the correlation between initial (excited) and final (detected) vibrational transition frequencies. Such correlations can be represented by a time correlation function of vibrational frequency fluctuations ($C_\omega(t)$) defined as:

$$C_\omega(t) = \langle \Delta\omega(t)\Delta\omega(0) \rangle \tag{2.1}$$

where $\Delta\omega(t)$ represents the deviation in the instantaneous vibrational frequency ($\omega(t)$) from its time-averaged value ($<\omega>$): $\Delta\omega(t) = \omega(t) - <\omega>$. The $C_\omega(t)$ corresponds to the two point joint probability of finding a vibrational frequency of $\omega(t)$ at time t. Two-dimensional infrared (2D-IR) spectroscopy can resolve the correlation between the excited and detected vibrational frequencies with high time resolution. In other words, 2D-IR spectroscopy can monitor spectral diffusions in solution, in which the transition frequency of an initially excited vibrational mode is changed due to the time-dependent interactions with its environment. Moreover, the method can provide insight into chemical exchange. For instance, suppose that a molecule which initially forms a non-covalent bond (*e.g.* hydrogen bond) with another molecule. At later time, the bond of such a non-covalent bonded complex is broken by interactions with the surrounding solvents. If the dissociation leads to the vibrational frequency shifts, one can observe the spectral feature associated with the chemical exchange in the 2D-IR spectrum.

However, to obtain microscopic information on molecular dynamics in the condensed phase from 2D-IR experiments, numerical simulations based on the response function formula are often needed. Therefore, in this chapter, I summarized a theoretical background with respect

to the third-order nonlinear response functions and the related lineshape broadening functions. The following derivation is mainly based on the theoretical treatments of Nitzan [37], Mukamel [38], Cho [39], and Hamm and Zanni [40].

2.2. Equation Motion for Solute under Solute-solvent Interaction

The total Hamiltonian of a solute-solvent system (H) is represented by the sum of the molecular Hamiltonian (H_0) and perturbation Hamiltonian (H'):

$$\hat{H}(t) = \hat{H}_0(t) + \hat{H}'(t) \tag{2.2}$$

where H_0 represents the behavior of the system without an external electric fields, which is given by:

$$\hat{H}_0(t) = \hat{H}_{\mathrm{S}}(\hat{\mathbf{p}}, \hat{\mathbf{q}}) + \hat{H}_{\mathrm{B}}(\hat{\mathbf{P}}, \hat{\mathbf{Q}}). \tag{2.3}$$

Here, the H_{S} and H_{B} are the Hamiltonian of the solutes (denoted by subscript "S") and solvents (denoted by subscript "B"), respectively. The **p** and **q** denote the positions and momenta of the solutes, and the **P** and **Q** denote those of the solvents. The molecular Hamiltonian of independent harmonic oscillators is adopted as the Hamiltonian of the solutes:

$$\hat{H}_{\mathrm{S}}(\hat{\mathbf{p}}, \hat{\mathbf{q}}) = \sum_{i=1}^{N} \left(\frac{\hat{\mathbf{p}}_i^2}{2m} + m\omega_0^2 \hat{\mathbf{q}}_i^2 \right) \tag{2.4}$$

where m and ω_0 are the reduced masses and vibrational frequencies of the solutes, respectively, and N is the number of the solutes. For simplicity, the solution is supposed to contain a single solute (*i.e.* N = 1), unless mentioned. The solutes are assumed not to interact each other either directly or through their interaction with the bath. Here, let the basis set ({| ν>}, ν: non-negative integer) be the eigenstates with respect to the following time-independent Schrödinger equation:

$$\hat{H}_{\mathrm{S}}(\hat{\mathbf{p}}, \hat{\mathbf{q}}) |\nu\rangle = E_{\mathrm{S},\nu} |\nu\rangle \tag{2.5}$$

where $E_{\mathrm{S},\nu}$ represents the energy level of | ν>. On the other hand, perturbation Hamiltonian is assumed to be the sum of the solute-solvent interaction (H_{SB}) and the matter-field interaction (H_{Int}):

$$\hat{H}'(t) = \hat{H}_{\mathrm{SB}}(\hat{\mathbf{q}}, \hat{\mathbf{Q}}, t) + \hat{H}_{\mathrm{Int}}(t). \tag{2.6}$$

The functional form of the solute-solvent interaction is assumed by Eq. (2.49) and Eq. (2.67), and

the matter-field interaction is represented as follows:

$$\hat{H}_{\mathrm{Int}}(t) = -\sum_{i=1}^{N} \hat{\boldsymbol{\mu}}_i(t)\cdot\mathbf{E}(t) = -\sum_{i=1}^{N} \left(\bar{\boldsymbol{\mu}}_i(t)\cdot\bar{\mathbf{E}}(t)\right)\hat{\mu}_i E(t) \tag{2.7}$$

where $\boldsymbol{\mu}_i$ and $\mathbf{E}$ are the electric dipole moment of ith solute and an external laser pulse, respectively. The μ_i and $\bar{\boldsymbol{\mu}}_i$ are the magnitude and unit vector of the dipole moment, respectively, and the same for $\bar{\mathbf{E}}$ and E. Here, the rotational motion is assumed to be uncorrelated from the vibrational dynamics. Unless mentioned, assume that the polarization of $\mathbf{E}$ is parallel to the direction of $\boldsymbol{\mu}_i$ in order to ignore the dot-product of $\bar{\boldsymbol{\mu}}_i\cdot\bar{\mathbf{E}}$. An Electric field of the laser pulse, $E(t)$ is represented as follows:

$$E(t) = E_0(t)\exp\left[-i(\mathbf{k}\cdot\mathbf{r}-\omega t+\phi)\right] + E_0^*(t)\exp\left[i(\mathbf{k}\cdot\mathbf{r}-\omega t+\phi)\right] \equiv \varepsilon(t)+\varepsilon^*(t) \tag{2.8}$$

where E_0 is the pulse envelope, $\mathbf{k}$ is the wavevector which represents the propagating direction of the electric field, ω is the frequency, and ϕ is the phase. Ideally, laser pulses are enough short compared to any dynamics in solutions, which is so-called semi-impulsive limit. In this limit, $\varepsilon(t)$ can be represented by a δ-functions as:

$$\varepsilon(t) \propto \delta(t)\exp\left[-i(\mathbf{k}\cdot\mathbf{r}-\omega t+\phi)\right]. \tag{2.9}$$

The state of the solution at time t can be described by a density matrix (ρ). In the Schrödinger picture, the time evolution of the density matrix is determined by the Liouville-von Neumann equation:

$$\frac{\partial}{\partial t}\hat{\rho}_S(t) = -\frac{i}{\hbar}\left[\hat{H},\hat{\rho}_S(t)\right]. \tag{2.10}$$

First, by using unitary operator of $e^{-\frac{i}{\hbar}\hat{H}_0(t-t_0)}$ with a reference time (t_0), any valuables (A) are transformed from in the Schrödinger picture into the interaction picture (denoted by the subscript "I"):

$$\hat{A}_I(t) \equiv e^{-\frac{i}{\hbar}\hat{H}_0(t-t_0)}\hat{A}e^{\frac{i}{\hbar}\hat{H}_0(t-t_0)}. \tag{2.11}$$

Therefore, the Liouville-von Neumann equation in the interaction picture is given by:

$$\frac{\partial}{\partial t}\hat{\rho}_I(t) = -\frac{i}{\hbar}\left[\hat{H}_I'(t),\hat{\rho}_I(t)\right]. \tag{2.12}$$

Next, assume that the state of the solute-solvent system is represented by the direct product of those of the solute ($\rho^{(S)}$) and solvents ($\rho^{(B)}$):

$$\hat{\rho}(t) = \hat{\rho}^{(\mathrm{B})}(t)\hat{\rho}^{(S)}(t). \tag{2.13}$$

In order to obtain the equation of motion for the solute under the interaction with solvents, two projection operators are introduced as follows:

$$\hat{P}\hat{\rho}(t) = \hat{\rho}_0^{(\mathrm{B})}\mathrm{Tr}^{(\mathrm{B})}\left[\hat{\rho}(t)\right] = \hat{\rho}_0^{(\mathrm{B})}(t)\hat{\sigma}^{(\mathrm{S})}(t) \tag{2.14}$$

$$\hat{Q} = \hat{I} - \hat{P} \tag{2.15}$$

$$\hat{P}\hat{Q} = \hat{Q}\hat{P} = 0 \tag{2.16}$$

where $\mathrm{Tr}^{(\mathrm{B})}[\cdots]$ is the partial trace over the degrees of freedom of the solvents, $\rho_0^{(\mathrm{B})}$ is the reference density matrix of the bath, $\hat{I}$ is the identity operator, $\sigma^{(\mathrm{S})}$ is the reduced density matrix of the solute defined by:

$$\hat{\sigma}^{(\mathrm{S})}(t) \equiv \mathrm{Tr}^{(\mathrm{B})}\left[\hat{\rho}(t)\right]. \tag{2.17}$$

The $\hat{P}$ is an operator that projects the total density matrix operator on a product of the solute's reduced density matrix operator and solvent's density matrix operator. The $\hat{Q}$ is the complementary projection operator. By using the projection operators of $\hat{P}$ and $\hat{Q}$, the equation of motion for the solute, so-called quantum master equation, is given in the description of the interaction picture as:

$$\frac{\partial}{\partial t}\hat{\sigma}_{IS}^{(\mathrm{S})}(t) = -\frac{i}{\hbar}\left[\hat{\bar{H}}'_{IS}(t), \hat{\sigma}_{IS}^{(\mathrm{S})}(t)\right] - \left(\frac{i}{\hbar}\right)^2 \int_0^t d\tau \mathrm{Tr}^{(\mathrm{B})}\left[\hat{H}'_I(t), \hat{Q}\left[\hat{H}'_I(\tau), \hat{\rho}_{IB}^{(\mathrm{B})}(\tau)\hat{\sigma}_{IS}^{(\mathrm{S})}(\tau)\right]\right] \tag{2.18}$$

where

$$\hat{\bar{H}}'(t) = \mathrm{Tr}^{(\mathrm{B})}\left[\hat{H}'(t)\rho_{IB}^{(\mathrm{B})}(t)\right]. \tag{2.19}$$

and the subscript "*IS*" and "*IB*" in Eq. (2.18) represents the description in the interaction picture corresponding to the *P*-space and *Q*-space, respectively:

$$\hat{A}_{IS}^{(\mathrm{S})}(t) \equiv e^{-\frac{i}{\hbar}\hat{H}_{\mathrm{S}}(t-t_0)}\hat{A}^{(\mathrm{S})}e^{\frac{i}{\hbar}\hat{H}_{\mathrm{S}}(t-t_0)} \tag{2.20}$$

$$\hat{A}_{IB}^{(\mathrm{B})}(t) \equiv e^{-\frac{i}{\hbar}\hat{H}_{\mathrm{B}}(t-t_0)}\hat{A}^{(\mathrm{B})}e^{\frac{i}{\hbar}\hat{H}_{\mathrm{B}}(t-t_0)} \tag{2.21}$$

where $\hat{A}^{(\mathrm{S})}$ and $\hat{A}^{(\mathrm{B})}$ are any operators written in the Schrödinger picture for *P*-space and *Q*-space, respectively.

First, the solute-solvent interaction is so weak that the solvent states can be treated as approximately time-independent and the reference solvent state is in thermal equilibrium:

$$\hat{\rho}_0^{(\mathrm{B})}(t) = \hat{\rho}_{\mathrm{eq}}^{(\mathrm{B})} . \tag{2.22}$$

Second, in the first term in the right-hand side of Eq. (2.18), the matter-field interaction is independent of solvent states:

$$\hat{\bar{H}}'_{IS}(t) = \mathrm{Tr}^{(\mathrm{B})}\left[\left(\hat{H}_{\mathrm{SB},IS}\left(\hat{\mathbf{q}},\hat{\mathbf{Q}},t\right) + \hat{H}_{\mathrm{Int},IS}(t)\right)\rho_{\mathrm{eq}}^{(\mathrm{B})}\right] = \hat{\bar{H}}_{\mathrm{SB},IS}(\hat{\mathbf{q}}) + \hat{H}_{\mathrm{Int},IS}(t) . \tag{2.23}$$

Here, the first term, $\hat{\bar{H}}_{\mathrm{SB}}(\hat{\mathbf{q}})$, represents the thermally averaged solute-solvent interaction, which can only affect the eigenstates and associated energy levels of the solute. Hence, in order to include the correction associated with thermally averaged solvent effect, the Hamiltonian of the solute is redefined as follows:

$$\hat{H}_{\mathrm{S}}(\hat{\mathbf{p}},\hat{\mathbf{q}}) \equiv \hat{H}_{\mathrm{S}}(\hat{\mathbf{p}},\hat{\mathbf{q}}) + \hat{\bar{H}}_{\mathrm{SB}}(\hat{\mathbf{q}}) \tag{2.24}$$

and the eigenstates ({| ν_c >}, ν_c : non-negative integer) and associated energy levels ($E_{\mathrm{Sc},\nu}$) with respect to this renormalized Hamiltonian are represented as follows:

$$\hat{H}_{\mathrm{S}}(\hat{\mathbf{p}},\hat{\mathbf{q}})\left|\nu_c\right\rangle = E_{\mathrm{Sc},\nu}\left|\nu_c\right\rangle \tag{2.25}$$

$$E_{\mathrm{Sc},\nu} = E_{\mathrm{S},\nu} + \left\langle E_{\mathrm{SB}}^{(\mathrm{B})}\right\rangle \tag{2.26}$$

where $\langle E_{\mathrm{SB}}^{(\mathrm{B})}\rangle$ is the energy shift for the solute due to the thermally averaged solute-solvent interaction. Finally, in the second term, the matter-field interaction is uncorrelated to the *Q*-space:

$$\hat{Q}\hat{H}_{\mathrm{Int},I}(t) = \hat{H}_{\mathrm{Int},I}(t)\hat{Q} = 0 . \tag{2.27}$$

Therefore, by using Eq. (2.27) and cyclic permutation of $\mathrm{Tr}^{(\mathrm{B})}$, the integrand is written as follows:

$$\mathrm{Tr}^{(\mathrm{B})}\left[\hat{H}'_I(t),\hat{Q}\left[\hat{H}'_I(\tau),\hat{\rho}_{\mathrm{eq}}^{(\mathrm{B})}\hat{\sigma}_{IS}^{(\mathrm{S})}(\tau)\right]\right] = \mathrm{Tr}^{(\mathrm{B})}\left[\hat{H}_{\mathrm{SB},I}(t),\hat{Q}\left[\hat{H}_{\mathrm{SB},I}(\tau),\hat{\rho}_{\mathrm{eq}}^{(\mathrm{B})}\hat{\sigma}_{IS}^{(\mathrm{S})}(\tau)\right]\right] \tag{2.28}$$

Moreover, assume that solute-solvent interaction destroy the past memory of the solute, that is, the motion of the solute is determined by its present state (Markov approximation for a motion of the solute):

$$\mathrm{Tr}^{(\mathrm{B})}\left[\hat{H}_{\mathrm{SB},I}(t),\hat{Q}\left[\hat{H}_{\mathrm{SB},I}(\tau),\hat{\rho}_{\mathrm{eq}}^{(\mathrm{B})}\hat{\sigma}_{IS}^{(\mathrm{S})}(\tau)\right]\right]=\mathrm{Tr}^{(\mathrm{B})}\left[\hat{H}_{\mathrm{SB},I}(t),\hat{Q}\left[\hat{H}_{\mathrm{SB},I}(\tau),\hat{\rho}_{\mathrm{eq}}^{(\mathrm{B})}\hat{\sigma}_{IS}^{(\mathrm{S})}(t)\right]\right]. \quad (2.29)$$

By combining these three considerations together, the time evolution equation for the solute states are written in the description of the interaction picture as:

$$\begin{aligned}\frac{\partial}{\partial t}\hat{\sigma}_{\mathrm{c},IS}^{(\mathrm{S})}(t)=&-\frac{i}{\hbar}\left[\hat{H}_{\mathrm{Int},IS}(t),\hat{\sigma}_{\mathrm{c},IS}^{(\mathrm{S})}(t)\right]\\&-\left(\frac{i}{\hbar}\right)^2\int_0^t d\tau\,\mathrm{Tr}^{(\mathrm{B})}\left[\hat{H}_{\mathrm{SB},I}(\hat{\mathbf{p}},\hat{\mathbf{q}},t),\hat{Q}\left[\hat{H}_{\mathrm{SB},I}(\hat{\mathbf{p}},\hat{\mathbf{q}},\tau),\hat{\rho}_{\mathrm{eq}}^{(\mathrm{B})}\hat{\sigma}_{\mathrm{c},Is}^{(\mathrm{S})}(t)\right]\right]\end{aligned} \quad (2.30)$$

and in the description of the Schrödinger picture as:

$$\frac{\partial}{\partial t}\hat{\sigma}_{\mathrm{c}}^{(\mathrm{S})}(t)=-\frac{i}{\hbar}\left[\hat{H}_{\mathrm{S}},\hat{\sigma}_{\mathrm{c}}^{(\mathrm{S})}(t)\right]-e^{-\frac{i}{\hbar}\hat{H}_{\mathrm{S}}(t-t_0)}\left(\frac{\partial}{\partial t}\hat{\sigma}_{\mathrm{c},Is}^{(\mathrm{S})}(t)\right)e^{\frac{i}{\hbar}\hat{H}_{\mathrm{S}}(t-t_0)} \quad (2.31)$$

where $\sigma_{\mathrm{c}}^{(\mathrm{S})}$is the reduced density matrix of the solute with respect to the renormalized system Hamiltonian. Hereafter, for simplicity, the subscript "*c*" will be omitted. The first and second terms in the right-hand side of Eq. (2.30) reflect the different dynamics of the solute: The first term is related to optical responses of the solute to incident electric fields, that is, optical transitions of the solute. On the other hand, the second term is related to the relaxations of the solute, such as vibrational energy relaxation and dephasing. The first and second terms determine the center frequency of the absorption spectrum and the line broadening, respectively. In the next section, the detail discussions regarding to Eq. (2.30) are given.

2.3. Formalism of Absorption Spectrum of Solute

In this section, based on semi-impulsive limits (see Eq. (2.9)), I will discuss the optical response and relaxation processes. By combining them together, the *n*th-order nonlinear signal ($E_{\mathrm{sig}}^{(n)}$) can be represented as:

$$E_{\mathrm{sig}}^{(n)}(t_n,t_{n-1},\cdots,t_1)\propto R^{(n)}(t_n,t_{n-1},\cdots,t_1)\Gamma^{(n)}(t_n,t_{n-1},\cdots,t_1) \quad (2.32)$$

where $R^{(n)}$ and $\Gamma^{(n)}$ are the response function and line broadening function related to the *n*th-order nonlinear polarization, respectively. Moreover, the $\Gamma^{(n)}$ is decomposed into the following three components:

$$\Gamma^{(n)}(t_n,\cdots,t_1)=\Gamma_{\mathrm{Vib}}^{(n)}(t_n,\cdots,t_1)\Gamma_{\mathrm{Rot}}^{(n)}(t_n,\cdots,t_1)\Gamma_{\mathrm{Flu}}^{(n)}(t_n,\cdots,t_1) \quad (2.33)$$

where $\Gamma_{\mathrm{Vib}}^{(n)}$, $\Gamma_{\mathrm{Rot}}^{(n)}$, and $\Gamma_{\mathrm{Flu}}^{(n)}$ represent the spectral broadenings due to vibrational energy relaxation, rotational relaxation, and frequency fluctuation, respectively. The components of the

$\Gamma_{\mathrm{Vib}}^{(n)}$ and $\Gamma_{\mathrm{Rot}}^{(n)}$ cause homogeneous broadening of the absorption spectra of solutes. On the other hand, depending on dynamics of frequency fluctuations, the components of the $\Gamma_{\mathrm{Flu}}^{(n)}$ provides homogeneous and/or inhomogeneous broadenings.

First, the formalism of $R^{(n)}$ will be discussed in Section 2.3.1. Then, the formalism of line broadening functions, $\Gamma_{\mathrm{Vib}}^{(n)}$, $\Gamma_{\mathrm{Rot}}^{(n)}$, and $\Gamma_{\mathrm{Flu}}^{(n)}$ will be discussed in Section 2.3.3, Section 2.3.4, and Section 2.3.3, respectively.

2.3.1. Nonlinear Response Function and Signal Field

The differential equation of Eq. (2.30) without the second term is formally solved by integrating it with respect to time:

$$\hat{\sigma}_{IS}(t) = \hat{\sigma}_{IS}(t_0) - \frac{i}{\hbar}\int_{t_0}^{t} d\tau \left[\hat{H}_{\mathrm{Int},IS}(\tau), \hat{\sigma}_{IS}(t)\right] \tag{2.34}$$

where, for simplicity, the reduced density operator is denoted just as $\hat{\sigma}_{IS}(t)$. By iteratively plugging the solution for $\hat{\sigma}_{IS}(t)$ back into Eq. (2.34), the formal solution of $\hat{\sigma}_{IS}(t)$, that is, the perturbation expansion of $\hat{\sigma}_{IS}(t)$ is obtained as:

$$\begin{aligned}\hat{\sigma}_{IS}(t) = \hat{\sigma}_{IS}(t_0) + \sum_{n=1}^{\infty}\left(-\frac{i}{\hbar}\right)^n \int_{t_0}^{t} d\tau_n \int_{t_0}^{\tau_n} d\tau_{n-1} \\ \cdots \int_{t_0}^{\tau_2} d\tau_1 \left[\hat{H}_{\mathrm{Int},IS}(\tau_n), \left[\hat{H}_{\mathrm{Int},IS}(\tau_{n-1}), \cdots, \left[\hat{H}_{\mathrm{Int},IS}(\tau_1), \hat{\sigma}_{IS}(t_0)\right]\cdots\right]\right]\end{aligned} \tag{2.35}$$

Here, assume that $\sigma_{IS}(t_0)$ represents the solute states at thermal equilibrium, which does not evolve in time under the time evolution operator of $\hat{H}_{\mathrm{S}}$ (given by Eq. (2.24)), and t_0 is set to 0. Moreover, by changing the time variables from the absolute time points τ_i to the relative time intervals t_i (see Figure 2.1) and substituting Eq. (2.7) into $\hat{H}_{\mathrm{Int}}$, the final formalism with respect to $\hat{\sigma}_{IS}(t)$ is written in the description of the powers of E as:

$$\begin{aligned}\hat{\sigma}_{IS}(t_n, \cdots, t_1) = \hat{\sigma}_{IS}(0) + \sum_{n=1}^{\infty}\left(-\frac{i}{\hbar}\right)^n \int_0^{\infty} dt_n \cdots \int_0^{\infty} dt_1 E(t-t_n)\cdots E(t-t_n-t_{n-1}-\cdots-t_1) \\ \times \Theta(t_{n-1}, \cdots, t_0)\left[\hat{\mu}_{IS}(t_{n-1}+\cdots+t_1), \left[\cdots, \left[\hat{\mu}_{IS}(t_0), \hat{\sigma}(0)\right]\cdots\right]\right]\end{aligned} \tag{2.36}$$

where $\Theta(t)$ is the product of Heaviside step functions ($\theta(t)$) to reflect the fact that the nonlinear polarizations are created after the matter-field interactions.

$$\Theta(t_n,\cdots,t_1)\equiv\theta(t_n)\cdots\theta(t_1)=\prod_{i=1}^{n}\theta(t_i)\,. \tag{2.37}$$

Furthermore, by using Eq. (2.20), Eq. (2.36) is transformed into the Schrödinger picture:

$$\begin{aligned}\hat{\sigma}(t_n,\cdots,t_1)&=\hat{\sigma}(0)+\sum_{n=1}^{\infty}\left(-\frac{i}{\hbar}\right)^n\int_0^{\infty}dt_n\cdots\int_0^{\infty}dt_1E(t-t_n)\cdots E(t-t_n-t_{n-1}-\cdots-t_1)\Theta(t_{n-1},\cdots,t_0)\\&\qquad\times e^{-\frac{i}{\hbar}\hat{H}_{\mathrm{S}}(t_n+\cdots+t_0)}[\hat{\mu}_{IS}(t_{n-1}+\cdots+t_1),[\cdots,[\hat{\mu}_{IS}(t_0),\hat{\sigma}(0)]\cdots]]e^{\frac{i}{\hbar}\hat{H}_{\mathrm{S}}(t_n+\cdots+t_0)}\,.\\&\equiv\sum_{n=0}^{\infty}\hat{\sigma}^{(n)}(t_n,\cdots,t_1)\end{aligned} \tag{2.38}$$

where $\sigma^{(n)}$ is the nth-order reduced density matrix in terms of the powers of E and $\sigma^{(0)}$ is defined as $\sigma^{(0)}=\sigma(0)$.

In general, a macroscopic polarization (P) is defined as the expectation value of $\hat{\mu}$:

$$P(t)\equiv\langle\hat{\mu}\rangle=\mathrm{Tr}^{(\mathrm{T})}[\hat{\mu}\hat{\rho}(t)]\equiv\langle\hat{\mu}\hat{\rho}(t)\rangle^{(\mathrm{T})} \tag{2.39}$$

where $\mathrm{Tr}^{(\mathrm{T})}[\ldots]$ is the trace over the degrees of freedom of both the solutes and solvents. Note that, because $\mathrm{Tr}^{(\mathrm{T})}[\ldots]=\mathrm{Tr}^{(\mathrm{S})}[\mathrm{Tr}^{(\mathrm{B})}[\ldots]]$ ($\mathrm{Tr}^{(\mathrm{S})}[\ldots]$: partial trace over the degrees of freedom of the solutes), Eq. (2.39) is rewritten as follows:

$$P(t)=\mathrm{Tr}^{(\mathrm{S})}\left[\mathrm{Tr}^{(\mathrm{B})}[\hat{\mu}\hat{\rho}(t)]\right]=\mathrm{Tr}^{(\mathrm{S})}\left[\hat{\mu}\mathrm{Tr}^{(\mathrm{B})}[\hat{\rho}(t)]\right]=\mathrm{Tr}^{(\mathrm{S})}[\hat{\mu}\hat{\sigma}(t)]\equiv\langle\hat{\mu}\hat{\sigma}(t)\rangle^{(\mathrm{S})}\,. \tag{2.40}$$

Therefore, by substituting Eq. (2.38) into Eq. (2.40), after the proper cyclic permutation of the trace, a nth-order polarization ($P^{(n)}$) in powers of E is given by:

$$\begin{aligned}P^{(n)}(t_n,\cdots,t_1)&\equiv\langle\hat{\mu}\hat{\sigma}^{(n)}(t_n,\cdots,t_1)\rangle\\&=-\left(-\frac{i}{\hbar}\right)^n\int_0^{\infty}dt_n\int_0^{\infty}dt_{n-1}\cdots\int_0^{\infty}dt_1E(t-t_n)\cdots E(t-t_n-t_{n-1}-\cdots-t_1)\Theta(t_n,\cdots,t_0)\\&\qquad\times\langle\hat{\mu}_{IS}(t_n+t_{n-1}+\cdots+t_1)[\hat{\mu}_{IS}(t_{n-1}+\cdots+t_1),[\cdots,[\hat{\mu}_{IS}(t_0),\hat{\sigma}(0)]\cdots]]\rangle^{(\mathrm{S})}\\&=-\left(-\frac{i}{\hbar}\right)^n\int_0^{\infty}dt_n\cdots\int_0^{\infty}dt_1E_{n-1}\cdots E_0\\&\qquad\times\Theta(t_n,\cdots,t_0)\langle\hat{\mu}_{IS,n}[\hat{\mu}_{IS,n-1},[\cdots,[\hat{\mu}_{IS,0},\hat{\sigma}(0)]\cdots]]\rangle^{(\mathrm{S})}\\&\equiv\int_0^{\infty}dt_n\int_0^{\infty}dt_{n-1}\cdots\int_0^{\infty}dt_1E_{n-1}\cdots E_0R^{(n)}(t_n,\cdots,t_1)\end{aligned} \tag{2.41}$$

where, by convention, short notations are used for incident electric fields and dipole operators in the second line: $\mu_{IS,n}$ for $\mu_{IS}(t_n+t_{n-1}+\ldots+t_1)$ and E_n for $E(t-t_n-t_{n-1}-\ldots-t_1)$. Here, $R^{(n)}$ is the nth-order response function defined by:

$$R^{(n)}(t_n,\cdots,t_1) \equiv -\left(-\frac{i}{\hbar}\right)^n \Theta(t_n,\cdots,t_1) \times \left\langle \hat{\mu}_{IS}(t_n+t_{n-1}+\cdots+t_1)[\hat{\mu}_{IS}(t_{n-1}+\cdots+t_1),[\cdots,[\hat{\mu}_{IS}(t_0),\hat{\sigma}(0)]\cdots]]\right\rangle^{(S)} \tag{2.42}$$

where $\theta(t)$ is the Heaviside step function used for reflecting the fact that the nonlinear polarizations are created after the matter-field interactions.

Here, based on the Maxwell equation for the electric field with the slowly evolving wave approximation, the nth-order nonlinear polarization generates the corresponding signal field ($E^{(n)}_{\text{sig}}$) in the phase matching direction (given by Eq. (2.45)):

$$E^{(n)}_{\text{sig}}(t_n,\cdots,t_0) \propto iP^{(n)}(t_n,\cdots,t_0). \tag{2.43}$$

The frequency (ω_{sig}) and wavevector ($\mathbf{k}_{\text{sig}}$) of $E^{(n)}_{\text{sig}}$ are represented by the sum of the frequencies and wavevecors of input electric fields:

$$\omega_{\text{sig}} = \sum_{\text{input}} \omega_{\text{input}} = \pm\omega_1 \pm \omega_2 \pm \omega_3 \pm \cdots \tag{2.44}$$

$$\mathbf{k}_{\text{sig}} = \sum_{\text{input}} \mathbf{k}_{\text{input}} = \pm\mathbf{k}_1 \pm \mathbf{k}_2 \pm \mathbf{k}_3 \pm \cdots \tag{2.45}$$

where ω_i and $\mathbf{k}_i$ are the frequencies and wavevectors of ith incident electric field, respectively. The combinations of signs in Eq. (2.44) and Eq. (2.45) are determined by the rotating wave approximation. Therefore, based on the rotating wave approximation, the frequencies of incident electric fields are assumed to be the same as those of vibrational transition.

By using the eigenstates with the solute Hamiltonian defined by Eq. (2.25), $\hat{\sigma}(t)$ can be expressed as:

$$\hat{\sigma}(t) = \sum_{\nu,\nu'} \sigma_{\nu,\nu'}(t)|\nu\rangle\langle\nu'| \tag{2.46}$$

where $\sigma_{\nu,\nu'}$ is the (ν,ν') element of $\hat{\sigma}$. From the viewpoint of optical Bloch vector, the diagonal and off-diagonal elements of $\hat{\sigma}$ are related to the population distribution and quantum mechanical coherence of the solute, respectively. Consequently, the states $|\nu\rangle\langle\nu|$ and $|\nu\rangle\langle\nu'|$ ($\nu \neq \nu'$) are referred to as population state and coherent state, respectively. Then, because a solute at thermal equilibrium is in the lowest vibrational state, the density matrix operator of the solute at $t = t_0$ is assumed to be as:

$$\hat{\sigma}(t_0) = |0\rangle\langle 0|. \tag{2.47}$$

Moreover, using the vibrational selection rule of $\Delta\nu = \pm 1$, $\hat{\mu}_{IS}(t)$ can be expressed with the same description as $\hat{\sigma}$ by:

$$\begin{aligned}\hat{\mu}_{IS}(t) &= \sum_{\nu=0}^{\infty}\left(\mu_{\nu+1,\nu} e^{-\frac{i}{\hbar}H_{\hat{S}}(t-t_0)}\left|\nu\right\rangle\left\langle\nu+1\right| e^{\frac{i}{\hbar}H_{\hat{S}}(t-t_0)} + c.c.\right) \\ &= \sum_{\nu=0}^{\infty}\left(\mu_{\nu+1,\nu} e^{-i\omega_{\nu+1,\nu}}\left|\nu\right\rangle\left\langle\nu+1\right| + c.c.\right)\end{aligned} \tag{2.48}$$

where $\mu_{\nu+1,\nu}$ and $\omega_{\nu+1,\nu}$ are the transition dipole strength and vibrational transition frequency between the $|\nu+1\rangle$ and $|\nu\rangle$ states, respectively. Hereafter, an *n*th-order response function and related line broadening function will be derived with Eq. (2.47) and Eq. (2.48).

2.3.2. Line Broadening Function: Vibrational Energy Relaxation

In order to discuss the influence of solute-solvent interactions on temporal evolution of the solute density matrix, assume that the coordinate of the solute couple to those of the solvents in the linear manner [21-23, 41, 42]:

$$\hat{H}_{\mathrm{SB}}\left(\hat{\mathbf{q}},\hat{\mathbf{Q}},t\right) = \sum_{i=1}^{N}\left(\sum_{j=1}^{N'} f_{ij}(t)\hat{\mathbf{Q}}_j\right)\hat{\mathbf{q}}_i \tag{2.49}$$

where f_{ij} is the time-dependent coupling strength between the *i*th solute and *j*th solvent and N (again set $N = 1$) and N' are the numbers of solutes and solvents, respectively. By convention, the following notations are introduced:

$$\hat{V}^{(\mathrm{S1})} \equiv \hat{\mathbf{q}} \tag{2.50}$$

$$\hat{V}^{(\mathrm{B1})} \equiv \sum_{j=1}^{N'} f_{ij}(t)\hat{\mathbf{Q}}_j \ . \tag{2.51}$$

Here, assume that the solvents can be treated as a Markovian noise bath, *i.e.*, the dynamics of the solvents are much faster than those of the solutes [22]. Under this assumption, by plugging Eq. (2.49) in the notations given by Eq. (2.50) and Eq. (2.51) into Eq. (2.30) without the matter-field interaction term (*i.e.* $\hat{H}_{\mathrm{Int}} = 0$), after some calculations, the time evolution of $\hat{\sigma}^{(\mathrm{S})}$ is expressed in the representation defined by the eigenstates of the solute Hamiltonian as:

$$\frac{d\sigma_{ab}^{(\mathrm{S})}}{dt} = -i\omega_{ab}\sigma_{ab}^{(\mathrm{S})}(t) - \frac{\sigma_{ab}^{(\mathrm{S})}(t)}{T_{ab}} \tag{2.52}$$

where the subscript "a" and "b" indicate any eigenstates of the solute defined by Eq. (2.25). The time constant of T_{ab} in Eq. (2.52) is related to the vibrational lifetime of $|\, a >$ and $|\, b >$ states (denoted as T_{aa} and T_{bb}, respectively):

$$\frac{1}{T_{ab}} \equiv \frac{1}{2}\left(\frac{1}{T_{aa}} + \frac{1}{T_{bb}}\right) \tag{2.53}$$

$$\frac{1}{T_{ii}} = \sum_{i>j} \frac{1}{\hbar^2}\left|\hat{V}_{ij}^{(\mathrm{S1})}\right| \int_{-\infty}^{\infty} d\tau e^{-i\omega_{ij}\tau} \left\langle \delta\hat{V}_{IB}^{(\mathrm{B1})}(\tau)\delta\hat{V}_{IB}^{(\mathrm{B1})}(0)\right\rangle^{(\mathrm{B})} \tag{2.54}$$

where $V_{ij}^{(\mathrm{S1})} = \langle i|\hat{V}^{(\mathrm{S1})}|\, j\rangle$, $\delta\hat{V}_{IB}^{(\mathrm{B1})}(t) = \hat{V}_{IB}^{(\mathrm{B1})}(t) - \mathrm{Tr}^{(\mathrm{B})}\left[\hat{V}_{IB}^{(\mathrm{B1})}(t)\rho_{\mathrm{eq}}^{(\mathrm{B})}\right]$, and ω_{ij} is the vibrational transition frequency between $|\, i >$ and $|\, j >$ states. By integrating Eq. (2.52) with respect to time, the analytical solution is given as:

$$\sigma_{ab}^{(\mathrm{S})}(t) = \sigma_{ab}^{(\mathrm{S})}(t_0)\exp[-i\omega_{ab}(t-t_0)]\exp\left(-\frac{t-t_0}{T_{ab}}\right) \tag{2.55}$$

where t_0 is a reference time. Note that the oscillating term of $\exp[-i\omega_{ab}(t - t_0)]$ in Eq. (2.55) is corresponding to the term of $\exp[-i\omega_{\nu+1,\nu}(t - t_0)]$ in Eq. (2.48). Therefore, the vibrational line broadening function ($\Gamma_{\mathrm{Vib}}^{(n)}$) can be expressed in the description of relative time variables as:

$$\Gamma_{\mathrm{Vib}}^{(n)}(t_n, \cdots, t_1) = \exp\left[-\sum_{i=1}^{n}\frac{t_i}{T_{ab,i}}\right] \tag{2.56}$$

where $T_{ab,i}$ is the T_{ab} during t_i period.

2.3.3. Line Broadening Function: Rotational Relaxation

So far, the polarizations of incident electric fields are assumed to be parallel to the directions of dipole moment of solutes, that is, the term $\bar{\boldsymbol{\mu}}_i(t)\cdot\bar{\mathbf{E}}(t)$ in Eq. (2.7) is supposed to be unity. However, in actual situation, the orientations of solutes are randomly changing in time due to collisions with neighboring solvents, which causes the loss of rotational coherence to solutes.

When the time dependence of the relative orientation between a dipole moment and polarization of the incident electric field, that is $\bar{\boldsymbol{\mu}}_i(t)\cdot\bar{\mathbf{E}}(t)$, is taken into account, the formalism

of $P^{(n)}$ given by Eq. (2.41) is modified as:

$$\mathbf{P}^{(n)}(t_n,\cdots,t_1)\propto\int_0^\infty dt_n\int_0^\infty dt_{n-1}\cdots\int_0^\infty dt_1 E_{n-1}\cdots E_0\left\langle\prod_{i=0}^{n-1}\left(\overline{\boldsymbol{\mu}}_i\cdot\overline{\mathbf{E}}_i\right)\right\rangle^{(\mathrm{S})}$$
$$\times\Theta(t_n,\cdots,t_1)\overline{\boldsymbol{\mu}}_n\left\langle\hat{\mu}_{IS,n}\left[\hat{\mu}_{IS,n-1},\left[\cdots\left[\hat{\mu}_{IS,0},\hat{\sigma}(0)\right]\cdots\right]\right]\right\rangle^{(\mathrm{S})} \tag{2.57}$$

where rotational motions of the solutes are assumed to be uncorrelated from the vibrational motions of them. Note that, because the last dipole moment operator ($\overline{\boldsymbol{\mu}}_n\hat{\mu}_{IS,n}$) remains a vector, it provides a vectorial property to $\mathbf{P}^{(n)}$. In the semi-impulsive limits, in which electric fields are treated as δ-functions (see Eq. (2.9)), the convolution in Eq. (2.57) disappear:

$$\mathbf{P}^{(n)}(t_n,\cdots,t_1)\propto E_{n-1}\cdots E_0\left\langle\prod_{i=0}^{n-1}\left(\overline{\boldsymbol{\mu}}_i\cdot\overline{\mathbf{E}}_i\right)\right\rangle^{(\mathrm{S})}\Theta(t_n,\cdots,t_1)$$
$$\times\overline{\boldsymbol{\mu}}_n\left\langle\hat{\mu}_{IS,n}\left[\hat{\mu}_{IS,n-1},\left[\cdots,\left[\hat{\mu}_{IS,0},\hat{\sigma}(0)\right]\cdots\right]\right]\right\rangle^{(\mathrm{S})}. \tag{2.58}$$

When the signal field is heterodyne detected by a local oscillator (mentioned in Section 3.3.3), the observed signal ($S^{(n)}$) will be the dot-product between the signal field and local oscillator:

$$S^{(n)}(t_n,t_{n-1},\cdots,t_1)\propto\mathbf{E}_{\mathrm{sig}}^{(n)}(t_n,\cdots,t_1)\cdot\mathbf{E}_{\mathrm{LO}}(t_n-t_{LO})\propto i\mathbf{P}^{(n)}(t_n,\cdots,t_1)\cdot\mathbf{E}_{\mathrm{LO}}(t_n-t_{LO}) \tag{2.59}$$

where $\mathbf{E}_{\mathrm{LO}}(t)$ indicates the local oscillator, which is in the semi-impulsive limit as well. Therefore, by plugging Eq. (2.58) into Eq. (2.59), another dot-product appears:

$$S^{(n)}(t_n,t_{n-1},\cdots,t_1)\propto E_nE_{n-1}\cdots E_0\Gamma_{\mathrm{Rot}}{}^{(n)}(t_n,t_{n-1}\cdots,t_1)$$
$$\times\Theta(t_n,\cdots,t_1)\left\langle\hat{\mu}_{IS,n}\left[\hat{\mu}_{IS,n-1},\left[\cdots,\left[\hat{\mu}_{IS,0},\hat{\sigma}(0)\right]\cdots\right]\right]\right\rangle \tag{2.60}$$

where, based on the definition of short notation introduced in Eq. (2.41), $\mathbf{E}_{\mathrm{LO}}$ is represented as $\mathbf{E}_n$. Therefore, the rotational line broadening function ($\Gamma_{\mathrm{Rot}}{}^{(n)}$) is expressed as the orientational multi-point correlation function:

$$\Gamma_{\mathrm{Rot}}^{(n)}(t_n,\cdots,t_1)=\left\langle\prod_{i=0}^{n}\left(\overline{\boldsymbol{\mu}}_i\cdot\overline{\mathbf{E}}_i\right)\right\rangle^{(\mathrm{S})}. \tag{2.61}$$

Note that, due to the dot-products of $\overline{\boldsymbol{\mu}}_i\cdot\overline{\mathbf{E}}_i$ in Eq. (2.61), $\Gamma_{\mathrm{Rot}}{}^{(n)}$ depends on the polarizations of incident electric fields. Therefore, in order to represent the polarization dependence, $\Gamma_{\mathrm{Rot}}{}^{(n)}$ should be described as:

$$\mathrm{Y}_{IJKL\cdots}^{(n)}(t_n,\cdots,t_1)\equiv\Gamma_{\mathrm{Rot}}^{(n)}(t_n,\cdots,t_1). \tag{2.62}$$

Here, the polarizations of electric fields are supposed to be oriented along either axes of the

experimental frame (denoted as X, Y, and Z), and subscripts of $Y^{(n)}$ represent the polarization of each electric field.

In order to evaluate Eq. (2.60), it is necessary to consider the rotational diffusion of solutes between laser pulses. Based on the diffusion model for rotational motion, the time evolution of $G(\mathbf{\Omega}, \tau)$ can be modeled as [43]:

$$\frac{\partial G(\mathbf{\Omega}, t)}{\partial t} = -D\hat{J}^2 G(\mathbf{\Omega}, t) \tag{2.63}$$

where D is the rotational diffusion constant of the solutes, and $\hat{J}$ is the angular momentum operator. Moreover, $G(\mathbf{\Omega},t)$ is the distribution function corresponding to that the solutes are pointing in $\mathbf{\Omega}$ direction ($\mathbf{\Omega}$: spherical coordinates) after time t if the solutes start out to rotate from the $\mathbf{\Omega}_0$ direction. In other words, $G(\mathbf{\Omega},t)$ is interpreted as the time propagator with respect to the rotational diffusion of the solutes during t period.

$$G(\mathbf{\Omega}, t) \equiv G(\mathbf{\Omega}, t \mid \mathbf{\Omega}_0). \tag{2.64}$$

The solution of Eq. (2.63) can be expressed by a liner combination of the spherical harmonic functions $Y_{lm}(\mathbf{\Omega})$, which is the eigenfunction of the operator $\hat{J}^2$, as:

$$G(\mathbf{\Omega}, t \mid \mathbf{\Omega}_0) = \sum_{l,m} e^{-l(l+1)t} Y_{lm}(\mathbf{\Omega}_0) Y_{lm}^*(\mathbf{\Omega}). \tag{2.65}$$

Consequently, $Y^{(n)}$ can be expressed in the description of relative time coordinates as:

$$Y_{IJKL\cdots}^{(n)}(t_n, \cdots, t_1) = \left\langle \int d\mathbf{\Omega}_{n+1} \cdots \int d\mathbf{\Omega}_1 \left(\prod_{i=1}^{n} (\overline{\boldsymbol{\mu}}_i \cdot \overline{\mathbf{E}}_i) G(\mathbf{\Omega}_{i+1}, t_i \mid \mathbf{\Omega}_i) \right) (\overline{\boldsymbol{\mu}}_0 \cdot \overline{\mathbf{E}}_0) p(\mathbf{\Omega}_1) \right\rangle^{(S)} \tag{2.66}$$

where $p(\mathbf{\Omega}_1)$ is the initial probability density function. By assuming that solutes are randomly oriented before interacting with the first laser pulse, $p(\mathbf{\Omega}_1) = 1/4\pi$.

2.3.4. Line Broadening Function: Frequency Fluctuations

In this section, to discuss the effect of higher order solute-solvent interaction, let the coordinate of the solute couple to those of the solvents in the nonlinear manner [21-23, 41, 42]:

$$\hat{H}_{\mathrm{SB}}(\hat{\mathbf{q}}, \hat{\mathbf{Q}}, t) = \sum_{i=1}^{N} \left(\sum_{j=1}^{N'} g_{ij}(t) \hat{\mathbf{Q}}_j \right) \hat{\mathbf{q}}_i^2 \tag{2.67}$$

where g_{ij} is the time-dependent coupling strength between the ith solute and jth solvent as well.

Again, by convention, the following notations are introduced:

$$\hat{V}^{(\mathrm{S2})} \equiv \hat{\mathbf{q}}^{2} \tag{2.68}$$

$$\hat{V}^{(\mathrm{B2})} \equiv \sum_{j=1}^{N'} g_{ij}(t)\hat{\mathbf{Q}}_{j}. \tag{2.69}$$

Same as in Section 2.3.2, from Eq. (2.30), Eq. (2.68), and Eq. (2.69), the time dependence of $\hat{\sigma}^{(\mathrm{S})}$ is written in the description of the eigenstates of the solute Hamiltonian as:

$$\frac{d\sigma_{ab}^{(\mathrm{S})}}{dt} = -i\omega_{ab}\sigma_{ab}^{(\mathrm{S})}(t) - \left[\int_{0}^{\infty} dt' \left\langle \delta\omega_{ab}(t')\delta\omega_{ab}(0)\right\rangle^{(\mathrm{B})}\right]\sigma_{ab}^{(\mathrm{S})}(t) \tag{2.70}$$

where $\delta\omega_{ab}$ is the instantaneous frequency shift of the vibrational transition between $|\, a >$ and $|\, b >$ states:

$$\delta\omega_{ab}(t) \equiv \frac{\left(V_{aa}^{(\mathrm{S2})} - V_{bb}^{(\mathrm{S2})}\right)\delta V^{(\mathrm{B2})}(t)}{\hbar} \tag{2.71}$$

where $V_{ii}^{(\mathrm{S2})} = \left\langle i \middle| \hat{V}^{(\mathrm{S2})} \middle| i \right\rangle$, $\delta\hat{V}_{IB}^{(\mathrm{B2})}(t) = \hat{V}_{IB}^{(\mathrm{B2})}(t) - \mathrm{Tr}^{(\mathrm{B})}\left[\hat{V}_{IB}^{(\mathrm{B2})}(t)\rho_{\mathrm{eq}}^{(\mathrm{B})}\right]$. It should be noted that because Eq. (2.70) for population states (*i.e.* $|\, a > = |\, b >$) becomes a trivial differential equation: $d\sigma_{ab}^{(\mathrm{S})}/dt = 0$, consider this motion equation only for coherent states (*i.e.* $|\, a > \neq |\, b >$).

Here, assume that the fluctuating term of the solute-solvent interaction (*i.e.* $\delta V^{(\mathrm{B2})}$) is statistically Gaussian distributed in time. By using this assumption, $\delta V^{(\mathrm{B2})}(t)$ can be replaced with a stochastic scalar function $R^{(\mathrm{B2})}(t)$, whose the time-averaged value is zero (*i.e.* $< R^{(\mathrm{B2})}(t) > = 0$). So far, the vibrational transition frequencies of solutes are implicitly assumed to be time-independent. However, Eq. (2.70) indicates that temporal frequency fluctuations due to the fluctuations of solute-solvent interactions destroy the coherence of the solute. Therefore, in order to take the effects of frequency fluctuations into account for the time evolution of solute density matrix, a time-dependent vibrational transition frequency ($\omega_{ab}(t)$) between $|\, a >$ and $|\, b >$ states is defined as follows:

$$\omega_{ab}(t) \equiv \omega_{ab} + \delta\omega_{ab}(t) \tag{2.72}$$

where ω_{ab} and $\delta\omega_{ab}(t)$ are the time-averaged vibrational transition frequency and its temporal

fluctuations, respectively. Here, the distribution of $\delta\omega_{ab}(t)$ is assumed to be Gaussian. Therefore, based on this procedure, Eq. (2.70) is rewritten as:

$$\frac{d\sigma_{ab}^{(\mathrm{S})}}{dt} = -i\left(\omega_{ab} + \delta\omega_{ab}(t)\right)\sigma_{ab}^{(\mathrm{S})}(t). \tag{2.73}$$

By formally integrating Eq. (2.73) with respect to time, the solution is given as:

$$\sigma_{ab}^{(\mathrm{S})}(t) = \sigma_{ab}^{(\mathrm{S})}(t_0)\exp\left[-i\omega_{ab}(t-t_0)\right]\exp\left[-i\int_{t_0}^{t} dt'\delta\omega_{ab}(t')\right] \tag{2.74}$$

where t_0 is a reference time. Hence, the ensemble average of the density matrix over the solvent states has to be considered:

$$\left\langle \sigma_{ab}^{(\mathrm{S})}(t)\right\rangle^{(\mathrm{B})} = \left\langle \sigma_{ab}^{(\mathrm{S})}(t_0)\right\rangle^{(\mathrm{B})}\exp\left[-i\omega_{ab}(t-t_0)\right]\left\langle \exp\left[-i\int_{t_0}^{t} dt'\delta\omega_{ab}(t')\right]\right\rangle^{(\mathrm{B})}. \tag{2.75}$$

Here, again, the oscillating term of $\exp[-i\omega_{ab}(t-t_0)]$ is corresponding to the term of $\exp[-i\omega_{v+1,v}(t-t_0)]$ in Eq. (2.48). Therefore, by replacing the vibrational transition frequency of ω_{ab} with the following term, the effect of frequency fluctuations can be considered:

$$\exp\left[\pm i\omega_{ab}(t-t_0)\right] \rightarrow \exp\left[\pm i\omega_{ab}(t-t_0)\right]\left\langle \exp\left[\pm i\int_{t_0}^{t} dt'\delta\omega_{ab}(t')\right]\right\rangle^{(\mathrm{B})}. \tag{2.76}$$

Therefore, based on Eq. (2.76), the line broadening function related to frequency fluctuations ($\Gamma_{\mathrm{Flu}}^{(n)}$) is expressed in the description of relative time coordinates as:

$$\Gamma_{\mathrm{Flu}}^{(n)}(t_n, t_{n-1}, \cdots, t_1) = \exp\left[\left\langle \sum_{\substack{i=1\\(a\neq b)}}^{n-1} \exp\left[i\xi_i \int_{t_i+\cdots+t_1}^{t_{i+1}+\cdots+t_1} dt'\delta\omega_{ab,i}(t')\right]\right\rangle^{(\mathrm{B})}\right] \tag{2.77}$$

where $\delta\omega_{ab,i}$ and ξ_i is the temporal fluctuations in vibrational transition frequency between $|a>$ and $|b>$ states and phase sign during t_i period, respectively.

Before closing this section, it should be noted that, by using the cumulant expansion truncated after the second order, a line shape function $g(t)$ is defined as follows [44]:

$$\left\langle \exp\left[-i\int_{0}^{t} dt'\delta\omega_{ab}(t')\right]\right\rangle^{(\mathrm{B})} = \exp\left[-g(t)\right] \tag{2.78}$$

and

$$g(t) \equiv \int_0^t dt' \int_0^t dt'' \langle \delta\omega(t'')\delta\omega(0) \rangle^{(\mathrm{B})} \tag{2.79}$$

where $<\delta\omega(t)\delta\omega(0)>$ is referred to as a frequency-frequency time correlation function (FFTCF). Kubo introduced the following exponential function to model a FFTCF [45]:

$$\langle \delta\omega(t)\delta\omega(0) \rangle^{(\mathrm{B})} = \Delta\omega^2 \exp\left(-|t|/\tau_{\mathrm{c}}\right) \tag{2.80}$$

where $\Delta\omega$ and τ_{c} are the amplitude and correlation time of the frequency fluctuations, respectively. And, its $g(t)$ is given by Eq. (2.79) as:

$$g(t) = (\Delta\omega \cdot \tau_{\mathrm{c}})^2 \left[\exp(-t/\tau_{\mathrm{c}}) + \frac{t}{\tau_{\mathrm{c}}} - 1 \right]. \tag{2.81}$$

In the fast modulation limits ($\Delta\omega \cdot \tau_c << 1$), Eq. (2.81) becomes:

$$g(t) = \frac{t}{\left(\Delta\omega^2 \tau_{\mathrm{c}}\right)^{-1}} \equiv \frac{t}{T_2^*} \tag{2.82}$$

where T_2^* is a pure dephasing constant. In this limit, the absorption spectra of the solutes will be represented by a Lorentzian function with the band width of T_2^*. On the other hand, in the slow modulation limits ($\Delta\omega \cdot \tau_{\mathrm{c}} >> 1$), Eq. (2.81) becomes:

$$g(t) = \frac{\Delta\omega^2}{2} t^2 . \tag{2.83}$$

In this limit, the absorption spectra of the solutes will be represented by a Gaussian function with the band width $\Delta\omega$.

2.4. Theoretical Background of 2D-IR Spectroscopy

In previous sections, the *n*th-order nonlinear response function and related line broadening functions are formalized. In this section, based on those results, the theoretical treatment of 2D-IR spectroscopy is discussed.

2.4.1. Double-side Feynman Diagram

Before discussing 2D-IR spectroscopy, briefly, a double-side Feynman diagram is introduced in this section. In order to consider the time evolution of density matrices under the matter-field interactions, double side Feynman diagrams provide physically clear pictures.

In order to demonstrate how to draw double-side Feynman diagrams, as an example, let us consider the linear polarization ($P^{(1)}$), which is given by Eq. (2.41):

$$P^{(1)}(t) \equiv \int_0^\infty dt_1 E(t-t_1) R^{(1)}(t_1) = \int_0^\infty dt_1 \left(\varepsilon_0 + \varepsilon_0^*\right) R^{(1)}(t_1) \tag{2.84}$$

and the linear response function ($R^{(1)}$) is obtained from Eq. (2.42) as:

$$R^{(1)}(t_1) \propto \theta(t_1)\left(\left\langle \hat{\mu}_{IS,1}\hat{\mu}_{IS,0}\hat{\sigma}(t_0)\right\rangle^{(\mathrm{S})} - \left\langle \hat{\sigma}(t_0)\hat{\mu}_{IS,0}\hat{\mu}_{IS,1}\right\rangle^{(\mathrm{S})}\right) \equiv R_1^{(1)}(t_1) + R_1^{(1)*}(t_1) \tag{2.85}$$

$$R_1^{(1)}(t) = \theta(t)\left|\mu_{10}\right|^2 e^{-i\omega_{10}t} \tag{2.86}$$

where, by convention, the cyclic permutation of the trace is used in order to write the two terms in a symmetric manner. The μ_{10} and ω_{10} are the transition dipole strength and vibrational transition frequency between the vibrational states of | 0 > and | 1 > states, respectively. Note that, for simplicity, the ω_{10} is treated as a time-independent constant and any line broadening functions are neglected. By plugging Eq. (2.85) into Eq. (2.84), the following four terms are obtained:

$$P^{(1)}(t) \propto R_1^{(1)}(t_1)\varepsilon_0 + R_1^{(1)}(t_1)\varepsilon_0^* - R_1^{(1)*}(t_1)\varepsilon_0 - R_1^{(1)*}\varepsilon_0^* . \tag{2.87}$$

Figure 2.2 describes the double-side Feynman diagrams corresponding to each term in Eq. (2.87). In the diagrams, two vertical lines indicate the time evolution of $|\nu>$ and $<\nu|$ of the density matrix of the solute and time flows from the bottom to the top. Interactions with $\hat{\mu}$ at a given time are represented by yellow arrows, which are regarded as input electric fields. Here, because the last interaction with $\hat{\mu}$, which is originated from $\left\langle \hat{\mu}\hat{\rho}(t)\right\rangle^{(\mathrm{T})}$, creates the output electric field (*i.e.* $E_{\mathrm{sig}}^{(n)}$ emitted from the solute), the last arrow is indicated by blue arrow. Yellow arrows pointing to the right and left are related to the $\varepsilon(t)$ and $\varepsilon^*(t)$, respectively. It should be noted that, based on the rotating wave approximation, arrows pointing toward and outward the diagram can be interpreted as the excitation and de-excitation of vibrational states, respectively. Therefore, the diagrams (a) and (c) in Figure 2.2 can survive the rotating wave approximation, and the sum of the components generates $P^{(1)}$. Because the diagram (c) is just complex conjugate of diagram (a), hereafter, diagrams with blue arrow only from $|\nu>$ will be considered.

2.4.2. Third-order Nonlinear Response Function

From Eq. (2.41) and Eq. (2.42), the third-order nonlinear polarization ($P^{(3)}$) and third-order nonlinear response function ($R^{(3)}$) are given by:

$$\begin{aligned} P^{(3)}(t) &\equiv \int_0^\infty dt_3 \int_0^\infty dt_2 \int_0^\infty dt_1 E(t-t_3)E(t-t_3-t_2)E(t-t_3-t_2-t_1)R^{(3)}(t_1,t_2,t_3) \\ &= \int_0^\infty dt_3 \int_0^\infty dt_2 \int_0^\infty dt_1 (\varepsilon_2+\varepsilon_2^*)(\varepsilon_1+\varepsilon_1^*)(\varepsilon_0+\varepsilon_0^*)R^{(3)}(t_1,t_2,t_3) \end{aligned} \tag{2.88}$$

$$\begin{aligned} R^{(3)}(t_1,t_2,t_3) &\equiv -\left(\frac{i}{\hbar}\right)^3 \Theta(t_3,t_2,t_1)\left\langle \hat{\mu}_{IS}(t_3+t_2+t_1)\left[\hat{\mu}_{IS}(t_2+t_1),\left[\hat{\mu}_{IS}(t_1),\left[\hat{\mu}_{IS}(t_0),\hat{\sigma}^{(S)}(0)\right]\right]\right]\right\rangle^{(S)} \\ &\propto \Theta(t_3,t_2,t_1)\left\langle \hat{\mu}_{IS,3}\left[\hat{\mu}_{IS,2},\left[\hat{\mu}_{IS,1},\left[\hat{\mu}_{IS,0},\hat{\sigma}^{(S)}(0)\right]\right]\right]\right\rangle^{(S)}. \end{aligned} \tag{2.89}$$

By expanding the commutators in Eq. (2.89), the following 16 terms are obtained:

$$\begin{aligned} R^{(3)}(t_1,t_2,t_3) \propto\ & \Theta(t_3,t_2,t_1)\left(\left\langle \hat{\mu}_{IS,3}\hat{\mu}_{IS,1}\hat{\sigma}^{(S)}(0)\hat{\mu}_{IS,0}\hat{\mu}_{IS,2}\right\rangle^{(S)} - c.c.\right) \quad \Rightarrow \quad R_1^{(3)} + R_1^{(3)*} \\ &+ \Theta(t_3,t_2,t_1)\left(\left\langle \hat{\mu}_{IS,3}\hat{\mu}_{IS,2}\hat{\sigma}^{(S)}(0)\hat{\mu}_{IS,0}\hat{\mu}_{IS,1}\right\rangle^{(S)} - c.c.\right) \quad \Rightarrow \quad R_2^{(3)} + R_2^{(3)*} \\ &- \Theta(t_3,t_2,t_1)\left(\left\langle \hat{\mu}_{IS,3}\hat{\mu}_{IS,2}\hat{\mu}_{IS,1}\hat{\sigma}^{(S)}(0)\hat{\mu}_{IS,0}\right\rangle^{(S)} - c.c.\right) \quad \Rightarrow \quad R_3^{(3)} + R_3^{(3)*} \\ &+ \Theta(t_3,t_2,t_1)\left(\left\langle \hat{\mu}_{IS,3}\hat{\mu}_{IS,0}\hat{\sigma}^{(S)}(0)\hat{\mu}_{IS,1}\hat{\mu}_{IS,2}\right\rangle^{(S)} - c.c.\right) \quad \Rightarrow \quad R_4^{(3)} + R_4^{(3)*} \\ &+ \Theta(t_3,t_2,t_1)\left(\left\langle \hat{\mu}_{IS,3}\hat{\mu}_{IS,2}\hat{\mu}_{IS,1}\hat{\mu}_{IS,0}\hat{\sigma}^{(S)}(0)\right\rangle^{(S)} - c.c.\right) \quad \Rightarrow \quad R_5^{(3)} + R_5^{(3)*} \\ &- \Theta(t_3,t_2,t_1)\left(\left\langle \hat{\mu}_{IS,3}\hat{\mu}_{IS,1}\hat{\sigma}^{(S)}(0)\hat{\mu}_{IS,0}\hat{\mu}_{IS,2}\right\rangle^{(S)} - c.c.\right) \quad \Rightarrow \quad R_6^{(3)} + R_6^{(3)*} \\ &+ \Theta(t_3,t_2,t_1)\left(\left\langle \hat{\mu}_{IS,3}\hat{\mu}_{IS,2}\hat{\mu}_{IS,1}\hat{\mu}_{IS,0}\hat{\sigma}^{(S)}(0)\right\rangle^{(S)} - c.c.\right) \quad \Rightarrow \quad R_7^{(3)} + R_7^{(3)*} \\ &- \Theta(t_3,t_2,t_1)\left(\left\langle \hat{\mu}_{IS,3}\hat{\mu}_{IS,1}\hat{\mu}_{IS,0}\hat{\sigma}^{(S)}(0)\hat{\mu}_{IS,2}\right\rangle^{(S)} - c.c.\right) \quad \Rightarrow \quad R_8^{(3)} + R_8^{(3)*} \end{aligned} \tag{2.88}$$

where the cyclic permutations of the trace are used again and each combination and its complex conjugate are referred to as $R_i^{(3)}$ and $R_i^{(3)*}$ ($i = 1 - 8$), respectively. Figure 2.3 displays the double-side Feynman diagrams of the $R_1^{(3)} - R_8^{(3)}$ response functions. By applying the rotating wave approximation, the combinations of electric fields are determined as $\varepsilon_1^*\varepsilon_2\varepsilon_3$ for $R_{1\text{-}3}^{(3)}$, $\varepsilon_1\varepsilon_2^*\varepsilon_3$ for $R_{4\text{-}6}^{(3)}$, and $\varepsilon_1\varepsilon_2\varepsilon_3^*$ for $R_{7\text{-}8}^{(3)}$.

From the viewpoint of phase matching condition of $P^{(3)}$, the $R_1^{(3)}$ – $R_8^{(3)}$ response functions can be separated into the following three categories: Eq. (2.45) gives $\mathbf{k}_{sig} = -\mathbf{k}_1 + \mathbf{k}_2 + \mathbf{k}_3$ for the $R_{1\text{-}3}^{(3)}$ response functions, $\mathbf{k}_{sig} = +\mathbf{k}_1 - \mathbf{k}_2 + \mathbf{k}_3$ for the $R_{4\text{-}6}^{(3)}$ response functions, and $\mathbf{k}_{sig} = +\mathbf{k}_1 + \mathbf{k}_2 - \mathbf{k}_3$ for the $R_{7\text{-}8}^{(3)}$ response functions. The $R_{1\text{-}3}^{(3)}$ and $R_{4\text{-}6}^{(3)}$ response functions are referred to as rephasing and non-rephasing response functions, respectively, of which the physical interpretations are discussed later.

As shown in Figure 2.3, while the coherence only between neighboring vibrational states (either | 0 > and | 1 > states or | 1 > and | 2 > states) are created in the $R_{1\text{-}6}^{(3)}$ diagrams, those between | 0 > and | 2 > states are created in the $R_{7\text{-}8}^{(3)}$ diagrams. Hence, generally, the $R_{7\text{-}8}^{(3)}$ response functions are called two-quantum response functions. When all incident electric fields temporally overlap with each other, the two-quantum response functions can contribute to $P^{(3)}$. However, because $P^{(3)}$ resulted from the two-quantum response functions oscillate at higher frequencies than those from the rephasing and non-rephasing response functions, the contribution can be separated by performing a Fourier transformation. Therefore, hereafter, $R_{7\text{-}8}^{(3)}$ response functions will not be considered.

For the $R_1^{(3)}$ and $R_4^{(3)}$ response functions, as examples of the rephasing and non-rephasing response functions, the first matter-field interactions create the coherence between | 0 > and | 1 > states. If many solutes (*i.e.* $N \neq 1$) exist in an inhomogeneous environment, such as condensed phase, this corresponds to the excitation of them with slightly different vibrational transition frequencies due to the different magnitude of solute-solvent interactions (see Section 2.3.4). Because the coherence of each solute oscillates at its vibrational transition frequency, the magnitude the ensemble average, that is $<\sigma_{01}^{(S)}(t)>$ in Eq. (2.75), is decaying during t_1 period (*i.e.* dephasing). The third matter-field interaction again creates the coherence between | 0 > and | 1 > states. Note that, during t_3 period, while the coherence of the solutes in the $R_1^{(3)}$ diagram oscillates in opposite sign to that during t_1 period (see Figure 2.4(a)), that in the $R_1^{(4)}$ diagram oscillate in the same sign (see Figure 2.4(b)). Therefore, for the $R_1^{(3)}$ diagram, $<\sigma_{01}^{(S)}(t)>$ rephases during this period and a complete rephasing of the original coherence will be achieved at $t_3 = t_1$. Physically, the rephasing of the original coherence is interpreted as the macroscopic alignment of the transition dipoles of the solutes. When this alignment happens, a macroscopic polarization is created by the solutes, which generates the corresponding signal field, so-called vibrational echo signal. On the other hand, for the $R_4^{(3)}$ diagram, this phenomena never happens. From this point

of view, $R_1^{(3)}$ and $R_4^{(3)}$ diagrams are referred to as rephasing and non-rephasing diagrams, respectively.

It should be noted that, during t_2 period in which the solutes are in their population states, fluctuations of solute-solvent interactions cause random modulations in their vibrational transition frequencies. Hence, even for rephasing diagrams, if the frequency memory are completely lost during this period due to the randomization of the vibrational frequencies (*i.e.* spectral diffusion), the recovering of the original coherence does not happen: the vibrational echo signal does not be generated. By systematically varying t_2 period, 2D-IR experiments can measure the correlation time of solutes (τ_C in Eq. (2.80)), which is the time scale to lose the frequency memory of the system (see Figure 2.4(c)).

From Eq. (2.90), the response functions for the $R_1^{(3)}$ and $R_4^{(3)}$ diagrams are obtained as:

$$R_1^{(3)}(t_1, t_2, t_3) \propto e^{-i\omega_{10}(t_3 - t_1)} \tag{2.89}$$

$$R_4^{(3)}(t_1, t_2, t_3) \propto e^{-i\omega_{10}(t_3 + t_1)} \tag{2.90}$$

where ω_{10} is the time-averaged vibrational transition frequency between | 0 > and | 1 > states. By transforming the t_1 and t_3 time-axes into the ω_1 and ω_3 frequency-axes, respectively, two-dimensional Fourier transformations of $R_1^{(3)}(t_1, t_2, t_3)$ and $R_4^{(3)}(t_1, t_2, t_3)$ provide the corresponding 2D-IR spectra. After that, by taking a summation of them, the purely absorptive 2D-IR spectrum is obtained. Here, it should be noted that, because the sign of the oscillations of the $R_1^{(3)}$ response function is opposite to that of the $R_4^{(3)}$ response function during t_1 period, the inversion of the sign of the ω_1 axis for the $R_1^{(3)}$ spectra is necessary to provide the 2D-IR spectrum (see Figure 2.5). Generally speaking, 2D-IR spectra from the $R_1^{(3)}$, $R_2^{(3)}$, $R_4^{(3)}$, and $R_5^{(3)}$ response functions defined by Eq. (2.90) show their peak at $(\omega_1, \omega_3) = (\omega_{10}, \omega_{10})$. However, in the $R_3^{(3)}$ and $R_6^{(3)}$ diagrams, because the third matter-field interaction creates the coherence between | 1 > and | 2 > states, these response functions are expressed as:

$$R_3^{(3)}(t_1, t_2, t_3) \propto e^{-i\omega_{21}t_3 + i\omega_{10}t_1} \tag{2.91}$$

$$R_6^{(3)}(t_1, t_2, t_3) \propto e^{-i\omega_{21}t_3 - i\omega_{10}t_1} \tag{2.92}$$

where ω_{21} is the time-averaged vibrational transition frequency between | 1 > and | 2 > states. Usually, due to the small anharmonicity of the oscillator, the vibrational transition frequency of

the ω_{21} is slightly down-shifted from that of the ω_{10}:

$$\omega_{21} = \omega_{10} - \Delta \tag{2.93}$$

where Δ is the anharmonic frequency shift. Therefore, 2D-IR spectra from the $R_3^{(3)}$ and $R_6^{(3)}$ response functions have their peak at (ω_1, ω_3) = (ω_{10}, $\omega_{10} - \Delta$) with the opposite signs to those from the $R_1^{(3)}$, $R_2^{(3)}$, $R_4^{(3)}$, and $R_5^{(3)}$ response functions.

2.4.3. Line Broadening Function of 2D-IR Spectrum

For a 2D-IR spectrum, the line broadening function ($\Gamma^{(3)}$) is given by Eq. (2.33) as:

$$\Gamma^{(3)}(t_3, t_2, t_1) = \Gamma_{\text{Vib}}^{(3)}(t_3, t_2, t_1)\mathrm{Y}_{\text{IJKL}}^{(3)}(t_3, t_2, t_1)\Gamma_{\text{Flu}}^{(3)}(t_3, t_2, t_1) \tag{2.94}$$

where, instead of $\Gamma_{\text{Rot}}^{(3)}$, the rotational line broadening function is represented by $\mathrm{Y}_{\text{IJKL}}^{(3)}$ in order to the polarization dependence of 2D-IR absorption spectra.

(1) Vibrational energy relaxation

Note that, the vibrational line broadening function ($\Gamma_{\text{Vib}}^{(3)}$) depends on the Feynman diagram, that is the excitation pathway of the solutes. As shown in Figure 2.3, while the vibrational transitions in the $R_1^{(3)}$, $R_2^{(3)}$, $R_4^{(3)}$, and $R_5^{(3)}$ diagrams occurs only between | 0 > and | 1 > states, the solutes in the $R_3^{(3)}$ and $R_6^{(3)}$ pathways can access up to | 2 > state. Therefore, from Eq. (2.56), $\Gamma_{\text{Vib}}^{(3)}$'s for the $R_1^{(3)}$, $R_2^{(3)}$, $R_4^{(3)}$, and $R_5^{(3)}$ diagrams are obtained as:

$$\Gamma_{\text{Vib}}^{(3)}(t_3, t_2, t_1) = \exp\left[-\frac{t_1}{T_{01}} - \frac{t_2}{T_{11}} - \frac{t_3}{T_{01}}\right] = \exp\left[-\frac{t_1 + t_3}{2T_{11}} - \frac{t_2}{T_{11}}\right]. \tag{2.95}$$

and those for the $R_3^{(3)}$ and $R_6^{(3)}$ diagrams are obtained as:

$$\Gamma_{\text{Vib}}^{(3)}(t_3, t_2, t_1) = \exp\left[-\frac{t_1}{T_{01}} - \frac{t_2}{T_{11}} - \frac{t_3}{T_{12}}\right] = \exp\left[-\frac{t_1}{2T_{11}} - \frac{t_2}{T_{11}} - \left(\frac{1}{2T_{11}} + \frac{1}{2T_{22}}\right)t_3\right] \tag{2.96}$$

where the time constant of T_{ij} is defined by Eq. (2.54). Moreover, by assuming the solutes are treated as harmonic oscillators, the vibrational lifetime of | 2 > state (T_{22}) is represented by the vibrational lifetimes of | 1 > state (T_{11}) as: $T_{22} = T_{11}/2$ [41]. Therefore, Eq. (2.95) and Eq. (2.96) become as:

$$\Gamma_{\text{Vib}}^{(3)}(t_3, t_2, t_1) = \exp\left[-\frac{t_1 + 2t_2 + t_3}{2T_{11}}\right] \tag{2.97}$$

$$\Gamma_{\mathrm{Vib}}^{(3)}(t_3,t_2,t_1)=\exp\left[-\frac{t_1+2t_2+3t_3}{2T_{11}}\right] \tag{2.98}$$

, respectively.

(2) Rotational relaxations

As mentioned in Section 2.3.3, the rotational line broadening function ($\mathrm{Y}_{\mathrm{IJKL}\cdots}^{(n)}$) depends on the polarization condition of laser pulses. Here, the parallel polarization conditions are considered for 2D-IR experiments, and the four subscripts of $\mathrm{Y}_{\mathrm{IJKL}}^{(3)}$ is denoted as ZZZZ. $\mathrm{Y}_{\mathrm{ZZZZ}}^{(3)}$ is obtained from Eq. (2.66) as:

$$\mathrm{Y}_{ZZZZ}^{(3)}(t_3,t_2,t_1)=\frac{1}{9}\exp\left(-\frac{t_1+t_3}{3T_{\mathrm{R}}}\right)\left[1+\frac{4}{5}\exp\left(-\frac{t_2}{T_{\mathrm{R}}}\right)\right] \tag{2.99}$$

where the rotational relaxation time of the vibrational transition (T_{R}) are used instead of the rotational diffusion constant (D): $T_{\mathrm{R}} = 1/(6D)$.

(3) Frequency fluctuations

Same as vibrational relaxation, the line broadening function of frequency fluctuations ($\Gamma_{\mathrm{Flu}}^{(3)}$) depends on the Feynman diagram. For the $R_1^{(3)}$ and $R_2^{(3)}$ rephasing diagrams and the $R_3^{(3)}$ and $R_4^{(3)}$ non-rephasing diagrams, in which the coherent states are created only between | 0 > and | 1 > states, $\Gamma_{\mathrm{Flu}}^{(3)}$'s of them are expressed by Eq. (3.77) as:

$$\Gamma_{\mathrm{Flu}}^{(3)}(t_3,t_2,t_1)=\exp\left[\left\langle\left[+i\int_0^{t_1}dt'\delta\omega_{10}(t')\pm i\int_{t_2+t_1}^{t_3+t_2+t_1}dt'\delta\omega_{10}(t')\right]\right\rangle^{(\mathrm{B})}\right]. \tag{2.100}$$

For the $R_3^{(3)}$ rephasing diagram and the $R_6^{(3)}$ non-rephasing diagram, in which the coherence state between | 1 > and | 2 > states occurs during t_3 period, they are given by:

$$\Gamma_{\mathrm{Flu}}^{(3)}(t_3,t_2,t_1)=\exp\left[\left\langle\left[+i\int_0^{t_1}dt'\delta\omega_{10}(t')\pm i\int_{t_2+t_1}^{t_3+t_2+t_1}dt'\delta\omega_{21}(t')\right]\right\rangle^{(\mathrm{B})}\right]. \tag{2.101}$$

Here, the signs in front of the second integral are positive and negative for the rephasing and non-rephasing diagrams, respectively. It should be noted that, by assuming the harmonic oscillator approximations, the frequency fluctuations of $\delta\omega_{10}$ and $\delta\omega_{21}$ are strictly correlated: $\delta\omega_{10}(t) = \delta\omega_{21}(t)$. Therefore, under this assumption, the cumulant expansions of Eq. (2.100) provide $\Gamma_{\mathrm{Flu}}^{(3)}$'s for the $R_{1\text{-}3}^{(3)}$ rephrasing diagrams as:

$$\Gamma_{\mathrm{Flu}}^{(3)}(t_3,t_2,t_1)=\exp\left[-g(t_1)+g(t_2)-g(t_3)-g(t_2+t_1)-g(t_3+t_2)+g(t_3+t_2+t_1)\right] \quad (2.102)$$

and those of Eq. (2.101) for the $R_{4\text{-}6}^{(3)}$ non-rephrasing diagrams provide as:

$$\Gamma_{\mathrm{Flu}}^{(3)}(t_3,t_2,t_1)=\exp\left[-g(t_1)-g(t_2)-g(t_3)+g(t_2+t_1)+g(t_3+t_2)-g(t_3+t_2+t_1)\right] \quad (2.103)$$

where $g(t)$ is the line broadening function defined by Eq. (2.79).

2.5. Summary

In this chapter, using the time-dependent perturbation theory, the *n*th-order nonlinear response function ($R^{(n)}$ in Eq. (2.42)) and related line broadening functions ($\Gamma_{\mathrm{Vib}}^{(n)}$ in Eq. (2.56), $\Gamma_{\mathrm{Rot}}^{(n)}$ in Eq. (2.66), and $\Gamma_{\mathrm{Flu}}^{(n)}$ in Eq. (2.77)) were derived. From these equations, the lineshape of a liner IR absorption spectrum ($S^{(1)}$) is given as (the derivation is not shown here):

$$S^{(1)}(\omega) \propto \mathrm{Re}\int_0^\infty dt \exp\{-i(\omega-\omega_{10})t\}\exp\left[-g(t)-\frac{t}{2T_{10}}-\frac{t}{3T_{\mathrm{Rot}}}\right] \tag{2.104}$$

and that of a 2D-IR absorption spectrum ($S^{(3)}$) is given as:

$$S^{(3)}(\omega_1,t_2,\omega_3) \propto \mathrm{Re}\left[S_{\mathrm{Re}}^{(3)}(\omega_1,t_2,\omega_3)+S_{\mathrm{NRe}}^{(3)}(\omega_1,t_2,\omega_3)\right] \tag{2.105}$$

where $S_{\mathrm{Re}}^{(3)}$ and $S_{\mathrm{NRe}}^{(3)}$ are the 2D-IR absorption spectra related to rephasing and non-rephasing diagrams, respectively:

$$\begin{aligned} S_{\mathrm{Re}}^{(3)}(\omega_1,t_2,\omega_3) = &\int_0^\infty dt_1 \int_0^\infty dt_3 \exp(i\omega_3 t_3 - i\omega_1 t_1) \\ &\times \exp[-g(t_1)+g(t_2)-g(t_3)-g(t_2+t_1)-g(t_3+t_2)+g(t_3+t_2+t_1)] \\ &\times\left(\exp\left[-\frac{t_1+2t_2+t_3}{2T_{11}}\right]e^{-i\omega_{10}(t_3-t_1)}+\exp\left[-\frac{t_1+2t_2+3t_3}{2T_{11}}\right]e^{-i\omega_{10}(t_3-t_1)-i\Delta t_3}\right) \\ &\times\frac{1}{9}\exp\left(-\frac{t_1+t_3}{3T_{\mathrm{R}}}\right)\left[1+\frac{4}{5}\exp\left(-\frac{t_2}{T_{\mathrm{R}}}\right)\right] \end{aligned} \tag{2.106}$$

$$\begin{aligned} S_{\mathrm{NRe}}^{(3)}(\omega_1,t_2,\omega_3) = &\int_0^\infty dt_1 \int_0^\infty dt_3 \exp(i\omega_3 t_3 + i\omega_1 t_1) \\ &\times \exp[-g(t_1)-g(t_2)-g(t_3)+g(t_2+t_1)+g(t_3+t_2)-g(t_3+t_2+t_1)] \\ &\times\left(\exp\left[-\frac{t_1+2t_2+t_3}{2T_{11}}\right]e^{-i\omega_{10}(t_3-t_1)}+\exp\left[-\frac{t_1+2t_2+3t_3}{2T_{11}}\right]e^{-i\omega_{10}(t_3-t_1)-i\Delta t_3}\right) \\ &\times\frac{1}{9}\exp\left(-\frac{t_1+t_3}{3T_{\mathrm{R}}}\right)\left[1+\frac{4}{5}\exp\left(-\frac{t_2}{T_{\mathrm{R}}}\right)\right] \end{aligned} \tag{2.107}$$

These equations will be used for lineshape analyses in 2D-IR experiments.

References

1. K. Ohta, H. Maekawa, S. Saito, and K. Tominaga, *J. Phys. Chem. A*, **107**, 5643 (2003).

2. K. Ohta, H. Maekawa, and K. Tominaga, *J. Phys. Chem. A*, **108**, 1333 (2004).

3. K. Ohta, H. Maekawa, and K. Tominaga, *Chem. Phys. Lett*, **386**, 32 (2004).

4. K. Ohta and K. Tominaga, *Chem. Soc. Jpn.*, **78,** 1581 (2005).

5. J. Tayama, M. Banno, K. Ohta, and K. Tominaga, *Sci. China Phys. Mech*, **53**, 1013 (2010).

6. J. Tayama, A. Ishihara, M. Banno, S. Saito, and K. Tominaga, *J. Chem. Phys.*, **133**, 014505 (2010).

7. K. Ohta, J. Tayama, S. Saito, and K. Tominaga, *Acc. Chem. Res*,, **45**, 1982 (2012).

8. K. Ohta, J. Tayama, and K. Tominaga, *Phys. Chem. Chem. Phys.*, **14**, 10455 (2012).

9. J. Tayama, K. Ohta, and K. Tominaga, *Chem. Lett.*, **41**, 366 (2012).

10. P. Hamm, M. Lim, R. M. Hochstrasser, *Phys. Chem. Lett*, **81**, 5326 (1998).

11. M. Kozinski, S. Garrett-Roe, and P. Hamm, *Chem. Phys.*, **341**, 5 (2007).

12. C. J. Fecko, J. J. Loparo, S. T. Roberts, and A. Tokmakoff, *J. Chem. Phys.*, **122**, 054506 (2005).

13. J. B. Asbury, T. Steinel, C. Stromberg, S. A. Corcelli, C. P. Lawrence, J. L. Skinner, and M. D. Fayer, *J. Phys. Chem. A*, **108**, 1107 (2004).

14. J. Stenger, D. Madsen, P. Hamm, E. T. J. Nibbering, and T. Elsaesser, *J. Phys. Chem. A*, **106**, 2341 (2002).

15. S. Yeremenko, M. S. Pshenichnikov, and D. A. Wiersma, *Chem. Phys. Lett*., **369**, 107 (2003).

16. D. Kraemer, M. L. Cowan, A. Paarmann, N. Huse, E. T. J. Nibbering, T. Elesaesser, and R. J. Miller, *Proc. Natl. Acad. Sci. USA*, **105**, 437 (2008).

17. J. B. Asbury, T. Steinel, K. Kwak, S. A. Corcelli, C. P. Lawrence, J. L. Skinner, and M. D. Fayer, *J. Chem. Phys.*, **121**, 12431 (2004).

18. C. J. Fecko, J. D. Eaves, J. J. Loparo, A. Tokmakoff, and P. L. Geissler, *Science*, **301**, 1698 (2003).

19. P. Hamm and R. M. Hochstrasser, Structure and dynamics of proteins and peptides: Femtosecond two-dimensional infrared spectroscopy, In: M. D. Fayer (ed.), "*Ultrafast Infrared and Raman Spectroscopy"*, New York, Marcel Dekker, 273–347 (2001).

20. K. Ohta, J. Tayama, S. Saito and K. Tominaga, Solvation Dynamics of Vibrational States in Hydrogen-Bonding Solvents *Vibrational Frequency Fluctuations Studied by the Three-Pulse*

Infrared Photon Echo Method, In: M. D. Fayer (ed.), "*Ultrafast infrared vibrational spectroscopy"*, New York, CRC Press (2013).

21. A. Ishizaki and Y. Tanimura, *J. Chem. Phys.*, **123**, 014503 (2005).

22. A. Ishizaki and Y. Tanimura, *J. Chem. Phys*, **125**, 084501 (2006).

23. Y. Tanimura, *J. Phys. Soc. Jpn.*, **75**, 082001 (2006).

24. T. Hasegawa and Y. Tanimura, *J. Chem. Phys*, **128**, 064511 (2008).

25. N. Demirdoeven, M. Khalil, and A. Tokmakoff, *Phys. Rev. Lett.*, **89**, 237401 (2002).

25. S. Li, J. R. Schmidt, A. Piryatinski, C. P. Lawrence, and. J. L. Skinner, *J. Chem. Phys. B*, **110**, 18933 (2006).

26. M. W. Lee, J. K. Carr, M. Göllner, P. Hamm, and M. Meuwly, *J. Chem. Phys.*, **139**, 054506 (2013).

27. S. A. Corecelli, C. P. Lawrence, and. J. L. Skinner, *J. Chem. Phys.*, **120**, 8107 (2004).

28. J. D. Eaves, A. Tokmakoff, and P. L. Geossler, *J. Phys. Chem. A*, **109**, 9424 (2005).

29. C. P. Lawrence and. J. L. Skinner, *J. Chem. Phys.*, **118**, 264 (2003).

30. B. Auer, R. Kumar, J. R. Schmidt, and J. L. Skinner, *Proc. Natl. Acad. Soc. USA*, **104**, 142115 (2007).

31. E. Harder, J. D. Eaves, A. Tokmakoff, and B. J. Berne, *Proc. Natl. Acad. Soc. USA*, **102**, 11611 (2005).

32. J. R. Schmidt, S. T. Roberts, J. J. Loparo, A. Tokmakoff, M. D. Fayer, and J. L. Skinner, *Chem. Phys.*, **341**, 143 (2007).

33. K. Kwak and M. Cho, *J. Chem. Phys.*, **119**, 2247 (2003).

34. K. Kwak and M. Cho, *J. Chem. Phys.*, **119**, 2256 (2003).

35. K. Kwak, H. Lee, and M. Cho, *J. Chem. Phys.*, **120**, 1477 (2004).

36. K. Kwak and M. Cho, *J. Phys. Chem. A.*, **107**, 5903 (2003).

37. A. Nitzan, *"Chemical Dynamics in Condensed Phases",* New York, Oxford University Press (2006).

38. S. Mukamel, "*Principles of Nonlinear Optical Spectroscopy"*, Oxford, Oxford University Press (1995).

39. M. Cho, "*Two-Dimensional Optical Spectroscopy*", Boca Raton, CRC Press (2009).

40. P. Hamm and M. Zanni, *"Concepts and Methods of 2D Infrared Spectroscopy"*, New York, Cambridge University Press. (2011).

41. J. S. Bader and B. J. Berne, *J. Chem. Phys.*, **100**, 8359 (1994).

42. M. Cho, *J. Chem. Phys.*, **115**, 4424 (2001).

43. B. J. Berne R. and Pecora, "*Dynamic Light Scattering*", New York, Dover (2000)

44. N. G. Van Kampen, "*Stochastic Processes in Physics and Chemistry*" Amsterdam, Elsevier (1992).

45. R. Kubo, *Adv. Chem. Phys.*, **15**, 101 (1969).

Figures

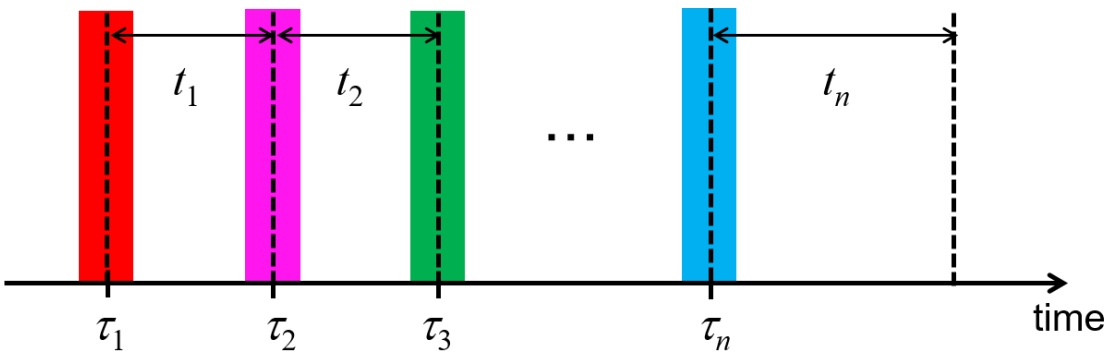

Figure 2.1. Definition of time variables: τ_i refer to an absolute time and t_i to a relative time.

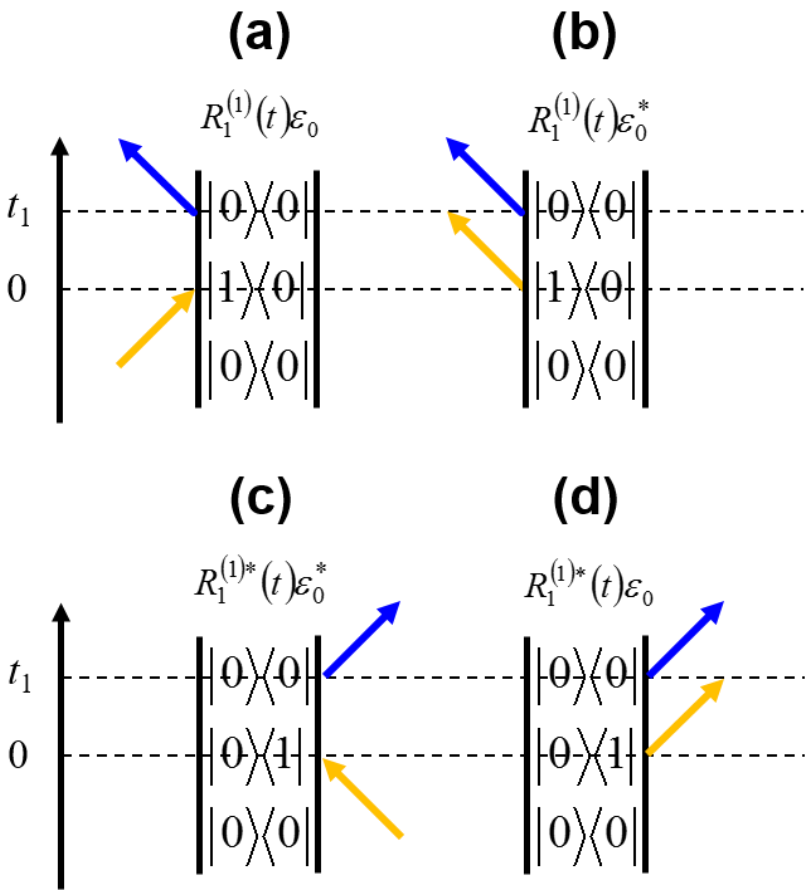

Figure 2.2. Four possible double-side Feynman diagrams for a linear response function. Time is running from the bottom to top. The left and right vertical lines indicate the time evolution of the $|\nu>$ and $<\nu|$. Yellow and blue arrows represent matter-field interaction and signal emission, respectively.

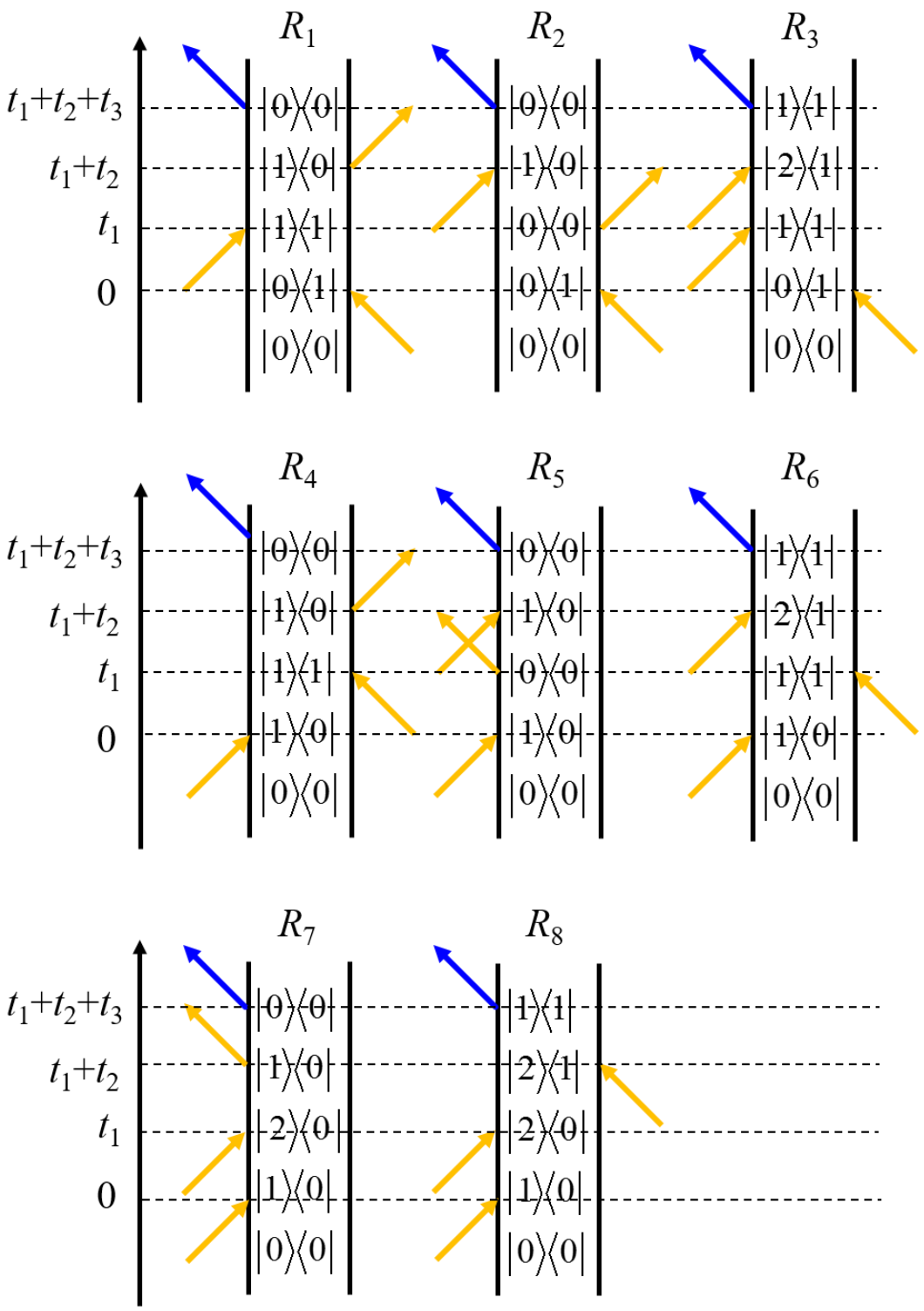

Figure 2.3. Eight possible double-side Feynman diagrams for a third-order nonlinear response function: (top) Rephasing response functions, (middle) non-rephasing response functions, and (bottom) two-quantum response functions.

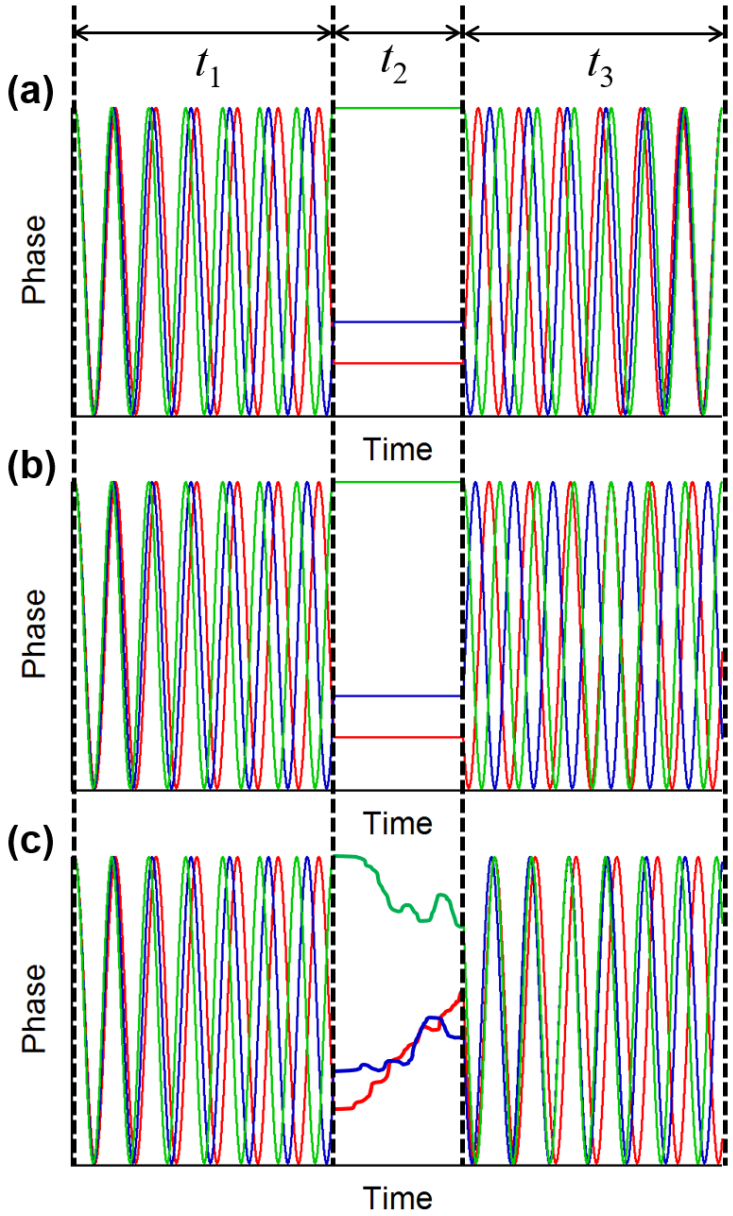

Figure 2.4. Temporal evolution of (a) rephasing and (b) non-rephasing signals. In (a) and (b), perfect frequency memory is assumed. The red, blue, and green traces represent the phases of three separated oscillators with slightly different vibrational frequencies. Due to the difference in the sign of the phase during t_3 time (*i.e.* second coherent state), qualitatively different signals are finally generated in rephasing and non-rephasing diagrams. In an actual case, because the fluctuations of the surrounding environment can randomize the phases and the vibrational frequencies of oscillators, these differences will disappear with increasing t_2 time.

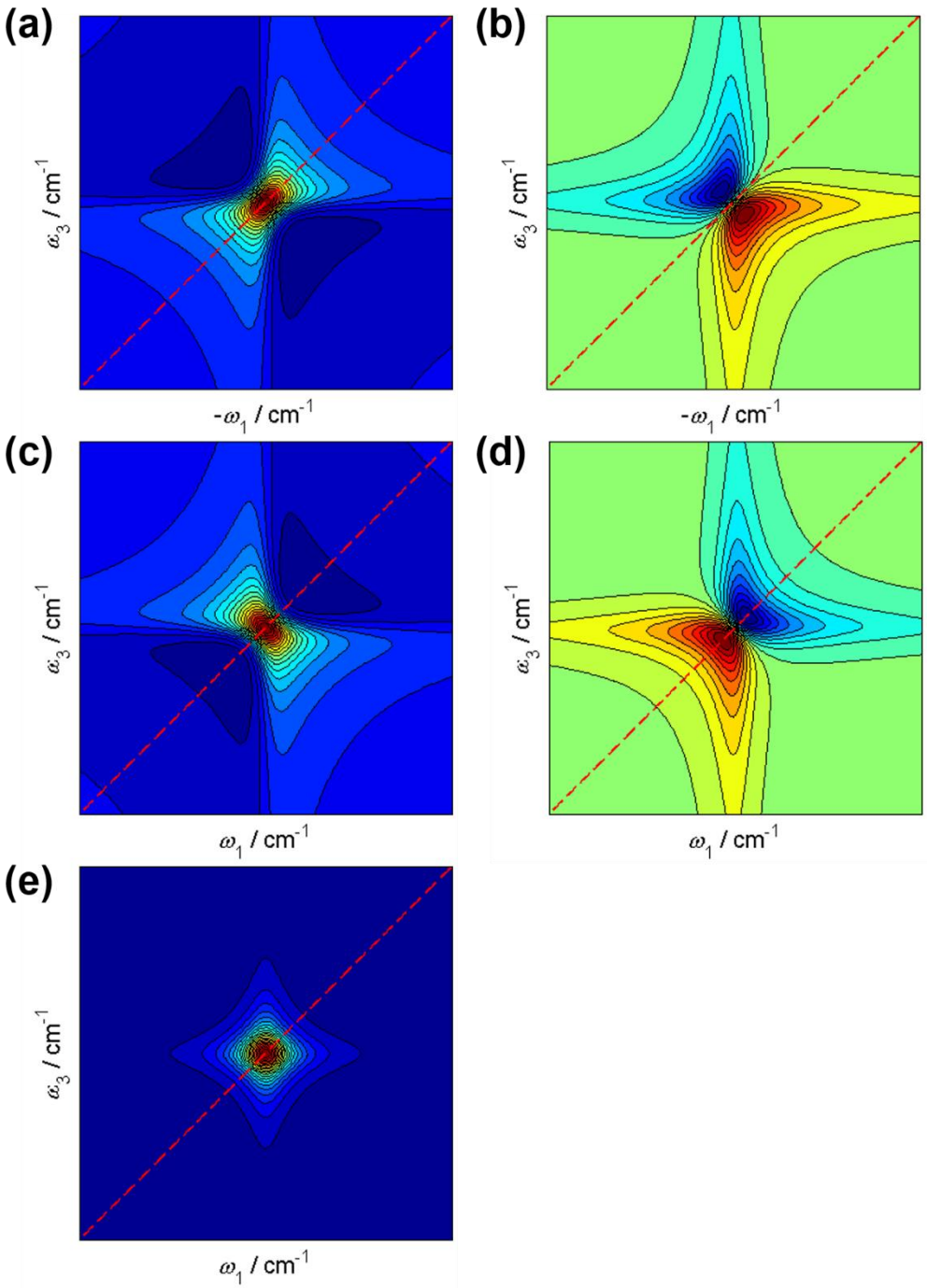

Figure 2.5. (a, c) Real and (b, d) imaginary parts of a 2D-IR spectra for a two-level system with a 2D Lorentzian lineshape. (top) rephasing diagram and (middle) non-rephasing diagram. (e) Purely absorptive 2D-IR spectrum given by a sum of signals (a) and (c). The red and blue regions represent the positive and negative values, respectively. The dashed lines are to highlight the diagonal directions of the 2D-IR spectra where $|\omega_1| = |\omega_3|$.

CHAPTER 3.

Experimental Setup: Two-dimensional Infrared Spectroscopy

3.1. Introduction

During the last two decades, two-dimensional (2D-IR) spectroscopy has been developed for investigation of ultrafast dynamics in chemical, physical, and biological systems [1-9]. In 1998, Hamm, Lim, and Hochstrasser have initially conducted 2D-IR measurement for several biomolecules in solutions [10]. The first 2D-IR experiment was based on a conventional IR pump-probe spectroscopy with a narrow band pump pulse, which was generated by a Fabry-Perot filter. Inspired by the development of heterodyne-detected photon echo spectroscopy by Wiersma *et al*., we have commonly use 2D-IR experiments in the pump-probe geometry [1]. In this method, two collinear pump pulses and the probe pulse are crossed at a small angle in the sample position. Data collection is conducted in a time-frequency domain. Since only Fourier transformation of the probe frequency axis is provided by a spectrometer, further data processing, that is, the Fourier transformation of the time-domain data along the t_1 axis (which corresponds to the temporal delay between first and second pump pulses, see Section 3.3.2) is necessary to determine the pump frequency axis. Consequently, phase stability and precise information on the relative phases between incident pulses at the sample have to be rigorously controlled to obtain the highest possible spectral resolution [11, 12]. To achieve this goal, in this study, I built the 2D-IR spectrometer with a Mach-Zehnder interferometer, which is based on the work done by Helbing and Hamm [13].

3.2. Generation of Mid-IR Pulses: OPA and DFG Processes

The mid-IR short pulses are generated by using two sequential nonlinear optical processes: optical parametric amplification (OPA) and difference frequency generation (DFG) [14, 15]. Figure 3.1 depicts the optical setup for generation of mid-IR pulses. This optical system is pumped by the outputs from a Ti:sapphire regenerative amplification (output energy : ~ 650 mW, repetition rate : 1 kHz, center frequency : ~800 nm, pulse width : ~100 fs).

By using two-step OPA processes, the amplified Ti:sapphire outputs are converted into near-infrared signal and idler pulses, ω_{signal} and ω_{idler} pulses. First, because a white-light pulse is needed as the seed pulse to pump the OPA, the 800 nm pulse with a several percent of the output power is focused on a sapphire crystal ([0001]-cut, thickness : 1 mm) to generate the white-light beam due to the self-phase modulation in the crystal. Before focusing into the sapphire crystal, the 800 nm pulse is passed through a $\lambda/2$ waveplate to rotate the polarization and an iris to control

the intensity and mode profile of the 800 nm pulse. Next, the white-light beam is spatially and temporally overlapped with 10 % of 800 nm pulse by passing through a delay stage (DS1 in Figure 3.1), and these two beams are focused on a β–BaB_2O_4 (BBO) crystal (TYPE II, thickness: 4 mm, phase-matching angle : 27.2) to generate ω_{signal} and ω_{idler} pulses. The frequencies of ω_{signal} and ω_{idler} pulses are determined to satisfy the phase-matching condition:

$$\omega_{pump} n_{eo}(\omega_{pump}, \theta) = \omega_{signal} n_o(\omega_{signal}) + \omega_{idler} n_{eo}(\omega_{idler}, \theta) \tag{3.1}$$

where $n_o(\omega)$ and $n_{eo}(\omega)$ are the frequency-dependent refractive indices of BBO crystal for ordinary and extraordinary polarization, respectively, and θ is the angle between the beam and optic axis. The undesirable ω_{idler} pulse and residual component of the 800 nm pulse form the first OPA process are removed by using a proper dichroic mirror (DM2 and DM3 in Figure 3.1), and the fresh ω_{signal} pulse is used for the second amplification step. After the ω_{signal} pulse is collimated by a concave mirror on a delay stage (DS2 in Figure 3.1), the ω_{signal} pulse returns back to the same BBO crystal at a different height. Finally, the ω_{signal} pulse is temporally and spatially overlapped with the remaining 800 nm pulse to generate the intensive ω_{signal} and ω_{idler} pulses (~100 mW of signal and idler output).

The ω_{signal} and ω_{idler} pulses are separated by a dichroic mirror (DM4 in Figure 3.1), and a temporal delay for the ω_{signal} pulse is given by a delay stage (DS3 in Figure 3.1). By temporally and spatially overlapping the two beams on the $AgGaS_2$ crystal (TYPE I, thickness: 1.5 mm, phase-matching angle : 37.5°), the mid-IR pulse is generated from the DFG process between the ω_{signal} and ω_{idler} pulses. The phase-matching condition in this process is given by:

$$\omega_{signal} n_{eo}(\omega_{signal}, \theta) = \omega_{IR} n_o(\omega_{IR}) + \omega_{idler} n_o(\omega_{idler}) \ . \tag{3.2}$$

As shown in Eq. (3.1) and Eq. (3.2), the frequencies of outputs from the OPA and DFG processes depend on the angle θ between the beams of extraordinary polarization and optic axes. Therefore, by changing the angle of BBO and/or $AgGaS_2$ crystals with respect to the direction of the beams, the mid-IR beams are continuously tunable in the frequency range from 3 μm to 10 μm.

For the 2D-IR experiments presented in Chapter 8, the center wavenumber of the mid-IR pulses was tuned to approximately 1700 cm^{-1}. In order to specify the properties of obtained mid-IR pulses, the following two measurements were conducted. First, the spectrum of the mid-IR pulse was measured by a N_2-cooled single-channel MCT (HgCdTe) detector after passing through a monochrometer, as displayed in Figure 3.2. The spectrum can be well reproduced by a

single Gaussian function, and the bandwidth of the mid-IR pulses is found to be approximately 85 cm^{-1}.

Next, in order to characterize the pulse duration of the mid-IR pulses, non-resonant frequency-resolved optical gating (FROG) measurement was conducted with a thin germanium wafer (thickness : ~ 300 μm). In this measurement, a pump pulses E_{pump2} induces a non-resonant response in the germanium wafer, which modifies the transmission of a probe pulse E_{probe}. Since the non-resonant response takes place only when E_{pump2} is present (*i.e.* the non-resonant response is instant), E_{pump2} can act as an optical gate with a femtosecond time resolution with respect to E_{probe}. Therefore, by scanning the temporal delay between these two pulses, the spectrally-resolved probe pulses were measured by liquid N_2-cooled 32 element-MCT array detectors with a monochromator. In practice, in order to avoid multi-photon absorption by the germanium wafer (band gap : ~ 5400 cm^{-1}), the pulse power of E_{pump2} was lowered to about 40 nJ. Figure 3.3(a) shows the result of the non-resonant FROG measurement with the germanium wafer as a function of probe wavenumber and time delay between E_{pump2} and E_{probe}, and Figure 3.3(b) shows the slices taken from the signal at three different probe wavenumbers. By fitting these signals to Gaussian functions, in average, the full width of half maximum (FWHM) is found to be approximately 220 fs, which is consistent with the experimental result using second harmonics generation (SHG) process in an $AgGaS_2$ crystal (see Appendix 3.A). Here, when the temporal duration of the mid-IR pulse is assumed to be a Gaussian shape, the width of the obtained signals becomes broader than the fundamental mid-IR pulses by a factor of $\sqrt{2}$. Consequently, the pulse duration of the mid-IR pulse can be estimated as 160 fs.

3.3. Compact Implementation of Two-dimensional Infrared Spectroscopy

3.3.1. Mach-Zehnder Interferometer

Figures 3.4(a) and 3.5(a) display a picture of the optical setups for 2D-IR measurements and the schematic overview, respectively. The mid-IR pulses from the OPA and DFG processes are used for this 2D-IR spectroscopy.

A small fraction of the mid-IR pulses reflected on the front and back of a wedge-shaped BaF_2 window (BS1 in Figure 3.5(a)) are used as the probe (E_{probe}, blue line in Figure 3.5(a)) and reference pulses (E_{ref}, light-blue line in Figure 3.5(a)), respectively. On the other hand, the pulses

passing through BS1 enter into a Mach-Zehnder interferometer with two interferometer arms [16]. Figure 3.4(b) shows the picture of the Mach-Zehnder interferometer. The interferometer outputs, which were generated by a single reflection at the beamsplitters per beam, are used as pump pulses (yellow lines in Figure 3.5(a)). The interferometer arms are made up with two CaF_2 plate beamsplitters (BS2 and BS3 in Figure 3.5(b)), four gold mirrors (M1, M2, M3, and M4 in Figure 3.5(b)). The incoming IR beam is split into two beams by BS2, which are recombined at BS3 after the reflection by the gold mirrors. Here, the pulses passing through the moving and static interference arms are referred to as E_{pump1} and E_{pump2}, respectively. An optical chopper (OC in Figure 3.5(b)) controls the on/off of E_{pump2}, which is synchronized with the laser repetition rate. With a parabolic mirror, E_{pump1}, E_{pump2}, and E_{probe} are focused and spatially overlapped at the sample position. Note that, as shown in Figure 3.5(a), E_{ref} is focused at the different point on the sample from the pump and probe pulses. After spectrally dispersing by a monochromator, the probe and reference pulses are observed with two arrays of liquid N_2-cooled 32 element-MCT detectors, respectively. The intensity of reference pulse is used to correct the intensity fluctuations of laser pulses during the measurements (see Eq. (3.11)). The 2D-IR measurements in this study were conducted with this setup under the parallel polarization condition.

3.3.2. 2D-IR Data Collection: Pump-probe Geometry

As mentioned in Section 3.1, to obtain 2D-IR spectra, it is necessary to determine the phase of the obtained signals very precisely [11, 12]. Here, the time delay between E_{pump1} and E_{pump2} is referred to as the coherence time (t_1), that between E_{pump2} and E_{probe} as the population time (t_2), that after E_{probe} as the detection time (t_3). The time delays of t_1 and t_2 are controlled by delay stages in and after the Mach-Zehnder interferometer (DS1 and DS2 in Figure 3.5(a)), respectively. During 2D-IR measurements, the monochromator in front of the MCT array detector principally performs the Fourier transformation for along the t_3, which provides the ω_3 axis (vertical axis in a 2D-IR spectrum). Therefore, in 2D-IR experiments, vibrational echo signals (E_{echo}) at a given ω_3 frequency are observed by scanning t_1 for a fixed t_2.

It should be noted that, because typical IR detectors are square-low detectors, the signal is expressed as:

$$
\begin{aligned}
I_{\mathrm{sig}}(t_{\mathrm{LO}}, t_2, \omega_3) &= \int_0^\infty dt_1 \left| E_{\mathrm{echo}}(t_1, t_2, \omega_3) + E_{\mathrm{LO}}(t_1 - t_{\mathrm{LO}}, \omega_3) \right|^2 \\
&\approx \int_0^\infty dt_1 \left| E_{\mathrm{LO}}(t_1 - t_{\mathrm{LO}}, \omega_3) \right|^2 + 2\,\mathrm{Re} \int_0^\infty dt_1 \left\{ E_{\mathrm{echo}}(t_1, t_2, \omega_3) \cdot E_{\mathrm{LO}}^*(t_1 - t_{LO}, \omega_3) \right\} \qquad (3.3) \\
&= I_{\mathrm{LO}}(\omega_3) + 2\,\mathrm{Re} \int_0^\infty dt_1 \left\{ E_{\mathrm{echo}}(t_1, t_2, \omega_3) \cdot E_{\mathrm{LO}}^*(t_1 - t_{LO}, \omega_3) \right\}
\end{aligned}
$$

where E_{LO} is the so-called local oscillator and I_{LO} is the integrated intensity of E_{LO}. Because $|E_{\mathrm{echo}}|^2$ is much weaker than $|E_{\mathrm{LO}}|^2$, the integrated signal of $|E_{\mathrm{echo}}|^2$ is neglected in the second line of Eq. (3.3). By assuming that E_{LO} is in semi-impulsive limit (see Eq. (2.9)), the convolution in Eq. (3.3) disappears ($t_{\mathrm{LO}} = t_1$):

$$
I_{\mathrm{sig}}(t_1, t_2, \omega_3) \propto \mathrm{Re}\left[E_{\mathrm{echo}}(t_1, t_2, \omega_3) \right]. \qquad (3.4)
$$

As presented Figure 3.5(a), E_{pump1} and E_{pump2} pass through the sample in the same direction, that is, the wavevectors of them are the same: $\mathbf{k}_{\mathrm{pump1}} = \mathbf{k}_{\mathrm{pump2}}$. This geometry is referred to as a pump-probe geometry [16-18]. From Eq. (2.45), the wavevectors of rephasing signals and non-rephasing signals (denoted as $\mathbf{k}_{\mathrm{Re}}$ and $\mathbf{k}_{\mathrm{NRe}}$, respectively) are obtained as:

$$
\mathbf{k}_{\mathrm{Re}} = -\mathbf{k}_{\mathrm{pump1}} + \mathbf{k}_{\mathrm{pump2}} + \mathbf{k}_{\mathrm{probe}} \qquad (3.5)
$$

$$
\mathbf{k}_{\mathrm{NRe}} = +\mathbf{k}_{\mathrm{pump1}} - \mathbf{k}_{\mathrm{pump2}} + \mathbf{k}_{\mathrm{probe}} \qquad (3.6)
$$

where $\mathbf{k}_{\mathrm{probe}}$ is the wavevector of E_{probe}. Therefore, by substituting $\mathbf{k}_{\mathrm{pump1}} = \mathbf{k}_{\mathrm{pump2}}$ into Eq. (3.5) and Eq. (3.6), both rephasing and non-rephasing signals are shown to be emitted in the direction of $\mathbf{k}_{\mathrm{probe}}$:

$$
\mathbf{k}_{\mathrm{Re}} = \mathbf{k}_{\mathrm{NRe}} = \mathbf{k}_{\mathrm{probe}}\,. \qquad (3.7)
$$

In other words, E_{probe} automatically overlaps with the rephasing and non-rephasing signals so that it can act as not only the probe pulse but also the local oscillator. Moreover, the sum of the rephasing and non-rephasing signals is automatically measured, which provides a purely absorptive 2D-IR spectrum.

In actual 2D-IR experiments, because E_{pump2} is modulated by the OC at a frequency of 500Hz, the heterodyne-detected signals with OC open (I_{on}) and close (I_{off}) are represented as:

$$I_{\text{on}}(t_1,t_2,\omega_3)=\int_0^\infty dt_1\left|E_{\text{echo}}(t_1,t_2,\omega_3)+E_{\text{pp1}}(t_1,t_2,\omega_3)+E_{\text{pp2}}(t_2,\omega_3)+E_{LO}(t_1-t_{LO},\omega_3)\right|^2$$
$$\propto I_{\text{LO}}(\omega_3)+\text{Re}\left[\left(E_{\text{echo}}(t_1,t_2,\omega_3)+E_{\text{pp1}}(t_1,t_2,\omega_3)+E_{\text{pp2}}(t_2,\omega_3)\right)E^*_{\text{LO}}(\omega_3)\right] \tag{3.8}$$

$$I_{\text{off}}(t_1,t_2,\omega_3)=\int_0^\infty dt_1\left|E_{\text{pp1}}(t_1,t_2,\omega_3)+E_{LO}(t_1-t_{LO},\omega_3)\right|^2$$
$$\propto I_{\text{LO}}(\omega_3)+\text{Re}\left[E_{\text{pp1}}(t_1,t_2,\omega_3)E^*_{\text{LO}}(\omega_3)\right] \tag{3.9}$$

Note that IR pump-probe signals due to the two field interactions between either E_{pump1} or E_{pump2} and E_{probe} (denoted as E_{pp1} and E_{pp2}, respectively) are generated in the $\mathbf{k}_{\text{probe}}$ directions, as well. Here, because of the same reason as in Eq. (3.3), the integrated signals of $|E_{\text{echo}}|^2$, $|E_{\text{pp1}}|^2$, and $|E_{\text{pp2}}|^2$ are ignored in Eq. (3.8) and Eq. (3.9). Therefore, by taking the difference between I_{on} and I_{off}, the intensity change (ΔI) is recorded as a function of t_1:

$$\Delta I(t_1,t_2,\omega_3)\equiv\frac{I_{\text{on}}(t_1,t_2,\omega_3)-I_{\text{off}}(t_1,t_2,\omega_3)}{I_{\text{off}}(t_1,t_2,\omega_3)}$$
$$\propto \text{Re}\left[E_{\text{echo}}(t_1,t_2,\omega_3)E^*_{\text{LO}}(\omega_3)\right]+\text{Re}\left[E_{\text{pp2}}(t_2,\omega_3)E^*_{\text{LO}}(\omega_3)\right] \tag{3.10}$$

Finally, in order to generate the ω_1 axis (horizontal axis in a 2D-IR spectrum) from the t_1 axis, the Fourier transform for $\Delta I(t_1, t_2, \omega_3)$ at each ω_3 frequency axis is numerically performed. Note that, although $\Delta I(t_1, t_2, \omega_3)$ given by Eq. (3.10) contains $E_{\text{echo}}E^*_{\text{LO}}$ and $E_{\text{pp2}}E^*_{\text{LO}}$ contributions, the Fourier transform along t_1 provides the spectra of E_{echo} and E_{pp2} at different frequency region: the spectrum related to $E_{\text{pp2}}E^*_{\text{LO}}$ is observed at zero-frequency region.

Here, to determine the time origin of t_1 axis, the interference between the interferometer outputs generated by a double reflection at the beamsplitters per beam is monitored with a pyroelectric detector (PED in Figure 3.5(b)). Moreover, by observing IR pump-probe signal due to the two field interaction between E_{pump2} and E_{probe}, the time origin of t_2 axis is determined.

3.4. Coherence Time Delay Calibration: Quadrate Fringe Counting Method with He-Ne Interferences

In order to obtain a true 2D-IR spectrum from the numerical Fourier transformation, the recorded echo signals has to be collected with an equidistant t_1 time grid. In this 2D-IR spectroscopy setup, the time delay of t_1 axis is controlled by a mechanically translating stage. However, the translational stage does not have enough accuracy and reproducibility to give the correct 2D IR

spectra. If there are sinusoidal variations in the encoder and the stepping motor to produce periodic variations in the actual step size, distortions and/or frequency shifts may occur in the 2D-IR spectrum. Therefore, a He-Ne continuous wave laser is used to provide an equidistant time grid for the 2D-IR experiments. From the analogy to the technique adopted in conventional FT-IR spectrometers, orthogonally polarized He-Ne interferograms are observed by using the quadrature fringe counting method.

Inside the Mach-Zehnder interferometer, a He-Ne laser beam propagates approximately 3 cm below the IR beam (red line in Figure 3.5(c)). The interferometer arms have two BK7 plate beamsplitters (BS2 and BS3 in Figure 3.5(c)) and four aluminum mirrors (M1', M2', M3', and M4' in Figure 3.5(c)) for the He-Ne beam. Similar to the IR beam, the He-Ne beam is split into two beams by BS4, which are recombined at BS5 after the reflection by the aluminum mirrors. The circular polarized He-Ne beam is generated by a zero-order $\lambda/4$ wave plate ($\lambda/4$ in Figure 3.5(c)) in the moving interferometer arm. The interference between the circular polarized beam from the moving arm and linear polarized beam from the static arm is resolved into two orthogonally polarized components by a polarization cube oriented at 45° with respect to the incident polarization. These signals are individually detected by using two photo diodes (PD1 and PD2 in Figure 3.5(c)).

Figure 3.6 displays the schematic picture of the two perpendicular polarized signals with a relative phase difference of 90° detected by PD1 and PD2. Because the He-Ne beam emits only a light with the wavelength of 632.8 nm, the fringes of the He-Ne interferogram appears at every 2.11 fs. Therefore, the number of fringes can provide the equidistant t_1 time grid with the accuracy of 2.11 fs. Fringe counting is performed in the computer as follows. The fringe counter is set to respond at each time when the signal intensity of the He-Ne interferogram passed through a trigger level of the counter. Then, at each data acquisition step, only a counting number is read to provide the actual coherent time (t_1'). Here, the order of the fringes with respect to the orthogonally polarized He-Ne interferograms is used to determine the moving direction of the delay stage. If the motions of the delay stage were perfect, the t_1' would increase at a given rate during 2D-IR experiments. Therefore, at each data acquisition, the deviation of t_1' from t_1 is used to provide the 2D-IR data in a uniform t_1 time step. By using a spline interpolation method, the recorded 2D-IR data is corrected with respect to t_1 axis. To demonstrate the effectiveness of the quadrate fringe counting method with He-Ne interferences, the 2D-IR spectrum of the NO stretching mode of

$[RuCl_5(NO)]^{2-}$ in D_2O was observed, whose result is summarized in Appendix 3.B.

3.5. Improvement of Signal to Noise Ratio

In 2D-IR experiments, for example, fluctuations of laser intensity and pulse scatterings on optical elements lead to the undesirable contribution to 2D-IR spectra. Therefore, in order to obtain reliable 2D-IR spectra, it is necessary to reduce such noises during 2D-IR experiments. In this 2D-IR spectroscopy setup, the high signal to noise (S/N) ratio is achieved by using the following two ways.

First, the intensity fluctuations of probe pulses are corrected with separately recorded reference pulses. In the 2D-IR experiments, the important quantity is the intensity change of probe pulse ΔI, which is defined by Eq. (3.10). However, while the intensity of laser pulse is fluctuating, the accurate ΔI cannot be determined. As mentioned in Section 3.3.1, spectrally-resolved reference pulses are detected by a liquid N_2-cooled 32 element-MCT array detector as well. Therefore, the final signal can be represented as:

$$\Delta I(t_1,t_2,\omega_3)=\sum_s \frac{\left(I_{\mathrm{on}}(t_1,t_2,\omega_3)/I_{\mathrm{ref,\,on}}(\omega_3)\right)-\left(I_{\mathrm{off}}(t_1,t_2,\omega_3)/I_{\mathrm{ref,\,off}}(\omega_3)\right)}{\left(I_{\mathrm{off}}(t_1,t_2,\omega_3)/I_{\mathrm{ref,\,off}}(\omega_3)\right)} \tag{3.11}$$

where $I_{\mathrm{ref,on}}$ and $I_{\mathrm{ref,off}}$ are the signal intensity of a reference pulse with the OC open and close, respectively, and where the sum is to average over 300 laser shots.

Second, the signals due to the interference between scattered pump pulses and probe pulses is minimized by modulating the time delays of probe pulses [19]. When there are scratches and/or fingerprints on optical elements (*e.g.* mirror, lens, and windows of a sample cell *etc.*), pump pulses are scattered into the direction of probe pulses. Therefore, the scattered pump pulses are also heterodyne detected by the probe pulse as:

$$\begin{aligned} I_{\mathrm{scatter,on}}(t_1,t_2,\omega_3) &\propto \left|E_{\mathrm{LO}}(\omega_3)+\alpha\left[E_{\mathrm{pump1}}(t_1,t_2,\omega_3)+E_{\mathrm{pump2}}(t_2,\omega_3)\right]\right|^2 \\ &= \left|E_{\mathrm{LO}}(\omega_3)\right|^2 + 2\alpha\,\mathrm{Re}\left[E^*_{\mathrm{LO}}(\omega_3)\left\{E_{\mathrm{pump1}}(t_1,t_2,\omega_3)+E_{\mathrm{pump2}}(t_2,\omega_3)\right\}\right] \\ &\quad + \alpha^2\left(\left|E_{\mathrm{pump1}}(t_1,t_2,\omega_3)\right|^2+\left|E_{\mathrm{pump2}}(t_2,\omega_3)\right|^2+2\,\mathrm{Re}\left[E_{\mathrm{pump1}}(t_1,t_2,\omega_3)E_{\mathrm{pump2}}(t_2,\omega_3)\right]\right) \end{aligned} \tag{3.12}$$

and

$$\begin{aligned} I_{\mathrm{scatter,off}}(t_1,t_2,\omega_3) &\propto \left|E_{\mathrm{LO}}(\omega_3)+\alpha E_{\mathrm{pump2}}(t_2,\omega_3)\right|^2 \\ &= \left|E_{\mathrm{LO}}(\omega_3)\right|^2 + 2\alpha\,\mathrm{Re}\left[E^*_{\mathrm{LO}}(\omega_3)E_{\mathrm{pump2}}(t_2,\omega_3)\right]+\alpha^2\left(\left|E_{\mathrm{pump2}}(t_2,\omega_3)\right|^2\right) \end{aligned} \tag{3.13}$$

where $I_{\mathrm{scatter,on}}$ and $I_{\mathrm{scatter,off}}$ are the signal intensity of scattered pump pulses with the OC open and

close, respectively, and where α (<<1) is a measure of the scattering strength. Even if the scattered pump pulses are weak, the undesired signals can easily reach the level of the desired signal: $\alpha E^*_{\mathrm{LO}} E_{\mathrm{pump1(pump2)}} \sim E^*_{\mathrm{LO}} E_{\mathrm{echo}}$. When $|E_{\mathrm{probe}}| >> \alpha\, |E_{\mathrm{pump1}}|$ and $|E_{\mathrm{probe}}| >> \alpha |E_{\mathrm{pump2}}|$, Eq. (3.12) and Eq. (3.13) are, respectively, approximated as:

$$I_{\mathrm{scatter,on}}(t_1, t_2, \omega_3) \propto |E_{\mathrm{LO}}(\omega_3)|^2 + 2\alpha\, \mathrm{Re}\left[E^*_{\mathrm{LO}}(\omega_3)\left\{E_{\mathrm{pump1}}(t_1, t_2, \omega_3) + E_{\mathrm{pump2}}(t_2, \omega_3)\right\}\right] \quad (3.14)$$

$$I_{\mathrm{scatter,off}}(t_1, t_2, \omega_3) \propto |E_{\mathrm{LO}}(\omega_3)|^2 + 2\alpha\, \mathrm{Re}\left[E^*_{\mathrm{LO}}(\omega_3) E_{\mathrm{pump2}}(t_2, \omega_3)\right] \quad (3.15)$$

Even though taking the difference between Eq. (3.14) and Eq. (3.15), the signal related to E_{probe} E^*_{pump1} still remains, which shows the t_1-dependence as well.

It should be noted that, the t_2-dependence of E_{echo} is much different from that of E_{pump1}: while E_{echo} is slowly decaying during t_2 period, E_{pump1} is highly oscillating at a mid-IR frequency. Therefore, by adding data recorded at two different population times of $t_2 \pm \pi/(2\omega_0)$ (ω_0: center frequency of the pump pulse), the oscillating term of $E^*_{\mathrm{LO}} E_{\mathrm{pump1}}$ can be removed from the ΔI. This time modulation is provided by using a piezoelectric actuator (PZA in Figure 3.4(a)) at a delay stage for probe and reference pulses (DS3 in Figure 3.4(a)). The PZA is driven by a sinusoidal-wave waveform generated by the computer at approximately 17 Hz. During the 2D-IR experiments, the amplitude of AC voltage applying to the PZA is adjusted to move the DS3 by approximately one wavelength at the center frequency of the IR pulse. By using the PZA, the average over a certain number of laser shots minimizes the scatter artifacts in the recorded signal.

3.6. Summary

In this chapter, I summarized the optical setup for 2D-IR spectroscopy. This setup was used in Chapter 8 to discuss the vibrational frequency fluctuations of solutes in aqueous solutions.

References

1. W. P. de Boeij, M. S. Pshenichnikov, and D. A. Wiersma, *Annu. Rev. Phys. Chem.*, **49**, 99 (1998).

2. S. Mukamel and R. M. Hochstrasser, *Chem. Phys.*, **266**, 135 (2001).

3. D. M. Jonas, *Annu. Rev. Phys. Chem.* **54**, 425 (2003).

4. M. L. Cowan, B. D. Bruner, N. Huse, J. R. Dwyer, B. Chugh, E. T. J. Nibbering, T. Elsaesser, and R. J. D. Miller, *Nature*, **434**, 199 (2005).

6. R. M. Hochstrasser, *Proc. Natl. Acad. Sci. U. S. A.*, **104**, 14190 (2007).

7. J. Bredenbeck, J. Helbing, C. Kolano, and P. Hamm, *Chem. Phys. Chem.*, **8**, 1747 (2007).

8. J. Zheng, K. Kwak, and M. D. Fayer, *Acc. Chem. Res*., **40**, 75 (2007).

9. Z. Ganim, H. S. Chung, A. W. Smith, L. P. DeFlores, K. C. Jones, and A. Tokmakoff, *Acc. Chem. Res.*, **41**, 432 (2008).

10. P. Hamm, M. Lim, and R. M. Hochstrasser, *J. Phys. Chem. B*, **102**, 6123 (1998).

11. M. Khalil, N. Demirdröven, and A. Tokmakoff, *Phys. Rev. Lett.*, **90**, 047401 (2003).

12. E. H. G. Backus, S. Garrett-Roe, and P. Hamm, *Opt. Lett.*, **33**, 2665 (2008).

13. J. Helbing and P. Hamm, *J. Opt. Soc. Am. B*, **28**, 171 (2011).

14. F. Seifert, V. Petrov, and M. Woerner, *Opt. Lett.*, **23**, 2009 (1994).

15. R. A. Kaindl, M. Wurm, K. Reimann, P. Hamm, A. M. Weiner, and M. Woerner, *J. Opt. Soc. Am. B*, **17**, 2086 (2000).

16. L. P. DeFlores, R. A. Nicodemus, and A. Tokmakoff, *Opt. Lett.*, **32**, 2966 (2007).

17. S. -H. Shim and M. T. Zanni, *Phys. Chem. Chem. Phys.*, **11**, 748 (2009).

18. S. -H. Shim, D. B. Strasfeld, Y. L. Ling, and M. T. Zanni, *Proc. Natl. Acad. Sci USA*, **104**, 14197 (2009).

19. I. C. Spector, C. M. Olson, C. J. Huber, and A. M. Massari, *Optics Lett.*, **40**, 1850 (2015).

Figures

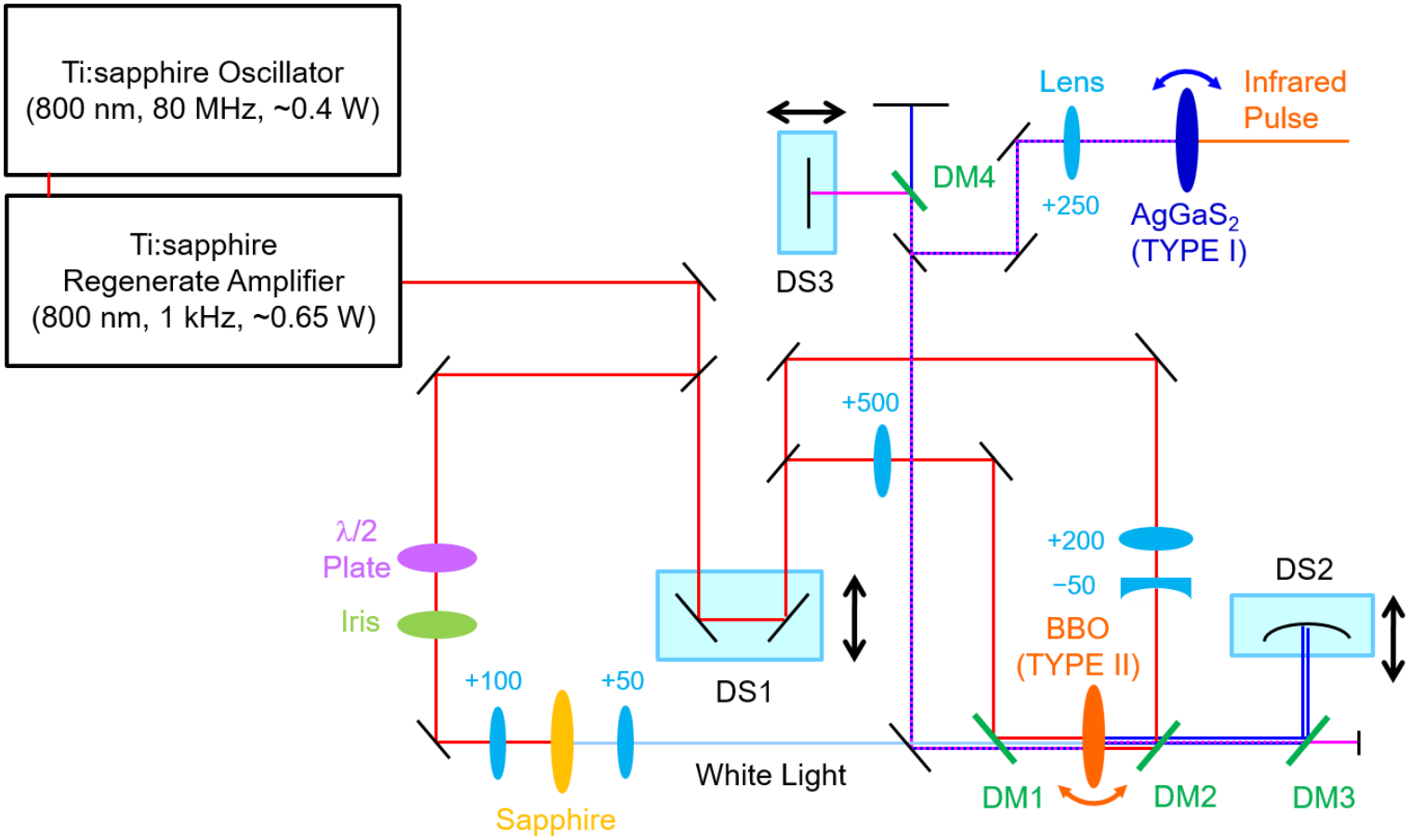

Figure 3.1. Optical setup for two-step OPA and DFG processes. The abbreviations are defined in text.

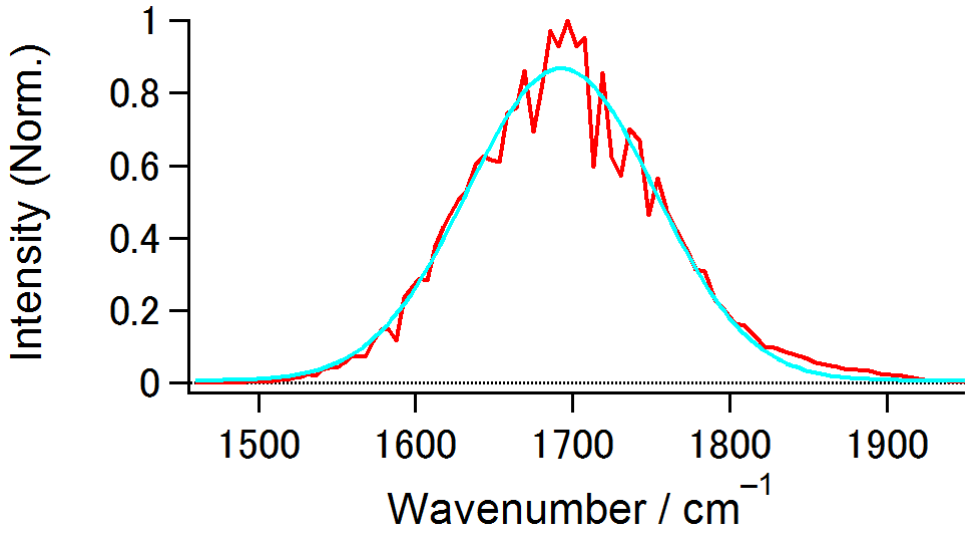

Figure 3.2. Spectrum of the mid-IR pulse used for the 2D-IR measurements in Chapter 8. The red and light-blue lines represent the experimental and fitting results, respectively.

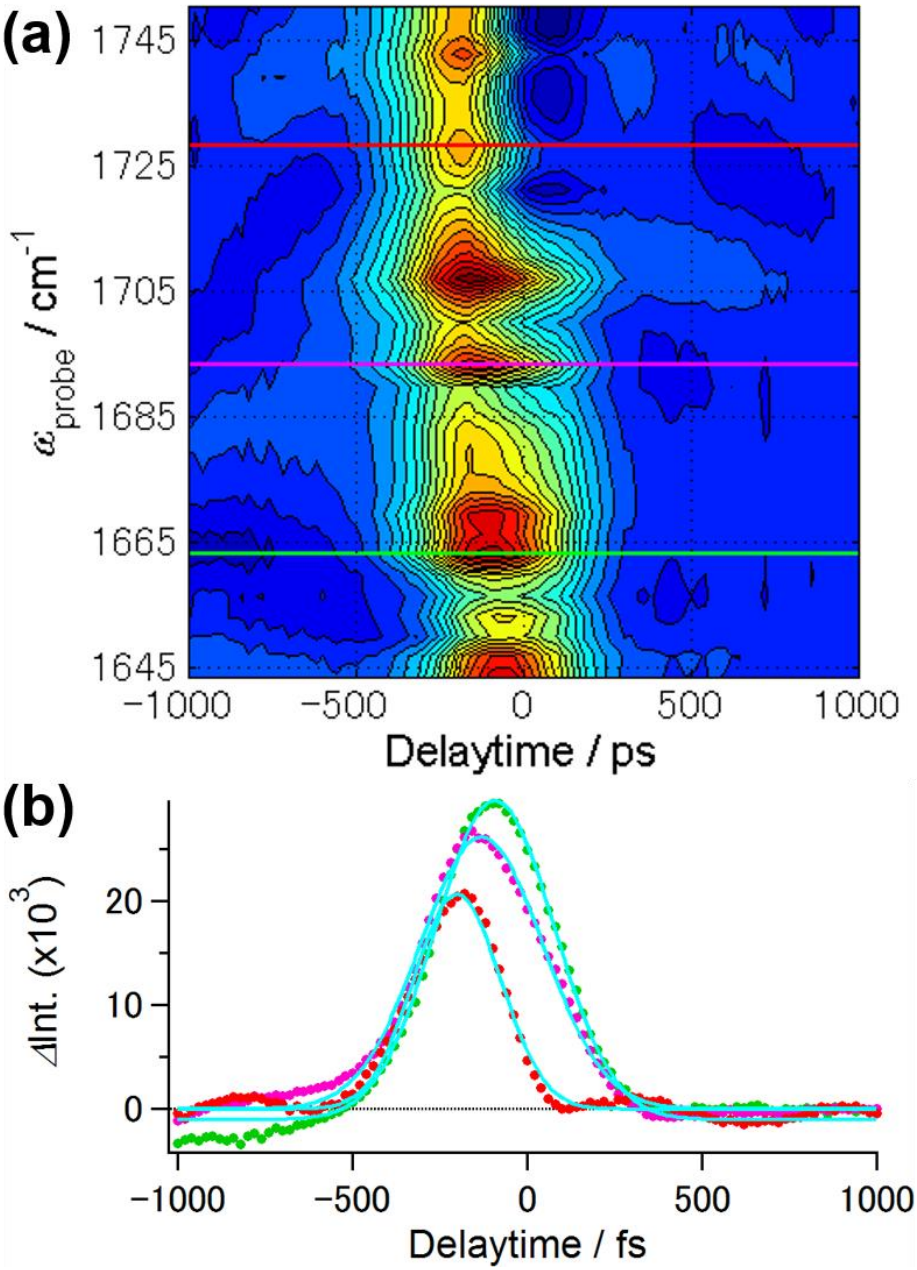

Figure 3.3. (a) Non-resonant FROG measurements for the 300 μm germanium wafer. The vertical and horizontal axes represent the probe wavenumber and temporal delay between E_{pump2} and E_{probe}, respectively. (b) Temporal profiles of FROG signals at three different probe wavenumbers: 1728.4 cm^{-1} (red), 1693.2 cm^{-1} (pink), and 1663.0 cm^{-1} (green). The closed circles are the experimental results. The light-blue lines are the fit to Gaussian functions. The full width of half maximum of the Gaussian fitting function for each signal is as follows: 176.0 fs (red), 247.7 fs (pink), and 238.9 fs (green).

(a)

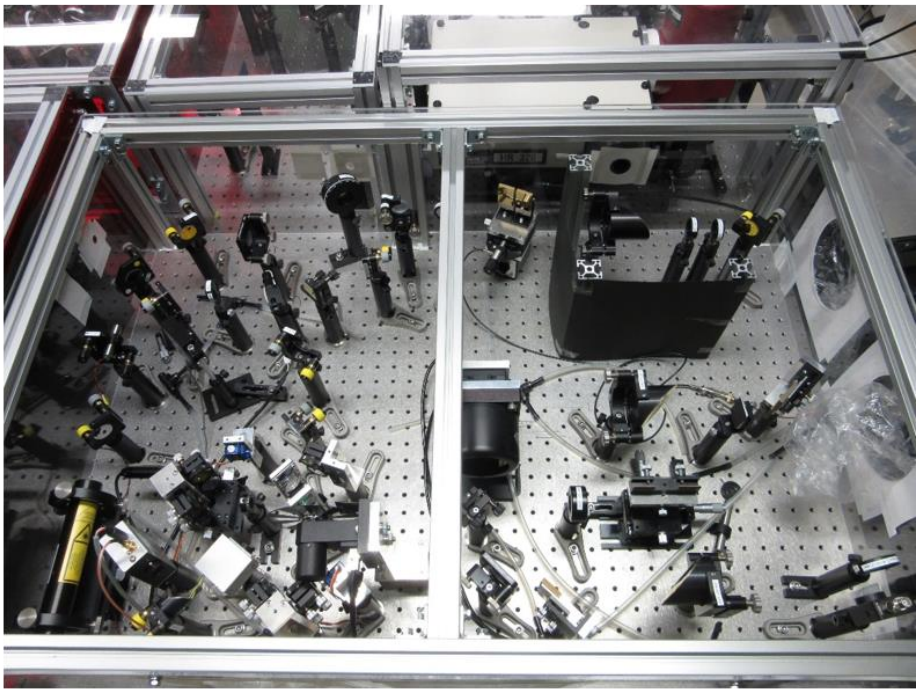

(b)

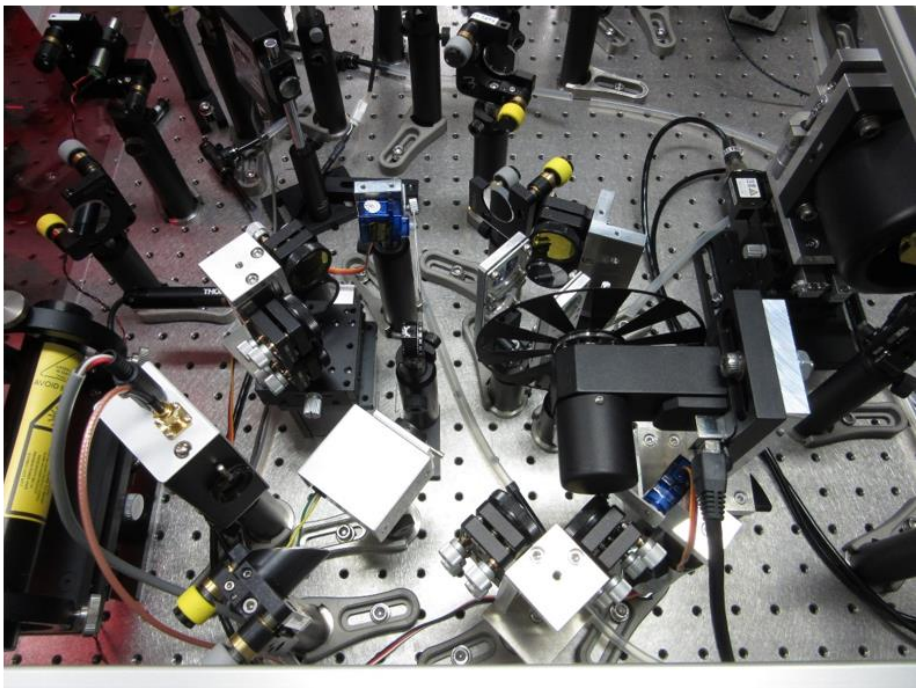

Figure 3.4. Pictures of (a) overview of the 2D-IR spectrometer and (b) close up of the Mach-Zehnder interferometer setup.

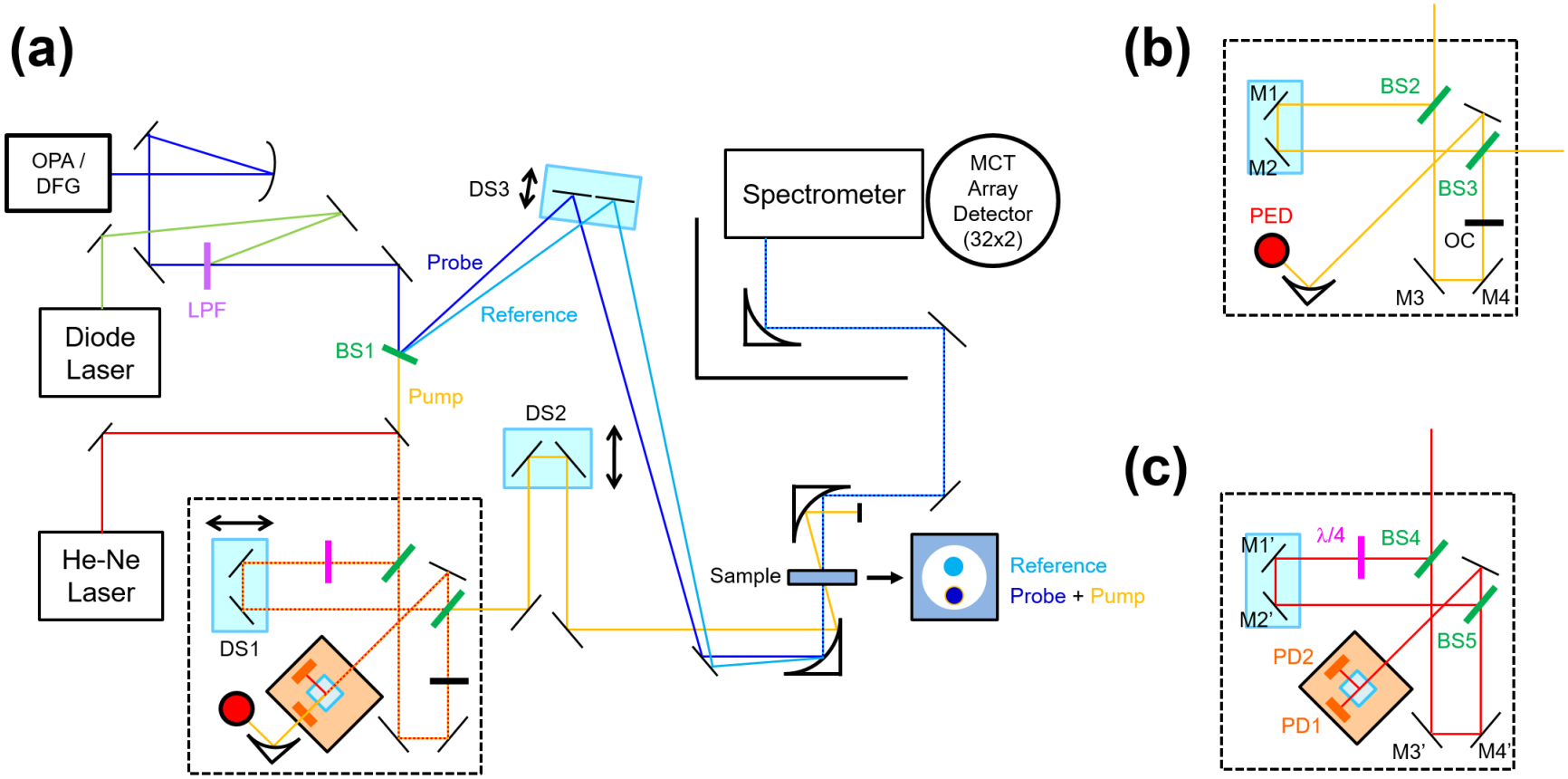

Figure 3.5. (a) Schematic overview of the 2D-IR spectrometer. Beam paths for (b) mid-IR pulses and (c) He-Ne laser in the Mach-Zehnder interferometer. Diode laser is spatially overlapped with mid-IR pulses on a long-path filter (abbreviated as LPF), and used as a guide beam for mid-IR pulses. The abbreviations are defined in text.

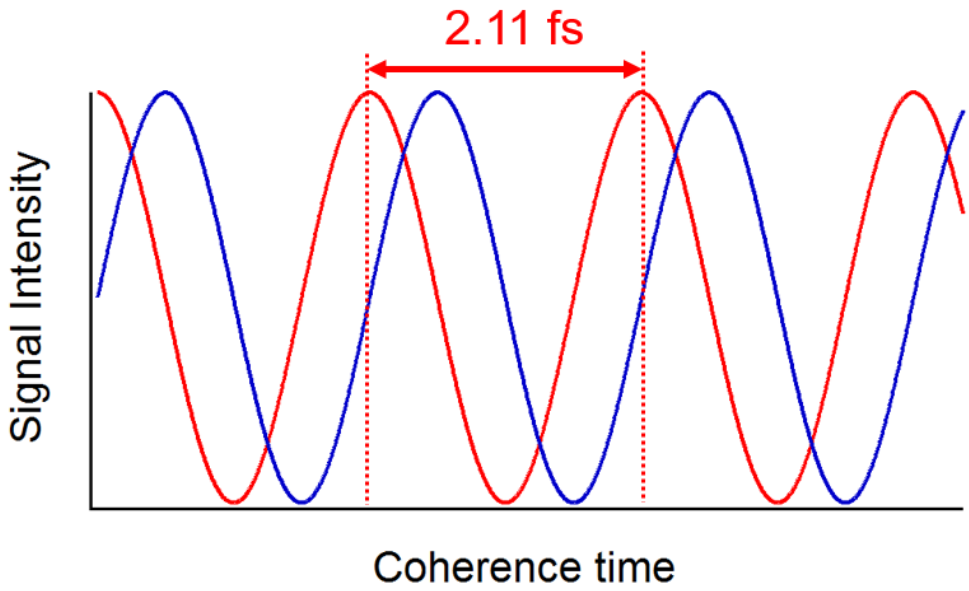

Figure 3.6. Schematic illustration of the interference between a circular polarized beam and a linear polarized beam. The two orthogonally polarized signals with a relative 90° phase shift are used for quadrature fringe counting method.

Appendix 3.A. Auto-correlation Measurement of Mid-IR Pulse with $AgGaS_2$ Nonlinear Crystal

In order to characterize the pulse duration, the auto-correlation function between the mid-IR pulses was measured by using the SHG process in an $AgGaS_2$ crystal (TYPE I, thickness : 0.5 mm, phase-matching angle : 34.5°). When the mid-IR pulses are temporally overlapped, their second harmonic is emitted into a given phase-matching direction from the crystal. Therefore, by changing the time delay between the IR pulses, time-dependence of the intensity of the SHG pulse was recorded with a PbSe detector as shown in Figure 3.A.1. Figure 3.A.2 shows the intensity change of the SHG pulse as a function of the time delay between the mid-IR pulses. This signal can be fitted by a Gaussian function with the FWHM of approximately 210 fs.

Figures

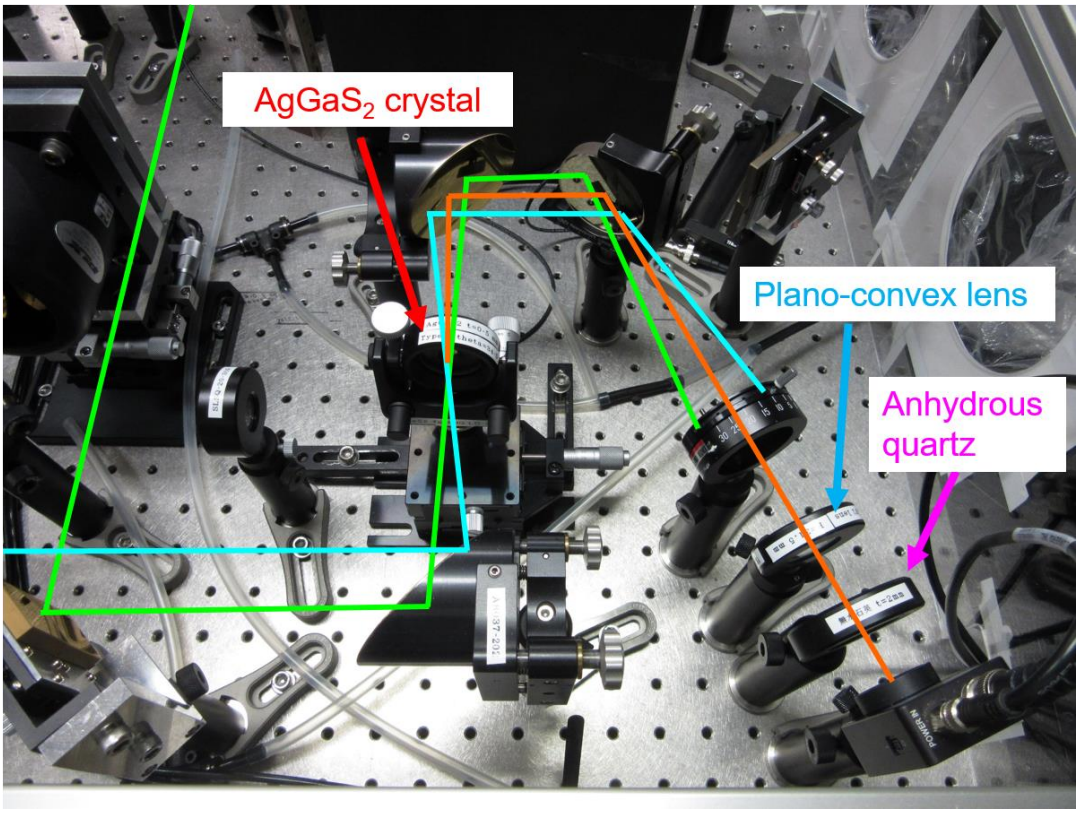

Figure 3.A.1. Optical setup for non-collinear auto-correlation measurement using an $AgGaS_2$ crystal. The green and light-blue lines represent the incident mid-IR pulses. The orange line represents the SHG signal emitted from the $AgGaS_2$ crystal.

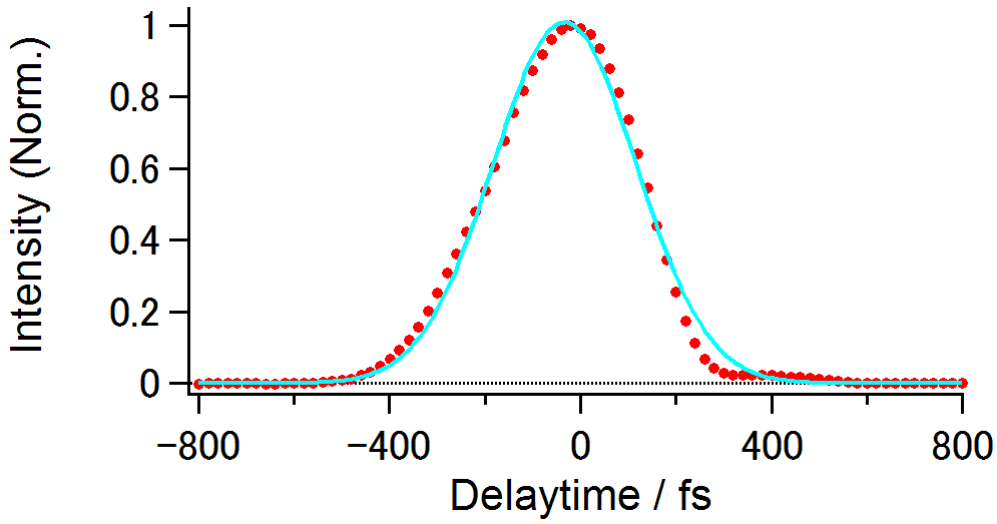

Figure 3.A.2. Temporal profile of the SHG signal between the mid-IR pulses emitted from the $AgGaS_2$ crystal. The red closed circles are the experimental results. The light-blue line represents the fit to a Gaussian function.

Appendix 3.B. 2D-IR Measurement for $[RuCl_5(NO)]^{2-}$ in D_2O

As the solute, potassium pentachloronitrosylruthenate(II) (abbreviated as $[RuCl_5(NO)]^{2-}$) were purchased from Sigma-Aldrich (St. Louis, Missouri, United States of America) and used without further purification. As the solvent, D_2O was purchased from Wako (Japan, 99.9%). The sample solution (concentration: ~100 mM) were confined in a 25 μm path length CaF_2 cell. The 2D-IR measurements was conducted at a room temperature (293 K).

Using the 2D-IR spectrometer built in this study, the 2D-IR signals of $[RuCl_5(NO)]^{2-}$ in D_2O at t_2 = 0 ps were collected from t_1 = 0 fs to 1800 fs in 4 fs step. Figure 3.B.1(a) displays the FT-IR spectrum of the NO stretching mode of $[RuCl_5(NO)]^{2-}$ in D_2O, which has the maximum absorption at 1882.2 cm^{-1}. Figures 3.B.1(b) and 3.B.1(c) describe the related 2D-IR spectra with and without the calibration of t_1 axis, respectively. Figure 3.B.2 plots the temporal t_1 value determined by the quadrate fringe counting method with He-Ne interferences as a function of the scan number in the measurement. Form the linear fit to this data, the actual time step of t_1 axis was found to be 3.96 fs. Therefore, the difference of the actual increasing rate from the desired one (*i.e.* 4 fs in this measurement) provided the frequency shift of the obtained 2D-IR spectrum toward the lower ω_1 frequency side by approximately 1.01% (*i.e.* ~19 cm^{-1}). The 2D-IR spectra shown in Figures 3.B.1(b) and 3.B.1(c) had their peaks along ω_1 axis at around 1865.3 cm^{-1} and 1882.5 cm^{-1}, respectively, which was in good agreement with the estimated frequency shift. Moreover, by calibrating the t_1 axis, the signal peaks of the 2D-IR spectrum along ω_1 axis were correctly observed at around the peak wavenumber of the FT-IR spectrum (= 1882.2 cm^{-1}).

Figures

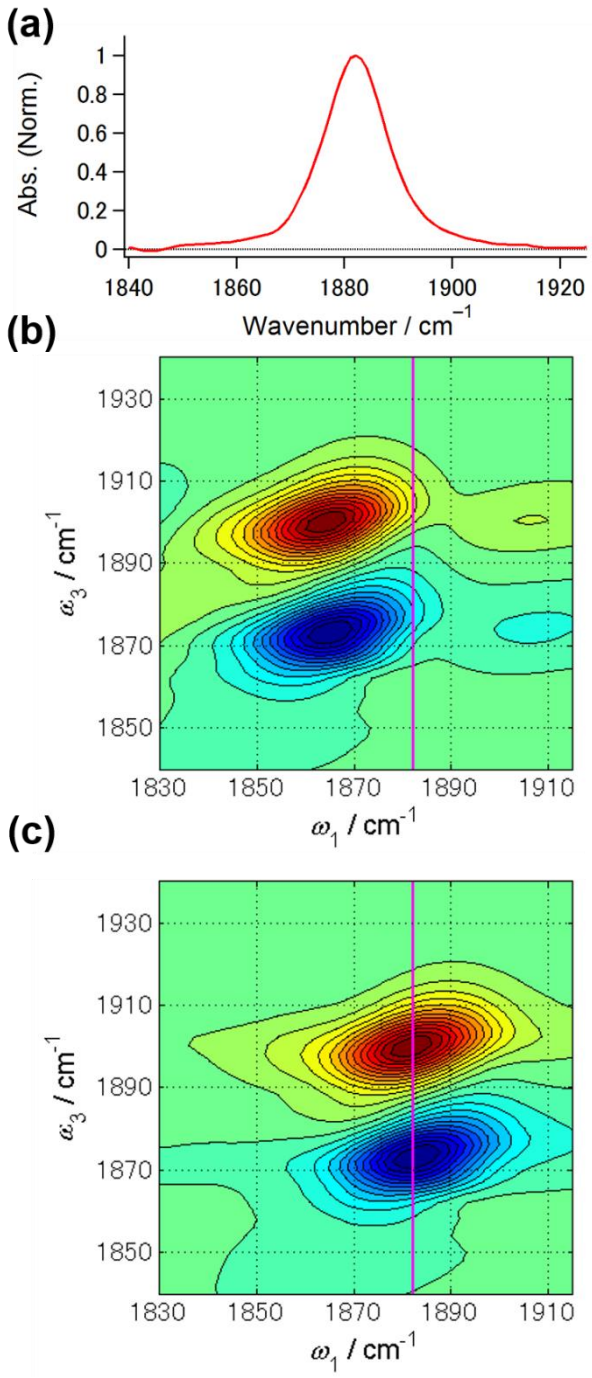

Figure 3.B.1. (a) IR absorption spectrum of the NO stretching mode of $[RuCl_5(NO)]^{2-}$ in D_2O. The associated 2D-IR spectra of $[RuCl_5(NO)]^{2-}$ in D_2O at t_2 = 0 ps (b) without and (c) with the calibration of the t_1 axis by the quadrate fringe counting method with He-Ne interferences. The pink line represents the line of ω_1 = 1882.2 cm^{-1}.

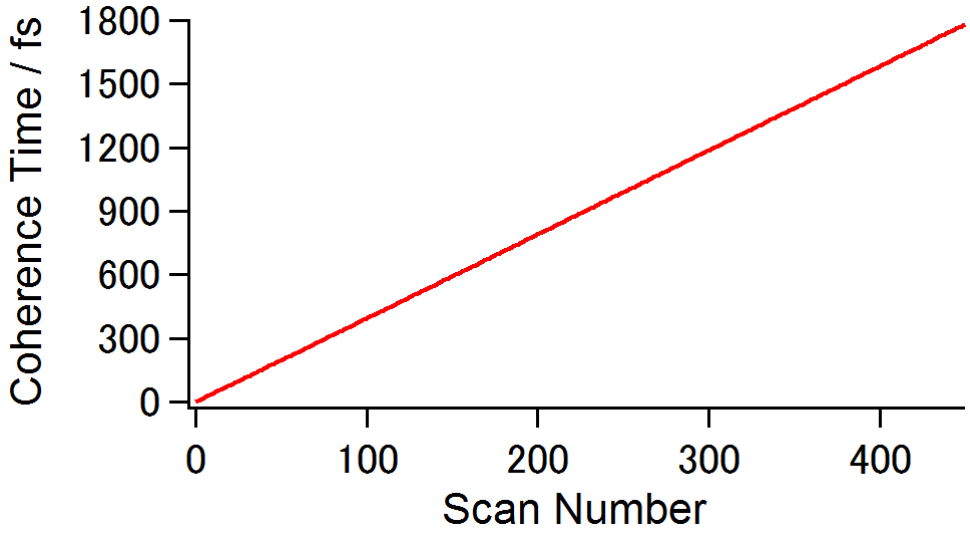

Figure 3.B.2. Temporal t_1 value determined by the quadrate fringe counting method with the He-Ne interferences as a function of the scan number in the measurement.

CHAPTER 4.

Frequency Fluctuations of Non-ionic Vibrational Probe Molecule in Aqueous Solution: Experimental Study by Two-dimensional Infrared Spectroscopy

4.1. Introduction

In aqueous solutions, hydrogen bond (HB) network structures are formed among water molecules. Due to the collective motions of water molecules, such as formation and breaking HBs, the network structure is temporally evolving. Because this structural rearrangement causes the fluctuations of solute-solvent interactions, the static and dynamic properties of the solutes in water are significantly affected [1]. Therefore, in order to understand various kinds of chemical reactions and relaxations in water, we must investigate the solute-solvent interactions and hydration dynamics around the solute molecules [2, 3].

The fluctuation in a physical quantity ($\Delta A(T)$) reflects the dynamical properties of the solute, which is defined as:

$$\Delta A(T) \equiv A(T) - \langle A \rangle \tag{4.1}$$

where $A(T)$ and $\langle A \rangle$ are a time-dependent observable at time T and its time-averaged value, respectively. Its time correlation function ($C_A(T)$) typically provides the information on the strength and time scale of the fluctuation, which is defined as:

$$C_\omega(T) \equiv \langle \Delta\omega(T)\Delta\omega(0) \rangle . \tag{4.2}$$

From infrared three-pulse photon echo (IR-3PE) technique and two-dimensional infrared (2D-IR) spectroscopy, we can obtain the time correlation function of the vibrational frequency fluctuation ($\Delta\omega$), that is, frequency-frequency time correlation function (FFTCF, $C_\omega(T)$) [4, 5].

So far, using these methods, several groups have experimentally investigated $C_\omega(T)$ of vibrational probes in water [5-22]. It has been shown that the FFTCF of ionic probes, such as SCN^- and $[Fe(CN)_6]^{4-}$, can be modeled by a double exponential function plus a quasi-static component:

$$C_\omega(T) = \Delta_0^2 + \Delta_1^2 \exp(-T/\tau_1) + \Delta_2^2 \exp(-T/\tau_2) \tag{4.3}$$

where Δ_i and τ_i are the amplitude and time constant of frequency fluctuations, respectively. The fast and slow decaying components of their FFTCF are approximately sub-picosecond and 1 ps, both of which show weak solute-dependence [5, 23-35]. On the other hand, Fayer and Tokmakoff groups conducted the 2D-IR experiments for HOD in H_2O and in D_2O, respectively [36-38]. They revealed that the spectral diffusions of OD stretching and OH stretching modes of HOD can be characterized by time constants of about 1.4 ps, which are similar to those of ions. Moreover, the

molecular dynamics (MD) simulations for these systems showed that the slow decaying components are originated from the structural evolution of a HB network in water. Therefore, these results suggests that the dynamics of the HB network around the ions is similar to pure water rather than depends on the ions [31].

Recently, the vibrational frequency fluctuations of biomolecules, which are labeled with non-ionic N_3 and CN groups as vibrational probes, in water have been investigated by 2D-IR spectroscopy [39-45]. Here, some of the FFTCFs for these molecules in water contain quasi-static components, which may be due to the long-lived inhomogeneous environment. Depending on the hydrophilic and hydrophobic groups around the vibrational probes, we can expect that the hydration structure and its dynamics around the non-ionic vibrational probes are different from those around the ionic ones. Furthermore, due to the high charge density of the ionic vibrational probes, they may possess stronger interactions with solvents than non-ionic ones. However, the reason why the slower time constant of FFTCF of solutes in water is primarily determined by the solvent remains unclear.

In this study, I investigated the vibrational frequency fluctuations of the SCN anti-stretching modes of 2-nitro-5-thiocyanate benzoic acid (abbreviated as NTBA, Figure 4.1) and thiocyanate ion (abbreviated as SCN^-) in water by using 2D-IR spectroscopy. The reasons why NTBA was used as a vibrational probe are as follows: Firstly, because the SCN group of NTBA forms covalent bond with an aromatic ring, the vibrational probe is electrically neutral and may possess the different charge distribution from that of SCN^-. Therefore, the dependence of the frequency fluctuations on the electric properties of the vibrational probe can be investigated. Secondly, because there is an aromatic ring, which is considered to as a hydrophobic group, nearby the SCN group, the hydration structure around the vibrational probe of NTBA is expected to differ from that of SCN^-. Therefore, the dependence of the frequency fluctuations on the hydration structure of the vibrational probe can be examined.

In addition to the 2D-IR measurements for NTBA and SCN^- in water, I conducted the polarization-controlled IR pump-probe experiments for the systems to observe the vibrational energy relaxations (VER) and rotational relaxations, which also reflect the microscopic details around the vibrational probe.

4.2. Materials and Methods

Experimental setups for the IR pump-probe and 2D-IR spectroscopies are described elsewhere [46, 47]. Briefly, an output from a self-mode locked Ti:sapphire oscillator (Tsunami, Spectra Physics, pulse duration: ~100 fs, center wavelength: ~800 nm, repetition rate: 80 MHz) driven by a frequency-doubled Nd:YVO_4 laser (Millenia, Spectra Physics, pump power: ~4.0 W, center wavelength: ~532 nm) is amplified by a Ti:sapphire regenerative amplifier (Spitfire, Spectra Physics, output energy: ~580 mW, repetition rate: 1 kHz) pumped by a frequency-doubled Q-switched Nd:YLF laser (Evolution, Spectra Physics, pump power: ~6.0 W, repetition rate: 1 kHz). An output from the Ti:sapphire regenerative amplifier is converted into a mid-IR pulse by sequential OPA and DFG processes (output energy: ~3 μJ). The center wavenumber of the IR pulses was tuned to approximately 2150 cm^{-1} for NTBA and 2050 cm^{-1} for SCN^-. Figure 4.2(a) displays the spectra of the obtained IR pulses, which were measured with the combination of monochrometer and single-channel MCT (HgCdTe) detector. In order to characterize the pulse duration, the auto-correlation function between the IR pulses was measured by using the second harmonic generation (SHG) process in an $AgGaS_2$ crystal (TYPE I, thickness : 0.5 mm, phase-matching angle : 34.5°). When the IR pulses are temporally overlapped, their second harmonic is emitted into a given phase-matching direction from the crystal. Therefore, by changing the time delay between the IR pulses, time-dependence of the intensity of the SHG pulse was recorded with a PbSe detector. Figure 4.2(b) shows the intensity change of the SHG pulse as a function of the time delay between the IR pulses. This signal can be fitted by a Gaussian function with its full width at half maximum (FWHM) of approximately 100 fs.

Figure 4.3(a) shows the experimental setup for the IR pump-probe measurements. The mid-IR pulses from the OPA/DFG system are split into two pulses with a wedge-shaped ZnSe window (BS in Figure 4.3(a)). Here, the residual components of the near-IR pulses from the DFG process are removed by a proper long-pass filter (LPF in Figure 4.3(a)). The transmitted pulses with approximately 90 % of the incident pulse energy are used as pump pulses (yellow line in Figure 4.3(a)), and the reflected pulses are used as probe pulses (blue line in Figure 4.3(a)). The pump and probe pulses are focused on the sample by a parabolic mirror. The time delay between the pump and probe pulses (T) is controlled by an optical delay stage (DS in Figure 4.3(a)). An optical chopper (OC in Figure 4.3(a)), which is synchronized with the laser repetition, chops the pump pulses at a 500 Hz. By inserting a wire-grid polarizer (Pol1 in Figure 4.3(a)) into the

pathway of the probe pulses, the polarization of the probe pulses is rotated by 45° with respect to that of the pump pulses (see Figure 4.3(b)). The pump-probe signals parallel and perpendicular to the polarization of the pump pulses are individually measured with a polarizer mounted on a motorized rotation mount (Pol2 in Figure 4.3(a)). The isotropic and anisotropic pump-probe signals ($N(T)$ and $r(T)$) are obtained as:

$$N(T) = \frac{\Delta A_{//}(T) + 2\Delta A_{\perp}(T)}{3} \tag{4.3}$$

and

$$r(T) = \frac{\Delta A_{//}(T) - \Delta A_{\perp}(T)}{\Delta A_{//}(T) + 2\Delta A_{\perp}(T)} \tag{4.4}$$

, respectively. Here, $\Delta A_{//}(T)$ and $\Delta A_{\perp}(T)$ are the absorbance changes in the parallel and perpendicular polarization configurations, respectively (see Figure 4.3(c)). After spectrally-resolved by a monochromator, the pump-probe signals are detected with a liquid N_2-cooled 64-channel MCT array detector. To remove undesirable signals due to the interference between the pump pulses scattered from the window of the sample cell and the probe pulses, the time delay of T is modulated with a piezoelectric actuator during the IR pump-probe measurements [51].

Figure 4.4 displays the experimental setup for the 2D-IR spectroscopy. The mid-IR pulses from the OPA/DFG system are split into three pulses by a beamsplitter (BS1 in Figure 4.4) and wedge-shaped CaF_2 window (BS2 in Figure 4.4). Here, same as the pump-probe measurements, the remaining near-IR pulses passing through a nonlinear optical crystal for the DFG process are removed by a proper long-pass filter (LPF in Figure 4.4). Two of them are used as pump pulses (red and yellow lines in Figure 4.4), and the other pulse is used as a probe pulse (blue line in Figure 4.4). These pulses are focused on the sample with a 30° off-axis parabolic mirror (effective focus length: 108.89 mm) in a collinear pump-probe geometry [48-50]. As mentioned in Chapter 3, in this geometry, the probe pulses can act as a local oscillator for heterodyne detection of the vibrational echo signals. The time delays of t_1 and t_2 (see these notations in Section 3.3.2) are controlled by two optical delay stages (DS1 and DS2 in Figure 4.4, respectively). An optical chopper (OC in Figure 4.4) chops the second pump pulses at a 500 Hz. Same as the pump-probe measurements, after passing through a monochrometer, which provides the ω_3 frequency axis of the 2D-IR spectrum, the vibrational echo signals are heterodyne detected by a liquid N_2-cooled 64-channel MCT array detector. Moreover, the interferograms between the two pump pulses are monitored by a N_2-cooled single-channel MCT detector with a

monochrometer and a N_2-cooled single-channel InSb detector, which are used to determine the time origin of the t_1 axis and correct the t_1 axis of 2D-IR signals, respectively. The detail of this data correction is described in Appendix 4.A. In the 2D-IR experiments, by scanning t_1 at a given t_2, the intensity difference ($\Delta I(t_1, t_2, \omega_3)$) of the probe pulses between the intensity with OC open and close states is recorded for each ω_3 frequency. 2D-IR spectra are obtained after performing a Fourier transform of $\Delta I(t_1, t_2, \omega_3)$ with respect to the t_1 axis, which provides ω_1 frequency axis. Same as the IR pump-probe experiments, during the 2D-IR experiment, the time delay of t_2 is modulated with a piezoelectric actuator [51].

NTBA and sodium thiocyanate were purchased from Sigma-Aldrich (St. Louis, Missouri, United States of America) and used without further purification. As the solvent, distilled H_2O was used. The concentration of the samples was approximately 250 mM. To dissolve NTBA into water, a small amount of NaOH (Wako, Japan, 40 w/w% solution in H_2O) was added to the NTBA aqueous solution (pH ~ 9.0). Note that, when a particle whose size is comparable with wavelength of the incident pulse exist in the solution, the pulse is strongly scattered by the particle, which is a so-called Mie scattering. Therefore, in order to remove the remaining undissolved, the sample solutions were passed through disposal membrane filters (ADVANTEC, Japan, diameter size: 0.20 μm). After that, they were contained in a cell with an optical path length of 25 μm and a pair of CaF_2 windows. All of the experiments were conducted at room temperature (293 K).

4.3. Results and Discussions

4.3.1. IR Absorption Spectra

Figure 4.5 presents the IR absorption spectra of the SCN anti-stretching modes of NTBA and SCN^- in H_2O with the fitting results. The IR spectra of NTBA and SCN^- were fitted by one Lorentzian and Gaussian functions, respectively. The fitting analysis for SCN^- shows that the IR spectrum of SCN^- is not symmetrical and exhibits a small band in the lower frequency side. Recently, Yuan *et al*. revealed that the IR spectrum of the selenocyanate anion ($SeCN^-$) in D_2O shows an asymmetric line shape [33]. Based on the isotropic pump-probe signals at different probe wavenumbers, they concluded that the low-frequency side of the absorption spectrum of $SeCN^-$ in D_2O is attributed to the vibrational transition of the SeCN anti-stretching mode with weaker HBs (*i.e*. non-Condon effect) [34]. From the similarity to $SeCN^-$, I expect that there may

be a distribution in the HB strengths between SCN^- and water molecules, and that SCN^- with weaker HBs may exhibit the absorption band of the SCN anti-stretching mode in the lower frequency region. To support these assumptions, the absorption spectrum of the SCN anti-stretching mode of SCN^- in dimethyl sulfoxide (DMSO, polar aprotic solvent) was observed, and the detailed IR pump-probe analysis for SCN^- in H_2O was conducted (see the results in Appendix 4.B.). These results indicates that the HB strength between SCN^- and water molecules possesses inhomogeneous distribution. Therefore, I consider that the asymmetrical line shape of the IR spectrum of SCN^- in H_2O originates from the non-Condon effect.

The peak wavenumber of the IR spectrum of SCN^- is 2065.4 cm^{-1}. On the other hand, NTBA exhibits a peak absorption at a higher frequency of 2169.3 cm^{-1}. In order to obtain the detailed information on the SCN anti-stretching modes of NTBA and SCN^-, I performed the quantum chemical calculations for these molecules in gas phase based on the density functional theory (DFT) with Gaussian 09 program package at B3LYP/6-311++G(3df,2pd) level [52]. The DFT results with respect to the normal mode analyses and partial charges of them are summarized in Table 4.1. The normal mode analyses show that the SCN anti-stretching modes of NTBA and SCN^- are localized as the CN stretching motions, whose result of SCN^- is consistent with the previous study [23]. Note that, as listed in Table 4.1, the SCN anti-stretching modes of NTBA and SCN^- have different force constants (k). Because of the covalent bond between the SCN group and aromatic ring, the potential surface of NTBA is likely different from that of SCN^-. Therefore, the difference in the potential surface of the vibrational probe may provide the different peak wavenumbers of the SCN anti-stretching modes of NTBA and SCN^-.

4.3.2. Polarization-controlled IR Pump-probe Experiments

Generally speaking, due to the vibrational energy relaxation, an isotropic pump-probe signal eventually decays to zero on a longer delay time. However, the IR pump-probe signals of the SCN anti-stretching modes of NTBA and SCN^- in H_2O possess non-zero offsets, which are attributed to the local heating effect originating from the relaxation of water molecules [54, 55]. Therefore, the isotropic pump-probe signals obtained from the IR pump-probe experiments ($N(\omega, T)$) were corrected as follows [56]:

$$P(\omega,T) = N(\omega,T) - N(\omega,\infty)\left(1-\exp\left(-T/T_{\mathrm{TE}}\right)\right) \tag{4.5}$$

where $P(\omega, T)$ is the corrected isotropic pump-probe signal at a probe wavenumber ω. The time

constant T_{TE} characterizes the time scale of the local heating process around the vibrational probe, and the heating process is assumed to be primarily due to the VER of the combination band of the HOH bending mode and the librational mode of H_2O. Therefore, the reported value of 0.14 ps was adopted as T_{TE} [57]. Figures 4.6(a) and (b) display the $P(\omega, T)$ of the SCN anti-stretching modes of NTBA and SCN^- in H_2O, respectively. The blue colors represent the signals originating from ground state bleaching (GSB; $\nu = 0 - 1$) and stimulated emission (SE; $\nu = 0 - 1$), and the red colors represent transient absorption (TA; $\nu = 1 - 2$). Moreover, Figure 4.6(c) describes the frequency-resolved pump-probe signals of NTBA and SCN^- at $T = 1$ ps. The spectrum of NTBA is fitted by two Lorentzian functions, and that of SCN^- is fitted by a sum of one Lorentzian function and one Gaussian function. Based on the fitting analyses, the anharmonicities of the SCN anti-stretching modes of NTBA and SCN^- are found to be 23.8 cm^{-1} and 32.7 cm^{-1}, respectively. The temporal profiles of $N(\omega, T)$ of NTBA and SCN^- at probe frequencies of the TA are shown in Figure 4.7, respectively. An exponentially decay function including the heating-induced contribution can reproduce these isotropic pump-probe signals:

$$f(T) = A_1 \exp(-T/T_1) + A_2 \{1 - \exp(-T/T_{TE})\}. \tag{4.6}$$

The time constant T_1 represents the VER time constant of the SCN anti-stretching mode, and those for NTBA and SCN^- in H_2O are listed in Table 4.2. It should be mentioned that, to exclude the coherent artifact signal due to the pump-probe interference, the signals after $T = 0.2$ ps were used for the fitting analyses [58]. As shown in Table 4.2, the vibrational lifetime of NTBA in H_2O is shorter than that of SCN^- in H_2O.

When a polyatomic molecule is vibrationally excited, the vibrational excited mode relaxes to the vibrational ground state by transferring energy to other intramolecular vibrational modes, that is, intramolecular vibrational redistribution (IVR) [59]. As the energy mismatch between donor and acceptor modes is larger, the efficiency of the IVR decreases. In earlier studies, Ohta *et al*. and Lenchenkov *et al*. revealed that the vibrational energy relaxation of SCN^- in H_2O is slower than that of N_3^- in H_2O [47, 60-62]. Because the vibrational frequency of the bending mode of SCN^- is lower than that of N_3^- [63], the longer vibrational lifetime results from a larger energy mismatch between the SCN anti-stretching band and the combination band of the SCN symmetric stretching and the SCN bending modes. Here, H_2O molecule shows a broad combination band of the HOH bending mode and the librational mode in the 2000 – 2200 cm^{-1} region, and NTBA and SCN^- can transfer excitation energy from the SCN anti-stretching modes

to this solvent mode. Figure 4.8 displays the isotropic IR pump-probe signals of NTBA and SCN^- in D_2O, respectively. The vibrational lifetimes of NTBA and SCN^- in D_2O are 1.9 ps and 20.4 ps, respectively, which are slower than those in H_2O. Therefore, this difference between the VER rates of NTBA and SCN^- in H_2O and D_2O suggests that the solute-solvent intermolecular energy transfer (IET) affects the vibrational energy relaxations of them in H_2O. Before, with respect the VER of XCN^- (X = O, S, or Se) in water, it was revealed that the stronger solute-solvent interaction owing to the larger partial charges should enhance the VER of the XCN anti-stretching mode by the IET process [62]. Based on this result, because the SCN group of NTBA has weaker solute-solvent interactions, the IET efficiency of NTBA is expected to be less than that of SCN^-. Nevertheless, the pump-probe signal of NTBA decays faster than SCN^-. Because NTBA possesses more intramolecular vibrational modes than SCN^-, the IVR processes may dominate the VER process of NTBA. Theoretical studies with MD simulations will help to provide detailed information on the mechanism of the VER process of NTBA.

Figure 4.9 shows the anisotropy decays of the SCN anti-stretching modes of NTBA and SCN^- in H_2O. The decay curve of SCN^- after T = 0.2 ps can be fitted by a single exponential function plus a constant, and the orientational relaxation time of SCN^- in H_2O is determined to be 2.9 ps (see Table 4.2). This time constant is consistent with previous works done by Zhong *et al*. and Lenchenkov *et al*. (T_R = 2.7 − 3 ps) [62, 63]. Rotational dynamics of solutes in solutions are often discussed based on the hydrodynamic theory of the Stokes-Einstein-Debye (SED) theory [64]. The SED theory says that the rotational relaxation time is proportional to the hydrodynamic volume of the solute molecule. NTBA has a larger molecular size than SCN^-. However, the orientational relaxation of NTBA in H_2O undergoes faster than that of SCN^-, whose rotational relaxation time is 1.3 ps. Consequently, the rotational motion of the entire NTBA molecule is less likely contributed to the observed anisotropic decay. If the reorientational relaxation of a vibrational probe occurs around a bond axis, the internal rotational motion plays an important role in the observed anisotropy decay [65, 66]. Based on these works, the internal rotational motion of the SCN group of NTBA around the C_{phenyl}–S bond axis may lead to the faster rotational relaxation time of NTBA than that of SCN^-. Furthermore, as the difference from SCN^-, the anisotropy decay of NTBA contains a long-lived component (A_∞), which does not decay to zero with in the observation window. According to the wobbling-in-a-cone model, the reorientational motion of a vibrational probe around a bond axis is expected to show bimodal anisotropy decay.

The faster decay is related to the wobbling motion of the restricted rotator, and the slow decay is related to the rotational motion as a whole, which leads to complete decay of anisotropy [67-70]. Therefore, the remaining component in the anisotropy decay of NTBA can be assigned to the rotational motion of the entire NTBA molecule. Although the anisotropy decay of NTBA contains a discernable remaining component, due to the short vibrational lifetime of NTBA, it is difficult to determine the amplitude of A_∞ accurately.

4.3.3. 2D-IR Experiments

The 2D-IR spectra of NTBA and SCN^- in H_2O were observed at different population times (t_2) ranging from 0 ps to 2 ps. Figure 4.10 describes the 2D-IR spectra of NTBA and SCN^- at t_2 = 0.2 ps, 1 ps, and 2 ps. Red and blue colors indicate the GSB + SE signals and the TA signal, respectively. The red lines represent the diagonal directions of the 2D-IR spectra ($\omega_1 = \omega_3$). At shorter population times, because there is a correlation between two vibrational frequencies (*i.e.* ω_1 and ω_3), the 2D-IR spectrum elongates along the diagonal direction. As the population time increases, reflecting that the correlation between these frequencies is getting lost owing to evolution of the local environment around the vibrational probe, the shape of the 2D-IR spectrum becomes round. Therefore, insight into the frequency fluctuations of the solutes is obtained from the t_2-dependence of the 2D line shape.

In this study, the time evolution of the spectral shape was analyzed using the center line slope (CLS) method developed by Kwak *et al*. [71, 72]. A fit to the decay of CLS as a function of the population time provides the correlation time constant and its amplitude. The green lines in Figure 4.10 are the center lines of the 2D-IR spectra, and the CLS was obtained from the slope of these lines with respect to the ω_1 axis. Figure 4.11 displays the CLSs of NTBA and SCN^- as a function of the population time. When the IR spectrum to some extent contains homogeneous broadening, which originates from frequency fluctuations in the fast modulation limit, the CLS at t_2 = 0 ps will be less than one. The initial CLS values of NTBA and SCN^- are approximately 0.16 and 0.33, respectively. Moreover, as shown in Figure 4.11, the CLSs of NTBA and SCN^- possess decaying components, which originated from the slower frequency fluctuations. Note that a motinally narrowed component in the FFTCF can be expressed by a delta function. Moreover, a decay component in the FFTCF can be represented by a Kubo function (see Eq. (2.80)). Therefore,

in order to reproduce these behaviors of the FFTCF, the FFTCF of NTBA and SCN^- are modeled as:

$$C_{\omega}(t_2) = \delta(t_2)/T_2^* + \Delta_C^2 \exp\left(-t_2/\tau_C\right) + \Delta_0^2 \tag{4.7}$$

where T_2^* is the pure dephasing time constant, which characterizes the homogeneous component. The Δ_C^2 and τ_C are the amplitude and correlation time of the frequency fluctuations, respectively, which reflect the spectral diffusion process. The Δ_0^2 is the static inhomogeneous component. The τ_C was obtained from the fitting analysis for the CLS curve with a single exponential function. Furthermore, using the mathematical formula of the linear IR and 2D-IR absorption spectra given by Eq. (2.106) and Eq. (2.107 − 109), respectively, the T_2^*, Δ_C^2, and Δ_0^2 values of the FFTCF in Eq. (4.7) were determined by numerical calculations to reproduce the experimentally obtained IR spectrum and the CLS [71, 72]. Here, the time constants of VER and orientational relaxation listed in Table 4.2 were used to calculate the vibrational and rotational line broadening functions (see Section 2.4.3). It is important to note that the non-Condon effect was not taken into account for the CLS analysis of SCN^-, and the CLS after t_2 = 0.2 ps was used to avoid the pulse overlapping effect.

The obtained FFTCF parameters are summarized in Table 4.2. Figure 4.12 displays the comparison between the experimental FT-IR spectra of NTBA and SCN^- in H_2O and the numerically calculated ones using the FFTCF parameters listed in Table 4.2. Here, the Δ_0 in the FFTCF reflects the slower decay of the FFTCF than the observation time. Previously, the 2D-IR experiments for trimethylamine-*N*-oxide (TMAO), tert-butyl-alcohol (TBA) and tetramethylurea (TMU) in water suggested that the hydration dynamics were slower than the bulk due to the hydrophobic effect of the methyl groups in these solutes [73, 74]. If such slow dynamics exists around the solutes, the FFTCF may contain a long-lived component. However, the CLS analysis revealed that the FFTCF of NTBA possess no static component (Δ_0). On the other hand, although the FFTCF of SCN^- has a static component, its amplitude relative to the other components is quite small. Therefore, the frequency fluctuations of the SCN anti-stretching modes of NTBA and SCN^- in H_2O are controlled by the motionally narrowed homogeneous contribution and solvation dynamics, which are characterized by the T_2^* and τ_C, respectively.

As shown in Table 4.2, the 2D-IR experiments for NTBA and SCN^- in H_2O showed that the FFTCFs of NTBA and SCN^- have a decay component of 1.1 ps and 0.9 ps, respectively. Here, Woutersen *et al*. used deuterated *N*-methylacetamide (NMAD), which is another non-ionic

vibrational probe, and measured the 2D-IR spectrum of the amide I mode of this molecule in D_2O [75]. Similar to the FFTCF of NTBA, that of NMAD exhibited a decaying component of 1.6 ps due to the solute-solvent HB dynamics and no quasi-static component [75, 76]. In previous studies of the OH stretching of HOD in D_2O and the OD stretching of HOD in H_2O, their FFTCFs contained the slowest decaying components (*i.e.* 1.2 − 1.4 ps) [36-38]. Moreover, the classical MD simulations for these systems revealed that the frequency fluctuations of the stretching mode of HOD are due to the collective motion of the HB network [18]. Therefore, because the FFTCFs of NTBA and SCN^- in H_2O exhibited decaying behaviors similar to those of HOD in H_2O and D_2O, the SCN anti-stretching modes of NTBA and SCN^- are also sensitive to the structural fluctuations of the HB network around the vibrational probes.

However, it should be noted that the magnitudes of the frequency fluctuations depend on the solute. To determine the sensitivity of the SCN anti-stretching mode to the hydration dynamics on a 1 ps time scale, the numerically calculated IR spectra of NTBA and SCN^- in H_2O without the slow decaying components are superimposed on Figure 4.12. Based on the spectra of NTBA and SCN^- shown in Figure 4.12, the ratios of the inhomogeneous bandwidth to the total bandwidth are approximately 0.29 and 0.46, respectively. Therefore, I found that the SCN anti-stretching mode of SCN^- is more sensitive to the hydration dynamics than that of NTBA, which is most likely due to the stronger interactions between SCN^- and water molecules.

It is important to note that the molecular properties of a solute including charge distribution and molecular structure are expected to affect the structure and dynamics of the hydrated water molecules. Therefore, the structure and dynamics of water molecules around NTBA likely differ from those around SCN^-. Nevertheless, the 2D-IR measurements revealed that the FFTCF of NTBA in H_2O decayed with a time constant of 1.1 ps, which is similar to that of SCN^-. In previous studies, it was revealed that the CN stretching modes of non-ionic and ionic CN groups in water exhibited similar behaviors: Chung *et al*. reported that the FFTCF of CN-Phe in water exhibited a decay of 2.1 ps [40], which is similar to that of CN^- in D_2O reported by Hamm group [10]. Furthermore, the FFTCF of CN-Phe possessed no quasi-static component, which is likely related to the hydrophobic hydration dynamics around the aromatic ring. Therefore, why are the FFTCFs of NTBA and SCN^- characterized by the approximately same time constants? Because the two vibrational probe molecules differ in their charge distributions and molecular structures, when the solvent dynamics in the vicinity of the probe molecule dominates

its vibrational frequency fluctuations, the FFTCFs of NTBA and SCN^- are expected to be different from each other.

In Chapter 5, based on the MD simulations for NTBA and SCN^- in H_2O, the relationship between the frequency fluctuations of the solute and its hydration structure and hydration dynamics will be discussed from theoretical aspects.

4.4. Conclusion

In this chapter, the vibrational dynamics of the SCN anti-stretching modes of NTBA and SCN^- in H_2O were investigated by polarized-controlled IR pump-probe spectroscopy and 2D-IR spectroscopy.

Based on the result that the vibrational lifetime of NTBA (0.8 ps) was much shorter than that of SCN^- (2.3 ps), the IVR processes played an important role in the VER of NTBA. Based on the comparison of the rotational relaxation times of NTBA and SCN^-, the internal rotational motion around the C_{phenyl}–S bond axis contributed the anisotropy decay of the SCN anti-stretching mode of NTBA.

The 2D-IR experiments of NTBA and SCN^- in H_2O revealed that the FFTCF of these molecules could be modeled by a delta function plus an exponential function and a constant (see Eq. (4.7)). Here, the delta function reflects the motionally narrowed water dynamics. On the other hand, based on the previous works on the frequency fluctuations of water, the other component can thought to reflect the collective motions of water molecules. Interestingly, although the solute properties of NTBA are significantly different from those of SCN^-, the FFTCFs of NTBA and SCN^- contained decaying components of approximately 1 ps. In Chapter 5, with respect to the reason why the FFTCFs of these molecules are characterized by the same time scale, the molecular interpretation will be discussed.

References

1. I. Ohmine and H. Tanaka, *Chem. Rev.*, **93**, 2545 (1993).

2. R. M. Stratt and M. Maroncelli, *J. Phys. Chem.*, **100**, 12981 (1996).

3. G. A. Voth and R. M. Hochstrasser, *J. Phys. Chem.*, **100**, 13034 (1996).

4. P. Hamm and M. T. Zanni, *Concepts and Methods of 2D Infrared Spectroscopy* (Cambridge University Press, 2011).

5. P. Hamm, M. Lim, and R. M. Hochstrasser, *Phys. Rev. Lett*, **81**, 5326 (1998).

6. P. Hamm, M. Lim, W. F. DeGrado, and R. M. Hochstrasser, *J. Phys. Chem. A*, **103**, 10049 (1999).

7. M. T. Zanni, M. C. Asplund, and R. M. Hochstrasser, *J. Chem. Phys*, **114**, 5479 (2001).

8. S. Woutersen, R. Pfistrer, P. Hamm, Y. Mu, D. S. Kosov, and G. Stock, *J. Chem. Phys.*, **117**, 6833 (2002).

9. N. -Hui Ge, M. T. Zanni, and R. M. Hochstrasser, *J. Phys. Chem. A*, **106**, 962 (2002).

10. M. Kozinski, S. Garrett-Roe, and P. Hamm, *Chem. Phys.*, **341**, 5 (2007).

11. K. F. Everitt, E. Geva, and J. L. Skinner, *J.Chem. Phys.*, **114**, 1326 (2001).

12. A. Piryatinski and J. L. Skinner, *J. Phys. Chem B*, **106**, 8055 (2002).

13. K. Kwac and M. Cho, *J. Chem. Phys.*, **119**, 2247 (2003).

14. C. P. Lawrence and J. L. Skinner, *J. Chem. Phys.*, **118**, 164 (2003).

15. K. Kwac, H. Lee, and M. Cho, *J. Chem. Phys.*, **120**, 1477 (2004).

16. S. A. Corcelli, C. P. Lawrence, J. B. Asbury, T. Steinel, M. D. Fayer, and J. L. Skinner, *J. Chem. Phys.*, **121**, 8897 (2004).

17. S. A. Corcelli, C. P. Lawrence, and J. L. Skinner, *J. Chem. Phys.*, **120**, 8107 (2004).

18. J. D. Eaves, A. Tokmakoff, and P. L. Geissler, *J. Phys. Chem. A*, **109**, 9424 (2005).

19. B. Auer, R. Kumar, R. Schmidt, and J. L. Skinner, *Proc. Natl. Acad. Sci. U. S. A*, **104**, 14215 (2007).

20. J. -Ho Choi, K. -Im Oh, and M. Cho, *J. Chem. Phys.*, **129**, 174512 (2012).

21. J. Jeon and M. Cho, *J. Phys. Chem. B*, **118**, 8148 (2014).

22. G. Prampolini, P. Yu, S. Pizzanelli, I. Cacelli, F. Yang, J. Zhao, and J. Wang, *J. Phys. Chem. B*, **118**, 14899 (2014).

23. K. Ohta, H. Maekawa, S. Saito, and K. Tominaga, *J. Phys. Chem. A*, **107**, 5645 (2003).

24. K. Ohta, H. Maekawa, and K. Tominaga, *J. Phys. Chem. A*, **108**, 1333 (2004).

25. H. Maekawa, K. Ohta, and K. Tominaga, *Res. Chem. Intermediat*, **31**, 703 (2005)

26. K. Ohta, J. Tayama, and K. Tominaga, *Phys. Chem. Chem. Phys.*, **14**, 10455 (2012).

27. K. Ohta, H. Maekawa, and K. Tominaga, *Chem. Phys. Lett.*, **386**, 32 (2004).

28. J. Tayama, M. Banno, K. Ohta, and K. Tominaga, *Sci. China Phys. Mech.*, **53**, 1013 (2010).

29. J. Tayama, K. Ohta, and K. Tominaga, *Chem. Lett.*, **41**, 366 (2012).

30. J. Tayama, A. Ishihara, M. Banno, K. Ohta, S. Saito, and K. Tominaga, *J. Chem. Phys.*, **133**, 014505 (2010).

31. K. Ohta, J. Tayama, S. Saito, and K. Tominaga, *Acc. Chem. Res.*, **45**, 1982 (2012).

32. D. Czurlok, M. von Domaros, M. Thomas, J. Gleim, J. Lindner, B. Kirchner, and P. Vöhringer, *Phys. Chem. Chem. Phys.*, **17**, 29776 (2015).

33. R. Yuan, C. Yan, A. Tamimi, and M. D. Fayer, *J. Phys. Chem B*, **119**, 13407 (2015).

34. S. Dutta, Z. Ren, T. Brinzer, and S. Garrett-Roe, *Phys. Chem. Chem. Phys.*, **17**, 26575 (2015).

35. K. M. Slenkamp, M. S. Lynch, J. F. Brookes, C. C. Bannan, S. L. Daifuku, and M. Khalil, *Structural Dynamics*, **3**, 023609 (2016).

36. J. B. Asbury, T. Steinel, K. Kwak, S. A. Corcelli, C. P. Lawrence, J. L. Skinner, and M. D. Fayer, *J. Chem. Phys.*, **121**, 12431 (2004).

37. C. J. Fecko, J. J. Loparo, S. T. Loberts, and A. Tokmakoff, *J. Chem. Phys.*, **122**, 054506 (2005).

38. J. J. Loparo, S. T. Roberts, and A. Tokmakoff, *J. Chem Phys.*, **125**, 194521 (2006).

39. R. Bloem, K. Koziol, S. A. Waldauer, B. Buchli, R. Walser, B. Samatanga, I. Jesarov, and P. Hamm, *J. Phys. Chem. B*, **116**, 13705 (2012).

40. J. K. Chung, M. C. Thielges and M. D. Fayer, *Proc. Natl. Acad. Sci. USA*, **108**, 3578 (2011).

41. M. C. Thielges, J. Y. Axup, D. Wong, H. S. Lee, J. K. Chung, P. G. Schultz, and M. D. Fayer, *J. Phys. Chem. B*, **115**, 11294 (2011).

42. S. Dutta, W. Rock, R. J. Cook, A. Kohen, and C. M. Cheatum, *J. Phys. Chem.* **135**, 055106 (2011).

43. S. Dutta, Y. -L. Li, W. Rock, J. C. D. Houtman, A. Kohen, and C. M. Cheatum, *J. Phys. Chem. B*, **116**, 542 (2012).

44. D. C. Urbanek, D. Y. Vorobyev, A. L. Serrano, F. Gai, and R. M. Hochstrasser, *J. Phys. Chem. Lett.*, **1**, 3311 (2010).

45. M. J. Tucker, X. S. Gai, E. E. Fenlon, S. H. Brewer, and R. M. Hochstrasser, *Phys. Chem. Chem. Phys.*, **13**, 2237 (2011).

46. M. Banno, K. Ohta, and K. Tominaga, *J. Phys. Chem. A*, **112**, 4170 (2008).

47. M. Okuda, K. Ohta, and K. Tominaga, *J Chem. Phys.*, **142**, 212418 (2015).

48. S. -H. Shim and M. T. Zanni, *Phys. Chem. Chem. Phys.*, **11**, 748 (2009).

49. S. -H. Shim, D. B. Strasfeld, Y. L. Ling, and M. T. Zanni, *Proc. Natl. Acad. Sci. USA*, **104**, 14197 (2009).

50. L. P. DeFlores, R. A. Nicodemus, and A. Tokmakoff, *Optics Lett.*, **32**, 2966 (2007).

51. I. C. Spector, C. M. Olson, C. J. Huber, and A. M. Massari, *Optics Lett.*, **40**, 1850 (2015).

52. M. J. Frisch *et al*., GAUSSIAN 09 (Revision B.01), Gaussian, Inc., Wallingford, CT (2009).

53. A. P. Scott and L. Radom, *J. Phys. Chem.*, **100**, 16502 (1996).

54. H. Son, K. -H. Park, K. -W. Kwak, S. Park, and M. Cho, *Chem. Phys.*, **422**, 37 (2013).

55. H. Bian, X. Wen, J. Li, and J. Zheng, *J. Chem. Phys.*, **133**, 034505 (2010).

56. M. Maj, C. Ahn, D. Kossowska, K. Park, K. Kwak, H. Han, and M. Cho, *Phys. Chem. Chem. Phys.*, **17**, 11770 (2015).

57. L. Chieffo, J. Shattuck, J. J. Amsden, S. Erramilli, and L. D. Ziegler, *Chem. Phys.*, **341**, 71 (2008).

58. P. Hamm, M. Lim, and R. M. Hochstrasser, *J. Phys. Chem. B*, **102**, 6123 (1998).

59. V. M. Kenkre, A. Tokmakoff, and M. D. Fayer, *J. Phys. Chem.*, **101**, 10618 (1994).

60. K. Ohta and K. Tominaga, *Chem. Phys. Lett.*, **429**, 136 (2006).

61. Q. Zhong, A. P. Baronavski, and J. C. Owrutsky, *J. Chem. Phys.*, **119**, 9171 (2003).

62. V. Lenchenkov, C. She, and T. Lian, *J. Phys. Chem. B*, **110**, 19990 (2006).

63. L. H. Jones, *J. Chem. Phys.*, **25**, 1069 (1956)

64. G. R. Fleming, *Chemical Application of Ultrafast Spectroscopy*, (Oxford University Press, 1986).

65. K. -K. Lee, K. -H. Park, C. Joo, H. -J. Kwon, H. Han, J. -H. Ha, S. Park, and M. Cho, *Chem. Phys.*, **396**, 23 (2012).

66. Y. L. Rezus, D. Madsen, and H. J. Bakker, *J. Chem. Phys.*, **121**, 10599 (2004).

67. K. J. Gaffney, I. R. Piletic, and M. D. Fayer, *J. Chem. Phys*., **118**, 2270 (2003).

68. H. -S. Tan, I. R. Piletic, and M. D. Fayer, *J. Chem. Phys*, **122**, 174501 (2005).

69. H. Son, Y. Kown, J. Kim, and S. Park, *J. Phys. Chem. B.*, **117**, 2748 (2013).

70. P. L. Kramer, C. H. Giammanco, and M. D. Fayer, *J. Chem. Phys.*, **142**, 212408 (2015).

71. K. Kwak, S. Park, I. J. Finkelstein, and M. D. Fayer, *J. Chem. Phys.*, **127**, 124503 (2007).

72. K. Kwak, D. E. Rosenfeld, and M. D. Fayer, *J. Chem. Phys.*, **128**, 204505 (2008).

73. A. Bakulin, C. Liang, T. L. Jansen, D. A. Wiersma, H. J. Bakker, and M. S. Pshenichnikv, *Acc. Chem. Res.*, **42**, 1229 (2009).

74. A. Bakulin, M. S. Pshenichnikv, H. J. Bakker, and C. Petersen, *J. Phys. Chem. A*, **115**, 1821 (2011).

75. S. Woutersen, R. Pfister, P. Hamm, Y. Mu, D. S. Kosov, and G. Stock, *J. Chem. Phys.*, **117**, 6833 (2002).

76. J. R. Schmidt, S. A. Corcelli, and J. L. Skinner, *J. Chem. Phys.*, **121**, 8887 (2004).

Figures and Tables

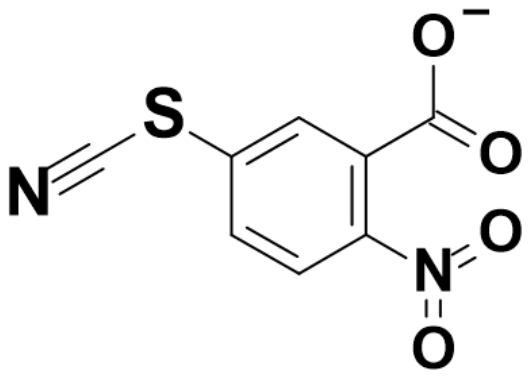

Figure 4.1. Molecular structure of 2-nitro-5-thiocyanate benzoic acid.

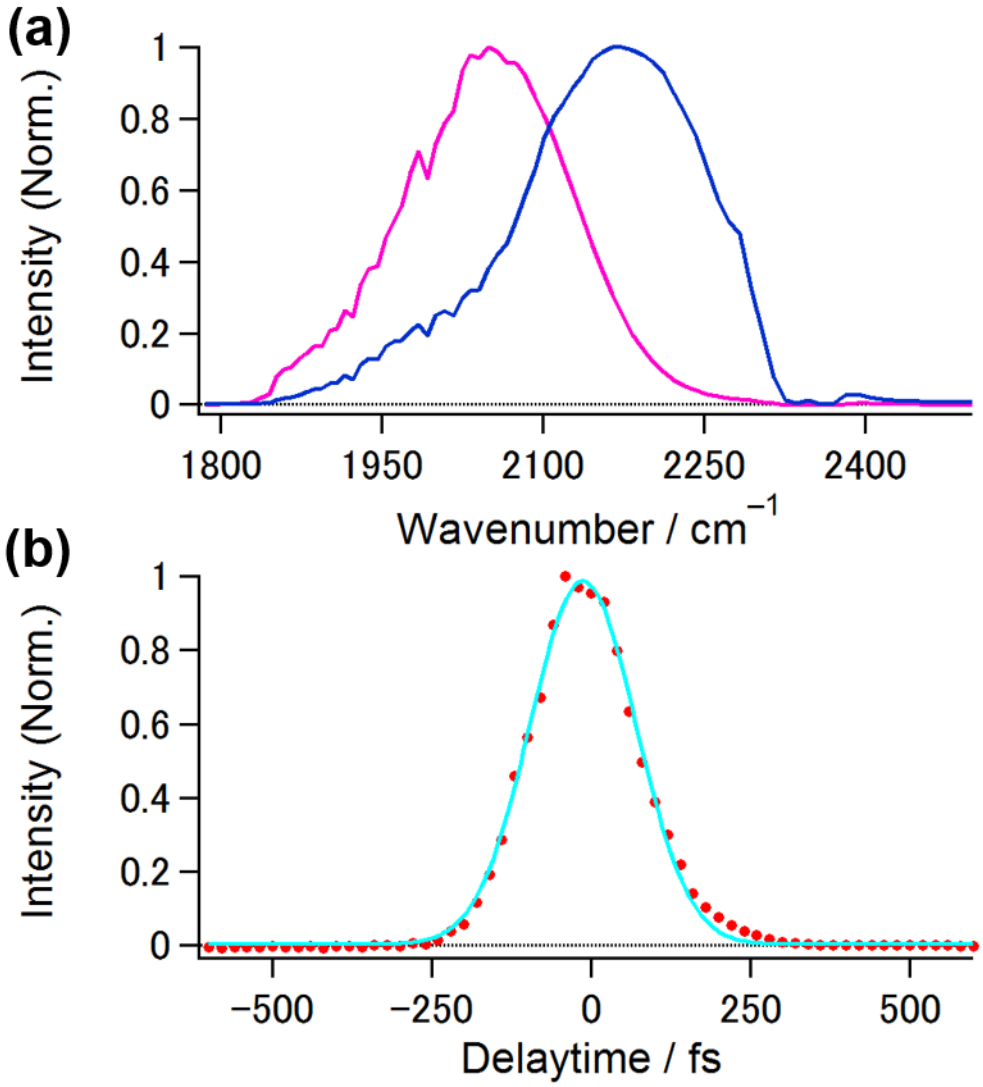

Figure 4.2. (a) Spectra of the IR pulses for the nonlinear IR experiments of NTBA (blue) and SCN^- (pink). The bandwidth of these spectra is approximately 100 cm^{-1}. (b) Temporal profile of the second harmonic generation signal between the IR pulses emitted from the $AgGaS_2$ crystal. The red closed circles are the experimental results. The light-blue line represents the fit to a Gaussian function.

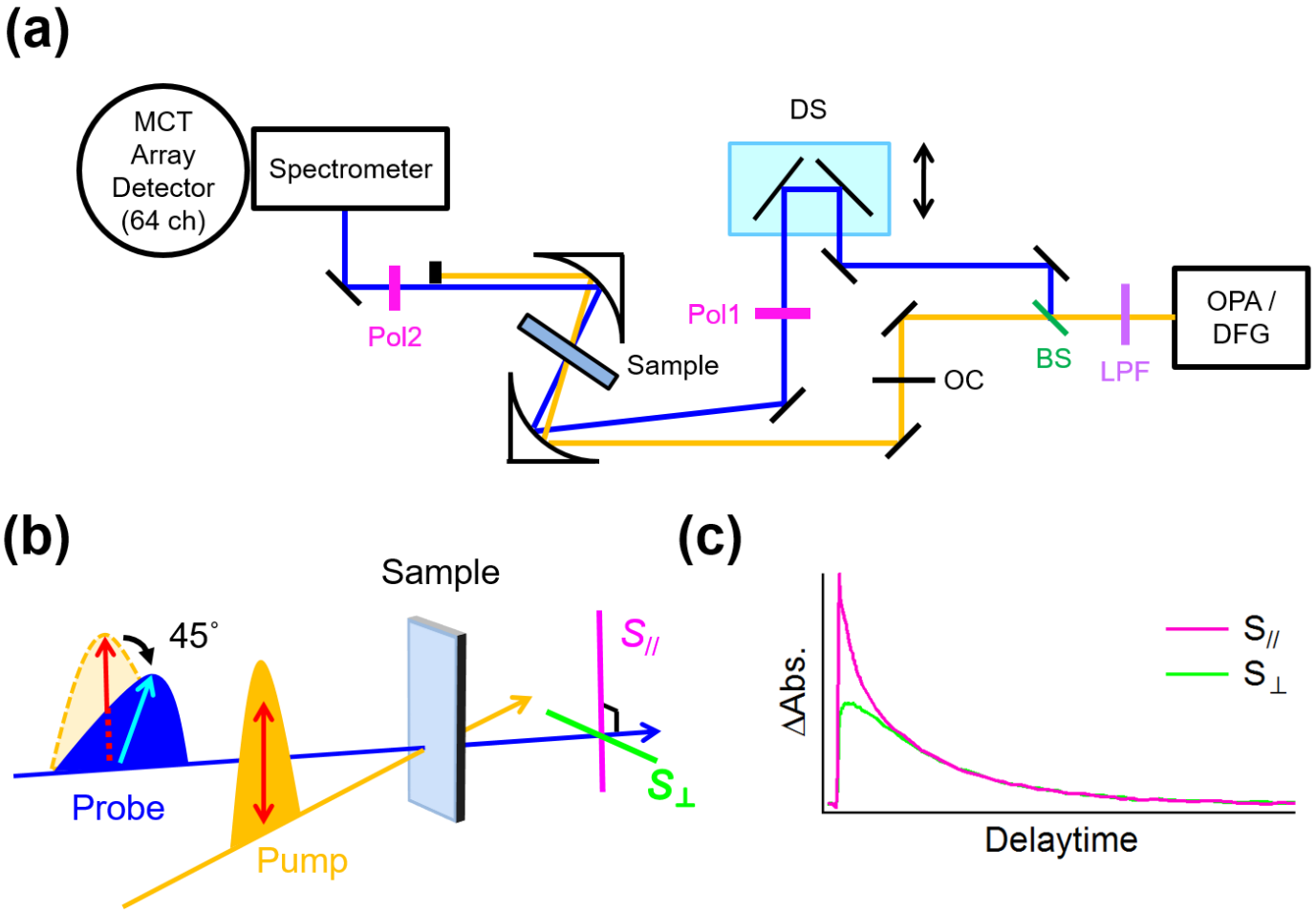

Figure 4.3. (a) Schematic overview of the 64 multi-channel IR pump-probe spectrometer. The abbreviations are defined in text. (b) Polarization of pump and probe pulses. (c) Typical IR pump-probe signals in the parallel (pink) and perpendicular (green) conditions.

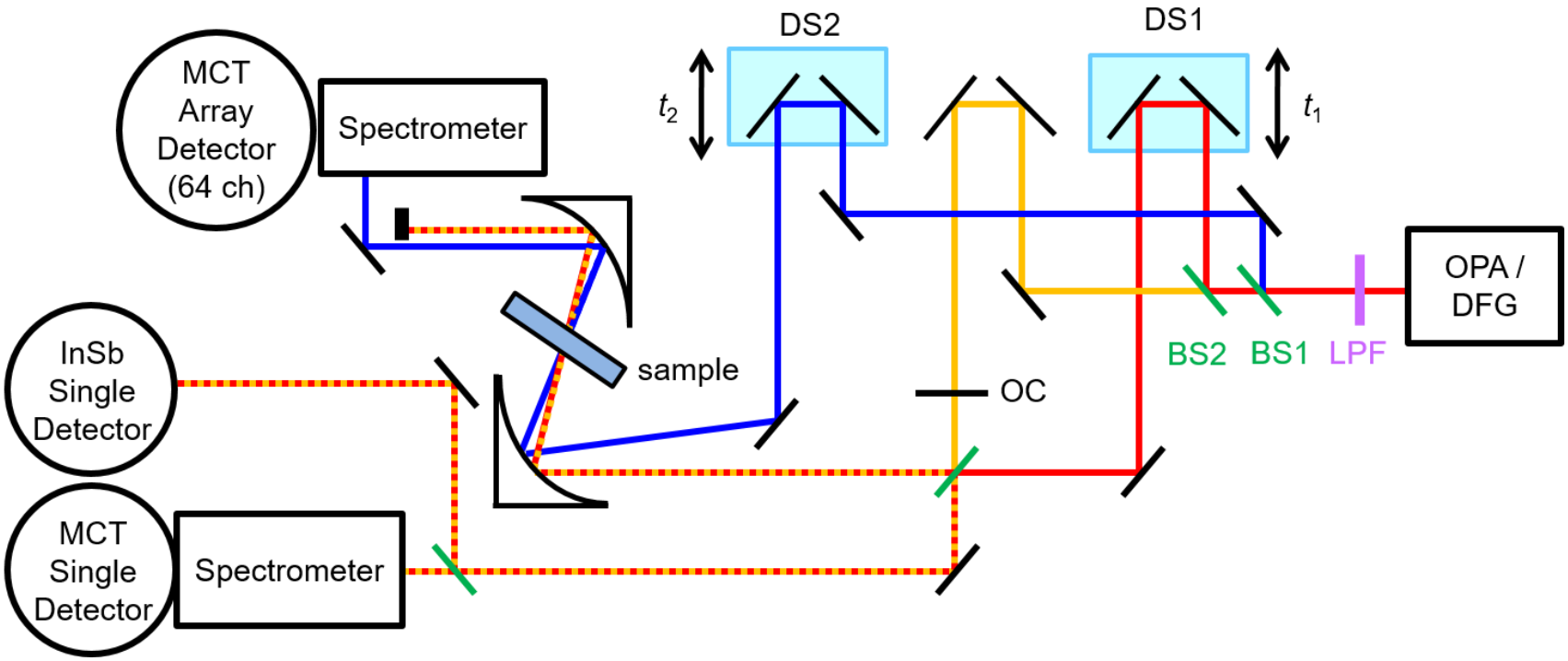

Figure 4.4. Schematic overview of the 64 multi-channel 2D-IR spectrometer. The abbreviations are defined in text.

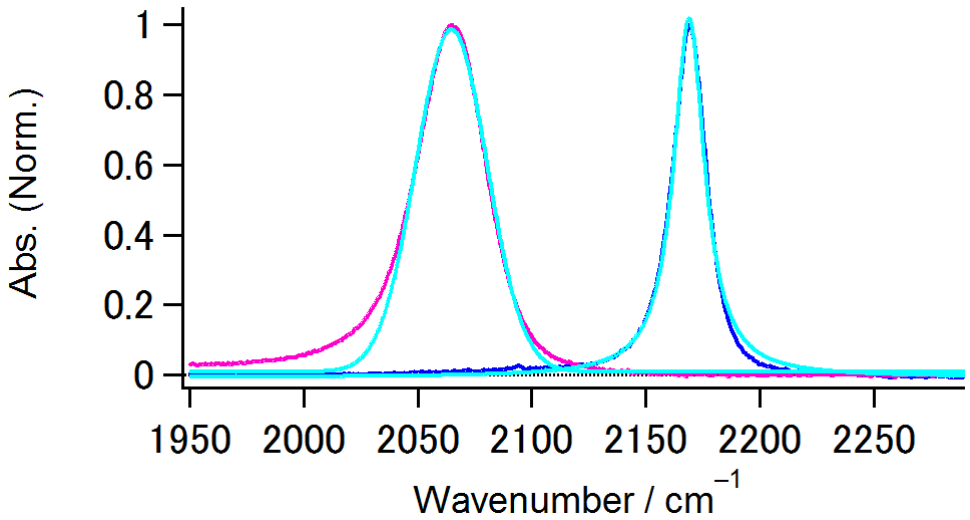

Figure 4.5. Absorption spectra of the SCN anti-stretching mode of NTBA (blue) and SCN^- (pink) at 293 K in H_2O. The light-blue lines represents fits to a Lorentzian and Gaussian function for NTBA and SCN^-, respectively. For the fitting analysis of SCN^-, the IR absorption spectrum on the higher frequency side was used, and the fit curve was extended toward lower frequency side.

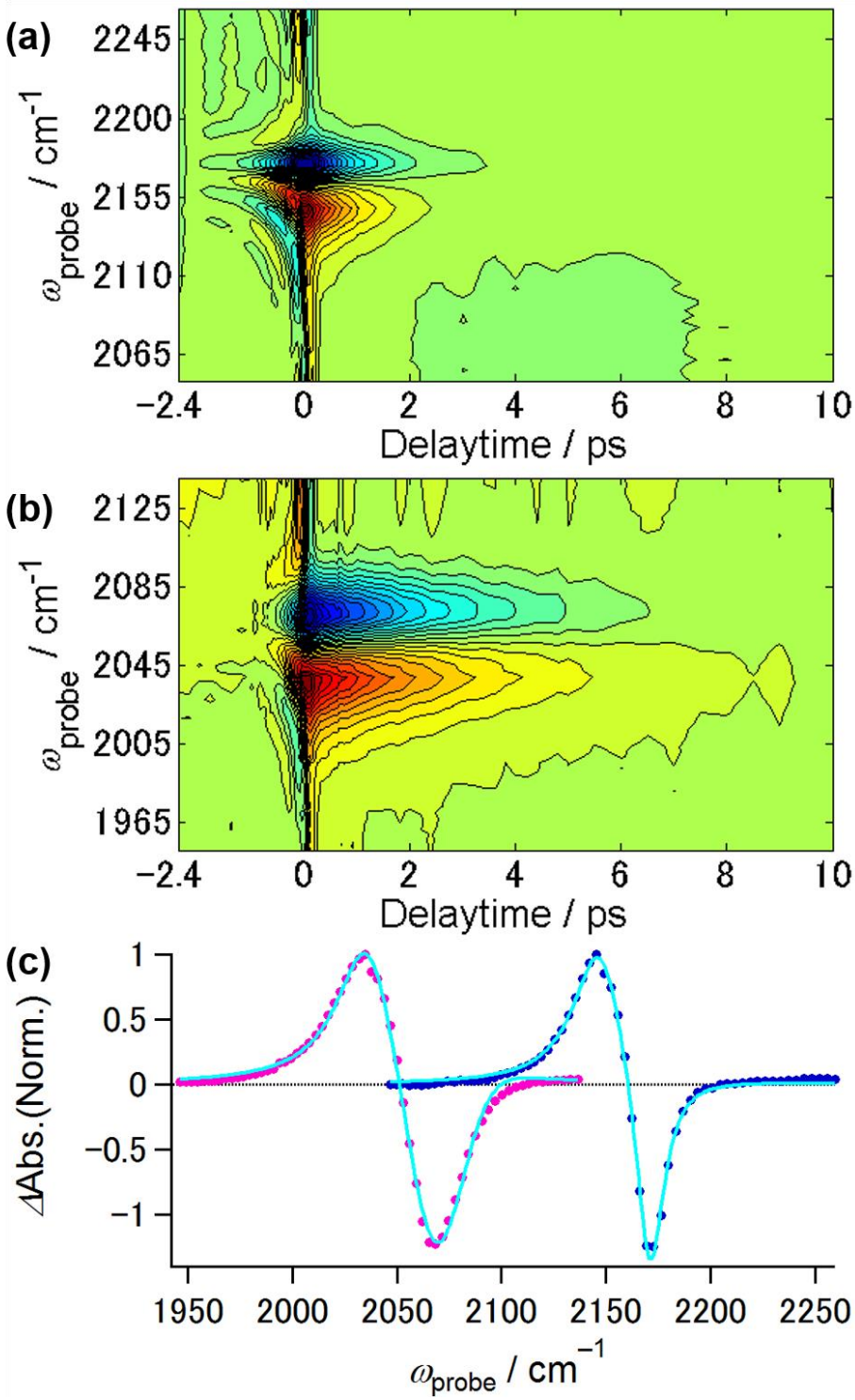

Figure 4.6. Frequency resolved IR pump-probe signals of the SCN anti-stretching mode of (a) NTBA and (b) SCN^- in H_2O. (c) Difference absorption spectra of NTBA (blue) and SCN^- (pink) at T = 1 ps. The closed circles and light-blue lines represent the experimental and fitting results, respectively.

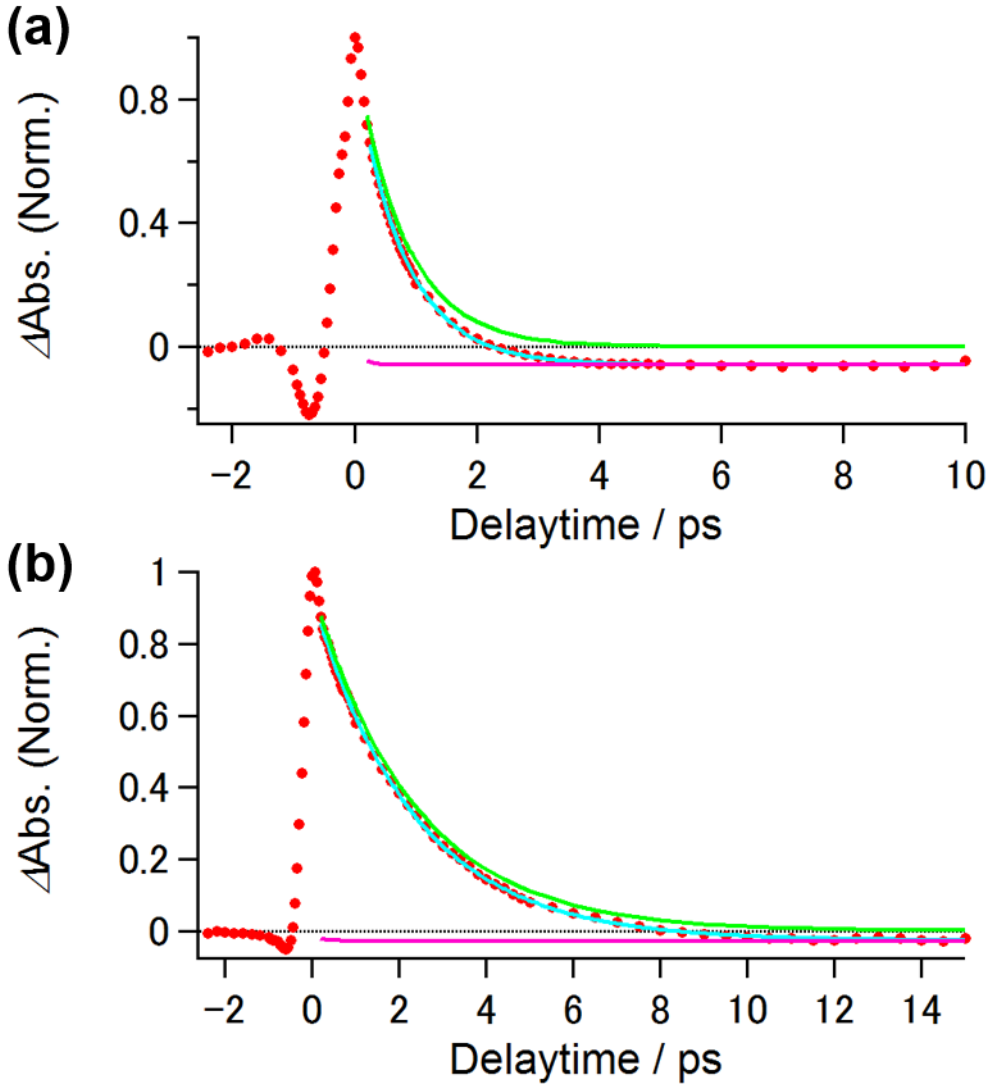

Figure 4.7. Temporal profiles of pump-probe signals of the SCN anti-stretching modes of (a) NTBA and (b) SCN^- in H_2O. These signals were taken from $N(\omega, T)$ of NTBA and SCN^- at the peak wavenumbers of the TA. The red closed circles are the experimental results. The light-blue lines describe fits to a fitting function given by Eq. (4.6). The green and pink lines indicate the components related to the population relaxation and heating effect, respectively.

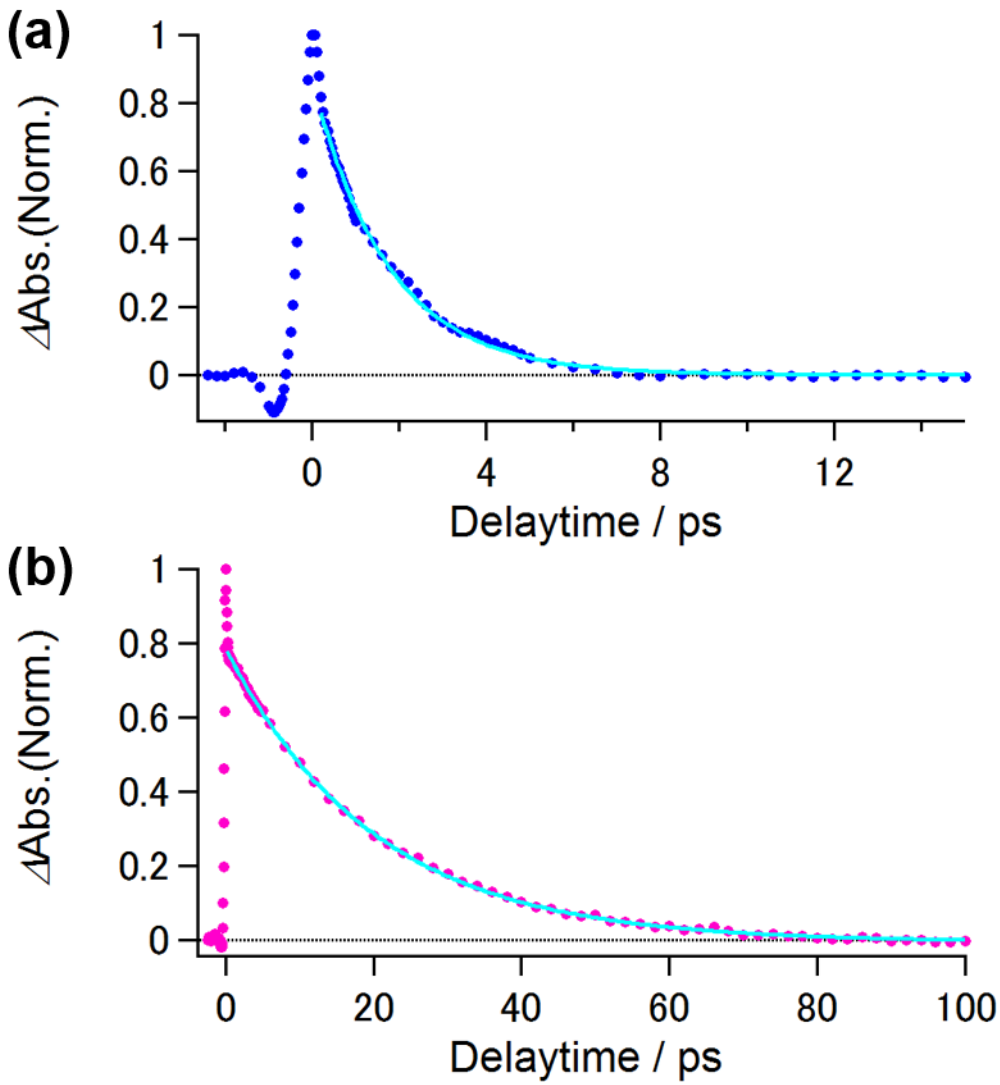

Figure 4.8. Temporal profiles of the IR pump-probe signals of the SCN anti-stretching mode of (a) NTBA and (b) SCN^- in D_2O. The signals of NTBA and SCN^- are taken from the peak wavenumbers of the transient absorption bands at 2142.6 cm^{-1} and 2033.3 cm^{-1}, respectively. The closed circles represent the experimental results. The light-blue lines indicate fits to a single exponential decay function.

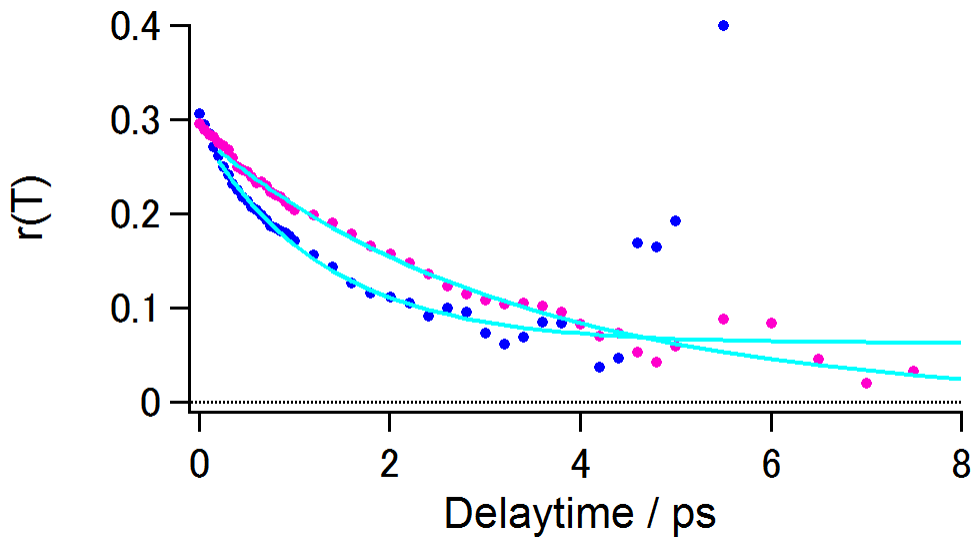

Figure 4.9. Temporal profiles of the anisotropy decays resulting from the TA signal of the SCN anti-stretching mode of NTBA (blue) and SCN^- (pink) in H_2O. The closed circles and light-blue lines represent the experimental and fitting results, respectively.

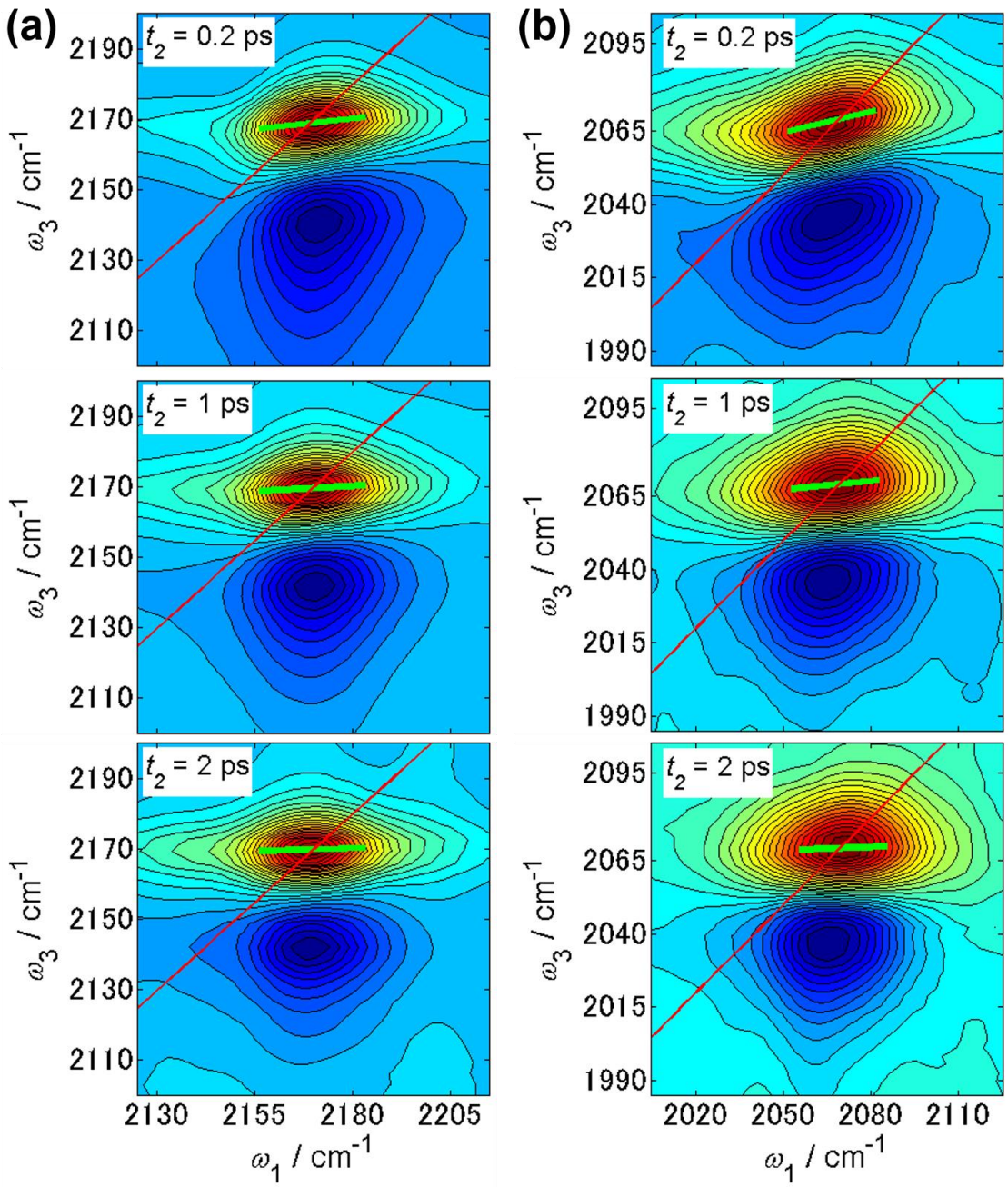

Figure 4.10. 2D-IR spectra of the SCN anti-stretching mode of (a) NTBA and (b) SCN^- in H_2O at population times of (top) 0.2 ps, (middle) 1 ps, and (bottom) 2 ps. The red lines indicate where $\omega_1 = \omega_3$. The green lines indicate the center lines of the 2D-IR signals that originate from the GSB + SE.

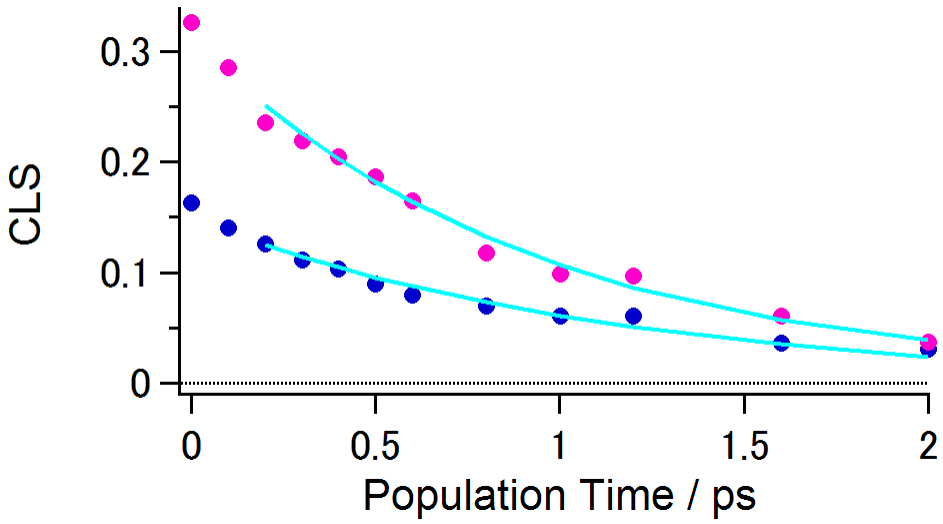

Figure 4.11. CLS decay curves of NTBA (blue) and SCN^- (pink). The closed circles indicate experimentally obtained CLSs, and the light-blue lines are the numerically calculated ones using the optimized FFTCF parameters shown in Table 4.2.

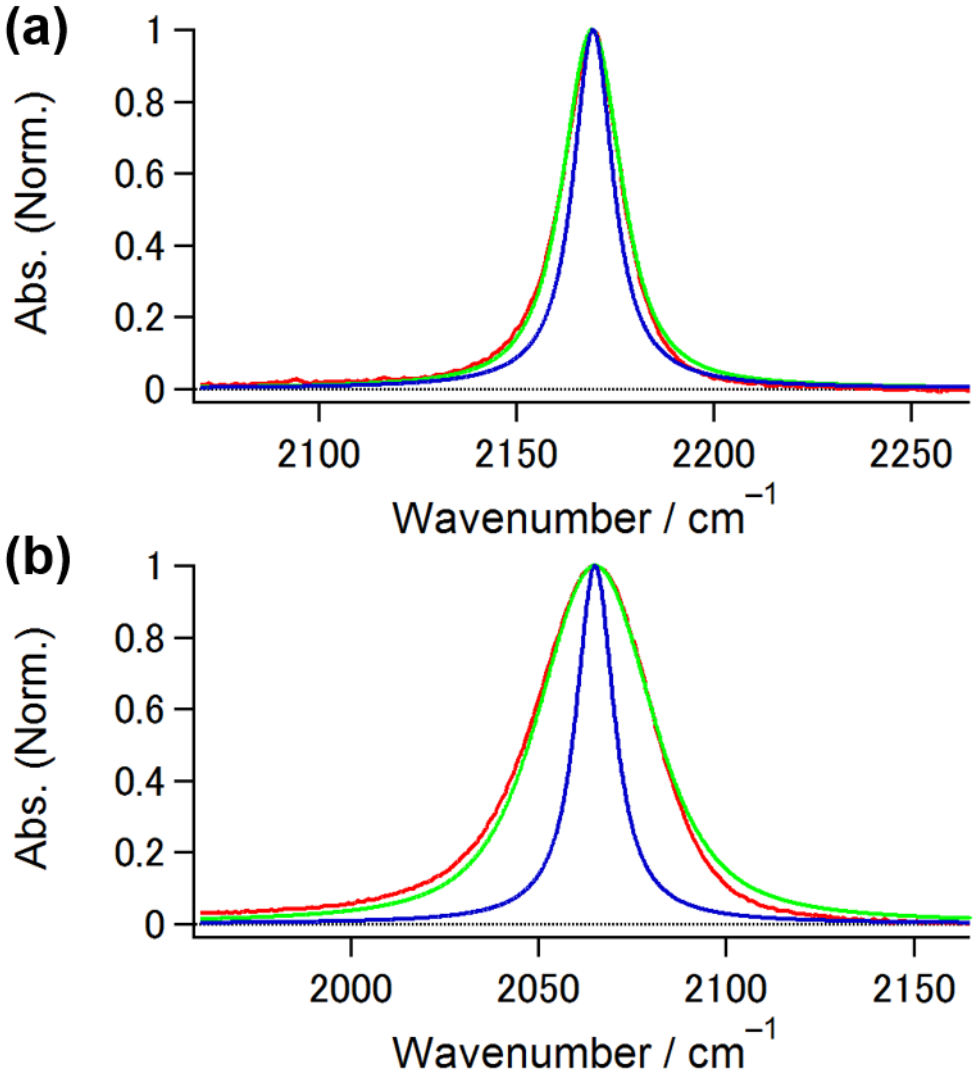

Figure 4.12. Comparison of the experimental and simulated FT-IR spectra of (a) NTBA and (b) SCN^- in H_2O. The red lines represent the experimentally obtained FT-IR spectra of NTBA and SCN^-. The green and blue lines are the numerically calculated FT-IR spectra with and without the slow decaying components in the FFTCF, respectively. The bandwidths of the inhomogeneous broadening of NTBA and SCN^- are 5.1 cm^{-1} and 16.4 cm^{-1}, respectively.

Table 4.1. Parameters of the normalized IR absorption spectra of the SCN anti-stretching mode of NTBA and SCN^- in H_2O and the summary of DFT calculations in the gas phase.

Solute	Linear Absorption Spectrum[a]		Normal Mode Analysis[b]				Partial Charge[c]		
	ω_{max} / cm^{-1}	FWHM / cm^{-1}	ω_0 / cm^{-1}	Intensity / km mol^{-1}	μ / amu	k / mDyne $Å^{-1}$	Q_S / e	Q_C / e	Q_N / e
NTBA	2169.3	17.3	2156.4	81.9	12.8	37.8	−0.27	0.18	−0.90
SCN^-	2065.4	35.4	2052.6	410.0	12.8	34.2	−0.57	0.52	−0.95

(a) ω_{max} : wavenumber at band peak.

(b) ω_0 : normal mode frequency of the SCN anti-stretching mode scaled by multiplying a factor of 0.9614 [52], μ: reduced mass, k: force constant.

(c) Q_i : Mulliken charge of each atom in the SCN group.

Table 4.2. Parameters that characterize the vibrational dynamics of the SCN anti-stretching mode of NTBA and SCN^- in H_2O.

Solute	Population Relaxation[(a)]		Anisotropy Decay[(b)]			Spectral Diffusion[(c)]			
	T_1 / ps	Δ / cm^{-1}	A_∞	A_0	T_R / ps	T_2^* / ps	Δ_C / ps^{-1}	τ_C / ps	Δ_0 / ps^{-1}
NTBA	0.8 ± 0.1	23.8 ± 0.5	0.1 ± 0.1	0.2 ± 0.1	1.3 ± 0.1	3.4	1.0	1.1	0
SCN^-	2.3 ± 0.1	32.7 ± 1.0	0 ± 0.1	0.3 ± 0.1	2.9 ± 0.3	0.7	2.2	0.9	0.2

(a) Δ: anharmonicity of the SCN anti-stretching mode.

(b) A_∞: constant component in the fitting function; $A_\infty + A_0\exp(-T/T_R)$.

(c) The uncertainty of the time constant τ_C is estimated to be about ±20%, and that of the other parameters is within a few percent.

Appendix 4.A. Correction Scheme for 2D-IR Signals

In order to perform Fourier transformations of 2D-IR signals with respect to t_1 axis correctly, the high accuracy of delay times for the DS1 is required. Even though the position of the DS1 is calibrated by a linear encoder with an accuracy of at least ±150 nm, distortions and/or spectral shifting of the 2D-IR spectrum were still observed. During the measurements, interferograms between two pump pulses are monitored by a N_2-cooled single-channel MCT detector after selecting the components at a certain wavenumber.

The following Fourier transform procedure is used to extract the temporal phase. The procedure is schematically presented in Figure 4.A. First, after the Fourier transform of a time domain mid-IR interferogram (see Figure 4.A(a)), its negative frequency components is removed by a high-pass filtering function (see Figure 4.A(b)). This filtering changes the frequency domain spectrum into an asymmetric spectrum about the zero frequency. Secondly, the inverse Fourier transformation of the filtered mid-IR spectrum yields a complex time domain interferogram ($S_{IR}(t_1)$):

$$S_{\mathrm{IR}}(t_1) = S'_{\mathrm{IR}}(t_1) + S''_{\mathrm{IR}}(t_1) \tag{4.A.1}$$

where S'_{IR} and S''_{IR} are the real and imaginary parts of S_{IR}, respectively. Finally, taking the arctangent of the ratio of S''_{IR} to S'_{IR} yields the time domain phase ($\phi(t_1)$, see Figure 4.A(c)):

$$\phi(t_1) = \arctan\left(\frac{S''_{\mathrm{IR}}(t_1)}{S'_{\mathrm{IR}}(t_1)}\right). \tag{4.A.2}$$

If the position of DS1 were perfect, it could be expected that the slope of ϕ would increase linearly at a rate of the mid-IR frequency selected by the monochrometer (ω_{IR}): $\phi(t_1) = \omega_{IR}t_1$. Therefore, the deviation of ϕ from $\omega_{IR}t_1$ ($\delta\phi(t_1)$, see Figure 4. A(d)) can be used to correct the position-dependent encoder error of DS1: $\delta\phi(t_1) = \phi(t_1) - \omega_{IR}t_1$.

Figure

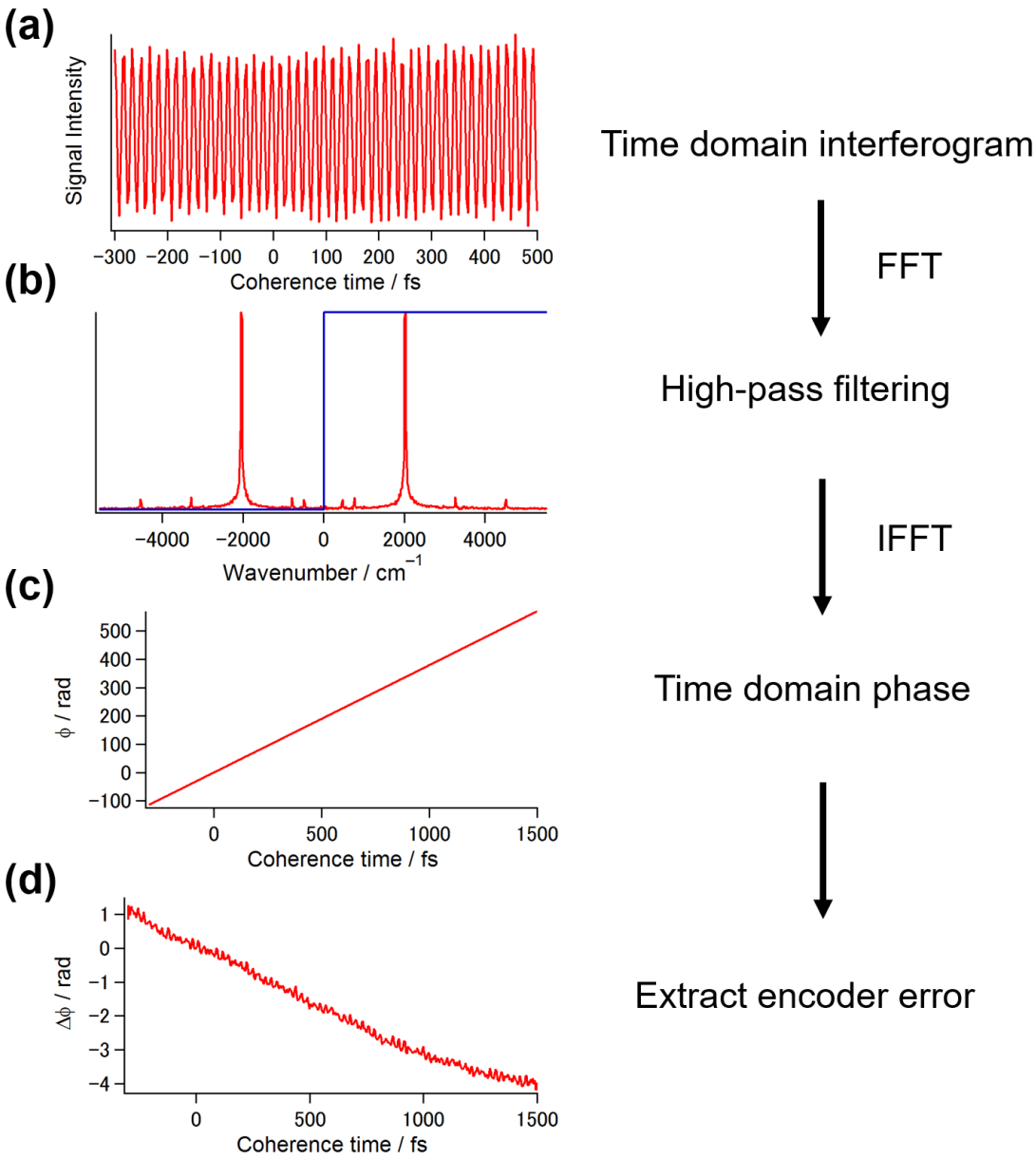

Figure 4.A. Scheme for correcting translation stage error from mid-IR interferogram.

Appendix 4.B. IR Spectrum of SCN^- in DMSO and the Detailed Analysis of the IR Pump-probe Signals of SCN^- in Water

Figure 4.B.1 shows the IR spectrum of the SCN anti-stretching mode of SCN^- in DMSO, which is a polar aprotic solvent. The IR spectrum of SCN^- in DMSO is reproduced by a single Lorenztian function. The band width of the IR spectrum of SCN^- in DMSO is 13.7 cm^{-1}, which is narrower than that in H_2O. On the other hand, as mentioned in Section 4.3.1, the IR spectrum of SCN^- in H_2O cannot be fitted by a single Gaussian function. A clear deviation is observed in the red side of the IR spectrum. As discussed below, an increase in the transition dipole moment due to the non-Condon effect causes the wing in the lower frequency region of the absorption spectrum.

Recently, Yuan *et al*. found that, similar to SCN^- in H_2O, the absorption spectrum of the SeCN anti-stretching mode of $SeCN^-$ in D_2O is also asymmetric line shape and exhibited a small band in the lower frequency side [33]. Based on the IR pump-probe signals at different probe wavenumbers, they concluded that the red wing is attributed to the non-Condon effect [34, 52]. The non-Condon effect indicates that, as the vibrational frequency decreases, the vibrational transition dipole moment becomes larger. In the IR pump-probe experiments for $SeCN^-$ in D_2O, due to the non-Condon effect, the pump pulses vibrationally excite more molecules with lower transition frequency than those with higher transition frequency. Then, in the earlier time period, the spectral diffusion causes more molecules to move from red to blue than blue to red. Therefore, the excited state population on the red and blue sides of the absorption spectrum are initially increasing and decreasing with the spectral diffusion time constant, respectively. Reflecting this reestablishment of equilibrium, Yuan *et al*. modeled the pump-probe signals of $SeCN^-$ in D_2O taken from the red and blue sides of the absorption spectrum as:

$$P_r(T) = A_1 \exp(-T/\tau_C) + A_2 \exp(-T/\tau_{VER}) \tag{4.B.1}$$

$$P_b(T) = A_1 \{1 - \exp(-T/\tau_C)\} \exp(-T/\tau_{VER}) + A_2 \exp(-T/\tau_{VER}) \tag{4.B.2}$$

where *r* and *b* indicate the red and blue sides, respectively. τ_C is the spectral diffusion time constant determined by the 2D-IR experiment, and τ_{VER} is the VER time constant.

Following the procedure of Yuan *et al.*, in order to confirm whether the red wing of the absorption spectrum is due to the non-Condon effect, the detailed fitting analysis was conducted for the pump-probe signal of SCN^- in H_2O. Figure 4.B.2 displays the isotropic pump-probe signals of SCN^- in H_2O at three different probe wavenumbers. First, in order to determine the

VER time constant without the contribution from the initial spectral diffusion, the pump-probe signals after T = 4 ps were fitted with a single exponential function. All fitting results produce the same VER time constants of 3.2 ps within the experimental error. Next, the pump-probe signals taken from the red and blue sides of the absorption spectrum of SCN^- were fitted by the Eq. (4.B.1) and Eq. (4.B.2), respectively. Here, in these fitting processes, the time constants of τ_C and τ_{VER} were fixed at 0.9 ps and 3.2 ps, respectively, and only the amplitudes of A_1 and A_2 in Eq. (4.B.1) and Eq. (4.B.2) were allowed to float. As shown in Figure 4.B.2, the fitting curves can reproduce the pump-probe signals of SCN^- in H_2O. Therefore, according to this fitting analysis, I indicated that the asymmetrical line shape of the SCN anti-stretching mode of SCN^- in H_2O is due to the non-Condon effect.

Figures

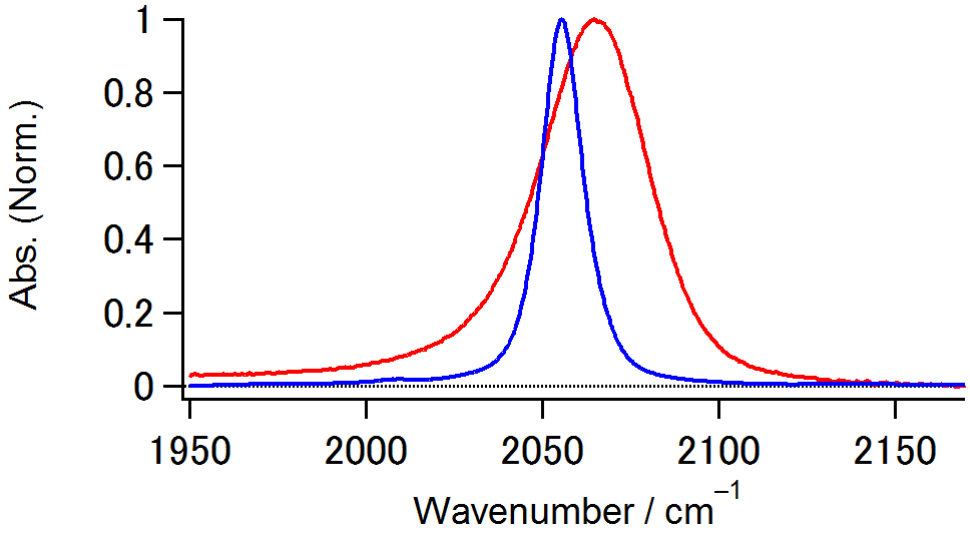

Figure 4.B.1. Absorption spectra of the SCN anti-stretching modes of SCN^- in H_2O (red) and DMSO (blue).

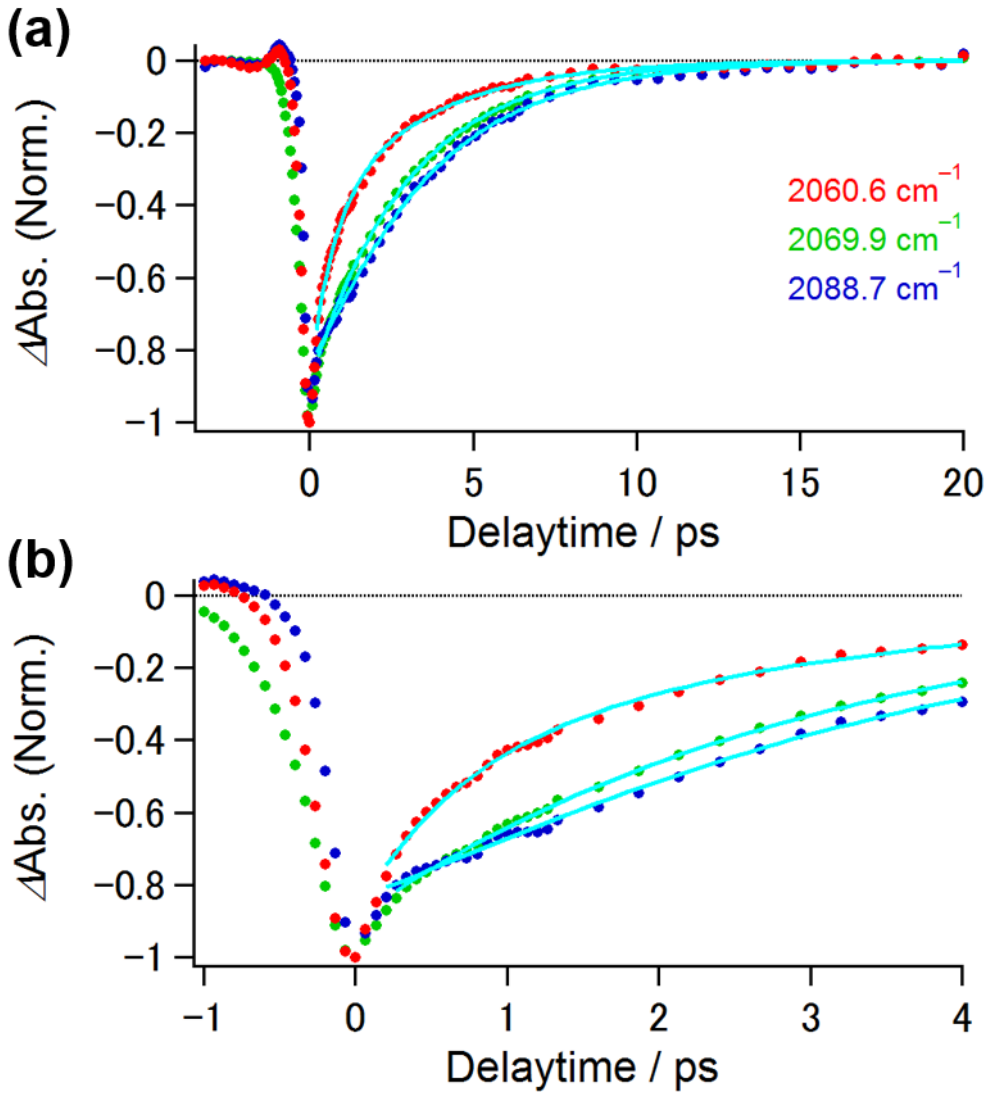

Figure 4.B.2. (a) Temporal profiles of pump-probe signals of the SCN anti-stretching mode of SCN^- in H_2O at three different probe wavenumbers and (b) the close up of these decays within T < 4 ps. The signal taken from near center frequency of the absorption spectrum (green closed circles, at 2069.9 cm^{-1}) is fitted by a single exponential decay function. The signal taken from the red side (red closed circles, at 2060.6 cm^{-1}) is fitted by a double exponential decay function (Eq. (4.B.1)). The signal taken from the blue side (blue closed circles, at 2088.7 cm^{-1}) is fitted by a sum of growth and decay function (Eq. (4.B.2)). The light-blue lines are the fitting results.

CHAPTER 5.

Frequency Fluctuations of Non-ionic Vibrational Probe Molecule in Aqueous Solution: Theoretical Study by Molecular Dynamics Simulation

5.1. Introduction

Various kind of chemical and biological reactions take place in aqueous solutions. Through solute-solvent interactions, reaction rate and pathway are strongly influenced by the structure and dynamics of the local environments. It is well known that vibrational frequency of a molecule is a good reporter of its surrounding environment. Since the hydration structure is continuously evolving in time due to the hydrogen bond (HB) rearrangement [1], the vibrational frequency is fluctuating accordingly. Therefore, insight into the hydration dynamics and solute-solvent interactions can be obtained from the measurements of vibrational frequency fluctuations.

So far, several groups investigated the vibrational frequency fluctuations of ions, such as N_3^- and SCN^-, in water by three-pulse infrared (IR-3PE) photon echo method [2-7]. In a series of these IR experiments, we found that the frequency-frequency time correlation functions (FFTCFs) of the ions can be represented by a double-exponential function with a constant term. Here, the FFTCF of a solute in solution is defined as follows:

$$C_{\omega}(T) \equiv \langle \Delta\omega(T)\Delta\omega(0) \rangle \tag{5.1}$$

where $\Delta\omega(T)$ is frequency shift from the mean value at time T and <…> denotes the time average. Interestingly, regarding to the slow decaying component of the FFTCF, although the pre-exponential factor depends on the ion, the time constant is found to be almost identical for the solute; the time constant ranges from 1.0 ps to 1.5 ps, although the pre-exponential factor depends on the ion. Moreover, Tokmakoff and Fayer groups performed the two-dimension infrared (2D-IR) measurements for diluted HOD in H_2O and D_2O , respectively, and reported that these systems also show that slow decaying components of the FFTCF are on the same time scale of about 1 ps [8, 9]. From the IR-3PE experiment for N_3^- in D_2O, Hamm *et al*. concluded that the slow decay component is due to the making and breaking of the HBs between the ion and water molecules [4]. If so, depending on molecular properties of the vibrational probe molecule such as charge distribution, the decay time constant should depend on the vibrational probe molecule as well.

In Chapter 4, in order to compare the vibrational frequency fluctuations of the non-ionic and ionic vibrational probe molecules from the viewpoint of their molecular properties, I conducted the two-dimension infrared (2D-IR) measurements for 2-nitro-5-thiocyanate benzoic acid (abbreviated as NTBA) and thiocyanate anion (abbreviated as SCN^-) in H_2O. NTBA and SCN^- possess the different molecular structures and charge distributions (see Figure 5.2 and Table 5.1, respectively). Consequently, if the water dynamics in the vicinity of the solutes determines

their frequency fluctuations, one can expect that NTBA and SCN^- in water exhibit different behaviors of vibrational frequency fluctuations. However, the 2D-IR experiments revealed that the frequency-frequency time correlation functions (FFTCFs) of NTBA and SCN^- in H_2O are characterized by the approximately same time constants of 1 ps (see τ_C in Table 4.2). Regardless the difference in the molecular properties, the reason why the vibrational frequency fluctuations are characterized by the same time constant (*i.e.* ~1 ps) regardless the difference in the molecular properties has not been clarified yet at a molecular-level. In order to answer this question, it is necessary to investigate water dynamics around the solutes and solute-solvent interactions that induce the SCN vibrational frequency fluctuations in detail.

A molecular dynamics (MD) simulation is a powerful tool to examine relationship between the vibrational frequency fluctuations of a solute and its surrounding environment (*e.g.* solvation dynamics and solute-solvent interactions). By using appropriate methodologies, we can theoretically obtain the FFTCF of a solute in solution from the MD simulations. To date, several groups performed theoretical investigation on the vibrational frequency fluctuations of water [9-16] and simple ionic vibrational probe molecules in water [17-19]. In earlier work, by performing the MD simulation for N_3^- in D_2O, Li *et al*. successfully reproduced the experimentally observed long-time decay of the FFTCF of N_3 anti-symmetric stretching mode (> 250 fs) [17]. They concluded that this slow decay of the FFTCF may result from the collective water dynamics around the solute due to long-range interactions because the time-correlation function of the HB number fluctuations decays slightly faster at long time than the FFTCF. However, it is still unclear whether this interpretation can be applied to the vibrational frequency fluctuations for non-ionic ones or not.

In this study, by using classical MD simulations, I aim to establish a molecular picture for the SCN vibrational frequency fluctuations of NTBA and SCN^- in H_2O. One of the final goals is to elucidate the molecular mechanism of the experimentally observed slow vibrational frequency fluctuations (*i.e.* 1-ps components of the FFTCFs) of the solutes. To achieve this goal, I theoretically investigated the SCN vibrational frequency fluctuations of NTBA and SCN^- in H_2O and water dynamics in the hydration shell in detail.

5.2. Computational Details

5.2.1. Quantum Chemical Calculations

Generally speaking, in a solution, the electrostatic interaction between the solute and solvent can induce a vibrational frequency shift, which is the so-called vibrational Stark effect [20-24]. So far, extensive theoretical efforts were made for modeling the solvent-induced vibrational frequency shifts of the solutes [9-11, 25-38]. By performing the *ab initio* calculations for MeSCN/water and SCN^-/water systems, Cho group demonstrated that the multi-site electrostatic potential theory works well for calculating the SCN frequency shifts induced by the interactions with surrounding water molecules (see Eq. (5.2)) [29, 30]. Therefore, in this study, I employed their method to theoretically calculate the FFTCFs of NTBA and SCN^- in H_2O.

In order to investigate the relationship between the SCN anti-symmetric stretching modes of the solute and the local hydration environment, by using with the Gaussian 09 program package [39], I performed the geometry optimizations and normal mode analyses for solute-water clusters by the B3LYP density functional [40, 41] with the 6-311++G(3df,2pd) basis set. The obtained vibrational frequencies of the SCN anti-symmetric stretching mode are scaled by multiplying a scaling factor of 0.9614 [42]. In this study, I considered the following two calculations for solute-water clusters.

In the first calculation, a cluster consists of one solute and one water molecule. The results are shown in the former part of Section 5.3.1. It is known that the vibrational frequencies of solutes depend on the HB structure [25-38]. With respect to the SCN anti-symmetric stretching mode, Cho group reported that the vibrational frequencies of MeSCN and SCN^- depend on the HB angle between the solute and a water molecule [29, 30]. Therefore, to examine the HB angle dependence of the SCN anti-symmetric stretching modes of NTBA and SCN^-, I calculated the SCN vibrational frequencies of NTBA/water and SCN^-/water clusters in gas phase by varying the solute-solvent HB angle.

In the second calculation, a cluster is composed of one solute and several water molecules. The results are shown in the latter part of Section 5.3.1. In this case, to determine parameters for describing the SCN frequency shifts of NTBA and SCN^- in water, I considered a variety of solute-water clusters with a various number of solvating water molecules. Here, in order to reflect realistic hydration structure around the solute in water, I sampled the geometries of solute-water clusters from classical MD simulations (see the next section).

5.2.2. Molecular Dynamics Simulations

I performed classical MD simulations for NTBA and SCN^- in water by using the PMEMD module of the AMBER 12 program package [43]. The Lennard-Jones parameters and partial charges (Q_i) of the solutes are determined by the ANTECHAMBER module and the RESP method [44] at the B3LYP/6-311++G(3df,2pd) level, respectively. The obtained partial charges of NTBA and SCN^- are summarized in Table 5.1. For the water molecules, I used the TIP4P water model [45].

NTBA and SCN^- are solvated by 1841 and 1387 water molecules in a cubic box with the periodic boundary condition, respectively. For the neutralization, one Na^+ cation is added to the systems, whose Lennard-Jones parameter is developed by Åqvist [46]. Moreover, for comparison, I conducted classical MD simulation for pure H_2O system composed of 1118 water molecules. The long-range electrostatic interactions are treated by the particle-mesh Ewald method [47]. For NTBA and SCN^- aqueous solutions, the geometries of the solutes are spatially fixed at the coordinates optimized by B3LYP/6-311++G(3df,2pd) in gas phase. The geometries of water molecules are also fixed by using the SHAKE method [48].

First, to determine the density of the system, an MD simulation was carried out for 500 ps with a time step of 0.5 fs under the *NPT* condition (1 atm, 293 K) with the Berendsen thermostat and barostat [49]. Next, to achieve the thermal equilibration of the system, an additional constant temperature MD simulation was performed for 1 ns with a time step of 1 fs under the *NVT* condition (293 K, 1.0 g/cm^3). Finally, a sampling MD simulation was performed for 6 ns, and all the MD trajectory data were used for further analyses.

5.3. Results and Discussions

5.3.1. Multi-site Interaction Model for SCN Vibrational Frequency Shift

In earlier works, from the theoretical calculations for the MeSCN/water and SCN^-/water clusters, Cho group proposed that there are two characteristic HB structures, that is, linear and distorted geometries [29, 30]. In the linear geometry, a water molecule forms the HB with the lone pair of the SCN group, which is referred to as a σ-type HB. On the other hand, in the distorted geometry, a water molecule forms the HB with the electrons in the π-orbital of the SCN group, which is referred to as a π-type HB. Moreover, they found that the σ-type and π-type HBs cause red and blue frequency shifts of the SCN stretching mode, respectively. Therefore, in order to illustrate the HB angle dependence of the SCN vibrational frequency (ω_{SCN}), I performed the normal mode

calculations for the NTBA/water and SCN^-/water clusters as a function of the θ_{CNH} (see Figure 5.1(a)). Note that, because SCN^- can form a HB between the lone pair of the S atom and a water molecule, I also examined the dependence of the ω_{SCN} on the θ_{CSH} (see Figure 5.1(a)). Figures 5.1(b) and (c) represent the results of the HB angle dependence of the ω_{SCN} for the NTBA/water and SCN^-/water clusters, respectively. As shown in Figures 5.1(b) and (c), the ω_{SCN} of NTBA and SCN^- exhibit the blue shifting behaviors with increasing the angle θ_{CNH}, and the borders between the σ-type and π-type HBs are found to be approximately 130° and 150° for NTBA and SCN^-, respectively. On the other hand, the ω_{SNC} of SCN^- does not show any clear dependence on the angle θ_{CSH}. These results are good in agreement with the previous works done by the Lee *et al*. [30]. However, there are many different types of solvation structures containing various numbers and strengths of σ-type and π-type HBs in the actual aqueous solution. Therefore, the experimentally observed SCN frequency shift must depend on the delicate balance of these two HB interactions. In order to discuss the microscopic picture on the SCN frequency fluctuations of NTBA and SCN^- in water, it is necessary to construct frequency-shift maps which properly take account of the σ-type and π-type HB effects.

As mentioned in Section 5.2.1, Cho group revealed that the multi-site electrostatic potential theory can be applied for theoretically calculating the SCN frequency shifts induced by the interactions with surrounding water molecules [29, 30]. In their theory, distributed interaction sites are placed at around solutes to calculate solute-solvent interactions. For a given solute-water configuration, by calculating the electrostatic potentials (ϕ) at all these interaction sites, the SCN frequency shift ($\Delta\omega(\phi)$) is expressed as follows:

$$\Delta\omega(\phi) \equiv \omega(\phi) - \omega_0 = \sum_{i=1}^{N_{solu}} (l_i + l_0) \sum_{j=1}^{N_{solv}} \phi_{ij}, \quad \text{with} \quad \sum_{i=1}^{N_{solu}} l_i = 0 . \tag{5.2}$$

Here, the N_{solu} is the number of the interaction sites. In this study, 35 and 28 interaction sites are considered for NTBA and SCN^-, respectively (*i.e.* N_{solu} = 35 for NTBA and N_{solu} = 28 for SCN^-, see Figure 5.2). The N_{solv} is the number of water molecules in the system (*i.e.* N_{solv} = 1841 for NTBA and N_{solv} = 1387 for SCN^-). The $\omega(\phi)$ and ω_0 are the SCN vibrational frequencies of the solute in a given cluster and the isolated one, respectively. The ϕ_{ij} is the Coulomb electrostatic potential at the *i*th interaction site created by the *j*th water molecule. The coefficient l_i is a measure of the sensitivity of the *i*th interaction site to the change in the ϕ_{ij}. The l_0 is the additional parameter to represent the charge transfer effect due to the solute-solvent HB on the vibrational frequency

shift [30]. Here, Choi *et al*. found that the contribution of the charge transfer effect to the SCN frequency shift of MeSCN is negligibly small [29]. Therefore, in this study, the parameter l_0 for NTBA is set to 0 as well.

In order to determine the parameters l_i for NTBA and SCN^-, I performed multivariate least-square fitting analyses with Eq. (5.2). Here, the following two constraint conditions are considered for the parameters l_i in Eq. (5.2) [29, 30]. The first condition is that a set of the parameters satisfies the charge neutrality: $\sum_{i=1}^{N_{\mathrm{solu}}} l_i = 0$. The second condition is that the corresponding parameters l_i for the additional eight interaction sites on the same circles are assumed to have the same values due to the approximately cylindrical symmetry of the π-orbitals. Therefore, to describe the solvent-induced SCN frequency shift, 20 and 7 (including the additional parameter l_0) independent interaction sites are considered for NTBA and SCN^-, respectively. For the multivariate least-square fitting analyses, I randomly sampled 110 NTBA−$(H_2O)_n$ ($1 \leq n \leq 6$) and 100 SCN^-−$(H_2O)_n$ ($1 \leq n \leq 16$) clusters from the MD simulations and performed structural optimization and normal mode analysis for the solute in each cluster. Then, by taking the difference between the SCN vibrational frequencies of the solute in the cluster and gas phase, I obtained the *ab initio* calculated SCN frequency shift (*i.e.* $\Delta\omega(\phi)$ in the left-hand side of Eq. (5.2)). Regarding the right-hand side of Eq. (5.2), I obtained all the electrostatic potentials $\sum_{j=1}^{N_{\mathrm{solv}}} \phi_{ij}$ (i = 1 − 35 for NTBA and i = 1 − 7 SCN^-) from the NTBA/water and SCN^-/water clusters.

The parameters l_i for NTBA and SCN^- determined by the multivariate least-square fitting are summarized in Table 5.1. Here, the l_0 value for SCN^- is found to be 9.27601×10^{-5} e. Figure 5.3 displays the comparison between the SCN frequency shifts obtained from the DFT calculations and Eq. (5.2) with the obtained parameters l_i. The linear fittings provide the correlation coefficients of 0.98 and 0.99 for NTBA and SCN^-, respectively. Here, it should be noted that the parameters l_i for SCN^- obtained in this study are different from those reported in Ref. 30. This difference is likely due to the difference in the configurations of the clusters used for normal mode analyses. However, similar to previous studies, the linear fit for the SCN^-/water clusters gives the sufficiently high correlation coefficient. Consequently, hereafter, the parameters l_i listed in Table 5.1 are used for the following theoretical analysis of the SCN frequency fluctuations of SCN^- in H_2O.

5.3.2. Hydration Structure around SCN Group

Hereafter, the results of the classical MD simulations for NTBA and SCN^- in H_2O and pure H_2O are discussed.

First, I discuss the hydration structure around NTBA and SCN^-. Figure 5.4 displays the pair radial distribution functions (RDFs) between the water H and O atoms and the N atom of the SCN group of NTBA and SCN^- (denoted as $g_{NH}(r)$ and $g_{NO}(r)$, respectively). The first minimum and maximum of the $g_{NH}(r)$ and $g_{NO}(r)$ are summarized in Table 5.2. As shown in Figure 5.4(a), $g_{NO}(r)$ for SCN^- shows a sharper first peak at around 2.6 Å, which is in good agreement with the reported value [50] and the amplitude of first peak for SCN^- is greater than that of NTBA. This difference can be explained in terms of the charge density of the vibrational probe: due to the larger partial charges in the vibrational probe, SCN^- can attract the surrounding water molecules more strongly than the SCN group of NTBA. Therefore, I consider that the water molecules around SCN^- is more structured than that around the SCN group of NTBA. Moreover, based on the result that the value of the peak amplitude of $g_{NO}(r)$ for NTBA is close to 1, the hydration structure around the SCN group of NTBA can be expected to be similar to the pure water itself.

On the other hand, as shown in Figure 5.4(b), the $g_{NH}(r)$ for NTBA and SCN^- have first sharp peaks at around 2 Å, which arises from the solute-solvent HBs. To define a HB between the vibrational probe and a water molecule (denoted as $-SCN\cdots H_2O$ for NTBA and $SCN^-\cdots H_2O$ for SCN^-), I adopted geometrical criteria with respect to the length r_{NH} and the angle θ_{NOH} of the HB. Based on the angle-resolved RDFs for NTBA and SCN^- (see the results in Figure 5.A), I defined the precise HB criteria for $-SCN\cdots H_2O$ and $SCN^-\cdots H_2O$ as follows: $r_{NH} \leq 2.6$ Å and $\theta_{NOH} \leq 30^\circ$. Here, it should be noted that NTBA and SCN^- possess the other HB sites, that is, the O atoms of the NO_2 and COO^- groups of NTBA and the S atom of SCN^-. Regarding to these HB sites, I also defined a HB in terms of geometrical criteria with respect to the length r_{XH} and the angle θ_{XOH} of the HB, where "X" represents a given HB site of NTBA and SCN^-. The r_{XH} is determined by the first minimum of the corresponding pair RDF $g_{XH}(r)$ (see $g_{XH}(r)$ for each HB site in Figure 5.B), and the θ_{XOH} is set to 30°.

5.3.3. Water Dynamics around SCN Group

As mentioned in the previous section, SCN^- has well-organized hydration structure than NTBA. Therefore, we can expect that the water dynamics around NTBA is different from that around SCN^-.

First, I discuss HB dynamics between the solute and surrounding water molecules. In order to evaluate the solute-solvent HB dynamics, I calculated the HB correlation functions (HBCFs) for $-SCN\cdots H_2O$ and $SCN^-\cdots H_2O$ as follows [51]:

$$C_{\mathrm{HB}}(T) \equiv \frac{\langle H(T)H(0)\rangle}{\langle H(0)H(0)\rangle} \tag{5.3}$$

where $H(T) = 1$ if a specific HB is formed at time T, and $H(T) = 0$ otherwise. Moreover, by using the geometrical definition given by Luzar and Chandler [51], I also calculated the HBCF for water-water HB (denoted as $H_2O\cdots H_2O$) from the MD simulations for pure H_2O system. Figure 5.5 shows the HBCFs for $-SCN\cdots H_2O$, $SCN^-\cdots H_2O$, and $H_2O\cdots H_2O$ (see Figure 5.C for the HBCFs associated to the other HB sites of NTBA and SCN^-). The HBCFs can be reproduced by a triple exponential function, and the corresponding time constants (τ_i) are listed in Table 5.2.

If a HBCF decays with a single time constant, the decay time constant can be interpreted as the HB lifetime. However, HBCFs typically show the multi-exponential decay due to the dynamics on different time scales, such as rotational motions and diffusion of water molecules [52-55]. Therefore, I characterized the HB lifetime by a single time constant $\tau_{1/e}$ defined as: $C_{\mathrm{HB}}(\tau_{1/e}) = e^{-1}C_{\mathrm{HB}}(0)$. The obtained time constants of $\tau_{1/e}$ for $-SCN\cdots H_2O$ and $SCN^-\cdots H_2O$ are 1.76 ps and 8.39 ps, respectively. Regarding the HB dynamics between SCN^- and H_2O molecules, $\tau_{1/e}$ is consistent with the previous result for that between SCN^- and D_2O molecules reported by Czurlok et al [55]. Moreover, $\tau_{1/e}$ for $H_2O\cdots H_2O$ is found to be 2.81 ps, which is also consistent with the result from the MD simulation for the TIP4P water system [56]. As the results that the $\tau_{1/e}$ for $SCN^-\cdots H_2O$ is longer than those of $-SCN\cdots H_2O$ and $H_2O\cdots H_2O$, I consider that SCN^- forms HBs with its neighboring water molecules more strongly than NTBA and H_2O. On the other hand, based on the results that the $\tau_{1/e}$ for $-SCN\cdots H_2O$ is close to that for $H_2O\cdots H_2O$, the HB between the SCN group of NTBA and a water molecule may not be significantly different from that between water molecules.

Next, I examined the reorientational motion of a single water molecule in the vicinity of NTBA and SCN^- (collective reorientational motion of water molecules in the first hydration

shell of the solutes will be discussed in the next section). In this study, I calculated the dipole moment reorientational correlation functions for a water molecule forming a HB with the solutes as follows:

$$C_{1,\mathrm{HB}}(T) = \left\langle P_1\left(\frac{\boldsymbol{\mu}(0)\cdot\boldsymbol{\mu}(T)}{|\boldsymbol{\mu}(0)||\boldsymbol{\mu}(T)|}\right)H(0)\right\rangle \tag{5.4}$$

and for bulk water as follows:

$$C_{1,\mathrm{bulk}}(T) = \left\langle P_1\left(\frac{\boldsymbol{\mu}(0)\cdot\boldsymbol{\mu}(T)}{|\boldsymbol{\mu}(0)||\boldsymbol{\mu}(T)|}\right)\right\rangle \tag{5.5}$$

where $\boldsymbol{\mu}(T)$ is the dipole moment vector of the water molecule, and $P_1(x)$ is the first-order Legendre polynomial. Figure 5.6 shows the obtained dipole moment reorientational correlation functions for water molecules neighboring to the SCN group of NTBA and the N atom of SCN^- and those in bulk (see Appendix 5.D for the dipole moment reorienattional correlation function associated to the other HB sites of NTBA and SCN^-). All the dipole moment reorientational correlation functions can be fitted well by a double exponential function and $\tau_{1/e}$ are 3.56 ps for NTBA, 5.04 ps for SCN^-, and 3.35 ps for bulk water. I revealed that the rotational relaxation of the water molecule hydrogen bonding with SCN^- is slower by approximately 50% than that of bulk water. On the other hand, the reorinetational motion of the water molecule nearby the SCN group of NTBA is found to be almost the same as that in bulk.

5.3.4. Theoretical Analysis for Vibrational Frequency Fluctuations

Based on Eq. (5.2), I calculated the solvent-induced SCN frequency shifts of NTBA and SCN^- at a given time T ($\Delta\omega(T)$) as follows:

$$\Delta\omega(T) \equiv \omega(T) - \omega_0 = \sum_{i=1}^{N_{\mathrm{solu}}}(l_i + l_0)\sum_{j=1}^{N_{\mathrm{solv}}}\phi_{ij}(T)\,. \tag{5.6}$$

By using Eq. (5.6) with parameters l_i listed in Table 5.1, I obtained the temporal evolution of the SCN frequency shifts of NTBA and SCN^- in H_2O from the trajectories of MD simulations up to 6ns. Obtained $\Delta\omega(T)$ of NTBA and SCN^- in H_2O were used for the following analyses.

First, I calculated the distributions of the SCN frequency fluctuations of NTBA and SCN^- in H_2O. Figure 5.7(a) shows the SCN frequency distributions of NTBA and SCN^-, which are reproduced well by Gaussian distributions with the peak frequencies of 2.0 cm^{-1} and 36.9 cm^{-1}, respectively. Figure 5.7(b) displays the experimentally obtained IR absorption spectra of

the SCN anti-symmetric stretching modes of NTBA and SCN^- in H_2O and dimethyl sulfoxide (DMSO). Here, DMSO was chosen as an aprotic solvent. Figure 5.7(b) indicates that, compared to the SCN frequencies of NTBA and SCN^- in DMSO, those in H_2O are shifted toward the higher frequency by 8.2 cm^{-1} and 9.4 cm^{-1}, respectively. Therefore, based on the vibrational solvatochromism theory, I successfully reproduce the blue-shifting behaviors of the SCN frequencies of NTBA and SCN^- in H_2O.

Next, I calculated the FFTCFs of the SCN anti-symmetric stretching modes of NTBA and SCN^- in H_2O, as shown in Figure 5.8. I found that the theoretically obtained FFTCFs of NTBA and SCN^- in H_2O can be fitted by a double exponential function, and the fitting results are summarized in Table 5.2. It should be noted that, from the theoretical analyses based on the multi-site electrostatic potential theory, I can reproduce the approximately 1-ps decay of the FFTCFs of the SCN anti-symmetric stretching modes of NTBA and SCN^- in H_2O, which are observed in the 2D-IR measurements for them (see Section 4.3.3). In previous studies of the classical MD simulations for SPC/E water system, Fayer and Tokmakoff groups independently concluded that the decay of FFTCF of bulk water on approximately 1 ps time scale reflect the collective motion of water molecules accompanying the HB rearrangements [9, 10]. Therefore, similarity of the time scale of τ_2 for NTBA and SCN^- to that of bulk water suggests that the slower SCN frequency fluctuations reflects the structural reorganization of the HB network around the solutes.

In order to extract more detailed information on the SCN frequency fluctuations of NTBA and SCN^- in H_2O, I examined the radial-dependence of the FFTCFs of the solutes. Here, I defined the spatially-resolved SCN frequency fluctuation ($\Delta\omega_S(T)$) as:

$$\Delta\omega_S(T,r) \equiv \sum_{i=1}^{N_{\mathrm{solu}}} (l_i + l_0) \sum_{j=1}^{N_{\mathrm{solv}}} \phi_{ij}(T) f_j(T,r) \tag{5.7}$$

where $f_j(T, r)$ is the filtering function to characterize the radial-dependence of the $\Delta\omega_S(T)$ which is represented as:

$$f_j(T,r) \equiv \max_{1 \le i \le N'_{\mathrm{solu}}} \left\{ \frac{1}{2} \left(1 - \tanh\left[\gamma \left(r_{ij}(T) - r \right) \right] \right) \right\} \tag{5.8}$$

where N'_{solu} is the number of atoms in NTBA and SCN^-: $N'_{\mathrm{solu}} = 18$ for NTBA and $N'_{\mathrm{solu}} = 3$ for SCN^-. The γ is the damping constant (set to 10 $Å^{-1}$). The r_{ij} is the distance between the ith interaction site of the solutes and the O atom of the jth water molecule, and the r is a given cutoff distance, which characterizes the dependence of the FFTCF on solute-solvent distance. In this

study, by varying r from 3.5 Å to 7.5 Å with a 1.0 Å step, I calculated the series of the spatially-resolved FFTCFs of NTBA and SCN^- in H_2O, as displayed in Figures 5.9 and 5.E. As shown in Figure 5.9(a), the spatially-resolved FFTCF of NTBA gradually approaches to the total FFTCF with increasing the cutoff distance r, which indicates that the SCN frequency fluctuations of NTBA reflect the electrostatic interactions induced by water molecules existing far from the solute (*i.e.* bulk-like water molecules). On the other hand, Figure 5.9(b) shows that the FFTCF of SCN^- is almost determined by the contribution form the water molecules within the distance of 3.5 Å from the solute (*i.e.* water molecules in the first hydration shell).

Here, I examined these results on the spatially-resolved FFTCFs of NTBA and SCN^- in H_2O from a different viewpoint. In order to evaluate how far water molecules away from the solutes can affect the SCN vibrational frequency fluctuations through the electrostatic interactions, I calculated the radial Coulomb electrostatic potentials for NTBA and SCN^- as follows [57]:

$$\phi(r) \equiv \left\langle \sum_{i=1}^{N_{\mathrm{solu}}} \sum_{j=1}^{N_{\mathrm{solv}}} \phi_{ij}(T) f_j(T, r) \right\rangle \tag{5.9}$$

where $f_j(T, r)$ is given in Eq. (5.8). Here, based on the parameter l_j for NTBA listed in Table 5.1, I consider that the SCN frequency shift of the solute is approximately characterized by the electrostatic interactions between the SCN group and surrounding water molecules. Therefore, for the comparison between the non-ionic and ionic SCN groups in terms of solute-solvent interactions, I calculated the Coulomb electrostatic potential only on the SCN group and its surrounding extra sites of NTBA, *i.e.*, ϕ_{ij} ($i \geq 16$) is considered for NTBA. Figure 5.10 clearly shows that the radial dependence of the electrostatic potentials on NTBA and SCN^- is different: while NTBA feels the Coulomb interaction induced by water molecules approximately ~7 Å away from the solute (~90% of the converged electrostatic potential), that on SCN^- is almost determined by the water molecules in the first and second hydration shell (< 5.0 Å, ~90% of the converged electrostatic potential) and the contribution from water molecules beyond the second hydration shell is negligibly small. Based on the results above, in the case of NTBA/water system, I consider that, since NTBA feels the electrostatic interactions induced by water molecules existing far from the solute, which are expected to behave as bulk water, the fluctuations of the HB network system in bulk can induce the SCN frequency fluctuations on the 1 ps time scale.

On the other hand, in the case of SCN^-/water system, I found that the electrostatic interaction further beyond the second hydration shell is “screened out”, which is in good

agreement with the theoretical work on dimethylphosphate ($(CH_3O)_2PO_2^-$) in H_2O reported by Fingerhut *et al*. [57]. Here, with respect to the water dynamics around SCN^-, it should be noted that the HB dynamics between SCN^- and water molecules is significantly slower than that between water molecules in bulk. Moreover, the reorientational motion of the water molecule forming the HB with SCN^- is about 50 % slower than that of the bulk water (see Figure 5.6). These results suggest that the SCN frequency fluctuation of SCN^- in H_2O is mainly dominated by the collective water dynamics in the first hydration shell, not the HB dynamics between water molecules and SCN^- (see Figure 5.F for the contribution from the hydrogen bonded water molecules to the FFTCF of SCN^- in H_2O). Consequently, in order to investigate the collective water dynamics around SCN^-, I calculated the normalized total dipole moment time correlation function for water molecules in the first and second hydration shells of SCN^- as follows:

$$C_{\mathrm{TDP,solv}}(T) \equiv \frac{\left\langle \left(\sum_{i=1}^{N_{\mathrm{solv}}} \boldsymbol{\mu}_i(T) f_i(T,r) \right) \cdot \left(\sum_{j=1}^{N_{\mathrm{solv}}} \boldsymbol{\mu}_j(0) f_j(0,r) \right) \right\rangle}{\left\langle \left| \sum_{i=1}^{N_{\mathrm{solv}}} \boldsymbol{\mu}_i(0) f_i(0,r) \right|^2 \right\rangle} \tag{5.10}$$

where the cutoff distance r is set to 5.0 Å. Moreover, for comparison, I calculated the corresponding time correlation function for bulk water system without SCN^- as follows:

$$C_{\mathrm{TDP,water}}(T) \equiv \frac{\left\langle \left(\sum_{i=1}^{N_{\mathrm{solv}}} \boldsymbol{\mu}_i(T) f_i'(T,r) \right) \cdot \left(\sum_{j=1}^{N_{\mathrm{solv}}} \boldsymbol{\mu}_j(0) f_j'(0,r) \right) \right\rangle}{\left\langle \left| \sum_{i=1}^{N_{\mathrm{solv}}} \boldsymbol{\mu}_i(0) f_i'(0,r) \right|^2 \right\rangle} \tag{5.11}$$

Here, in order to define the filtering function $f_i'(T, r)$, I considered a "hypothetical hydration shell" as shown in Figure 5.11. Inside a "hypothetical hydration shell", $f_i'(T, r)$ is set to 0. Outside a shell, $f_i'(T, r)$ is the same as that in Eq. (5.8). Figure 5.12 shows $C_{\mathrm{TDP,solv}}(T)$ and $C_{\mathrm{TDP,water}}(T)$ for the SCN^-/water and bulk water systems, respectively. These decays can be characterized by characteristic time constants of $\tau_{1/e}$ of 3.77 ps and 3.33 ps for SCN^-/water and bulk water systems, respectively. The difference is only 13%, which indicates that the collective water dynamics in the first and second hydration shells of SCN^- is "more similar" to that of bulk water than the single molecule dynamics of a water molecule forming the HB with the solute.

Here, as mentioned above, it should be noted that HBs between SCN^- and neighboring water molecules are very strong than that between bulk-water molecules. Therefore, one may

wonder why the water molecules in the first hydration shell can fluctuate similarly to the bulk water. In order to answer this question, I investigated the HBCF for water molecules in the first hydration shell of SCN^- by defining the following time correlation function:

$$C_{\mathrm{HB,Hyd}}(T) \equiv \frac{\langle H'(T)H'(0)R(T)\rangle}{\langle H'(0)H'(0)R(0)\rangle} \tag{5.12}$$

where $H'(T) = 1$ if the water molecule in the first-hydration shell forms HB with another water molecule at time T and $H'(T) = 0$ otherwise. $R(T)$ defines the region of the first-hydration shell of SCN^-: $R(T) = 1$ if the distance between the O atom of a specific water molecule and the X atom of SCN^- (here, X = S or N) is less than a cutoff distance ($R_{\mathrm{cut,X}}$) at time T and $R(T) = 0$ otherwise. In this study, based on the first minima of $g_{\mathrm{SO}}(r)$ and $g_{\mathrm{NO}}(r)$, the $R_{\mathrm{cut,S}}$ and $R_{\mathrm{cut,N}}$ are set to 3.6 Å and 3.3 Å, respectively (see Table 5.2).

Figure 5.13 displays the comparison between the HBCFs of water pairs in the first hydration shell of N atom (denoted as $H_2O_{\mathrm{HW,N}}\cdots H_2O$) and those in bulk (see the HBCF of water pairs in the first hydration shell of S atom, which is denoted as $H_2O_{\mathrm{HW,S}}\cdots H_2O$, in Figure 5.C(b)). The HBCF for $H_2O_{\mathrm{HW,N}}\cdots H_2O$ can be fitted by a triple-exponential function, and the fitting result and the characteristic time constants $\tau_{1/e}$ are summarized in Table 5.2. Based on the values of $\tau_{1/e}$ listed in Table 5.2, I found that the HB dynamics between water molecules in the vicinity of SCN^- is faster than that between SCN^- and water molecules and almost the same as that in bulk. Consequently, since SCN^- forms relatively strong HBs with surrounding water molecules, the motion of these water molecules (*e.g.* translational and rotational motions) can be controlled by the collective rearrangement of the HB network without breaking the HBs with the solute. In other words, the SCN anti-symmetric stretching mode of SCN^- is perturbed by the structural fluctuations of the HB network through the water molecules directly hydrogen-bonded to the solute, which results in the experimentally observed SCN frequency fluctuations on the 1 ps time scale.

5.4. Conclusion

In this chapter, in order to establish a molecular picture on the SCN vibrational frequency fluctuations of NTBA and SCN^- in H_2O experimentally observed by 2D-IR spectroscopy, I performed theoretical calculations with the classical MD simulations.

Reflecting the difference in partial charges of the vibrational probes of NTBA and SCN^-, I found that SCN^- exhibits more organized hydration structure than the SCN group of NTBA (see Figure 5.4). Moreover, by calculating the HBCFs for $-SCN\cdots H_2O$ and $SCN^-\cdots H_2O$, I revealed that the HB dynamics between SCN^- and a water molecule takes place much slower than that between NTBA and a water molecule (see Table 5.2). These results clearly show that the local environment around NTBA and SCN^- (*e.g.* hydration structure and HB dynamics) is significantly different.

Based on the vibrational solvatochromism theory, I theoretically calculated the FFTCFs for the SCN anti-symmetric stretching modes of NTBA and SCN^- in H_2O. Both the theoretically obtained FFTCFs of NTBA and SCN^- in H_2O are found to contain the decay components with time constants of approximately 1 ps (see Table 5.2), which is in good agreement with the 2D-IR results in Chapter 4. From the comparison with the FFTCF of OH (OD) vibrational frequency fluctuations of diluted HOD in H_2O (D_2O) [9, 10], I conclude that the 1-ps decay components in the FFTCFs of NTBA and SCN^- result from the collective motion of the HB network structure around the solutes.

Next, in order to understand the reason why the FFTCFs of NTBA and SCN^- in H_2O are characterized by the similar time constants of 1 ps, I investigated the radial-dependence of the SCN vibrational frequency fluctuations of the solutes in H_2O. By calculating spatially-resolved FFTCF (see Eqs. (5.7) and (5.8)), I found that the SCN vibrational frequency fluctuations of NTBA are affected by the electrostatic interactions from water molecules approximately 7.0 Å away from the solute (see Figure 5.9(a)). Therefore, I consider that the electrostatic interactions with such “bulk-like” water molecules are responsible for the slow decay component (*i.e.* 1-ps component) of the FFTCF of NTBA in H_2O.

On the other hand, Figure 5.9(b) shows that the SCN vibrational frequency fluctuations of SCN^- in H_2O are almost dominated by the interactions with water molecules in the first hydration shell of the solute. Here, it should be noted that the difference in the effective distance of the electrostatic potential between NTBA/water and SCN^-/water systems may indicate that,

depending on the molecular properties of the solutes, the relative dielectric constant around SCN^- is different form that around NTBA [58]. In order to explain the molecular mechanism of the SCN vibrational frequency fluctuations on 1 ps time scale of SCN^- in H_2O, first, I investigated the collective reorientational motion of water molecules in the first hydration shell of the solute. By calculating the normalized total dipole moment time correlation function, I found that collective dynamics of water molecules in the first hydration shell is similar to that in bulk (see Figure 5.10). Next, by calculating the HBCF for the hydrated water molecules (see Eq. (5.12)), I revealed that the HB dynamics between water molecules in the vicinity of SCN^- is approximately the same as that between water molecules in bulk. Consequently, I conclude that the SCN vibrational frequency of SCN^- is perturbed by the structural fluctuations of the HB network through water molecules directly hydrogen-bonded to the ion, which reflects the experimentally observed SCN frequency fluctuations on the 1 ps time scale.

References

1. I. Ohmine and H. Tanaka, *Chem. Rev.*, **93**, 2545 (1993).

2. K. Ohta, H. Maekawa, and K. Tominaga, *J. Phys. Chem. A*, **108**, 1333 (2004).

3. K. Ohta, J. Tayama, S. Saito, and K. Tominaga, *Acc. Chem. Res*, **45**, 1982 (2012).

4. P. Hamm, M. Lim, and R. M. Hochstrasser, *Phys. Chem. Lett*, **81**, 5326 (1998).

5. M. Kozinski, S. Garrett-Roe, and P. Hamm, *Chem. Phys.*, **341**, 5 (2007).

6. J. F. Brookes, K. M. Slenkamp, M. S. Lynch, and M. Khalil, *J. Phys. Chem. A*, **117**, 6234 (2013).

7. K. M. Slenkamp, M. S. Lynch, J. F. Brookes, C. C. Bannan, S. L. Daifuku, and M. Khalil, *Structural Dynamics*, **3**, 023609 (2016).

8. J. J. Loparo, S. T. Roberts, and A. Tokmakoff, *J. Chem. Phys.*, **125**, 194521 (2006).

9. J. B. Asbury, T. Steinel, K. Kwak, S. A. Corcelli, C. P. Lawrence, J. L. Skinner, and M. D. Fayer, *J. Chem. Phys.*, **121**, 12431 (2004).

10. J. D. Eaves, A. Tokmakoff, and P. L. Geissler, *J. Phys. Chem. A*, **109**, 9424 (2005).

11. J. R. Schmidt, S. T. Roberts, J. J. Loparo, A. Tokmakoff, M. D. Fayer, and J. L. Skinner, *Chem. Phys.*, **341**, 143 (2007).

12. B. S. Mallik, A. Semparithi, and A. Chandra, *J. Phys. Chem. A*, **112**, 5104 (2008).

13. T. Yagasaki and S. Saito, *J. Chem. Phys.*, **128**, 154521 (2008).

14. T. Yagasaki and S. Saito, *Acc. Chem. Res*, **42**, 1250 (2009).

15. S. Imoto, S. S. Xantheas, and S. Saito, *J. Chem. Phys.*, **139**, 044503 (2013).

16. T. Yagasaki and S. Saito, *Annu. Rev. Phys. Chem.*, **64**, 55 (2013).

17. S. Li, J. R. Schmidt, A. Piryatinski, C. P. Lawrence, and J. L. Skinner, *J. Phys. Chem. B*, **110**, 18933 (2006).

18. M. W. Lee, J. K. Carr, M. Göllner, P. Hamm, and M. Meuwly, *J. Chem. Phys.*, **139**, 054506 (2013).

19. A. Karmakar and A. Chandra, *J. Chem. Phys.*, **142**, 164505 (2015).

20. D. K. Lambert, *J. Chem. Phys.*, **89**, 3847 (1988).

21. A. Chattopadhyay and S. G. Boxer, *J. Am. Chem. Soc.*, **117**, 1449 (1995).

22. E. S. Park, S. S. Andrews, R. B. Hu, and S. G. Boxer, *J. Phys. CHem. B*, **103**, 9813 (1999).

23. S. S. Andrews and S. G. Boxer, *J. Phys. Chem. A*, **104**, 11853 (2000).

24. S. S. Andrews and S. G. Boxer, *J. Phys. Chem. A*, **106**, 469 (2002).

25. S. A. Corcelli, C. P. Lawrence, and J. L. Skinner, *J. Chem. Phys.*, **120**, 8107 (2004).

26. S. A. Corcelli and J. L. Skinner, *J. Phys. Chem. A*, **109**, 6154 (2005).

27. B. Auer, R. Kumar, J. R. Schmidt, and J. L. Skinner, *Proc. Natl. Acad. Soc.*, **104**, 14215 (2007).

28. J. -H. Choi and M. Cho, *J. Chem. Phys.*, **138**, 174108 (2013).

29. J. -H. Choi, K. -I. Oh, H. Lee, C. Lee, and M. Cho, *J. Chem. Phys.*, **128**, 134506 (2008).

30. H. Lee, J. -H. Choi, and M. Cho, *Phys. Chem. Chem. Phys.*, **12**, 12658 (2010).

31. J. -H. Choi, K. -I. Oh, and M. Cho, *J. Chem. Phys.*, **129**, 174512 (2008).

32. J. -H. Choi and M. Cho, *J. Chem. Phys.*, **134**, 154513 (2011).

33. M. Cho, *J. Chem. Phys.*, **118**, 3480 (2003).

34. S. Ham, J. -H. Kim, H. Lee, and M. Cho, *J. Chem. Phys.*, **118**, 3491 (2003).

35. H. Kim and M. Cho, *Chem. Rev.*, **113**, 5817 (2013).

36. B. Błasiak, H. Lee, and M. Cho, *J. Chem. Phys*, **139**, 044111 (2013).

37. B. Błasiak and M. Cho, *J. Chem. Phys*, **140**, 164107 (2014).

38. B. Błasiak and M. Cho, *J. Chem. Phys*, **143**, 164111 (2015).

39. M. J. Frisch *et al*., GAUSSIAN 09 (Revision B.01), Gaussian, Inc., Wallingford, CT (2009).

40. A. D. Becke, *J. Chem. Phys.*, **98**, 5648 (1993).

41. P. J. Stevens, F. J. Devlin, C. F. Chablowski, and M. J. Frisch, *J. Phys. Chem*, **98**, 11623 (1994).

42. A. P. Scott and L. Radom, *J. Phys. Chem.*, **100**, 16502 (1996).

43. D. A. Case *et al*., AMBER 12, University of California, San Francisco (2012).

44. X. Grabuleda, C. Jaime, and P. A. Kollman, *J. Compt. Chem.*, **21**, 901 (2000).

45. W. L. Jorgensen, J. Chandrasekhar, J. D. Madura, R. W. Impey, and M. L. Klein, *J. Chem. Phys.*, **79**, 926 (1983).

46. J. Aqvist, *J. Phys. Chem.*, **94**, 8021 (1990).

47. T. Darden, D. York, and L. Pedersen, *J. Chem. Phys.*, **98**, 10089 (1993).

48. J. P. Ryckaert, G. Ciccotti, and H. J. C. Berendsen, *J. Compt. Phys.*, **23**, 327 (1977).

49. H. J. C. Berendsen, J. P. M. Postma, W. F. van Gunsteren, A. DiNola, and J. R. Haak, *J. Chem. Phys.*, **81**, 3684 (1984).

50. A. Botti, S. E. Pagnotta, F. Bruni, and M. A. Ricci, *J. Phys. Chem.*,

51. A. Luzar and D. Chandler, *Nature*, **379**, 55 (1996).

52. A. Chandra, *Phys. Rev. Lett.*, **85**, 768 (2000).

53. M. Higashi, S. Hirai, M. Banno, K. Ohta, S. Saito, and K. Tominaga, *J. Phys. Chem. B*, **117**, 4723 (2013).

54. Pierre-André Cazade, T. Bereau, and M. Meuwly, *J. Phys. Chem. B*, **118**, 8135 (2014).

55. D. Czulok, M. von Domaros, M. Thomas, J. Gleim, J. Lindner, B. Kirchner, and P. Vöhringer, *Phys. Chem. Chem. Phys.*, **17**, 29776 (2015).

56. H. Xu, H. A. Stern, and B. J. Berne, *J. Phys. CHem. B*, **106**, 2054 (2002).

57. B. P. Fingerrhut, R. Costard, and T. Elsaesser, *J. Chem. Phys.*, **145**, 115101 (2016).

58. M. A. Young, B. Jayaram, and D. L. Beveridge, *J. Phys. Chem. B*, **102**, 7666 (1998).

Figures and Tables

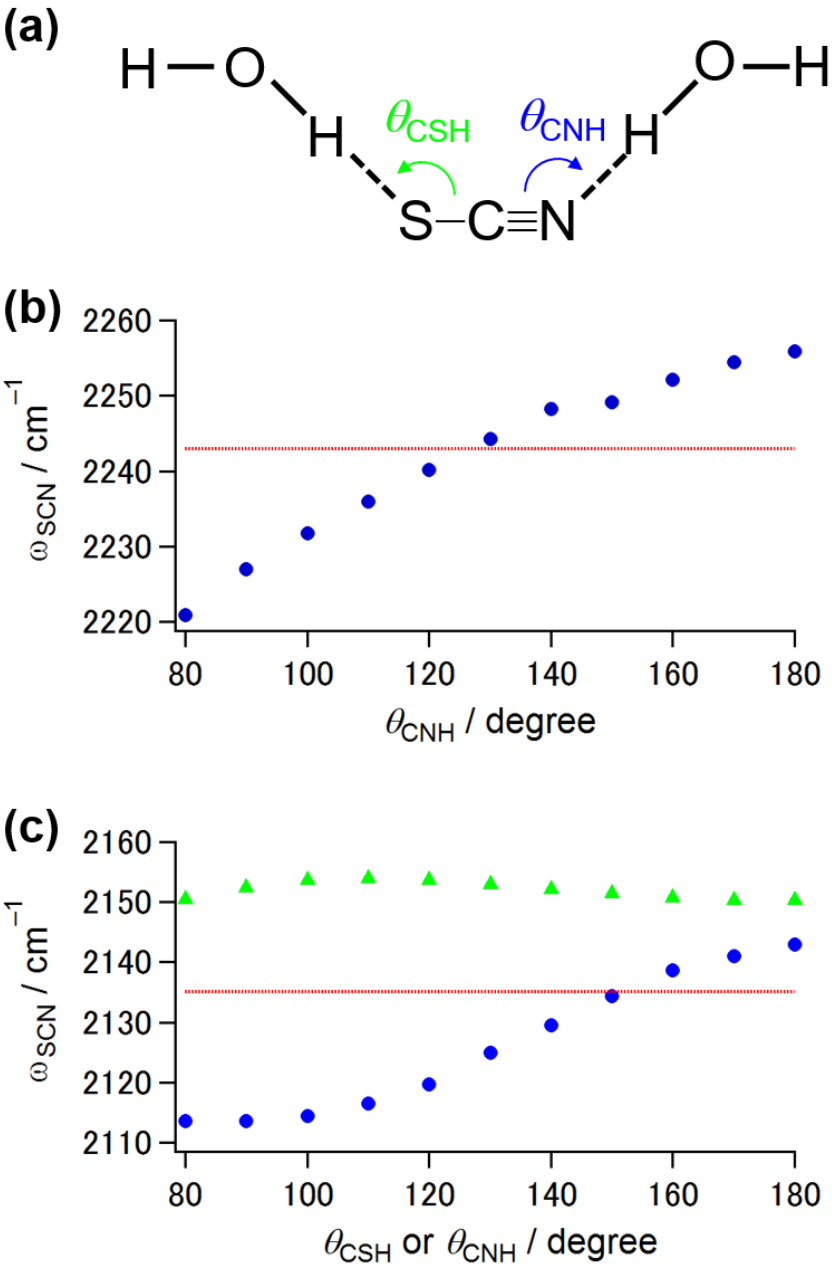

Figure 5.1. (a) Definition of the HB angles of θ_{CNH} (blue) and θ_{CSH} (green) between the SCN group and a single water molecule. The calculated SCN vibrational frequencies of (b) NTBA/water and (c) SCN^-/water clusters in gas phases as a function of θ_{CNH} (●) and θ_{CSH} (▲). For each calculation, the HB angle and distance were fixed at certain values, but all the other degrees of freedom were relaxed for a geometrical optimization. The dotted red lines represent the SCN vibrational frequencies of isolated NTBA and SCN^- in gas phases.

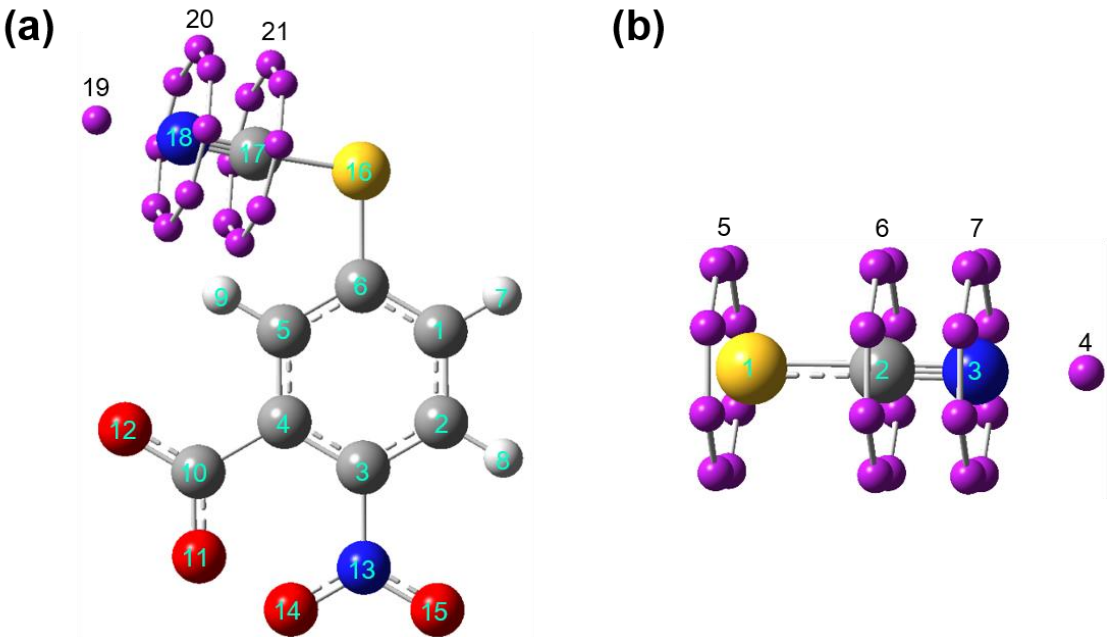

Figure 5.2. Distributions of the interaction sites of (a) NTBA and (b) SCN^-. The number on each atom corresponds to the index *i* in Eq. (5.2). The 19th interaction site of NTBA and 4th interaction site of SCN^- are placed to represent the σ-type HB interaction. Moreover, the additional eight interaction sites placed on the circles around the S, C, and N atoms of the SCN group represent the π-type HB interaction. The geometrical definitions of these additional interaction sites of NTBA and SCN^- are given in Ref. 29 and Ref. 30, respectively.

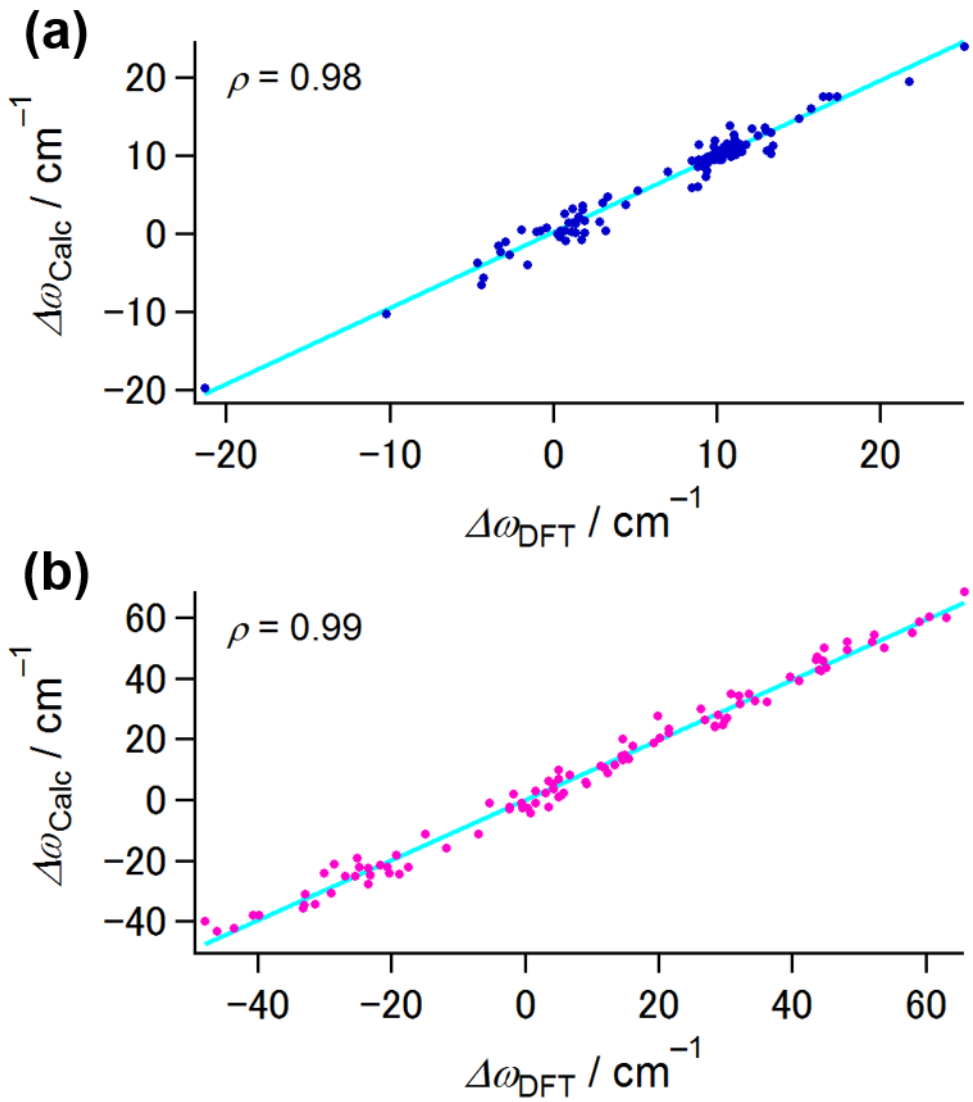

Figure 5.3. Results of multivariate least-square fitting for (a) NTBA and (b) SCN^-. The horizontal axis corresponds to the DFT calculated SCN frequency shift and the vertical axis to the SCN frequency shift obtained from Eq. (5.2). The light-blue lines represent the linear fits to the plot.

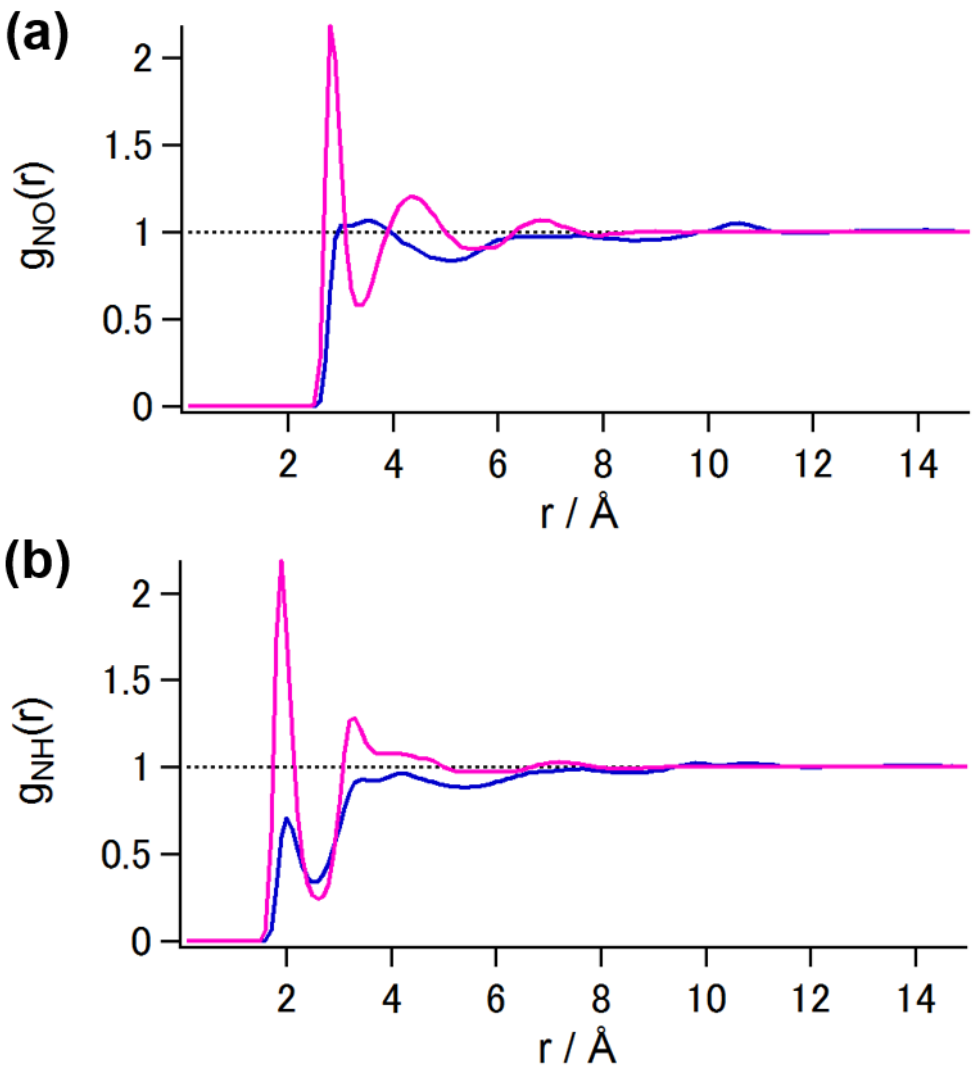

Figure 5.4. Pair radial distribution function between SCN nitrogen atom and H_2O (a) hydrogen and (b) oxygen atoms. The blue and pink lines are the results for NTBA and SCN^-, respectively.

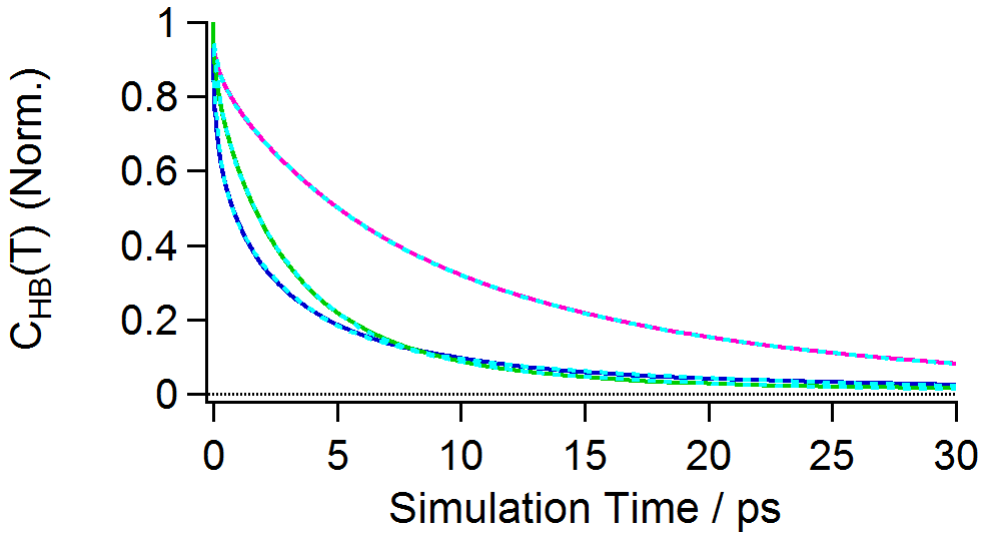

Figure 5.5. HB correlation functions of −SCN···H_2O (blue), SCN^-···H_2O (pink), and H_2O···H_2O (green). The dotted light-blue lines are the fitting results to triple-exponential functions.

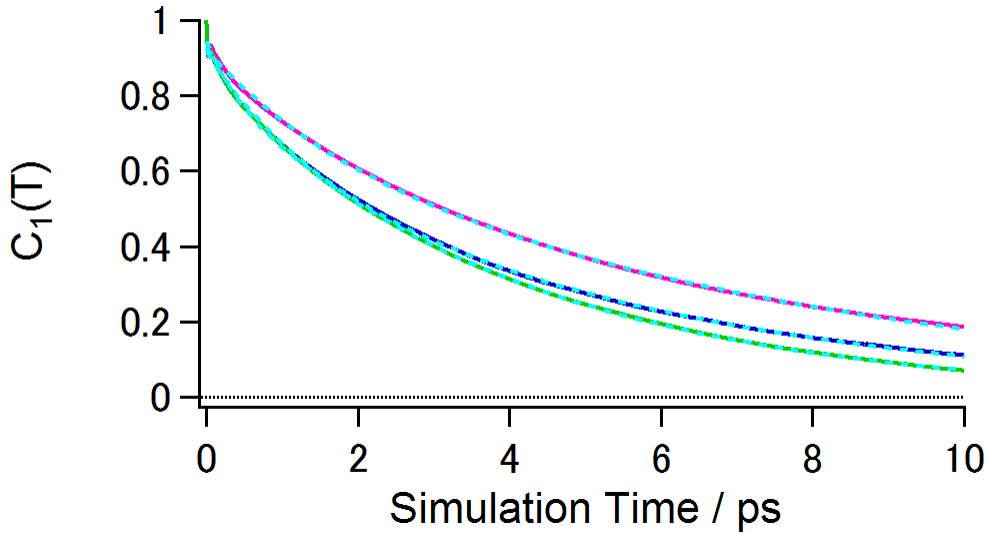

Figure 5.6. Dipole moment reorientational correlation functions for water molecules around the SCN nitrogen atoms of NTBA and SCN^- (pink), and those in bulk (green). The dotted light-blue lines are the fitting results to a double exponential functions; $A_1\exp(-T/\tau_1) + A_2\exp(-T/\tau_2)$. The fitting parameters are as follows; A_1 = 0.22, τ_1 = 1.20 ps, A_2 = 0.69, and τ_2 = 5.38 ps for NTBA/water system, A_1 = 0.18, τ_1 = 1.38 ps, A_2 = 0.75, and τ_2 = 7.05 ps for SCN^-/water system, and A_1 = 0.10, τ_1 = 0.34 ps, A_2 = 0.84, and τ_2 = 4.07 ps for bulk water system (error bars for these parameters are approximately less than 5%).

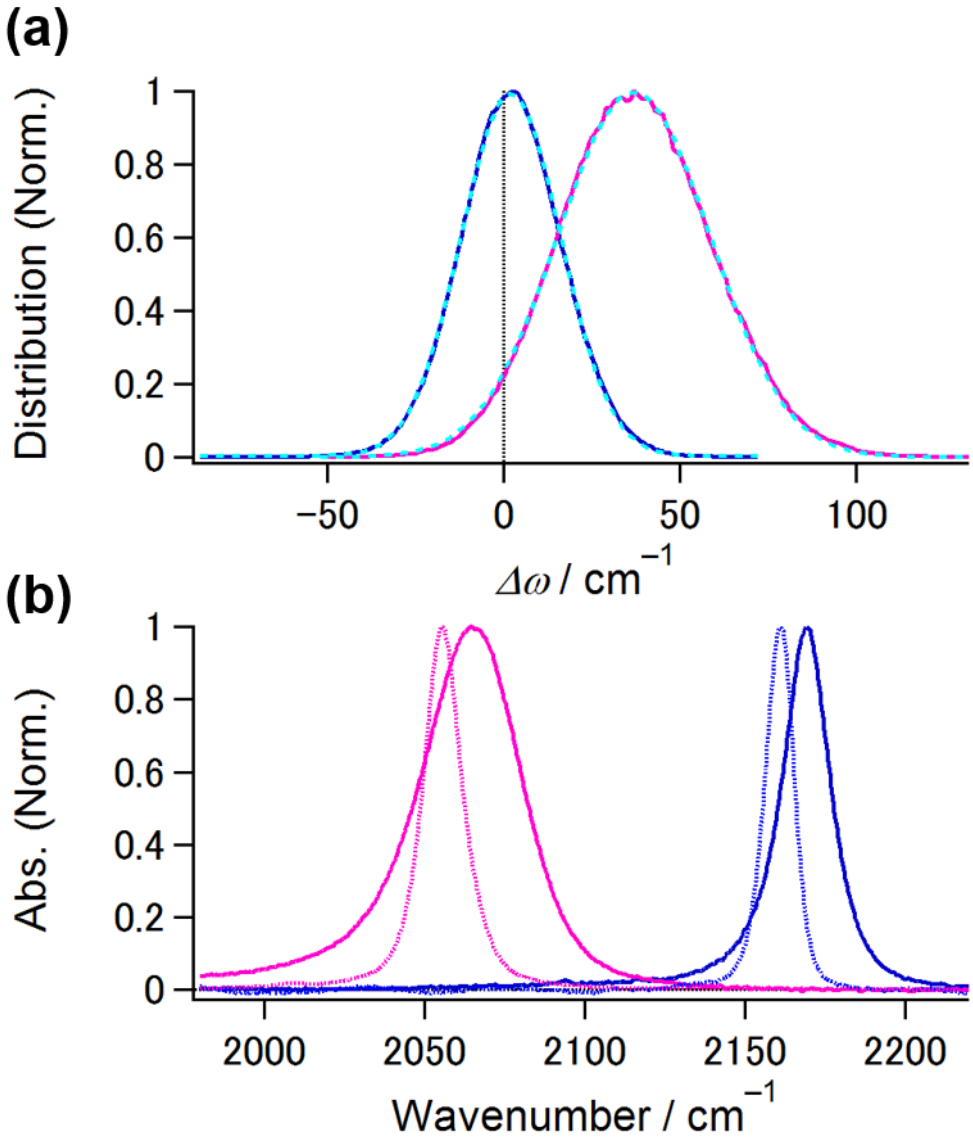

Figure 5.7. (a) Distributions of the SCN frequency shifts of NTBA (blue) and SCN^- (pink) calculated by Eq. (5.1). The dotted light-blue lines indicate the results of Gauss fittings. (b) Comparison of experimental IR absorption spectra of NTBA (blue) and SCN^- (pink) in H_2O (solid) and DMSO (dotted). The peak wavenumbers of these IR bands in H_2O and DMSO are 2169.3 cm^{-1} and 2161.1 cm^{-1} for NTBA, respectively, and, 2064.9 cm^{-1} and 2055.5 cm^{-1} for SCN^-, respectively.

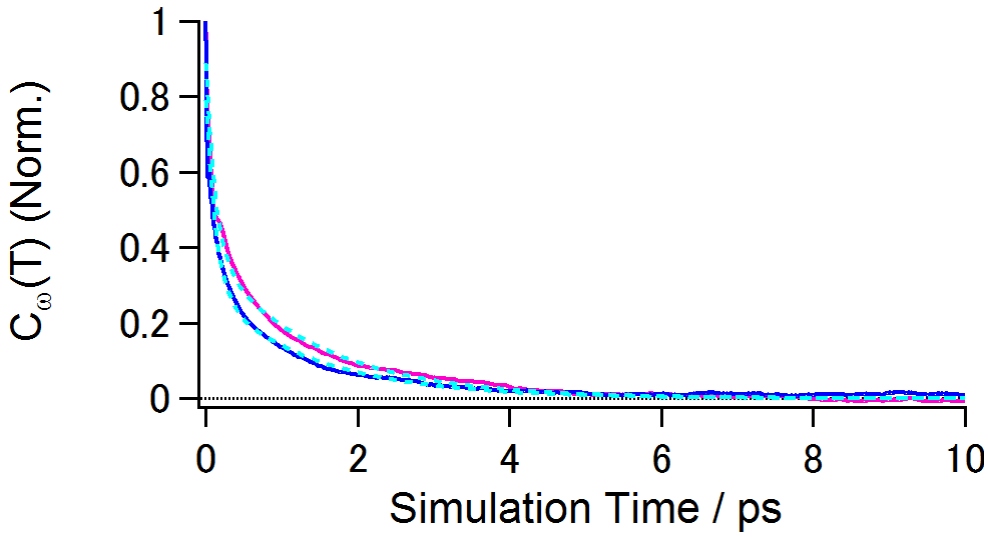

Figure 5.8. Normalized FFTCFs of the SCN stretching modes of NTBA (blue) and SCN^- (pink) calculated by Eq. (5.1) The dotted light-blue lines are the fitting results to double-exponential functions.

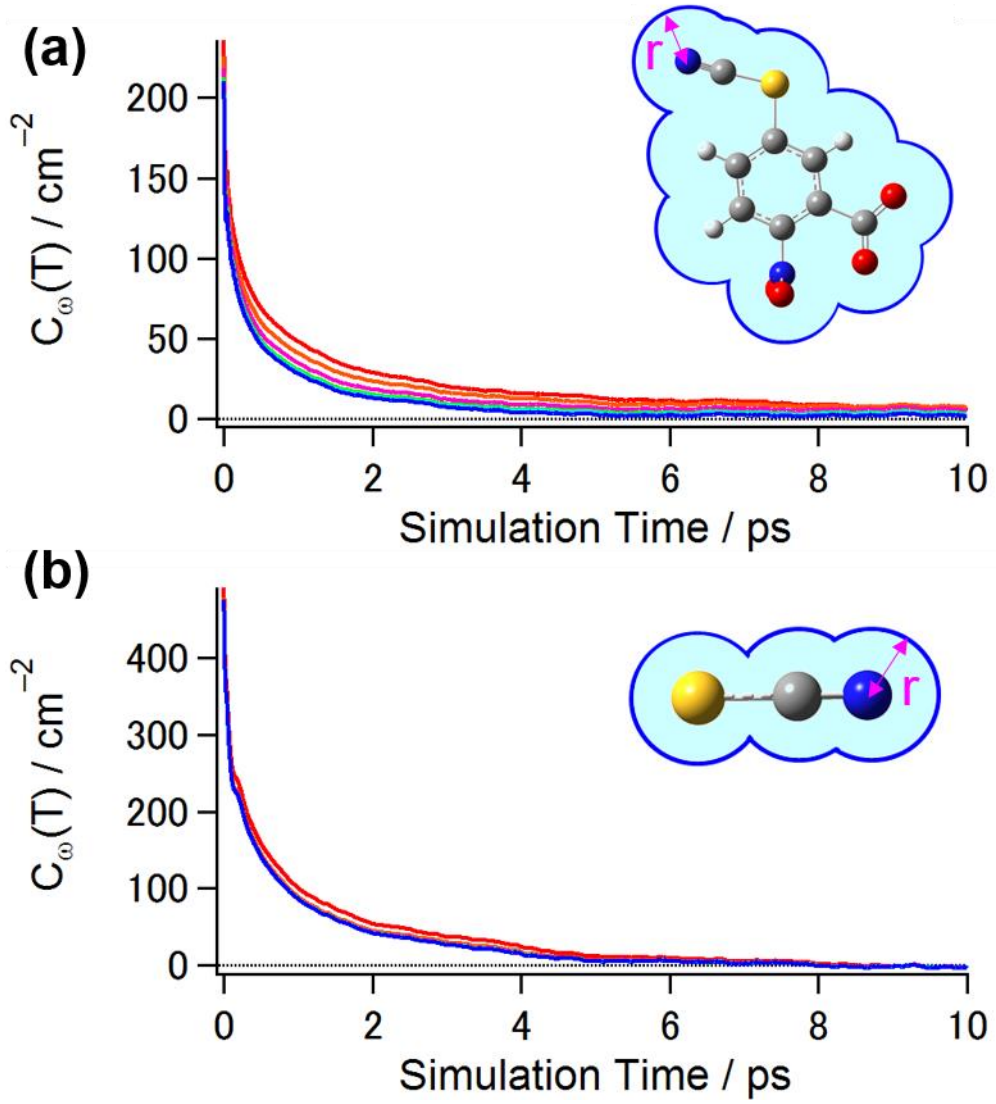

Figure 5.9. Spatially-resolved FFTCFs of (a) NTBA and (b) SCN^- in H_2O calculated with (red) and without (blue) the filtering function $f_j(T, r)$ defined by Eq. (5.8). The red line is the result for the cutoff distance r of 3.5 Å. (inset) Schematic illustration of the filtering function $f_j(T, r)$. By considering sphere with a radius of r on each atoms of the solutes, the union of the spherical regions (*i.e.* light-blue region within closed blue line) characterizes the radial-dependence of the SCN frequency fluctuations.

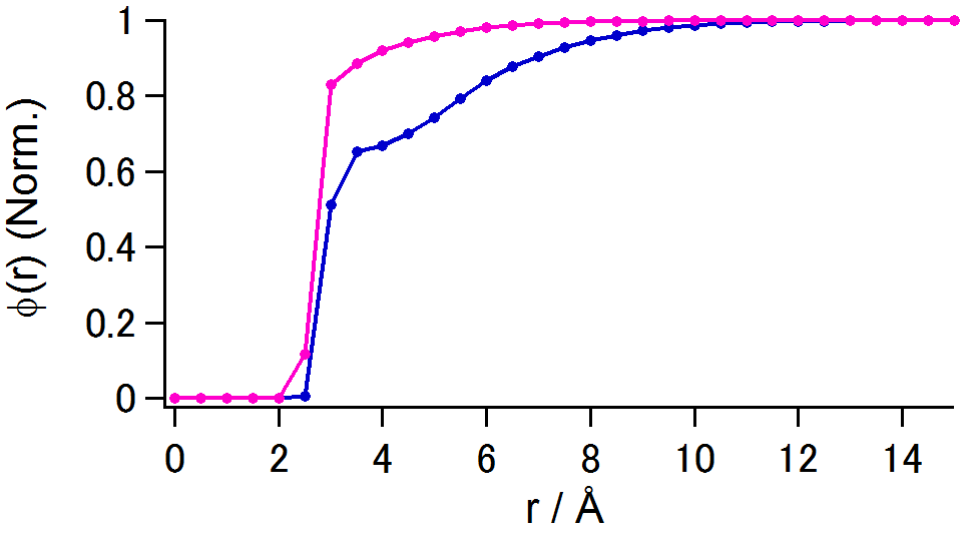

Figure 5.10. Normalized radial Coulomb electrostatic potential for NTBA (blue) and SCN^- (pink).

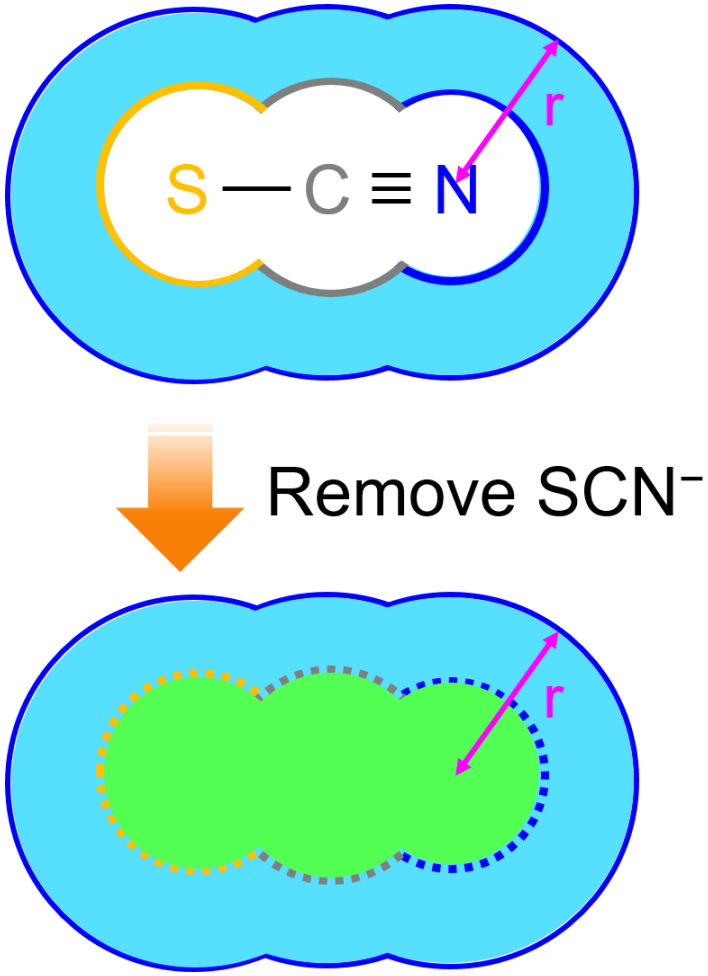

Figure 5.11. Schematic illustration of a "hypothetical hydration shell of SCN^-" in bulk water system. In order to define this hydration shell in the bulk water system, SCN^- molecule is simply removed from the hydration shell of SCN^-/water system. Here, the molecular structure of SCN^- (*i.e.* bond lengths and bond angle) is the same as that for SCN^-/water system. Regarding the size of each atom of this hypothetical SCN^- in bulk water system, radius r is defined as the shortest length in which the corresponding RDF $g_{XO}(r)$ (X = S, C, or N) has non-zero value. For the light-blue region (*i.e.* hydration shell of SCN^-), the filtering function $f_i'(T, r)$ is the same as that in Eq. (5.8). On the other hand, for the green region (*i.e.* inside of the hypothetical SCN^-), the filtering function $f_i'(T, r)$ is set to 0.

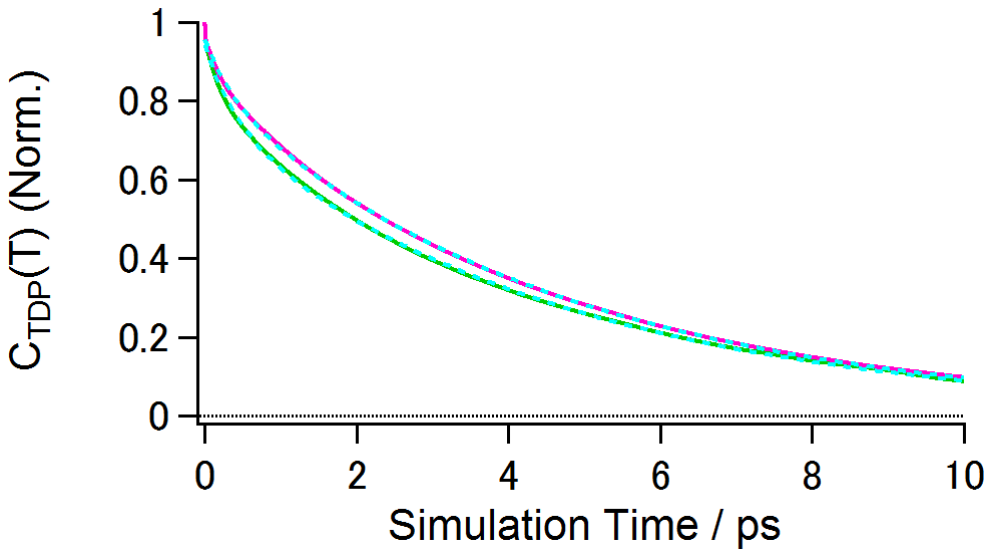

Figure 5.12. Total dipole moment time correlation functions for water molecules in SCN^-/water and bulk water systems. The pink and green lines correspond to the results given by Eqs. (5.10) and (5.11), respectively. The dotted light-blue lines are the fitting results with a double-exponential function; $A_1\exp(-T/\tau_1) + A_2\exp(-T/\tau_2)$. The fitting parameters are as follows; A_1 = 0.12, τ_1 = 0.37 ps, A_2 = 0.84, and τ_2 = 4.62 ps for SCN^-/water system, and A_1 = 0.18, τ_1 = 0.42 ps, A_2 = 0.76, and τ_2 = 4.68 ps for bulk water system (error bars for these parameters are approximately less than 5%).

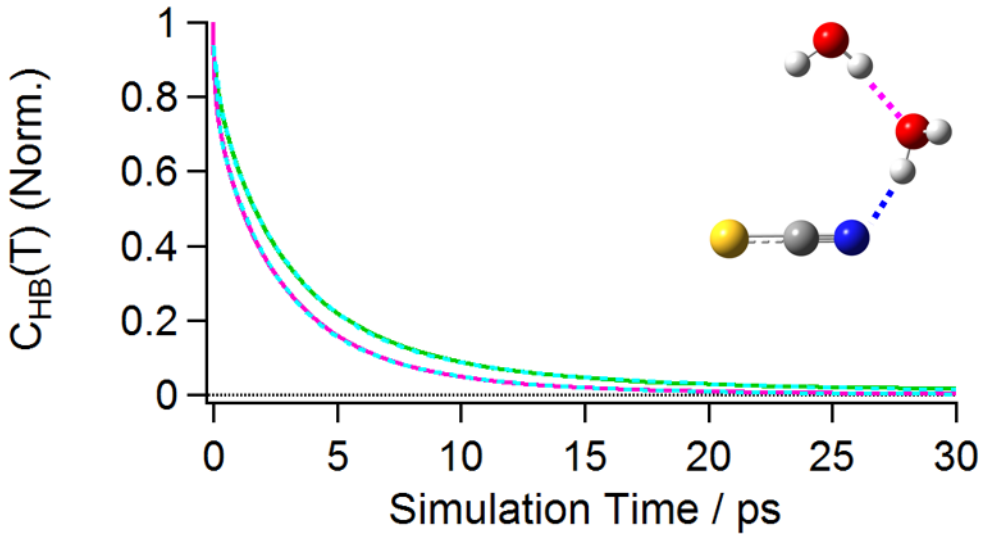

Figure 5.13. Comparison of the HBCFs between $H_2O_{HW,N}\cdots H_2O$ (pink) and bulk $H_2O\cdots H_2O$ (green). The dotted light-blue lines are the fitting results to triple-exponential functions. (inset) Snapshot of the MD simulation for water pairs in the first hydration shell of the N atom of SCN^-.

Table 5.1. Partial charges q_i of NTBA and SCN^- used for classical MD simulations and parameters l_i in Eq. (5.1) determined by the multi-variable least fitting.

NTBA		
Atom Symbol[(a)]	Q_i / e[(b)]	l_i / 10^{-5} $cm^{-1} \cdot e^{-1}$
C(1)	−0.066660	20.703815
C(2)	−0.014439	90.061409
C(3)	−0.005994	121.810399
C(4)	−0.271856	131.753672
C(5)	−0.058743	−177.299514
C(6)	−0.026808	11.749321
H(7)	0.123662	−16.626594
H(8)	0.147688	−10.119065
H(9)	0.128178	48.819213
C(10)	0.565413	−187.837173
O(11)	−0.615586	76.701802
O(12)	−0.615586	57.986181
N(13)	0.765212	−331.531148
O(14)	−0.427090	51.455200
O(15)	−0.427090	123.396328
S(16)	−0.067036	−92.093443
C(17)	0.315222	1404.467638
N(18)	−0.448488	777.456687
σ_N(19)	–	−43.992146
π_C(20)	–	−151.025520
π_N(21)	–	−0.0106082302

Table 5.1. (continued).

SCN^-		
Atom Symbol[(a)]	Q_i / e[(b)]	l_i / 10^{-5} $cm^{-1} \cdot e^{-1}$
S(1)	−0.685886	172.373048
C(2)	0.326060	325.218651
N(3)	−0.640175	88.984663
σ_N(4)	−	42.805917
π_S(5)	−	−25.116683
π_C(6)	−	−26.088043
π_N(7)	−	−27.468059

(a) The numbers in the parentheses correspond to those on atoms contained in NTBA and SCN^- shown in Figure 5.2.

Table 5.2. Obtained parameters of radial distribution functions, HBCFs, and FFTCFs for NTBA/water, SCN^-/water, and bulk water systems.

Solute	Radial Distribution Function				Hydrogen Bond Lifetime[a, b]				Frequency Fluctuation[a]	
	$r_{XH,min}$ / Å	$r_{XH,max}$ / Å	$r_{XO,min}$ / Å	$r_{XO,max}$ / Å	τ_1 / ps	τ_2 / ps	τ_3 / ps	$\tau_{1/e}$ ps	τ_1 / ps	τ_2 / ps
NTBA (SCN group)	2.6	2.0	5.0	3.5	0.28 (0.30)	2.76 (0.51)	15.03 (0.19)	1.76		
NTBA (COO^- group)	2.5	1.8	3.3	2.7	0.34 (0.09)	5.88 (0.31)	19.85 (0.60)	10.79	0.13 (0.64)	1.41 (0.36)
NTBA (NO_2 group)	2.3	1.9	4.2	3.1	0.23 (0.40)	2.17 (0.46)	15.01 (0.14)	0.89		
SCN^- (S atom)	2.8	2.1	3.6	3.0	0.41 (0.10)	5.96 (0.52)	18.93 (0.38)	7.70	0.13 (0.56)	1.44 (0.44)
SCN^- (N atom)	2.6	1.9	3.3	2.8	0.30 (0.09)	5.64 (0.44)	17.13 (0.47)	8.39		

Table 5.2. (continued).

Solute	Radial Distribution Function				Hydrogen Bond Lifetime[a, b]				Frequency Fluctuation[a]	
	$r_{XH,min}$ / Å	$r_{XH,max}$ / Å	$r_{XO,min}$ / Å	$r_{XO,max}$ / Å	τ_1 / ps	τ_2 / ps	τ_3 / ps	$\tau_{1/e}$ ps	τ_1 / ps	τ_2 / ps
Hydrated H_2O (S atom)	–	–	–	–	0.14 (0.20)	1.99 (0.47)	5.11 (0.33)	2.04	–	–
Hydrated H_2O (N atom)	–	–	–	–	0.15 (0.20)	2.31 (0.56)	5.98 (0.24)	2.05		
Bulk H_2O	–	–	–	–	0.34 (0.15)	3.08 (0.70)	12.76 (0.15)	2.80	–	–

(a) τ_i : time constant of ith component in the fitting function; $\sum_{i=1}^{2\text{ or }3} A_i \exp(-T/\tau_i)$. The relative amplitude of ith component A_i is shown in the parentheses. Error bars for these parameters are approximately less than 5%.

(b) $\tau_{1/e}$: time constant defined by $C_{HB}(\tau_{1/e}) = e^{-1}C_{HB}(0)$.

Appendix 5.A. Angle-resolved Pair-radial Distribution Functions for SCN Groups of NTBA and SCN^-

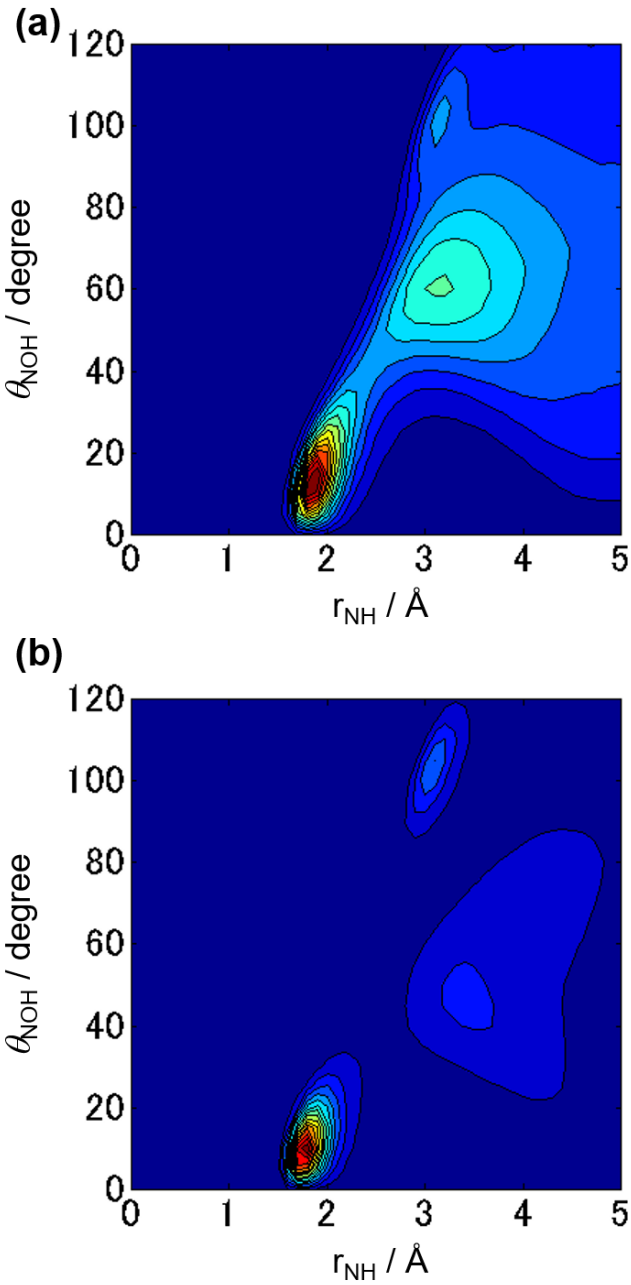

Figure 5.A. Angle-resolved RDFs of (a) NTBA and (b) SCN^- with respect to the r_{NH} (horizontal axis) and θ_{NOH} (vertical axis). The r_{NH} and θ_{NOH} correspond to the distance between SCN nitrogen atom and H_2O hydrogen atom and angle of ∠N···OH, respectively.

Appendix 5.B. Pair-radial Distribution Functions for Hydrogen Bond Sites of NTBA and SCN^-

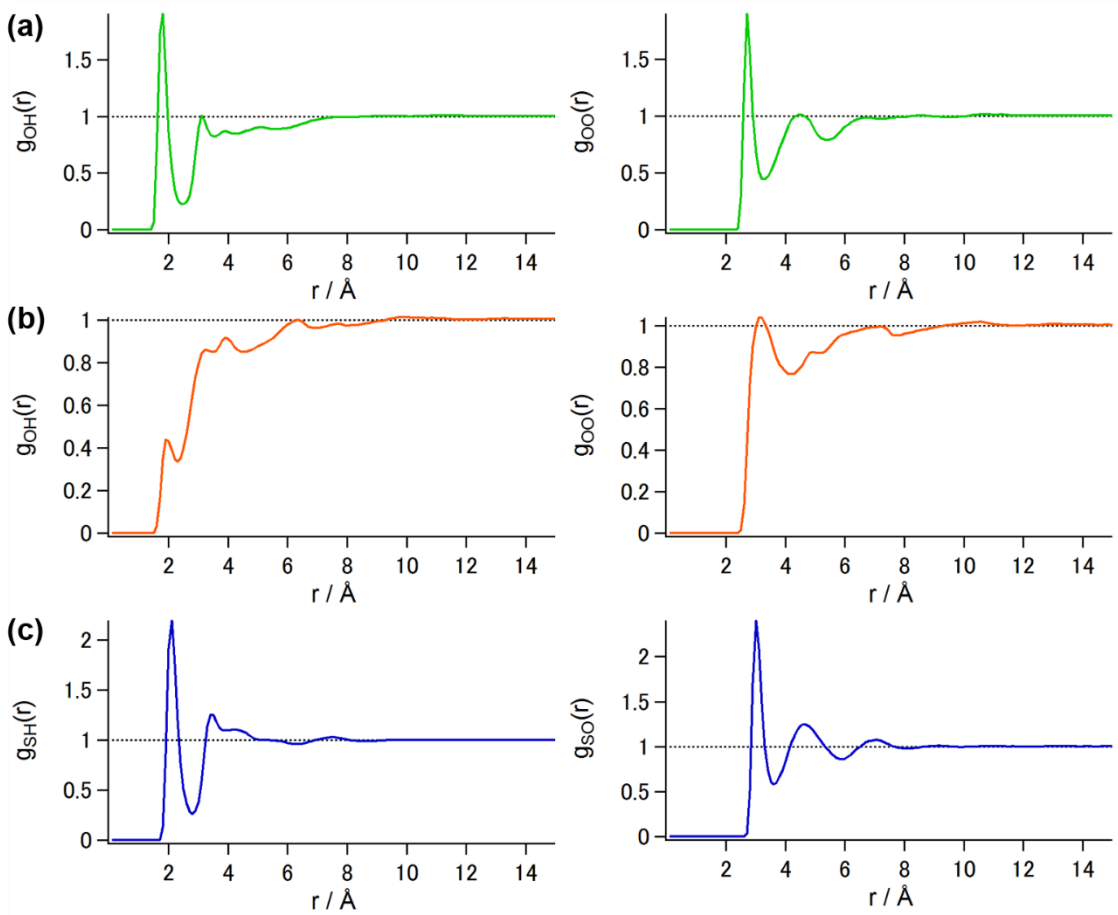

Figure 5.B. Pair RDFs between (a) COO^- oxygen and (b) NO_2 oxygen atoms of NTBA and (c) sulfur atom of SCN^- and H_2O hydrogen (left) and oxygen (right) atoms. With respect to the RDFs of the COO^- and NO_2 oxygen atoms, the mean values of the RDFs for the two oxygen atoms in the functional groups were calculated. The first minimum and maximum of $g_{XH}(r)$ and $g_{XO}(r)$ for each HB site are summarized in Table 5.2.

Appendix 5.C. Hydrogen Bond Correlation Functions for Hydrogen Bond Sites of NTBA and SCN^-

In this study, based on the first minimum position of the RDF, the HBs of COO^- oxygen and NO_2 oxygen atoms in NTBA and sulfur atom in SCN^- with a H_2O molecule were defined as follows: $r_{O(C)H} < 2.5$ Å and $\theta_{O(C)OH} < 30^\circ$ for a COO^- oxygen atom, $r_{O(N)H} < 2.3$ Å and $\theta_{O(N)OH} < 30^\circ$ for a NO_2 oxygen atom, and $r_{SH} < 2.8$ Å and $\theta_{SOH} < 30^\circ$ for a sulfur atom. Here, O(C) and O(N) represent the oxygen atoms in COO^- and NO_2 groups, respectively. The HBCFs for these HB sites are displayed in Figure 5.C. These decays could be fitted by triple-exponential functions, and the fitting parameters are summarized with characteristic time constants $\tau_{1/e}$ in Table 5.2.

Figure

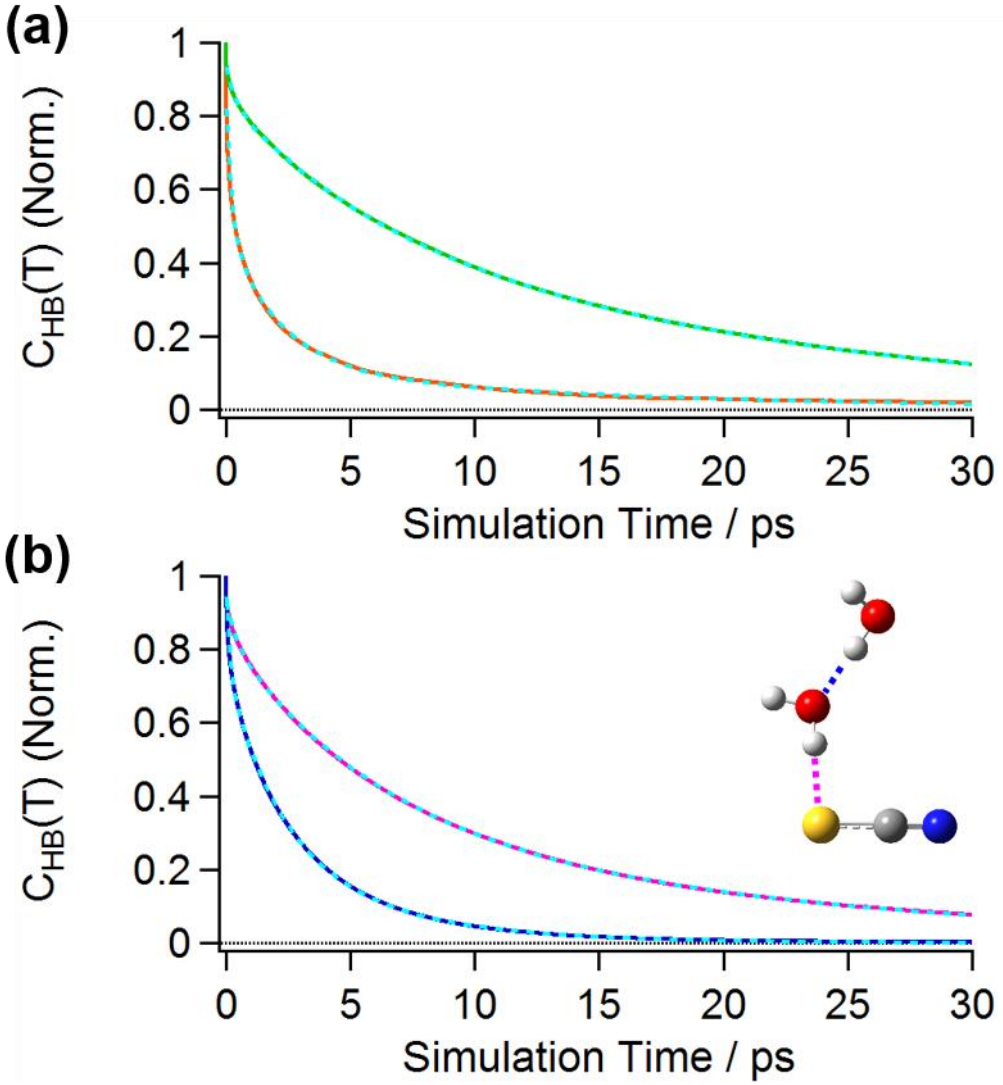

Figure 5.C. HBCFs for the HB sites of (a) NTBA and (b) SCN^-. Each profile corresponds as follows: COO^- oxygen (green), and NO_2 oxygen (orange) atoms of NTBA, and SCN sulfur atom (pink) and water pairs in the first hydration shell of the S atom (blue) of SCN^-. The dotted light-blue lines are the fitting results to triple-exponential functions. (inset) Snapshot of the MD simulation for water pairs in the first hydration shell of the S atom of SCN^-.

Appendix 5.D: Dipole Moment Reorientational Correlation Functions for Water Molecules around Hydrogen Bond Sites of NTBA and SCN^-

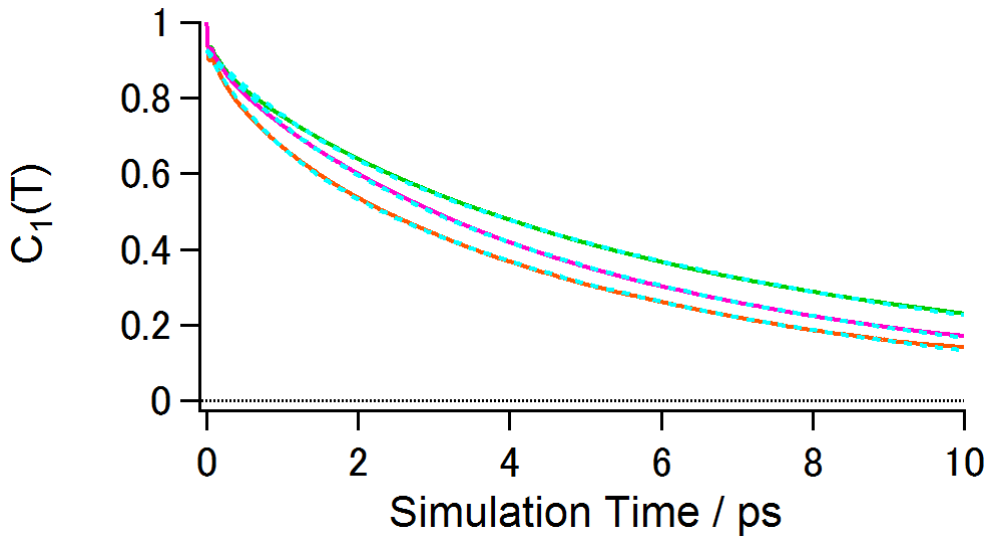

Figure 5.D. Dipole moment reorientational correlation functions for water molecules around the COO^- oxygen (green) and NO_2 oxygen (orange) atoms of NTBA, and those around SCN sulfur atom of SCN^- (pink). The dotted light-blue lines are the fitting results to a double exponential functions; $A_1\exp(-T/\tau_1) + A_2\exp(-T/\tau_2)$. The fitting parameters are as follows; $A_1 = 0.16$, $\tau_1 = 1.36$ ps, $A_2 = 0.76$, and $\tau_2 = 8.18$ ps for the COO^- oxygen atoms, $A_1 = 0.20$, $\tau_1 = 0.80$ ps, $A_2 = 0.73$, and $\tau_2 = 5.89$ ps for NO_2 oxygen atoms, and $A_1 = 0.18$, $\tau_1 = 1.49$ ps, $A_2 = 0.74$, and $\tau_2 = 6.67$ ps for the SCN sulfur atom (error bars for these parameters are approximately less than 5%). The $\tau_{1/e}$ are 5.98 ps for the COO^- oxygen atoms, 4.00 ps for the NO_2 oxygen atoms, and 4.77 ps for SCN sulfur atom.

Appendix 5.E: Spacitally-resolved Frequecny-frequecny Time Correlation Functions for NTBA/water and SCN^-/water Systems

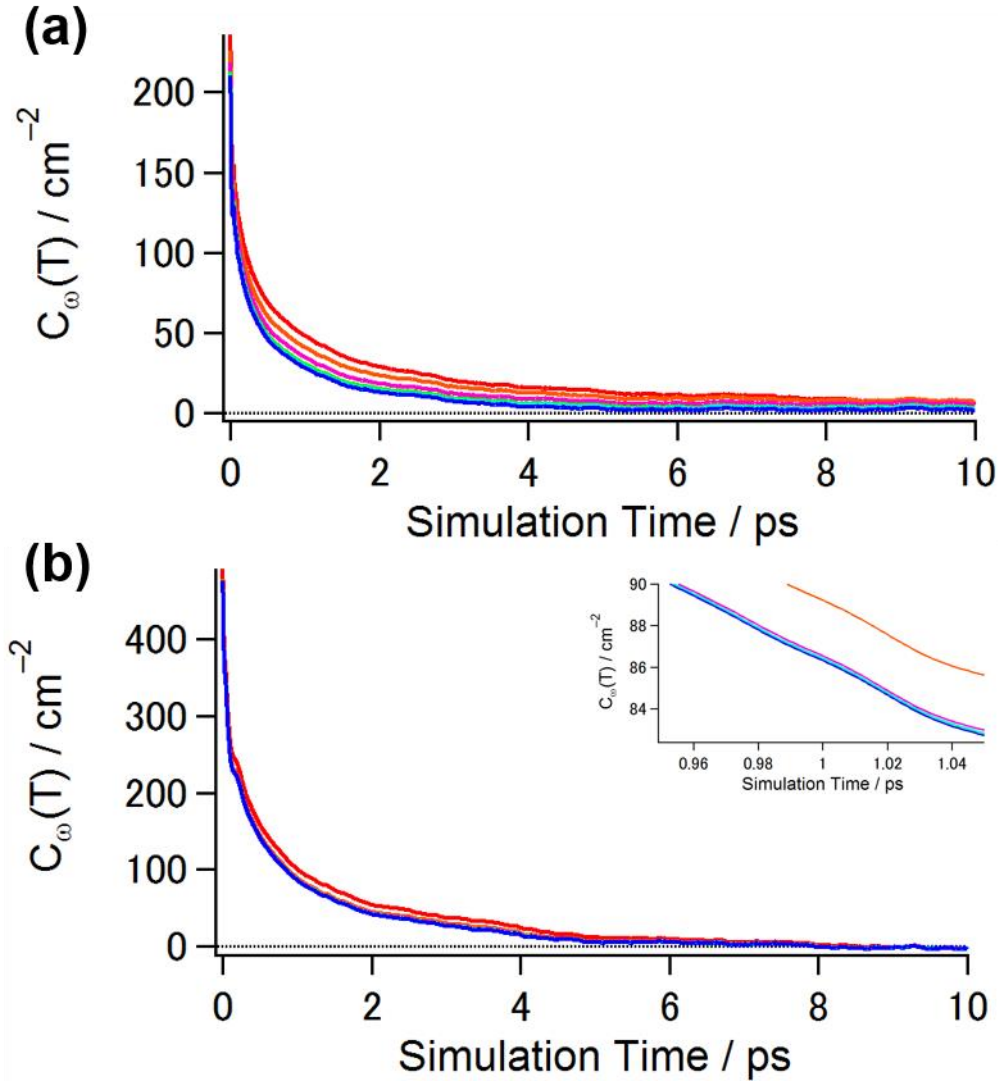

Figure 5.E. Spatially-resolved FFTCFs of (a) NTBA and (b) SCN^- with the filtering function $f_j(T, r)$ (see Eq. (5.8)). The cutoff distance r for each profile is as follows: r = 3.5 Å (red), 4.5 Å (orange), 5.5 Å (pink), 6.5 Å (green), 7.5 Å (light-blue), and no filtering (blue). For the spatially-resolved FFTCF of SCN^-, the lines other than the red lines are almost overlapped. The inset in Figure 5.E(b) highlights the difference among the overlapping lines.

Appendix 5.F: SCN Vibrational Frequecny Fluctuations Indeced by Electrostatic Interactions from Hydrogen Bonded Water Molcules

In order to evaluate the contribution of the electrostatic interactions caused by hydrogen-bonded water molecules to the SCN vibrational frequency fluctuations of NTBA and SCN^-, I considered the following filtering function:

$$f_j(T, r) = H_j(T) \tag{5.F.1}$$

where $H_j(T) = 1$ if the jth water molecule forms a HB with the HB sites of NTBA and SCN^-, and $H_j(T) = 0$ otherwise. Figure 5.F describes the corresponding FFTCFs of NTBA and SCN^- in H_2O given by the electrostatic interactions from the hydrogen-bonding water molecules. As shown in Figure 5.F, the SCN frequency fluctuations of NTBA and SCN^- are not determined by the interactions between a specific HB site and its neighboring water molecules.

Figure

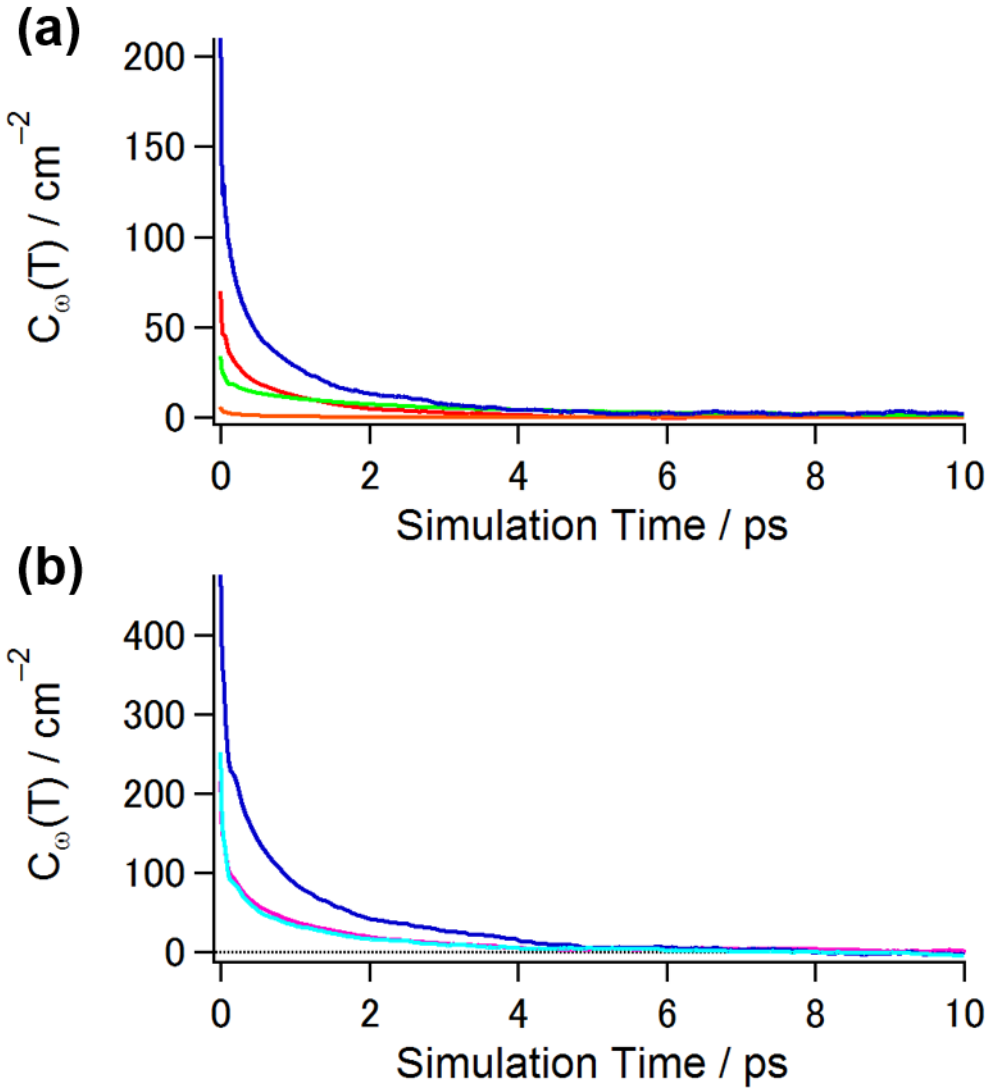

Figure 5.F. FFTCFs of (a) NTBA and (b) SCN^- with and without (blue) the filtering function $f_j(T, r)$ defined by Eq. (5.F.1). Each profile corresponds as follows: SCN nitrogen (red), COO^- oxygen (green), and NO_2 oxygen (orange) atoms of NTBA, and SCN sulfur (pink) and nitrogen (light-blue) atoms of SCN^-.

CHAPTER 6.

Vibrational Dynamics of N_3-derivatized Amino Acids in Aqueous Solutions Studied by Nonlinear Infrared Spectroscopy

6.1. Introduction

So far, the vibrational dynamics of tri-atomic ions, such as N_3^- and SCN^-, in water have been rigorously studied by nonlinear IR spectroscopy such as IR pump-probe and IR three-pulse photon echo method. Because the vibrational modes of these ions have the large IR activities and the sensitivity to the hydrogen bond (HB) interaction, these ions can be good vibrational probes to examine their surrounding environment. Moreover, their vibrational modes in water exhibit the absorption spectra with the peak wavenumbers ranging from 2000 cm^{-1} to 2100 cm^{-1}, which is called as a "transparent window" in aqueous solutions. As preliminary works, using ultrafast IR pump-probe spectroscopy, Hochstrasser and co-workers studied the vibrational energy relaxation and rotational dynamics of ions [6-8]. Hamm *et al.* investigated the vibrational frequency fluctuations of the N_3 anti-symmetric stretching mode of N_3^- in D_2O by three-pulse IR photon echo experiment, and found that the correlation function is characterized by time constants of 80 fs and 1.3 ps [9]. Tominaga and co-workers examined the temperature dependence of the vibrational dynamics of N_3^- in D_2O and the vibrational dynamics of OCN^- and SCN^- in methanol [10-13].

Recently, N_3-labeled artificial amino acids have been found to be excellent vibrational probes to study the molecular dynamics in water and biological environments. Bloem *et al.* used a peptide with the N_3 group as the solute, and studied the frequency fluctuations of the N_3 anti-symmetric stretching mode in protein by 2D-IR spectroscopy [14]. Thielges *et al.* also performed the 2D-IR measurement for azidophenylalanine site-specifically incorporated into myoglobin to study the dynamics of the protein [15]. Performing the polarization-controlled IR pump-probe and 2D-IR experiments, Cho and co-workers reported the vibrational energy relaxation and internal rotational motion of the N_3-derivatized proline in $CHCl_3$ [16-18]. Bredenbeck group synthesized an azulene-azide donor-acceptor model peptide, and observed the intramolecular vibrational energy transfer process between β-(1-azulenyl)-L-alanine and L-azidohomoalanine in the model peptide [19].

There are many types of unnatural amino acids with N_3 groups, and they can be incorporated into peptides and proteins by a peptide synthesis or a genetic procedure [20-22]. Here, it should be noted the vibrational dynamics of N_3-labeled amino acids are expected to depend on the molecular properties of the residues, such as structural flexibility, hydrophilicity, and hydrophobicity. Nevertheless, there are still a few works on the vibrational dynamics of the

N_3-labeled amino acids in water.

In this study, by using nonlinear IR spectroscopy, I examined the vibrational dynamics of the N_3 anti-symmetric stretching modes of two unnatural amino acids, Boc-3-azide-Ala-OH (dicyclohexylammonium) salt (abbreviated as N_3-Ala, Figure 6.1(a)) and *N*-Boc-cis-4-azide-L-proline **(**dicyclohexylammonium**)** salt (abbreviated as N_3-Pro, Figure 6.1(b)), in water. The motivations to choose these solutes for the vibrational probe molecules are as follows: First, as mentioned above, the frequency fluctuations of the ionic vibrational probe molecules in water were intensively investigated. Although the carboxylate groups ($-COO^-$) of N_3-Ala and N_3-Pro are electrically negative, the vibrational probes of the azide groups ($-N_3$) are electronically neutral. Consequently, same as the motivation in Chapter 4, one can examine the relationship between the observed frequency fluctuations and the electrical properties of the vibrational probe. Second, the structural degrees of freedom around the vibrational probes of N_3-Ala and N_3-Pro are different, that is, the structural flexibility around the azide group of N_3-Ala is higher than that of N_3-Pro due to the alkyl chain. Therefore, especially with respect to the rotational dynamics, one can expect that the different vibrational dynamics is observed. In this study, for comparison, I investigated the vibrational dynamics of azide anion (N_3^-) in water as well.

I studied the vibrational frequency fluctuations of N_3-Ala, N_3-Pro, and N_3^- in water with 2D-IR spectroscopy. Moreover, in order to study the vibrational energy relaxation (VER) and the rotational relaxation, I performed the polarization-controlled IR pump-probe measurements for them in water**.**

6.2. Materials and Methods

The details of the spectroscopy setups for the IR pump-probe and 2D-IR experiments are the same as those described in Chapter 4. The mid-IR pulse generated from the OPA/DFG system had a pulse duration of about 100 fs, a band width of about 100 cm^{-1}, and a pulse energy of about 3 μJ. The center wavenumbers of the mid-IR pulse were tuned to around 2150 cm^{-1} for N_3-Ala and N_3-Pro, and 2000 cm^{-1} for N_3^-.

N_3-Ala, N_3-Pro, and tetrabutylammonium azide were purchased from Sigma-Aldrich (St. Louis, Missouri, United States of America) and used without further purification. Distilled H_2O was used as the solvent. In order to dissolve N_3-Ala and N_3-Pro into water, a small amount of NaOH (40 w/w% solution in H_2O, Wako, Japan) added to the N_3-Ala and N_3-Pro aqueous

solutions (pH ~ 9.0). The concentrations of sample solutions were approximately 250 mM for N_3-Ala and N_3-Pro, and 50 mM for N_3^-. After passing through disposal membrane filters (diameter size: 0.20 μm, ADVANTEC, Japan), the sample solutions were confined in a 25 μm path length CaF_2 cell. The spectroscopy measurements were conducted at a room temperature (293 K).

6.3. Results and Discussions

6.3.1. IR Absorption Spectra

Figure 6.2 shows the IR absorption spectra of N_3-Ala, N_3-Pro, and N_3^- in H_2O in the 1950−2250 cm^{-1} region. The peak wavenumbers of the absorption spectra of N_3-Ala and N_3-Pro are 2116.3 cm^{-1} and 2115.8 cm^{-1}, respectively. On the other hand, the absorption spectrum of N_3^- exhibits the peak absorption at 2046.5 cm^{-1}. By performing the density functional theory (DFT) calculations for N_3-Ala, N_3-Pro and N_3^- in gas phases at B3LYP/6-311++G(3df,2pd) level with Gaussian 09 program package [23], these IR bands are assigned to N_3 anti-symmetric stretching modes. The DFT results of the normal mode analyses and partial charges on the vibrational probes in Table 6.1. As shown in Table 6.1, the charge distribution in N_3^- is almost symmetric. On the other hand, the partial charges on the N_3 groups of N_3-Ala and N_3-Pro are asymmetrically distributed, which may result from the breakings of the structural symmetries due to the formation of the covalent bonds with carbon atoms. Therefore, as reflected by the force constants (k) of N_3-Ala, N_3-Pro, and N_3^- in Table 6.1, the potential energy surfaces of the N_3 anti-symmetric stretching modes are expected to be different between the non-ionic and ionic N_3 groups, which likely causes the difference in the vibrational frequency of N_3 anti-symmetric stretching mode.

The IR absorption spectrum of N_3^- can be fitted by one Lorentzian function. On the other hand, the IR absorption spectra of N_3-Ala and N_3-Pro can be fitted by a sum of Gaussian and/or Lorentzian functions; three Gaussian functions for N_3-Ala and one Lorentzian function plus one Gaussian function for N_3-Pro. The fitting results are also shown in Figure 6.2, and their band width and peak wavenumbers are summarized in Table 6.2. Note that, although the absorption spectrum of N_3-Ala exhibits a small band at 2047.8 cm^{-1}, which has not been assigned yet, the vibrational coupling between this vibrational mode and the N_3 anti-symmetric stretching mode is not observed in the 2D-IR spectra of N_3-Ala (see Figure 6.6(a)). Therefore, the unassigned vibrational mode of N_3-Ala will not be discussed any more.

As mentioned above, the absorption spectra of the N_3 anti-symmetric stretching modes

of N_3-Ala and N_3-Pro exhibit the asymmetric band shapes, and this type of asymmetry was also observed in the previous studies [24-28]. Brewer and co-workers reported that the IR absorption spectra of 4-azido-L-phenylalanine and 4-azidomethyl-L-phenylalanine in water show the asymmetric line shapes, and they concluded that the asymmetric line shapes result from accidental Fermi resonance [24]. Moreover, Nydegger *et al.* performed the 2D-IR measurements for of 3-azidopyridine in CH_2Cl_2, and found that the 2D-IR spectra of this molecule exhibit the cross-peak signals at short population time, which a due to the vibrational coupling between the N_3 anti-symmetric stretching mode and a combination band or overtone [28]. However, in this study, clear signals cannot been observed in the off-diagonal regions of the 2D-IR spectra of N_3-Ala and N_3-Pro at t_2 = 0.2 ps (see Figures 6.6(a) and (b)). Consistent with this study, Thielges *et al.* also reported that, although a similar type of the asymmetric N_3 anti-symmetric stretching band is observed in the IR spectrum of N_3-labeled myoglobin, the 2D-IR spectra of the molecule do not have distinct cross-peak signals [15]. Therefore, the asymmetric band shapes of N_3-Ala and N_3-Pro are not likely due to Fermi resonance [29].

A more likely possibility is that multiple conformers of N_3-Ala and N_3-Pro exist in the aqueous solutions. Previously, Tucker *et al.* suggested that two different structures of 2'-azido-2'-deoxyuridine (abbreviated as N_3dU) are present in THF, which causes the inhomogeneous environment around the N_3 group of this molecule [30]. Moreover, Lee *et al.* showed that the IR spectrum of Ac-(4S)-Azp-NHMe (abbreviated as SA) in $CHCl_3$ has two peaks, which are due to the different two conformers in the solution [16, 17]. An asymmetric band is also observed in the IR spectrum of azidealanine dipeptide in THF, as a result of two distinct conformers of the peptide [31]. Because N_3-Ala and N_3-Pro are composed of many atoms, different types of structures are expected to exist in water. Therefore, based on the previous works, I consider that different structures of N_3-Ala and N_3-Pro yield inhomogeneous distributions of the vibrational transition frequencies of the N_3 anti-symmetric stretching modes.

6.3.2. Vibrational Energy Relaxation

In the polarization-controlled IR pump-probe experiments, after vibrational excitation of the N_3 anti-symmetric stretching modes of the solutes by IR pump pulses, the temporal pump-probe signals in the parallel and perpendicular conditions ($\Delta A_{//}(T)$ and $\Delta A_{\perp}(T)$, respectively) were observed. The isotropic and anisotropic IR pump-probe signals are given as:

$$N(T) = \frac{\Delta A_{//}(T) + 2\Delta A_{\perp}(T)}{3} \tag{6.1}$$

and

$$r(T) = \frac{\Delta A_{//}(T) - \Delta A_{\perp}(T)}{\Delta A_{//}(T) + 2\Delta A_{\perp}(T)}. \tag{6.2}$$

, respectively. The results of the isotropic IR pump-probe signals of N_3-Ala, N_3-Pro, and N_3^- are discussed in this section, and those of anisotropic ones will be discussed in the next section.

Figures 6.3(a − c) depict the frequency-resolved isotropic IR pump-probe signals of N_3-Ala, N_3-Pro, and N_3^- in H_2O. The blue colors represent the signals originating from ground state bleaching (GSB; $\nu = 0 - 1$) and stimulated emission (SE; $\nu = 0 - 1$), and the red colors represent transient absorption (TA; $\nu = 1 - 2$). Figure 6.3(d) displays the dispersed pump-probe signals of N_3-Ala and N_3-Pro at $T = 0.4$ ps and N_3^- at $T = 0.5$ ps. The IR pump-probe spectra of N_3-Pro and N_3^- can be reproduced by a sum of two Lorentzian functions. On the other hand, due to the small band in the lower-frequency region, a sum of four Lorentzian functions is needed for N_3-Ala. From the fitting analysis, the anharmonicity of the N_3 anti-symmetric stretching mode of N_3^- is found to be 27.0 cm^{-1}, which is consistent with the earlier work on N_3^- in D_2O [13, 32, 33]. On the other hand, the anharmonicities of N_3-Ala and N_3-Pro are 29.1 cm^{-1} and 25.6 cm^{-1}, respectively, which are similar to that of N_3dU in water [30]. Figure 6.4 presents the time evolution of the TA signals of N_3-Ala, N_3-Pro, and N_3^-. As mentioned in Section 4.3.2, in order to exclude the coherent artifact signal, the pump-probe signal after $T = 0.2$ ps was used for the fitting analysis [34]. The decay curves of N_3-Ala and N_3-Pro can be fitted by a double exponential function, and that of N_3^- can be fitted by a single exponential function. The fitting parameters are summarized in Table 6.3. As shown in Table 6.3, the IR pump-probe signals of N_3-Ala and N_3-Pro contain the ultrafast VER component with a time constant of 0.1 ps. Because the N_3 groups of N_3-Ala and N_3-Pro are attached to the carbon atoms, the covalent bonds can be expected to provide efficient pathways for the VER [35]. On the other hand, the slow time constants of N_3-Ala and N_3-Pro are close to those reported by several groups [34, 36, 37]. Tucker *et al*. revealed that the VER of N_3dU in water proceeds with a time constant of 1.1 ± 0.1 ps [30]. Dutta *et al.* observed that the VER of the N_3 anti-symmetric stretching modes of azido-nicotinamide adenine dinucleotide (abbreviated as azide-NAD^+) and 3-picolyl azide adenine dinucleotide (abbreviated as $PAAD^+$) in water undergoes with time constants of about 1.0 ps [36, 37].

Previously, Morita and Kato performed the molecular dynamics (MD) simulation to theoretically investigate the vibrational relaxation pathways of N_3^- in water [38]. They revealed that the intramolecular vibrational redistribution (IVR) to the N_3 symmetric stretching and bending modes and the energy transferring to the solvent mode have almost the same contribution to the VER of the N_3 anti-symmetric stretching mode. Moreover, they elucidated that the charge fluctuation effect significantly enhances both the direct VER and the IVR processes of N_3^- in water. Based on the MD simulation for the same system, Skinner group suggested that the IVR to the N_3 symmetric stretch mode dominates the VER of N_3^- in water [39]. Although N_3-Ala and N_3-Pro have much more intramolecular vibrational modes than N_3^-, the VER time constant of N_3^- in H_2O is shorter than those of N_3-Ala and N_3-Pro in H_2O. Here, note that the covalently bonded N_3 group has less resonance structures than ionic one; for covalently bonded N_3 group: $-N{=}N^{1+}{=}N^{1-} \leftrightarrow -N^{1-}{-}N^{1+}{\equiv}N$, for ionic N_3 group: $N{\equiv}N^{1+}{-}N^{2-} \leftrightarrow N^{2-}{-}N^{1+}{\equiv}N \leftrightarrow N^{1-}{=}N^{1+}{=}N^{1-}$. Consequently, I conclude that the amplitude of the charge fluctuations in N_3-Ala and N_3-Pro is smaller than that in N_3^-, which results in the less efficiency of the VER of N_3-Ala and N_3-Pro.

6.3.3. Rotational Relaxation

Figure 6.5 describes the anisotropy decays of the N_3 anti-symmetric stretching modes of N_3-Ala, N_3-Pro, and N_3^- in H_2O. The anisotropy decay after T = 0.2 ps can be characterized by a single exponential plus a constant, and the fitting parameters are summarized in Table 6.3. The rotational relaxation time of N_3^- is good agreement with the previous study [40].

According to the Stokes-Einstein-Debye (SED) theory, the rotational relaxation time is proportional to the hydrodynamic volume of the rotator: as the hydrodynamic volume is larger, the reorientation relaxation is slower. Previously, Sando *et al.* examined the rotational dynamics of $[Fe(CN)_5NO]^{3-}$, whose volume is much larger than that of N_3^-, and reported that the anisotropy decay of the NO stretching mode in H_2O is characterized by the time constant of 16 ps [41]. Therefore, based on the SED theory, one can expect that the reorientation relaxation of N_3-Ala and N_3-Pro undergoes on much longer time scales than that of N_3^-. However, as shown in Table 6.3, the rotational relaxation times are similar to each other.

In earlier work, by performing the polarization-controlled IR pump-probe measurement for phenol-*d* in $CHCl_3$, Rezus *et al*. elucidated that the internal rotational motion of the OD group around the CO bond axis contributes to the anisotropy decay of the OD stretching mode [42].

Moreover, Lee *et al*. studied the internal rotational relaxation of the N_3 group of SA in $CHCl_3$ with 2D-IR spectroscopy [16]. They obtained a time constant of 5.1 ± 2 ps, which is associated with the interconversion between the bound and free N_3 group. Therefore, based on the result that the time scales of the rotational relaxation times of N_3-Ala and N_3-Pro are similar to that of N_3^-, I consider that the internal rotation of the N_3 group plays an important role for the anisotropy decays of N_3-Ala and N_3-Pro in H_2O.

Here, it should be noted that the anisotropy of phenol-*d* contains a long-lived component, which is considered to reflect the slower rotational motion as a whole. Because the rotational motion of the OD group around the CO bond axis restricts the reorientation of the OD group to a limited portion of the unit sphere, the C−O−D angle determines the offset level of the anisotropy. Although it is difficult to measure the anisotropy decays of N_3-Ala and N_3-Pro accurately due to the short vibrational lifetimes (see Table 6.3), the rotational relaxation time of N_3-Ala is considered to be shorter than that of N_3-Pro within the present experimental accuracy. Moreover, only the anisotropy decay of N_3-Pro contains a nonzero constant component (A_∞). These differences may be explained in terms of the number of the internal rotational modes which contribute to the reorientation of the N_3 group. Similar to phenol-*d*, because the N_3 group of N_3-Pro connects to the cyclic structure of the pyrrolindine ring, internal rotational motion around the CN bond axis can restrict the reorientation of the N_3 group in a certain space. On the other hand, because the N_3 group of N_3-Ala connects to the methylene group, the rotational motion around the CC bond axis (indicated by a green line in Figure. 6.1) can provide less angular restriction for the rotational motion of the N_3 group, which results in the faster anisotropy decay of N_3-Ala. However, in order to give definitive conclusion for this issue, it is necessary to characterize the anisotropy decay of the solutes precisely.

Before closing this section, it should be noted that rotational dynamics around multi-bond axes is expected to play a crucial role for conformational changes of macromolecules. Therefore, to obtain more detailed insight into the relationship between the structural flexibility around the vibrational probe and its anisotropy decay behavior, the polarization-controlled IR pump-probe experiments for solutes with multi-bond axes in alcohol solutions were conducted in Chapter 7.

6.3.4. Spectral Diffusion

The 2D-IR spectra of N_3-Ala, N_3-Pro, and N_3^- in H_2O were measured at different population times (t_2) ranging from 0 ps to 2 ps. Figure 6.6 displays the 2D-IR spectra measured at t_2 = 0.2 ps, 1 ps, and 2 ps. The blue and red colors represent the GSB + SE and TA signals, respectively.

As mentioned in Section 4.3.3, the t_2-dependence of 2D-IR spectra reflects the frequency fluctuations of solutes. In this study, by using the center line slope (CLS) method [43, 44], the t_2-dependence of the 2D-IR spectra were evaluated to determine the FFTCFs of N_3-Ala, N_3-Pro, and N_3^- in H_2O. The green lines in Figure 6.6 represent the center lines of the 2D-IR spectra, and the CLS values were obtained from the slope of these lines with respect to the ω_1 axis. Figure 6.7 depicts the CLSs of N_3-Ala, N_3-Pro, and N_3^- as a function of the population time. The initial values of these CLSs are less than one, which are due to the motional narrowing. Moreover, the CLSs exhibit the decays with a time constant, which reflects the spectral diffusion processes of the solutes. Therefore, same as the SCN anti-symmetric stretching modes of NTBA and SCN^-, the FFTCFs of N_3-Ala, N_3-Pro, and N_3^- in H_2O are expressed as follows:

$$C_\omega(t_2) = \delta(t_2)/T_2^* + \Delta_C^2 \exp\left(-t_2/\tau_C\right) + \Delta_0^2 \tag{6.3}$$

where T_2^* is the pure dephasing time constant, which characterizes the homogeneous component. The Δ_C^2 and τ_C are the amplitude and correlation time of the frequency fluctuations, respectively, which reflect the spectral diffusion process. The Δ_0^2 is the static inhomogeneous component. Following the procedure mentioned in Section 4.3.3, the FFTCF parameters of the T_2^*, Δ_0^2, Δ_C^2, and τ_C were determined [43, 44]. Here, to exclude the pulse overlapping effects due to coherent interactions among three IR pulses, the CLS after t_2 = 0.2 ps was used for the analysis [34]. Moreover, the VER and rotational relaxation time constants listed in Table 6.3 were used to calculate the spectral broadening due to the vibrational and reorientational relaxation processes. The obtained FFTCF parameters are summarized in Table 6.4. Here, because the N_3-anti symmetric modes of N_3-Ala and N_3-Pro in H_2O exhibit the blue wings of the absorption spectra (see Figure 6.2), the decays of the CLS in the presence of two transitions ($\omega_{N3,low}$ and $\omega_{N3,high}$ bands) were simulated to estimate the contribution of the wings to the 2D-IR spectra of them. The detail of the CLS analyses is described in Appendix 6.A. Based on the analyses, I found that the CLSs of N_3-Ala and N_3-Pro mainly reflect the frequency fluctuations of the $\omega_{N3,low}$ band.

As shown in Table 6.4, the CLS analysis revealed that the FFTCF of N_3^- in H_2O decays with a time constant of 1.3 ps, which is consistent with the results of the three-pulse IR photon

echo measurements for N_3^- in D_2O [12, 13]. Moreover, those of N_3-Ala and N_3-Pro in H_2O are characterized by similar time constants of 1.5 ps and 1.0 ps, respectively, which are in good agreement with the earlier 2D-IR experiments for N_3-derivatized biomolecules in water [30, 36, 37]. In earlier works, several groups experimentally and theoretically investigated the frequency fluctuations of ions and dilute HOD in water, and elucidated that the frequency fluctuations with a time constant of approximately 1 ps are caused by the structural arrangement of the hydrogen bonding network [9-13, 45-48]. Therefore, by assuming that the frequency fluctuations of N_3-Ala and N_3-Pro on 1 ps time scale are also due to the fluctuations of the hydrogen bonding network, the 2D-IR experiments for N_3-Ala and N_3-Pro in H_2O suggest that the water dynamics around the non-ionic N_3 group is similar to that around the ionic one.

On the other hand, notable difference in the FFTCFs between the non-ionic and ionic N_3 groups is the quasi-static inhomogeneous component Δ_0, which reflects the slower dynamics than the experimental time window of population time. There are likely two interpretations of the Δ_0. First, the Δ_0 reflects slower water dynamics nearby the solutes than bulk water. Bakker *et al.* conducted the anisotropy decay measurements for trimethylamine-*N*-oxide (abbreviated as TMAO), tertiary butyl alcohol (abbreviated as TBA), and tetramethyl urea (abbreviated as TMU) in water, and demonstrated that the hydrophobic effects of the methyl groups in TBA, TMAO, and TMU cause the slower rotational motions of hydrated water molecules [49, 50]. Moreover, based on the 2D-IR experiments for these systems, they showed that the 2D-IR spectra of hydrated waters exhibit the longer-lived elongation along the diagonal direction than those of bulk water [51, 52]. On the other hand, the theoretical studies with the classical MD simulations for TBA, TMAO, and TMU in water pointed out that not only the hydrophobic groups but also the hydrophilic groups in the solute affect the dynamics of water molecules surrounding the solutes [53, 54]. Because N_3-Ala and N_3-Pro contain both the hydrophobic and hydrophilic groups, they may contribute to the static component of the FFTCFs.

The second interpretation of the Δ_0 is that the conformational changes of the solutes induce the frequency fluctuations on a slower time scale. In the previous studies, Hochstrasser and Cheatum groups reported that the FFTCFs of $PAAD^+$ and N_3dU in water contain a static inhomogeneous component, which is considered to reflect the structural dynamics of the probe molecules [30, 36]. As discussed in Section 6.3.1, the asymmetric lineshapes of the N_3-anti symmetric stretching modes of N_3-Ala and N_3-Pro may be related to the distinct molecular

structures. Because the structural fluctuations of N_3-Ala and N_3-Pro in H_2O are expected to take place much slower than the observation time, such fluctuations may provide the Δ_0 to their FFTCFs.

6.4. Conclusion

In this chapter, the vibrational dynamics of the non-ionic vibrational probe molecules of N_3-Ala and N_3-Pro and ionic vibrational probe molecule of N_3^- in H_2O were investigated by nonlinear IR nonlinear spectroscopy.

Using polarization-controlled IR pump-probe spectroscopy, the VER and rotational relaxation processes of the vibrational probe molecules were examined. Even though N_3-Ala and N_3-Pro are expected to possess more numbers of energy accepting modes in IVR processes than N_3^-, the VER time constants of N_3-Ala and N_3-Pro are slower than that of N_3^-. Based on the results, I consider that the charge fluctuations in the N_3 group likely play an important role for the VER of the N_3 anti-symmetric stretching mode, which was suggested in Ref. 42. From the comparison of the rotational relaxation times of the solutes, I conclude that internal rotational motions of N_3-Ala and N_3-Pro promote the rotational relaxation of the N_3 groups. Moreover, I found that the anisotropy decays of N_3-Ala and N_3-Pro exhibit the different behaviors at longer pump-probe delay time, which suggests the importance of the structural flexibility around the N_3 group for the anisotropy decay.

The 2D-IR measurements for N_3-Ala, N_3-Pro, and N_3^- in H_2O revealed that the FFTCFs of them can be expressed by a delta function plus an exponential function and constant, which are reflected the homogeneous and inhomogeneous components, respectively. From the CLS analyses, I revealed that the frequency fluctuations of the solutes can be characterized by time constants of approximately 1 ps. Based on the similarity of the correlation times of N_3-Ala and N_3-Pro to that of N_3^-, it is suggested that the frequency fluctuations of the N_3 anti-symmetric stretching modes of N_3-Ala and N_3-Pro in H_2O are expected to reflect the structural rearrangement of the HB network system. Different from the FFTCF of N_3^-, those of N_3-Ala and N_3-Pro are found to contain nonzero constant components. I consider that the slower frequency fluctuations than the experimental window time (*i.e.* 2 ps in this study) are due to the hydration dynamics affected by the solute and/or the structural fluctuations of solute.

References

1. I. Ohmine and H. Tanaka, *Chem. Rev.*, 93, 2545 (1993).

2. R. M. Stratt and M. Maroncelli, *J. Phys. Chem.*, 100, 12981 (1996).

3. J. C. Owrutsky, D. Raftery, and R. M. Hochstarsser, *Anuu. Rev. Phys. Chem.*, 45, 519 (1994).

4. E. T. J. Nibbering and T. Elesaesser, *Chem. Rev.*, 104, 1887 (2004).

5. K. Ohta, J. Tayama, S. Saito, and K. Tominaga, *Acc. Chem. Res.*, 45, 1982 (2012).

6. J. C. Owrutsky, Y. R. Lim, M. Li, M. J. Sarisky, and R. M. Hochstrasser, *Chem. Phys. Lett*, 184, 368 (1991).

7. M. Li, J. C. Owrutsky, M. J. Sarisky, J. P. Culver, A. Yodh, and R. M. Hochstrasser, *J. Chem. Phys.*, 98, 5499 (1993).

8. J. C. Owrutsky, D. Raftery, and R. M. Hochstrasser, *Annu. Rev. Phys. Chem.*, 45, 519 (1994).

9. P. Hamm, M. Lim, and R. M. Hochstrasser, *Phys. Rev. Lett*, 81, 5326 (1998).

10. K. Ohta, H. Maekawa, S. Saito, and K. Tominaga, *J. Phys. Chem. A*, 30, 5645 (2003).

11. K. Ohta, H. Maekawa, and K. Tominaga, *J. Phys. Chem. A*, 108, 1333 (2004).

12. K. Ohta, J. Tayama, and K. Tominaga, *Phys. Chem. Chem. Phys.*, 14, 10455 (2012).

13. J. Tayama, A. Ishihara, M. Banno, K. Ohta, S. Saito, and K. Tominag, *J. Chem. Phys.*, 133, 014505 (2010).

14. R. Bloem, K. Koziol, S. A. Waldauer, B. Buchli, R. Walser, B. Samatanga, I. Jesarov, and P. Hamm, *J. Phys. Chem. B*, 116, 13705 (2012).

15. M. C. Thielges, J. Y. Axup, D. Wong, H. S. Lee, J. K. Chung, P. G. Schultz, and M. D. Fayer, *J. Phys. Chem. B*, 115, 11294 (2011).

16. K. -K. Lee, K. -H. Park, C. Joo, H. -J. Kwon, H. Han, J. -H. Ha, S. Park, and M. Cho, *Chem. Phys.*, 396, 23 (2012).

17. K. -K. Lee, K. -H. Park, C. Joo, H. -J. Kwon, J. Jeon, H. -I. Jung, S. Park, H. Han, and M. Cho, *J. Phys. Chem. B*, 116, 5097 (2012).

18. K.-H. Park, J. Joen, Y. Park, S. Lee, H.-J. Kown, C. Joo, S. Park, H. Han, and M. Cho, *J. Phys. Chem. Lett.*, **4**, 2105 (2013).

19. H. M. Müeller-Werkmeister and J. Bredenbeck, *Phys. Chem. Chem. Phys.*, 16, 3261 (2014).

20. K. L. Kiick, D. A. Tirrell, and C. R. Bertozzi, *Proc. Natl. Acad. Sci. U. S. A*, 99, 19 (2002)

21. D. P. Nguyen, H. Lusic, H. Neunann, P. B. Kapadnis, A. Deiters, and J. W. Chin, *J. Am. Chem. Soc.*, 131, 8720 (2009).

22. D. B. Oliver, R. J. Cabelli, K. M. Dolan, and G. P. Jarosik, *Proc. Natl. Acad. Sci. U. S. A*, 87, 8227 (1990).

23. M. J. Frisch *et al*., GAUSSIAN 09 (Revision B.01), Gaussian, Inc., Wallingford, CT (2009).

24. C. G. Bazewicz, M. T. Liskov, K. J. Hines, and S. H. Brewer, *J. Phys. Chem. B*, 117, 8987 (2013).

25. E. Lieber, C. N. Rao, A. E. Thomas, E. Oftedahl, R. Minnis, and C. V. N. Nambury, *Spectrochim. Acta*, 19, 1135 (1963).

26. Y. N. Sheinker, L. B. Senyavin, and V. N. Zheltova, *Dokl. Akad. Nauk*, 160, 1339 (1965).

27. L. K. Dyall and J. E. Kemp, *Aust. J.Chem.*, 20, 1395 (1967).

28. M.W. Nydegger, S. Dutta, and C. M. Cheatum, *J. Chem. Phys.*, 133, 134506 (2010).

29. J. Edler and P. Hamm, *J. Chem. Phys.* 119, 2709 (2003).

30. M. J. Tucker, X. S. Gai, E. E. Fenlon, S. H. Brewer, and R. M. Hochstrasser, *Phys. Chem. Chem. Phys.*, 13, 2237 (2011).

31. K. -I. Oh, J. -H. Lee, C. Joo, H. Han, and M. Cho, *J. Phys. Chem. B*, 112, 10352 (2008).

32. M. C. Asplund, M. Lim, and R. M. Hochstrasser, *Chem. Phys. Lett.*, 323, 269 (2000).

33. M. Li, J. Owrutsky, M. Sarisky, J. P. Culver, A. Yodh, and R. M. Hochstrasser, *J. Chem. Phys.*, 98, 5499 (1993).

34. P. Hamm, M. Lim, and R. M. Hochstrasser, *J. Phys. Chem. B*, 102, 6123 (1998).

35. V. M. Kenkre, A. Tokmakoff, and M. D. Fayer, *J. Phys. Chem.*, 101, 10618 (1994).

36. S. Dutta, Y. -L. Li, W. Rock, J. C. D. Houtman, A. Kohen, and C. M. Cheatum, *J. Phys. Chem. B*, 116, 542 (2012).

37. S. Dutta, W. Rock, R. J. Cook, A. Kohen, and C. M. Cheatum, *J. Phys. Chem.* 135, 055106 (2011).

38. A. Morita and S. Kato, *J. Chem. Phys*. 109, 5511 (1998).

39. S. Li, J. R. Schmidt, and J. L. Skinner, *J. Chem. Phys.*, 125, 244507 (2006).

40. Q. Zhong, A. P. Baronavski, and J. C. Owrutsky, *J. Chem. Phys.*, 119, 9171 (2003).

41. G. M. Sando, Q. Zhong, and J. C. Owrutsky, *J. Chem. Phys.*, 121, 2158 (2004).

42. Y. L. Rezus, D. Madsen, and H. J. Bakker, *J. Chem. Phys.*, 121, 10599 (2004).

43. K. Kwak, S. Park, I. J. Finkelstein, and M. D. Fayer, *J. Chem. Phys.*, 127, 124503 (2007).

44. K. Kwak, D. E. Rosenfeld, and M. D. Fayer, *J. Chem. Phys.*, 128, 204505 (2008).

45. C. J. Fecko, J. J. Loparo, S. T. Roberts, and A. Tokmakoff, *J. Chem. Phys.*, 122, 054506 (2005).

46. D. Kraemer, M. L. Cowan, A. Paarmann, N. Huse, E. T. J. Nibbering, T. Elsaesser, and R. J. D. Miller, *Proc. Natl. Acad. Sci USA*, 105, 437 (2008).

47. S. Z. Li, J. R. Schmidt, A. Piryatinski, C. P. Lawrence, and J. L. Skinner, *J. Phys. Chem. B*, 110, 18933 (2006).

48. J. D. Eaves, A. Tokmakoff, and P. L. Geissler, *J. Phys. Chem. A*, 109, 9424 (2005).

49. Y. L. A. Rezus and H. J. Bakker, *J. Phys. Chem. A*, 112, 2355 (2008).

50. Y. L. A. Rezus and H. J. Bakker, *Phys. Rev. Lett.*, 99, 148301(2007).

51. A. Bakulin, M. S. Pshenichnikv, H. J. Bakker, and C. Petersen, *J. Phys. Chem. A*, 115, 1821 (2011).

52. A. Bakulin, C. Liang, T. L. Jansen, D. A. Wiersma, H. J. Bakker, and M. S. Pshenichnikv, *Acc. Chem. Res*, 42, 1229 (2009).

53. D. Laage, G. Strinemann, and J. T. Hynes, *J. Phys. Chem. B*, 113, 2428 (2009).

54. G. Strinemann, J. T. Hynes, and D. Laage, *J. Phys. Chem. B*, 114, 3052 (2010).

55. E. E. Fenn and M. D. Fayer, *J. Chem. Phys.*, 135, 074502 (2011).

Figures and Tables

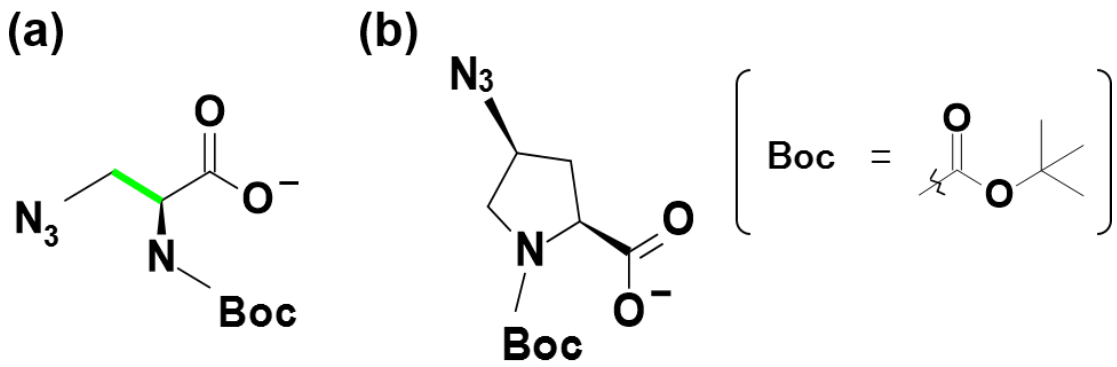

Figure 6.1. Molecular structures of (a) Boc-3-azide-Ala-OH (dicyclohexylammonium) salt and (b) *N*-Boc-cis-4-azide-L-proline **(**dicyclohexylammonium**)** salt. The green line indicates the rotational motion around the CC bond axis (see Section 6.3.3).

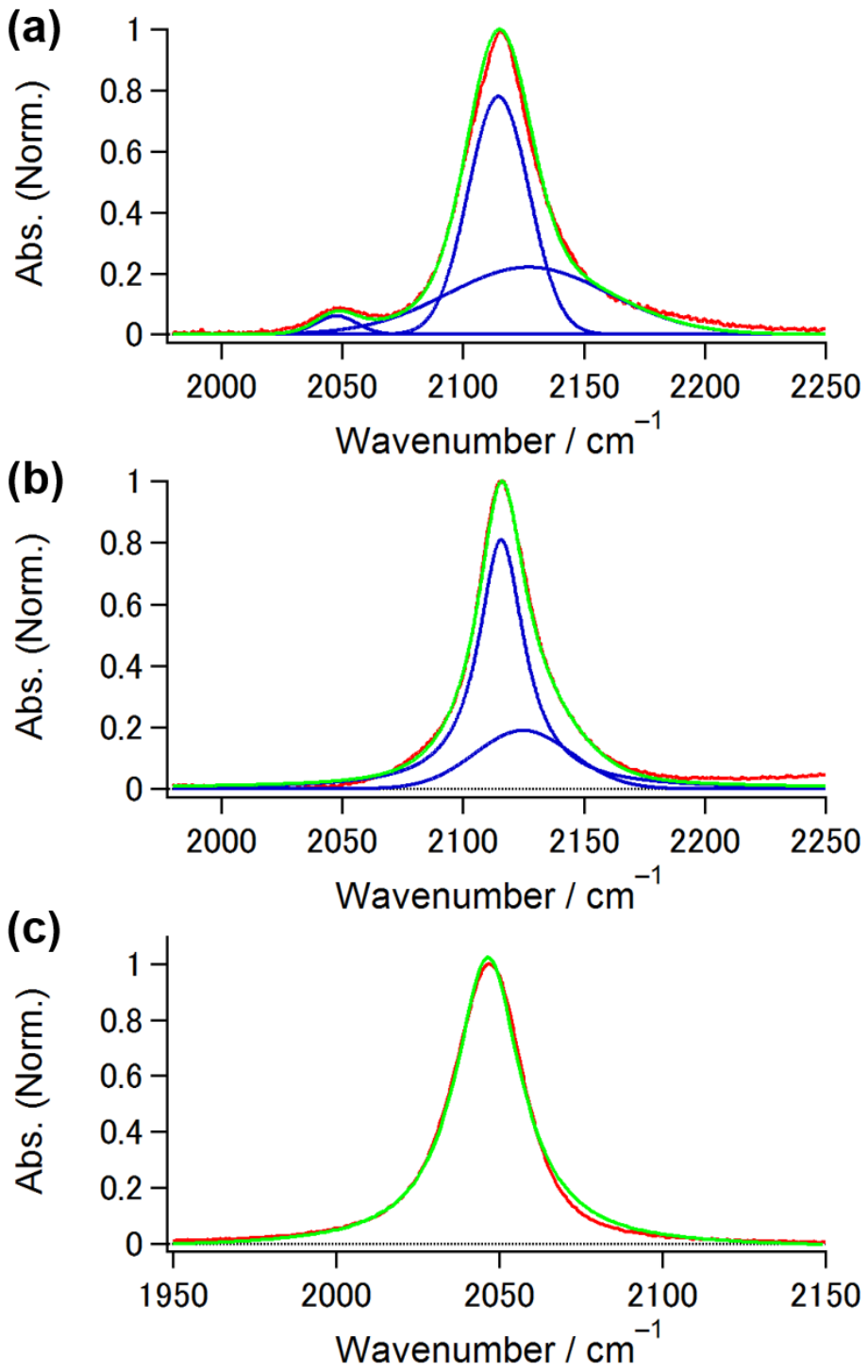

Figure 6.2. IR absorption spectra of the N_3 anti-symmetric stretching mode of (a) N_3-Ala, (b) N_3-Pro, and (c) N_3^- in H_2O. The red line indicates the experimental data. The green lines represent the fitting result of the IR band, and blue lines are each component of the involved transitions.

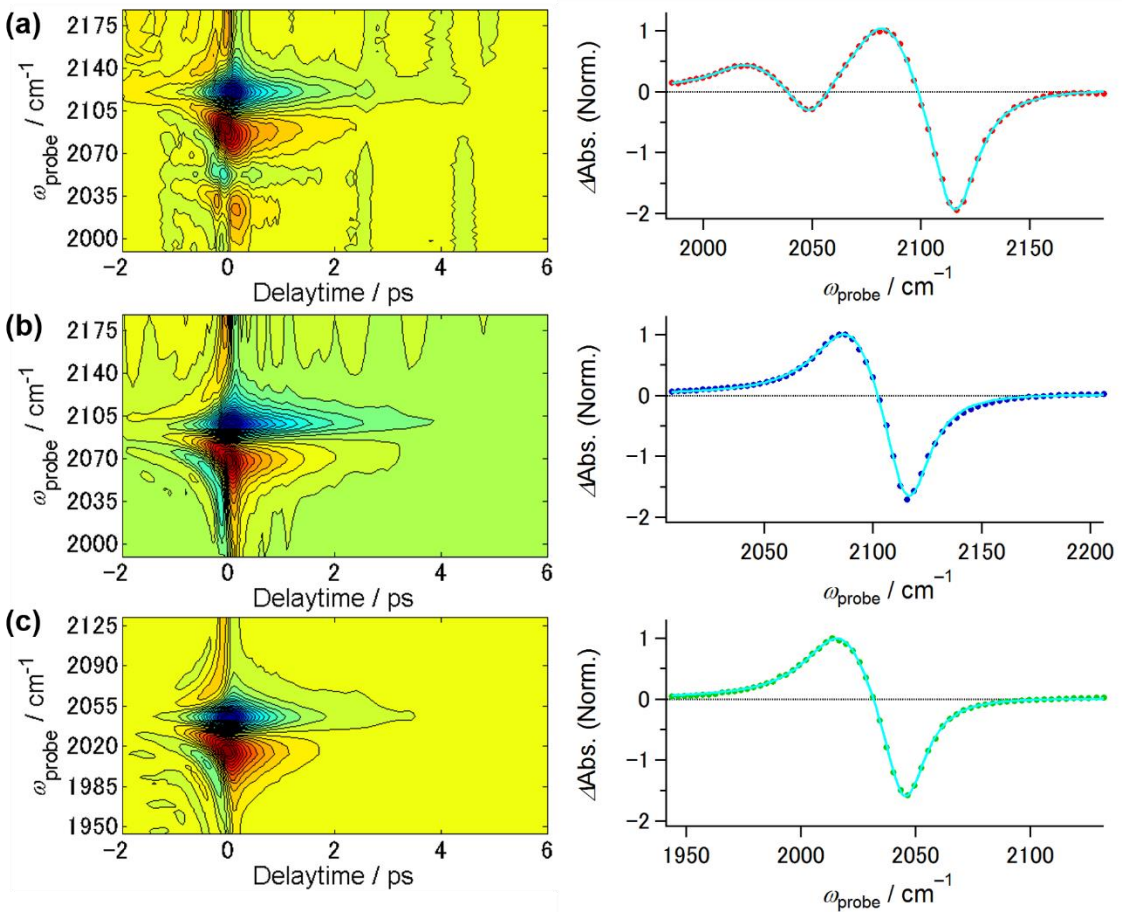

Figure 6.3. Frequency-resolved IR pump-probe signals of (a) N_3-Ala, (b) N_3-Pro, and (c) N_3^- in H_2O. (d) Difference absorption spectra of N_3-Ala (red) and N_3-Pro (blue) at T = 0.4 ps and N_3^- (green) at T = 0.5 ps in H_2O. Close circles indicate the experimental results. The light-blue lines represent fits to a sum of four Lorentzian functions for N_3-Ala and a sum of two Lorentzian functions for N_3-Pro and N_3^-.

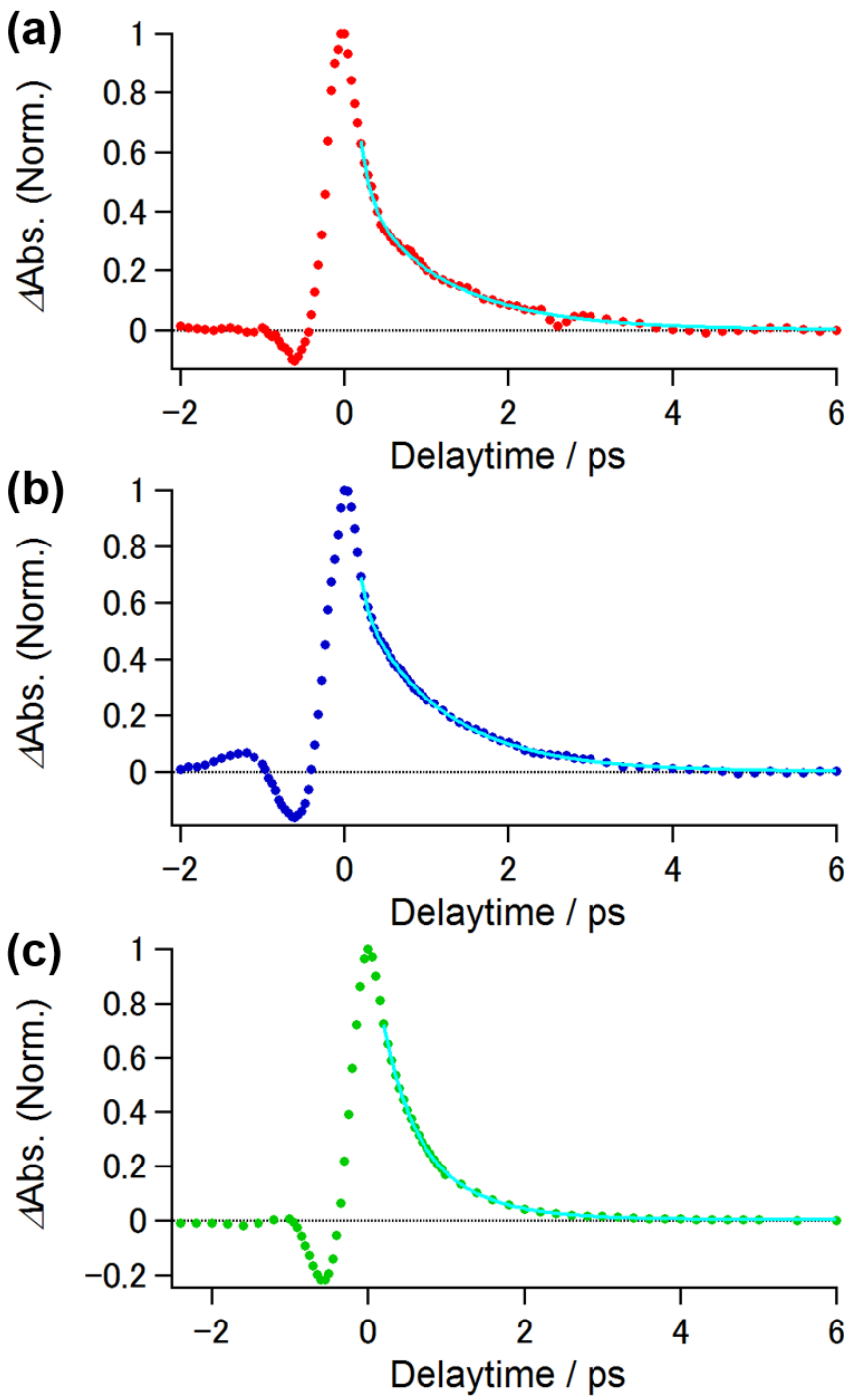

Figure 6.4. Temporal profiles of the IR pump-probe signals taken from the peak wavenumbers of the TA signal of (a) N_3-Ala, (b) N_3-Pro, and (c) N_3^- in H_2O. Close circles are the experimental results. The light-blue lines represent the fits to a single exponential functions for N_3^- and a double exponential function for N_3-Ala and N_3-Pro.

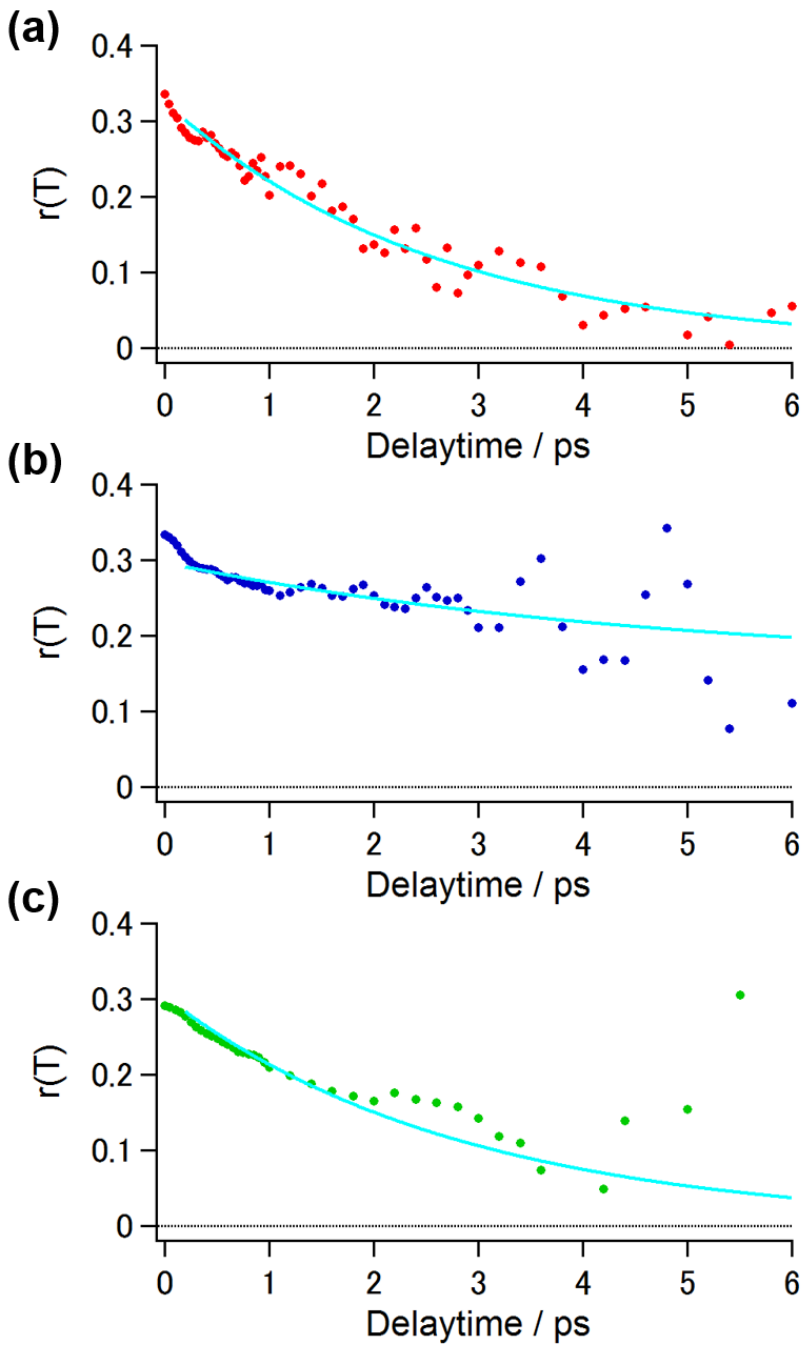

Figure 6.5. Time-resolved anisotropy decays of (a) N_3-Ala, (b) N_3-Pro, and (c) N_3^- in H_2O. Close circles represent the experimental results. The light-blue lines correspond to the fitting results to a single exponential plus a constant.

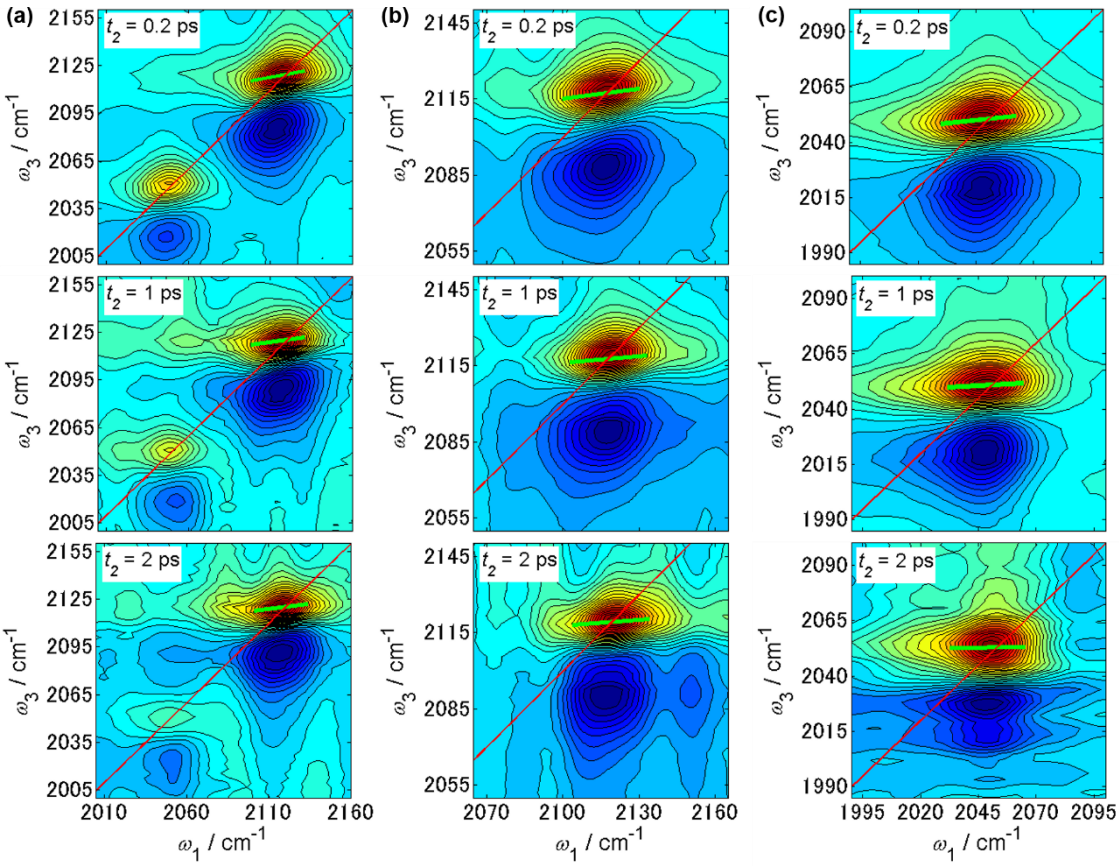

Figure 6.6. 2D-IR spectra of (a) N_3-Ala, (b) N_3-Pro, and (c) N_3^- in H_2O at T = (top) 0.2 ps, (middle) 1 ps, and (bottom) 2 ps. Red lines in the 2D-IR spectra are the diagonal direction ($\omega_1 = \omega_3$) of the 2D-IR spectra. Green lines depict the center lines of the 2D-IR signals, whose slope provide the CLS.

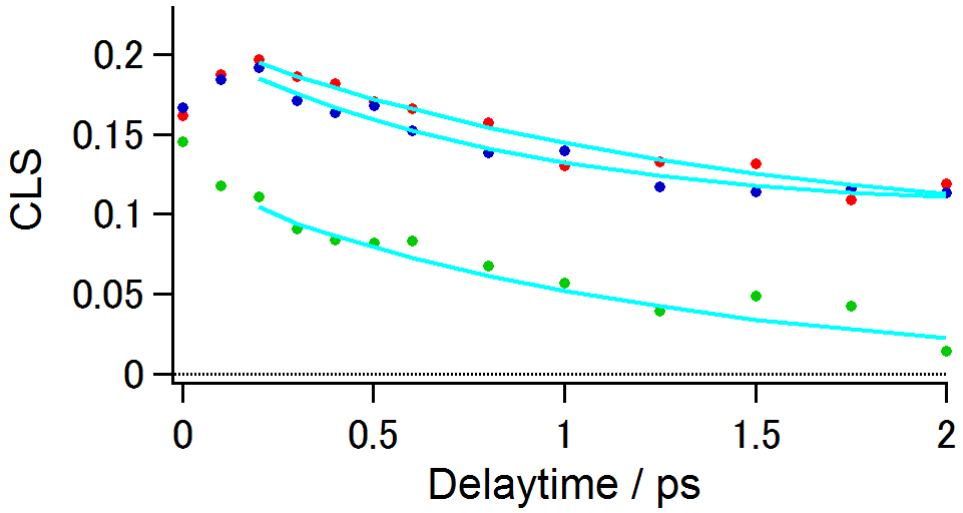

Figure 6.7. CLS decay curves of N_3-Ala (red), N_3-Pro (blue), and N_3^- (green). The closed circles indicate the experimentally obtained CLSs, and the light-blue lines are the numerically calculated ones using the optimized FFTCF parameters listed in Table 6.4.

Table 6.1. The parameters of normalized IR absorption spectra of the N_3 anti-symmetric stretching mode of N_3-Ala, N_3-Pro, and N_3^- in H_2O and summary of DFT calculations in the gas phase.

Solute	Linear IR Absorption[(a)]		Normal Mode Analysis[(b)]				Mulliken Charge[(c)]		
	ω_{max} / cm^{-1}	FWHM / cm^{-1}	ω_0 / cm^{-1}	IR Intensity / km mol^{-1}	μ / amu	k / mDyne Å^{-1}	$Q_{N(1)}$ / e	$Q_{N(2)}$ / e	$Q_{N(3)}$ / e
N_3-Ala	2116.3	31.3	2219.21	621.91	13.62	39.52	−0.80	0.89	−0.63
N_3-Pro	2115.8	27.2	2220.42	892.99	13.68	39.75	−0.78	1.06	−0.72
N_3^-	2046.5	25.6	2079.94	1274.91	14.00	35.69	−0.76	0.52	−0.72

(a) ω_{max}: wavenumber at band peak, FWHM: full width at half maximum.

(b) ω_0: normal mode frequency of the N_3 anti-symmetric stretching mode, μ: reduced mass, k : force constant.

(c) $Q_{N(i)}$: partial charge on ith nitrogen atom in the N_3 group. N(1) ; covalently bonded nitrogen atom, N(2) ; middle nitrogen atom, N(3) ; terminal nitrogen atom.

Table 6.2. Parameters of normalized IR absorption spectra of the N_3 anti-symmetric stretching mode of N_3-Ala, N_3-Pro, and N_3^- in H_2O.

Solute	A_1	$\omega_{max,1}$ / cm^{-1}	$\Delta\omega_1$ / cm^{-1}	A_2	$\omega_{max,2}$ / cm^{-1}	$\Delta\omega_2$ / cm^{-1}	A_3	$\omega_{max,3}$ / cm^{-1}	$\Delta\omega_3$ / cm^{-1}
N_3-Ala	0.1 ± 0.1	2047.8 ± 0.1	20.2 ± 0.7	0.8 ± 0.1	2114.7 ± 0.1	29.7 ± 0.1	0.2 ± 0.1	2127.2 ± 0.1	79.3 ± 0.6
N_3-Pro	0.2 ± 0.1	2115.8 ± 0.1	22.2 ± 0.1	0.8 ± 0.1	2125.2 ± 0.1	47.8 ± 0.1	—	—	—
N_3^-	1.0 ± 0.1	2046.5 ± 0.1	25.6 ± 0.1	—	—	—	—	—	—

A_i : Intensity at band peak of ith component, $\omega_{max,i}$: peak wavenumber of ith component, $\Delta\omega_i$: FWHM of ith component.

Table 6.3. Parameters of population relaxation and anisotropy decay of the N_3 anti-symmetric stretching mode of N_3-Ala, N_3-Pro, and N_3^- in H_2O.

Solute	Population Relaxation[(a)]					Anisotropy Decay[(b)]		
	A_1	T_{11} / ps	A_2	T_{12} / ps	Δ / cm^{-1}	A_∞	A_0	T_R / ps
N_3-Ala	0.9 ± 0.1	0.1 ± 0.1	0.5 ± 0.1	1.1 ± 0.1	29.1	0 ± 0.1	0.3 ± 0.1	2.6 ± 0.4
N_3-Pro	0.8 ± 0.2	0.1 ± 0.1	0.7 ± 0.1	1.0 ± 0.1	25.6	0.2 ± 0.1	0.1 ± 0.1	4.8 ± 2.6
N_3^-	1.0 ± 0.1	0.6 ± 0.1	—	—	27.0	0 ± 0.1	0.3 ± 0.1	2.8 ± 0.7

(a) T_{11}, T_{12} : time constants in the fitting function ; $A_1\exp(-T/T_{11}) + A_2\exp(-T/T_{12})$.

Δ: anharmonicity of the N_3 anti-symmetric stretching mode.

(b) A_∞ : constant component in the fitting function ; $A_\infty + A_0\exp(-T/T_R)$.

Table 6.4. Parameters of the FFTCF for N_3-Ala, N_3-Pro, and N_3^- in H_2O

Solute	T_2^* / ps	Δ_C / ps^{-1}	τ_C / ps	Δ_0 / ps^{-1}
N_3-Ala	0.7	1.0	1.5	0.8
N_3-Pro	1.2	1.0	1.0	0.6
N_3^-	1.0	1.0	1.3	0.1

The uncertainty of the time constant τ_C is estimated to be about 20%, and the other parameters are within a few percent.

Appendix 6.A. Numerical Calculation for Multi-component Absorption Spectrum

If there is a chemical exchange process between the $\omega_{\mathrm{N3,low}}$ and $\omega_{\mathrm{N3,high}}$ bands, cross-peak signals will be observed in the off-diagonal directions of the 2D-IR spectra at longer population times. However, as shown in Figure 6.6, because clear cross-peak signals did not appear in the 2D-IR spectra of N_3-Ala and N_3-Pro within 2 ps, the chemical exchange process between two transitions may proceed slower than the observation time. Therefore, the contribution from the chemical exchange was not taken into account for the simulations of the 2D-IR spectra mentioned below.

Following the procedure of Fenn and Fayer [55], the linear absorption spectra and the 2D-IR spectra of the $\omega_{\mathrm{N3,low}}$ and $\omega_{\mathrm{N3,high}}$ modes of N_3-Ala and N_3-Pro were calculated as follows:

$$I_{\mathrm{tot,linear}}(\omega_1) = a_1 I_{1,\mathrm{linear}}(\omega_1) + (1-a_1) I_{2,\mathrm{linear}}(\omega_1) = S_{1,\mathrm{linear}}(\omega_1) + S_{2,\mathrm{linear}}(\omega_1) \tag{6.A.1}$$

$$S_{\mathrm{tot,2D\text{-}IR}}(\omega_1, t_2, \omega_3) = f_1(\omega_1) S_{1,\mathrm{2D\text{-}IR}}(\omega_1, t_2, \omega_3) + (1 - f_1(\omega_1)) S_{2,\mathrm{2D\text{-}IR}}(\omega_1, t_2, \omega_3) \tag{6.A.2}$$

where $I_{i,\mathrm{linear}}(\omega_1)$ and $S_{i,\mathrm{2D\text{-}IR}}(\omega_1, t_2, \omega_3)$ are the ith component of the linear absorption spectrum and 2D-IR spectrum, respectively, and a_1 is a weighting factor for component 1. The term $f_1(\omega_1)$ in Eq. (6.A.2) was defined as:

$$f_1(\omega_1) \equiv \frac{S_{1,\mathrm{linear}}(\omega_1)}{S_{1,\mathrm{linear}}(\omega_1) + S_{2,\mathrm{linear}}(\omega_1)} \tag{6.A.3}$$

where $S_{i,\mathrm{linear}}(\omega_1)$ is the ith linear absorption spectrum in Eq. (6.A.1). In these simulations, the values of A_2 and A_1 given in Table 6.2 were used as those of the a_1's for N_3-Ala and N_3-Pro, respectively. By assuming that the VER and anisotropy decay of the N_3 anti-symmetric stretching mode do not significantly depend on the probe wavenumber in the IR pump-probe measurement, the T_{12} and T_R of the $\omega_{\mathrm{N3,high}}$ band (Table 6.3) were used as the VER and rotational relaxation time constants of the $\nu_{\mathrm{N3,low}}$ band. Moreover, the FFTCF of the $\omega_{\mathrm{N3,high}}$ is assumed to be represented by Eq. (6.3). During the CLS analysis, the FFTCF parameters of the $\omega_{\mathrm{N3,low}}$ band were fixed at those given in Table 6.4. On the other hand, the FFTCF parameters of $\omega_{\mathrm{N3,high}}$ band were determined to reproduce the lineshape of the $\omega_{\mathrm{N3,high}}$ band, which is shown in Figure 6.2. Note that, to investigate the dependence of the results on the FFTCF parameters of the $\omega_{\mathrm{N3,high}}$ band, three individual simulations were conducted with different sets of the $\omega_{\mathrm{N3,high}}$-FFTCF parameters. The parameters of $\omega_{\mathrm{N3,high}}$ band used in the simulations are given in Table 6.A.1.

Figure 6.A.1 displays the linear absorption spectra of the $\omega_{N3,low}$ and $\omega_{N3,high}$ modes of N_3-Ala and N_3-Pro simulated with respect to each set of the $\omega_{N3,high}$-FFTCF parameters. As shown in Figure 6.A.1, the experimental absorption spectra of N_3-Ala and N_3-Pro were well reproduced by a sum of the $\omega_{N3,low}$ and $\omega_{N3,high}$ bands. Figure 6.A.2 and 6.A.3 present the 2D-IR spectra simulated at t_2 = 0.2 ps and 1 ps of N_3-Ala and N_3-Pro, respectively. Figure 6.A.4 describes the CLSs of N_3-Ala and N_3-Pro obtained from the 2D-IR spectra of the $\omega_{N3,low}$, $\omega_{N3,high}$, and whole (*i.e.* $\omega_{N3,low}$ + $\omega_{N3,high}$) bands. As shown in Figure 6.A.4, the CLS for whole band was similar to that for $\omega_{N3,low}$ band. Moreover, the simulated CLSs showed the weak dependence on the $\omega_{N3,high}$-FFTCF parameters. To observe the contribution from the 2D-IR spectra of the $\omega_{N3,high}$ band to that of the whole band, the slices of their 2D-IR spectra were taken from the two different ω_1 frequencies, which are indicated by the dotted black lines in Figure 6.A.2 and 6.A.3. Figure 6.A.5 and 6.A.6 display the slices of the 2D-IR spectra at t_2 = 0.2 ps and 1 ps of N_3-Ala and N_3-Pro, respectively. As described in Figure 6.A.5 and 6.A.6, the traces of the $\omega_{N3,low}$ band were dominant components in those of the whole band, which indicates that the 2D-IR spectrum of the whole band is almost characterized by that of the $\omega_{N3,low}$ band. These results may be due to that, in the absorption spectra of the N_3 anti-symmetric stretching modes of N_3-Ala and N_3-Pro, the peak intensity of the $\omega_{N3,low}$ band is about four times larger than that of the $\omega_{N3,high}$ band, and the band width of the $\omega_{N3,high}$ band is broader than that of the $\omega_{N3,low}$ band (see Table 6.2). Therefore, in spite of the presence of the $\omega_{N3,high}$ band, it can be considered that the experimentally obtained CLSs of N_3-Ala and N_3-Pro still represents the FFTCF for the $\omega_{N3,low}$ band.

Figures and Table

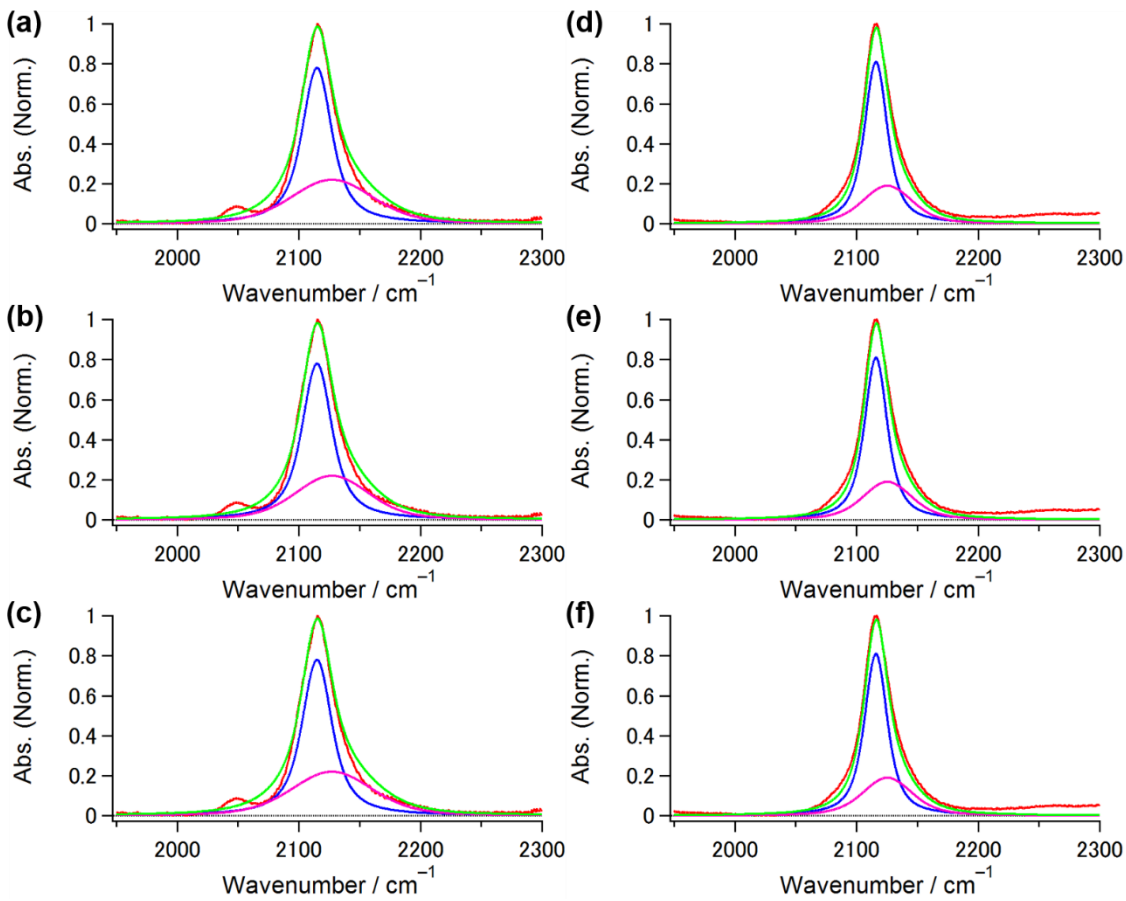

Figure 6.A.1. IR absorption spectra of (a-c) N_3-Ala and (d-f) N_3-Pro in H_2O simulated with (a, d) FFTCF parameters 1, (b, e) FFTCF parameters 2, and (c, f) FFTCF parameters 3 listed in Table 6.A.1. Red line indicates the experimental data. Blue and pink lines are the simulated $\omega_{N3,low}$ and $\omega_{N3,high}$ absorption bands, respectively, and green line corresponds to the sum of the two bands (*i.e.* $\omega_{N3,low}$ absorption band + $\omega_{N3,high}$ absorption band).

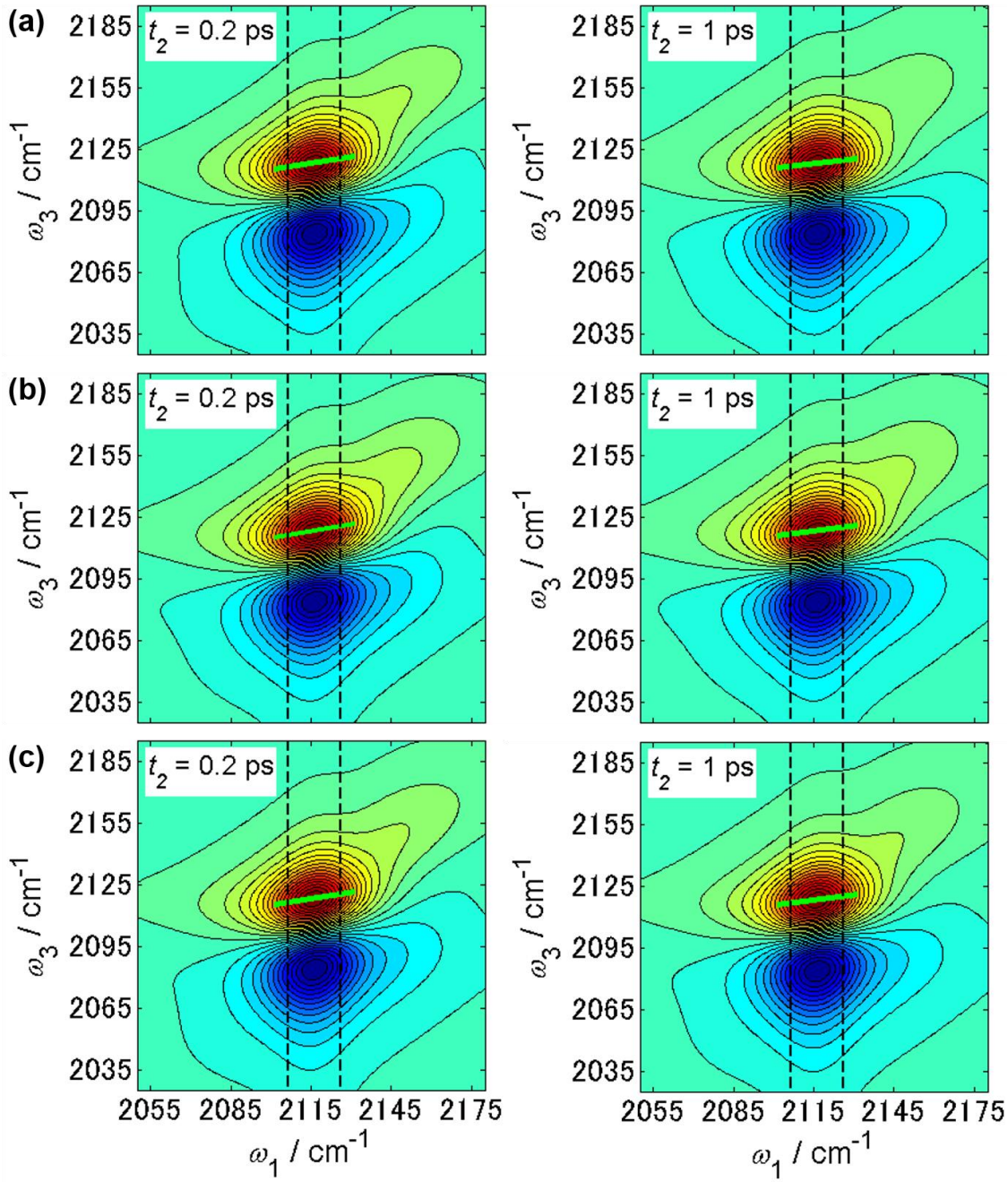

Figure 6.A.2. Simulated 2D-IR spectra of N_3-Ala in H_2O with (a) FFTCF parameters 1, (b) FFTCF parameters 2, and (c) FFTCF parameters 3 given in Table 6.A.1 at T = (left) 0.2 ps and (right) 1 ps. Green lines represent the center lines of the 2D-IR spectra. Dotted black lines indicate the frequencies where slices of the 2D-IR spectrum are taken.

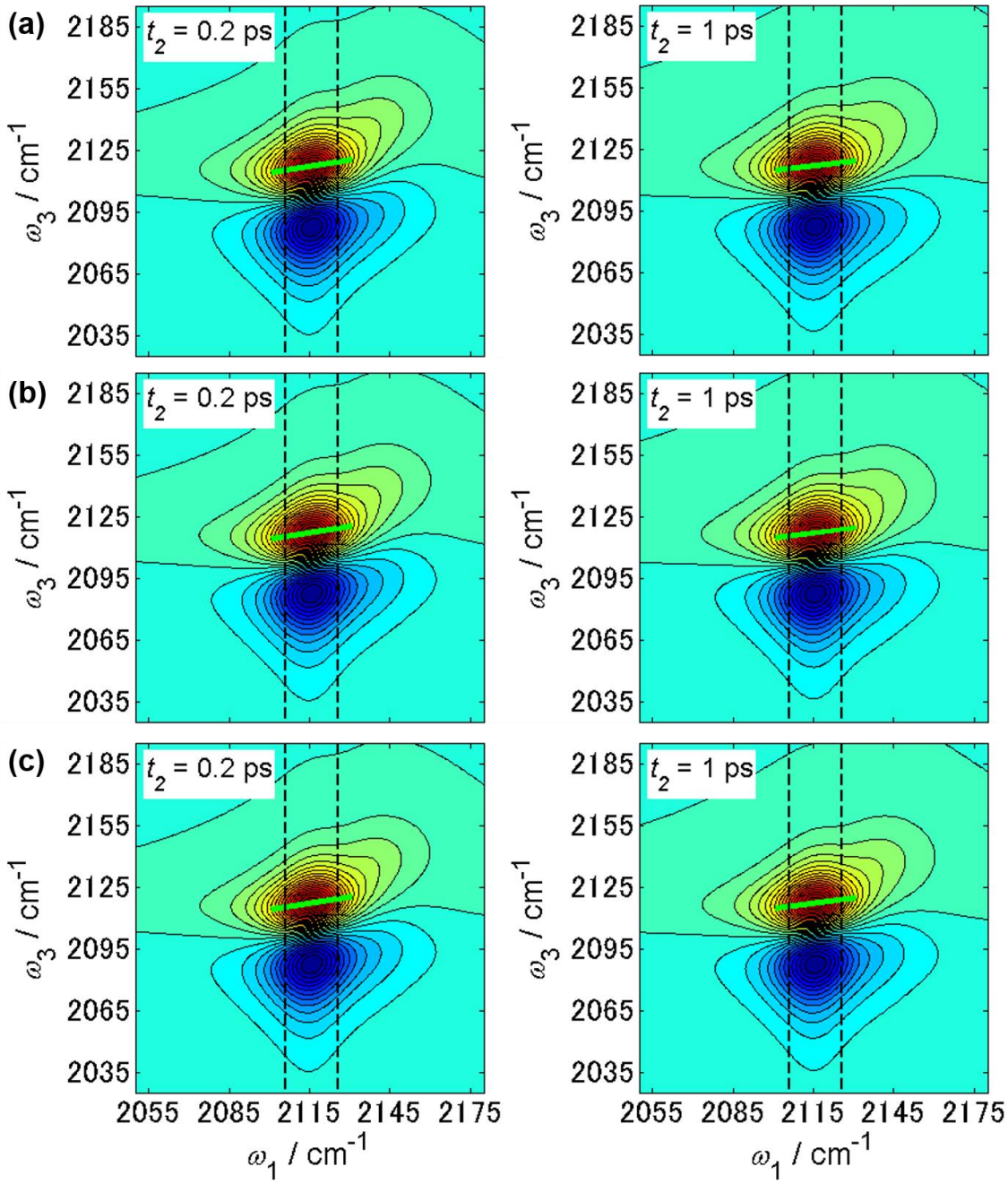

Figure 6.A.3. Same as Figure 6.A.2 except for N_3-Pro in H_2O.

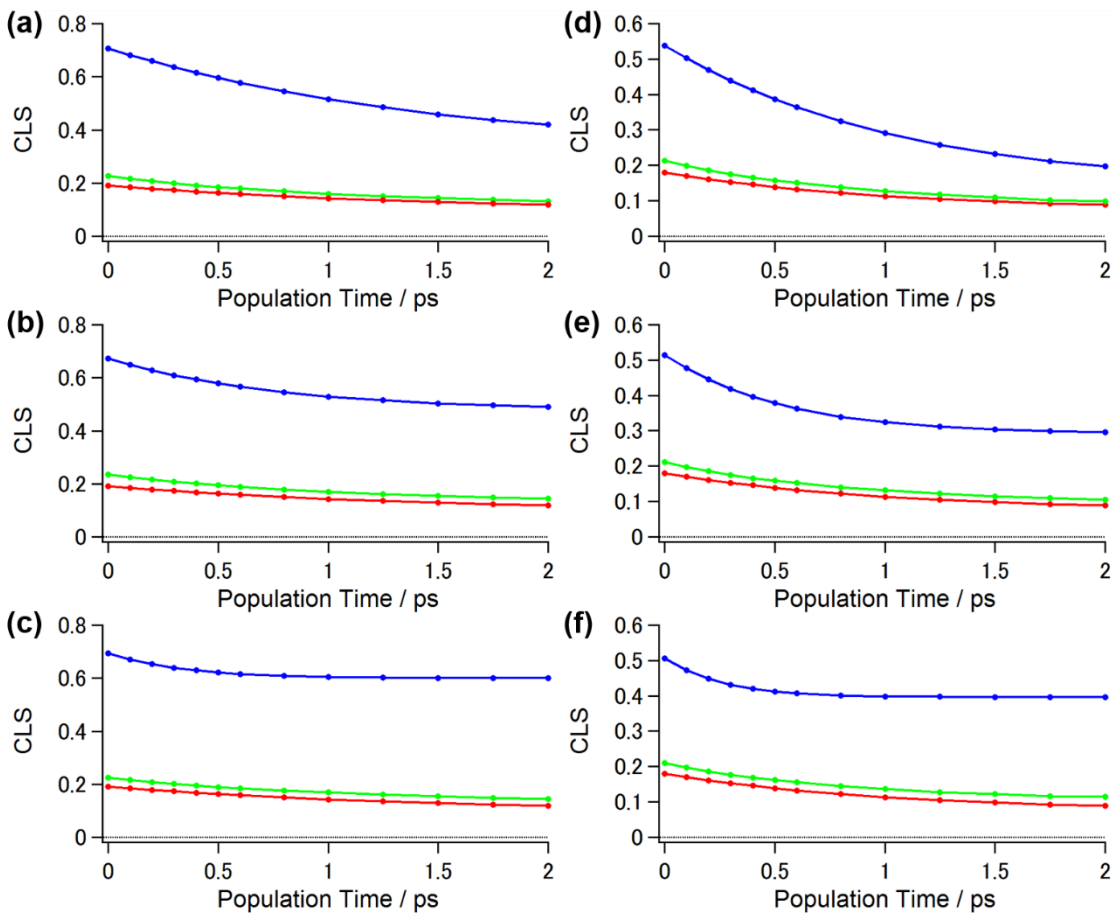

Figure 6.A.4. Simulated CLSs (solid line with close circles) of (a-c) N_3-Ala and (d-f) N_3-Pro simulated with (a) FFTCF parameters 1, (b) FFTCF parameters 2, and (c) FFTCF parameters 3 given in Table 6.A.1. Red and blue close circles indicate the CLSs for $\omega_{N3,low}$ and $\omega_{N3,high}$ absorption bands, respectively, and green ones are the CLS for sum of the two bands.

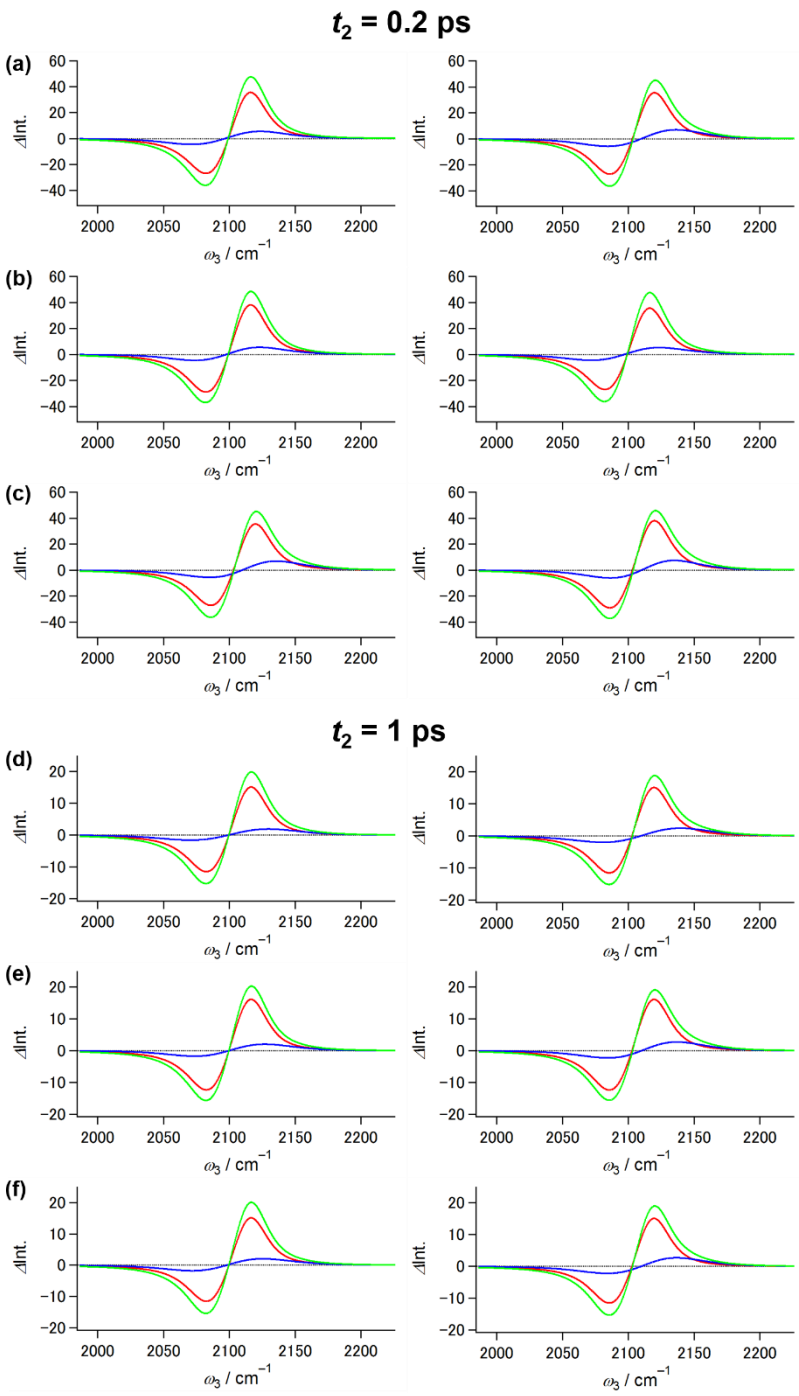

Figure 6.A.5. Slices of the 2D-IR spectra of N_3-Ala in H_2O at T = 0.2 ps and 1 ps simulated with (a, d) FFTCF parameters 1, (b, e) FFTCF parameters 2, and (c, f) FFTCF parameters 3 given in Table 6.A.1 at the (left) lower and (right) higher frequencies indicated by the dotted black lines in Fig. 6.A.2. Red and blue lines indicate the component of $\omega_{N3,low}$ and $\omega_{N3,high}$ band, respectively, and green line is the sum of the two components.

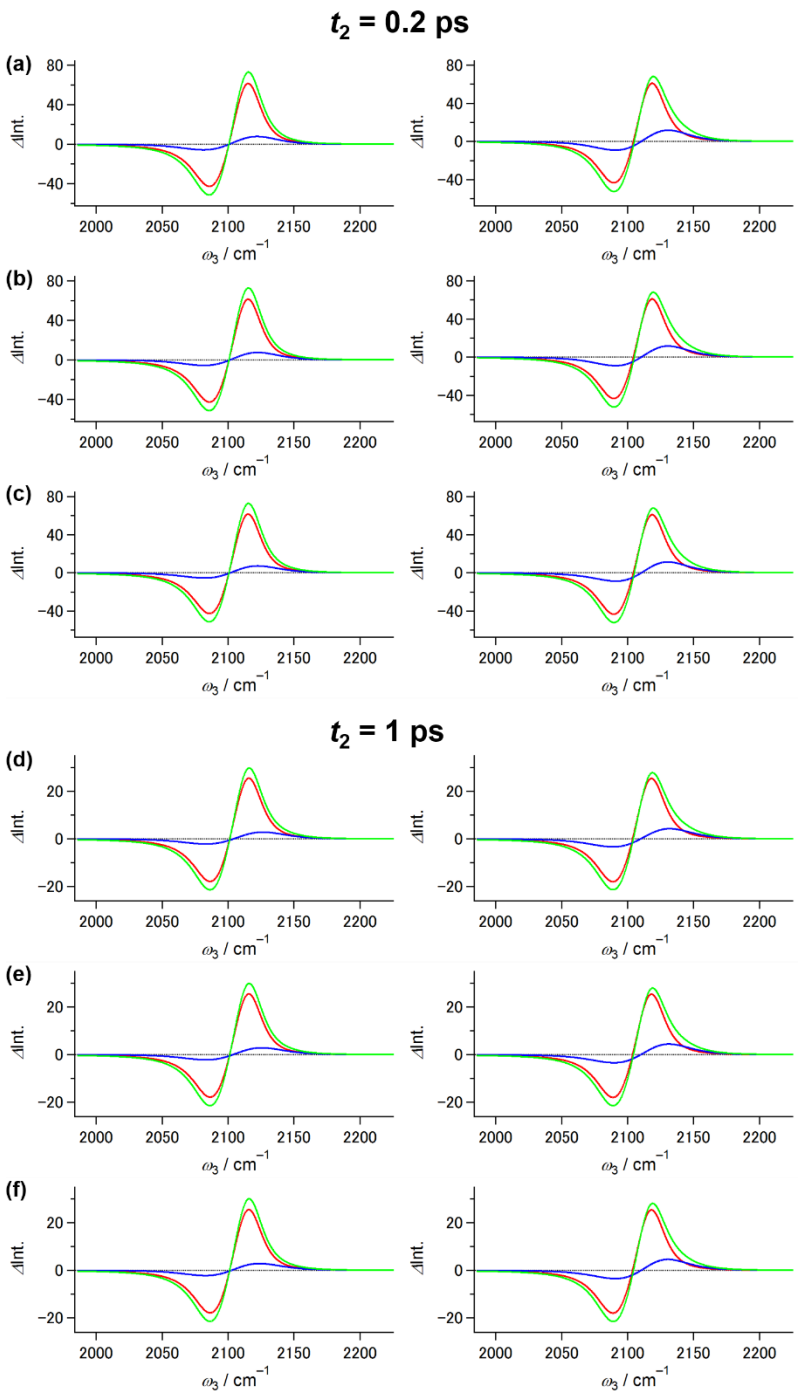

Figure 6.A.6. Same as Figure 6.A.5 except for N_3-Pro in H_2O. These slices of the 2D-IR spectra are taken from Figure 6.A.3.

Table 6.A.1. Parameters in the FFTCF of $\omega_{N3,high}$ absorption band used for the simulation of IR absorption spectra and 2D-IR spectra of N_3-Ala and N_3-Pro in H_2O.

Solute	Parameters	T_2^* / ps	Δ_C / ps^{-1}	τ_C / ps	Δ_0 / ps^{-1}	$\Delta\omega$ / cm^{-1}
	Parameters 1	0.7	4.2	1.5	3.6	79.5
N_3-Ala	Parameters 2	0.7	3.0	0.75	3.9	78.9
	Parameters 3	0.7	3.0	0.325	4.7	78.9
	Parameters 1	1.2	3.1	1.0	1.5	47.7
N_3-Pro	Parameters 2	1.2	2.8	0.5	2.1	47.8
	Parameters 3	1.2	2.8	0.25	2.4	47.8

$\Delta\omega$: full width at the half maximum of the calculated $\omega_{N3,high}$ band.

CHAPTER 7.

Rotational Dynamics of Solutes with Multiple-bond Axes in 1-alcohol Solutions Studied by Infrared Pump-probe Spectroscopy

7.1. Introduction

Conformational dynamics of molecules, such as local orientational motions of functional groups, plays a critical role in chemical processes in condensed phase. It is well known that, for instance, the photoisomerization of a retinal chromophore drives biological signal transportation in living organisms [1-7]. So far, ultrafast spectroscopy in the ultraviolet (UV) to visible region can provide insight into cis-trans photoisomerization of organic molecules and biomolecules [8], such as stilbene [9-11], retinal [3, 12], and azobenzene [13, 14]. In addition, recently, time-resolved infrared (IR) measurements were conducted to investigate the structural dynamics of molecules in solutions as well. Since vibrational transition dipole moments are more localized in a molecule than electronic ones, we can expect that vibrational states are more sensitive to local structural changes than electronic ones. By performing the polarization-controlled IR pump-probe measurement for phenol-*d* in $CHCl_3$, Rezus *et al.* revealed that the internal rotation of the OD group around the CO bond axis proceeds with a time constant of 3.7 ps [15]. Lee *et al*. also performed IR pump-probe measurement for azide-derivatized proline in $CHCl_3$, and found that the internal rotation of the N_3 group is characterized by a time constant about 5 ps [16]. From two-dimensional infrared measurements for 1-fluoro-2-isocyanate-ethane in CCl_4, Zhang *et al*. revealed that the rotational isomerization around carbon-carbon bond axis undergoes with a time constant of 43 ps [17]. In theoretical studies, the cis-trans isomerizations of stilbene and azobenzene were examined by the molecular dynamics (MD) simulations [18-22]. Moreover, several groups studied the trans-gauche isomerization kinetics of *n*-butane by the MD simulations [23-28].

When a molecule possesses many covalent bonds, we can expect that it exhibits a rotational motion around every bond axis. Such multiple rotational motions greatly influence structural dynamics of macromolecules, such as proteins and polymer chains. As mentioned above, extensive experimental and theoretical efforts have been made for the investigation of the rotational dynamics of the solutes around a certain bond axis. However, there are no works to examine the rotational dynamics of a solute with multiple rotational axes in a solution. In Chapter 6, from the polarization-controlled IR pump-probe experiments, I found that the anisotropy of the N_3 anti-symmetric stretching modes of Boc-3-azide-Ala-OH (abbreviated as N_3-Ala) and *N*-Boc-cis-4-azide-L-proline (abbreviated as N_3-Pro) in H_2O show the different decay behavior at longer pump-probe delay time: only for N_3-Pro, the anisotropy decay contains a long-lived component

(*i.e.* A_∞ component in Table 6.3). Based on these results, I consider that the structural difference around the N_3 groups of N_3-Ala and N_3-Pro results in the different rotational dynamics. In this study, in order to obtain more detailed information on relationship between observed anisotropy decay and degree of freedom (*i.e.* structural flexibility) around the N_3 group, I investigated the viscosity- and temperature-dependence of N_3 reorientional motions of three different azide-derivatized amino acids (N_3-AAs). In addition to N_3-Ala and N_3-Pro, *N*-Boc-6-azide-norleucine (dicyclohexylammonium) salt (abbreviated as N_3-Nle) was chosen as a vibrational probe molecule. The molecular structures of the three N_3-AAs are shown in Figure 7.1. As shown in Figure 7.1, the structural flexibility around the N_3 group is different among these three N_3-AAs: while the flexibility of N_3-Nle is the highest due to a longer alkyl chain, that of N_3-Pro is the lowest due to a pyrrolindine ring. Therefore, depending on the molecular structures around the N_3 group, the anisotropy decays of the N_3-AAs may exhibit different viscosity- and temperature-dependence.

7.2. Materials and Methods

The detail of the optical setup for the polarization-controlled IR pump-probe measurements is the same as that described in Chapter 4. The OPA/DFG system generates mid-IR pulses with a pulse duration of about 100 fs, a band width of about 100 cm^{-1}, and a pulse energy of about 3.0 μJ. The center wavenumber of the mid-IR pulse was set to be around 2150 cm^{-1}. In the polarization-controlled IR pump-probe spectroscopy, an isotropic and anisotropic pump-probe signals are obtained as:

$$N(T) = \frac{\Delta A_{//}(T) + 2\Delta A_{\perp}(T)}{3} \tag{7.1}$$

and

$$r(T) = \frac{\Delta A_{//}(T) - \Delta A_{\perp}(T)}{\Delta A_{//}(T) + 2\Delta A_{\perp}(T)} \tag{7.2}$$

, respectively. Here, the $\Delta A_{//}(T)$ and $\Delta A_{\perp}(T)$ are the temporal IR pump-probe signals under the parallel and perpendicular conditions after the vibrational excitation of the N_3 anti-symmetric stretching mode by the IR pump pulse, respectively.

For solutes, N_3-Ala, N_3-Pro, and N_3-Nle were purchased from Sigma-Aldrich (St. Louis, Missouri, United States of America) and used without further purification. For solvents, four

primary 1-alcohols ($CH_3(CH_2)_nOH$, $n = 0 - 3$) were used. Methanol (abbreviated as MeOH, > 99.5%) and ethanol (abbreviated as EtOH, > 99.5%) were purchased from Wako (Osaka, Japan), and 1-propanol (abbreviated as 1-PrOH, > 99.9%) and 1-butanol (abbreviated as 1-BtOH, > 99.8%) from Sigma-Aldrich. The concentrations of the sample solutions were at approximately 300 mM. After passing through disposal membrane filters (diameter size: 0.20 μm, ADVANTEC, Japan), the sample solutions were contained in the optical cell with a pair of CaF_2 windows. The optical path length was set to be 25 μm with a Teflon spacer. The solvent-dependent measurements were conducted under a room temperature (293 K). On the other hand, the temperature- dependent measurements were performed at from 283 K to 333 K for the 1-butanol solutions. It should be noted that the results of solvent- and temperature-dependent measurements for the N_3-AAs in 1-alcohol solutions are shown in Appendix A (IR absorption spectra) and Appendix B (isotropic IR pump-probe signals), unless otherwise specified.

7.3. Results and Discussions

7.3.1. IR Absorption Spectra

Figure 7.2(a) displays the IR absorption spectra of the N_3 anti-symmetric stretching mode of N_3-Pro in MeOH and 1-BtOH. The peak wavenumber and bandwidth of the IR absorption spectrum in MeOH are 2105.9 cm^{-1} and 18.3 cm^{-1}, respectively. Compared to the IR absorption spectrum in MeOH, that in 1-BtOH is shifted slightly toward lower frequency side by 2.4 cm^{-1}. In previous studies, depending on the local electrostatic interactions between the N_3 group and solvents, the N_3 anti-symmetric stretching mode is found to exhibit a vibrational solvatochromic shift [29-32]. Therefore, this frequency shift of N_3-Pro may also result from the vibrational solvatochromic shift. Here, compared to the IR absorption spectrum of N_3-Pro in H_2O, those in 1-alcohol solutions exhibit the red-frequency shifts of approximately 10 cm^{-1}, which may be due to the weaker hydrogen bond (HB) interactions with 1-alcohol molecules [33]. On the other hand, the bandwidth does not depend significantly on the 1-alcohol. Note that, as shown in Figure 7.2(a), the IR absorption spectra of N_3-Pro in alcohol solutions have shoulders at higher frequency sides, which are similar spectral feature to that in H_2O (see Figure 6.2(b)). Same as the case in H_2O, the asymmetrical lineshape may be due to various conformers of N_3-Pro in 1-alcohol solutions.

Figure 7.2(b) shows the temperature-dependent IR absorption spectra of the N_3 anti-symmetric stretching mode of N_3-Pro in 1-BtOH. The peak wavenumber and bandwidth of the IR

absorption spectrum at 283 K are 2103.0 cm^{-1} and 18.3 cm^{-1}, respectively. As shown in Figure 7.2(b), the IR absorption spectrum of N_3-Pro in 1-BtOH does not show significant temperature dependence; as temperature increases, the IR absorption spectrum of N_3-Pro exhibits a slight red-frequency shift and spectral broadening by approximately 1 cm^{-1} and 4 cm^{-1}, respectively. The red-shifting behavior may be due to weakening the strength of solute-solvent HBs [34].

7.3.2. Vibrational Energy Relaxation

Figure 7.3(a) shows the isotropic IR pump-probe signals of the N_3 anti-symmetric stretching mode of N_3-Pro in MeOH measured at the $\nu = 0 - 1$ vibrational transition. The signal exhibits a sharp peak at around $T = 0$ ps, which is attributed to the pulse overlapping effect between pump and probe pulses [35]. Therefore, in order to exclude this contribution, the isotropic pump-probe signals after $T = 0.2$ ps were used for the fitting analyses with a double-exponential function. The solvent dependence of the vibrational energy relaxation (VER) time constants for the N_3-AAs in 1-alcohol solutions is summarized in Table 7.1. From these fitting analyses, I found that the VER time constants of fast and slow decaying components are almost identical for the three N_3-AAs, and that the vibrational lifetimes of them in 1-alcohol solutions are longer than those of N_3-Ala and N_3-Pro in H_2O (see Table 6.3). In the earlier theoretical work on the VER mechanism of the N_3 anti-symmetric stretching mode of N_3^- in water, it was suggested that the VER takes place through the intermolecular and intramolecular vibrational energy transfer [36, 37]. While 1-alcohol molecules used in this study have no characteristic IR absorption bands in around 2100 cm^{-1} region, H_2O molecule is known to possess the broad IR absorption band assigned to the combination band between the HOH bending and librational modes. Therefore, I consider that the intermolecular energy transfer to the combination mode of H_2O molecule leads to the faster VER in H_2O than that in 1-alcohol solutions. Very recently, Son *et al*. reported the VER of the N_3 anti-symmetric stretching mode of HN_3 in MeOH is characterized by a time constant of 5.6 ps [38]. Since the number of the intramolecular vibrational modes of N_3-Pro is greater than that of HN_3, we can expect that various kinds of IVR pathways enhance the VER of the N_3 anti-symmetric mode of N_3-Pro. Moreover, based on the fact that the VER of N_3-Pro does not significantly depend on the 1-alcohol solvents (see Table 7.1), it is suggested that IVR processes may be dominate the VER of N_3-Pro in 1-alcohol solutions.

Figure 7.3(b) displays the isotropic IR pump-probe signals of N_3-Pro in 1-BtOH

measured at 283 K and 333 K. These signals are well reproduced by a double-exponential function. The temperature-dependence of the VER time constants for the N_3-AAs in 1-BtOH is summarized in Table 7.1. The theoretical studies on the VER of solutes in solutions suggests that VER is enhanced owing to the increase of the number of accepting modes at higher temperature [39-42]. Regarding to experimental works, for example, Fayer group revealed that the VER of $W(CO)_6$ and $Cr(CO)_6$ in CCl_4 becomes faster with increasing temperature [43, 44]. However, the VER of N_3-Pro does not show clear temperature dependence (see Table 7.1). As mentioned above, the VER of N_3-Pro in 1-alcohol solutions is expected to be controlled by the IVR processes. Consequently, I consider that, because accepting modes of N_3-Pro may be insensitive to temperature, the VER of N_3-Pro in 1-alcohol solutions is independent of temperature.

7.3.3. Solvent- and Temperature-dependent Anisotropy Decays

Figures 7.4 and 7.5 display the solvent- and temperature-dependent anisotropy decays of the N_3-AAs in 1-alcohol solutions associated with the $\nu = 0 - 1$ vibrational transition, respectively. As shown in Figure 7.4, the anisotropies of the N_3-AAs in 1-alcohol solutions exhibit multiple-exponential decaying behavior. Hence, different from the case in H_2O (see Section 6.3.3), the anisotropy decays of the N_3-AAs in 1-alcohol solutions after T = 0.2 ps are fitted by a double-exponential function:

$$f(T) = A_1 \exp(-T/T_{R1}) + A_2 \exp(-T/T_{R2}) \tag{7.3}$$

where $T_{R1} < T_{R2}$. The obtained fast and slow rotational time constants of T_{R1} and T_{R2} are listed in Table 7.2 (see all of the fitting parameters in Tables 7.3 − 7.5). From the fitting analyses, I found that the anisotropy decays of N_3-Pro in 1-alcohol solutions are characterized by the sub-picosecond decay (minor component, A_1 and T_{R1}) and picosecond decay (major component, A_2 and T_{R2}). Figures 7.6 and 7.7 display the T_{R1} and T_{R2} of the N_3-AAs as a function of viscosity of 1-alcohol solvents (η) and viscosity over temperature (η / T), respectively.

Previously, several groups examined the rotational dynamics of N_3^- in MeOH by IR pump-probe measurements, and reported the overall orientational relaxation times of N_3^- range from 11.0 ps to 12.7 ps [45-47]. Here, based on the Stokes-Einstein-Debye (SED) theory, a rotational relaxation time is proportional to the hydrodynamic volume of a rotating molecule in a solution (see Eq. (7.6)). Therefore, one can expect that the rotational motions of the entire N_3-AAs occur on much longer time scale than that of N_3^-. However, as shown in Figure 7.4, the

anisotropies of the N_3-AAs in 1-alcohol solutions decay faster than that of N_3^- in MeOH observed by Lee *et al*. (see Figure 5(A) in Ref. 47). Consequently, the fast and slow anisotropy decays of the N_3-AAs in 1-alcohol solutions reflect two different types of internal rotational motions involving the N_3 group (the assignment will be discussed later). Therefore, I consider that the contribution of the anisotropy decay induced by the overall reorientations of the N_3-AAs is small. It should be noted that, of course, the rotational motions of the entire N_3-AAs are necessary for the complete randomization of the anisotropy. However, because of the short vibrational lifetimes of the N_3-AAs in 1-alcohol solutions (see Table 7.1), the contribution of such slow dynamics cannot be determined accurately.

In hydrogen-bonding liquids, a solute with hydrogen-bonding site, such as oxygen atom of a carbonyl group, can form HB complexes with solvents. In previous studies, based on the detailed analysis for isotropic IR pump-probe signals, Hirai *et al*. suggested that 9-fluorenone in 1-octanol forms the HB complexes with one and two alcohol molecules [48]. Therefore, the N_3-AAs may also form specific HB complexes between the N_3 group and 1-alcohol molecules. In this case, the T_{R1} and T_{R2} are most likely related to the rotational dynamics of different species, such as hydrogen-bonded and non-hydrogen-bonded N_3-AAs. However, even in an aprotic solvent of dimethyl sulfoxide (DMSO, Sigma Aldrich), the anisotropy decays of N_3-Ala and N_3-Nle (see Figure 7.C) are characterized by fast and slow decaying time constants; 0.80 ps and 15.28 ps for N_3-Ala, and 0.81 ps and 8.11 ps for N_3-Nle. Here, because of the low solubility of N_3-Pro in DMSO, the anisotropy decay of N_3-Pro in DMSO cannot be measured. Consequently, I consider that the fast and slow anisotropy decays reflect different kinds of the internal rotational motions of the N_3-AAs rather than the rotational relaxations of different HB complexes in 1-alcohol solutions.

First, the fast rotational relaxation with the time constant T_1 is discussed. When a restricted orientational motion (*e.g.* internal rotation around a specific bond axis) contributes the rotational relaxation process, the corresponding anisotropy decay shows a multiple-exponential decaying behavior. Such rotational dynamics is often discussed in terms of a wobbling-in-a-cone model [49-52]. Based on the fact that the observed anisotropy decays are characterized by the double-exponential function, the corresponding orientational correlation function ($C_2(T)$) can be related to $r(T)$ in Eq. (7.2) as follows:

$$C_2(T) = \left(1 - P^2\right)\exp\left(-T/T_{\mathrm{in}}\right) + P^2\left(1 - Q^2\right)\exp\left(-T/T_{\mathrm{w1}}\right) + P^2 Q^2 \exp\left(-T/T_{\mathrm{w2}}\right) = \frac{5}{2} r(T) \quad (7.4)$$

where T_{w1} and T_{w2} are the rotational correlation time constants. The derivation of Eq. (7.4) is shown in Appendix 7.D following the method by Tan *et al*. [53]. The P and Q are the order parameters for inertial and diffusive cones, which are related to the semi-angles of the inertial and diffusive cones (θ_{in} and θ_1), respectively. Generally, the order parameter X ($X = P$ or Q) can be characterized by the associated cone half angle (θ_0) by:

$$X = \frac{1}{2}\cos\theta_0\left(1 + \cos\theta_0\right). \quad (7.5)$$

The T_{in} in Eq. (7.4) corresponds to the time constant for the orientational randomization in the inertial cone, which takes place much faster than the experimental time resolution. Therefore, by assuming that the ultrafast randomization finishes within the initial 100 fs, the magnitude of P^2 was determined as: $P^2 = 5/2r(T = 100\ \mathrm{fs})$. Moreover, the $C_2(T)$ exhibits a double-exponential decay on a long pump-probe delay time of $T >> T_{in}$. Consequently, by comparing Eqs. (7.3) and (7.4), the other parameters in Eq. (7.4) (*i.e.* T_{w1}, T_{w2}, and Q^2) can be represented as: $T_{w1} = T_{R1}$, $T_{w2} = T_{R2}$, and $Q^2 = 5A_2/(2P^2)$. The obtained θ_{in} and θ_1 of the N_3-AAs are listed in Table 7.2. As shown in Table 7.2, only the θ_1 shows the solute-dependence. Moreover, while the θ_{in} is independent of the solvent and temperature, the θ_1 slightly depends on the solvent and temperature (for N_3-Nle, the dependence is unclear).

Here, by optimizing the geometries of the N_3-AAs in gas phase with the Gaussian 09 program at B3LYP/6-311++G(3df,2pd) level [54], I found that the angle between the N_3 group and its neighboring carbon atom (*i.e.* θ_{C-N-N}) is close to 120°: 118.0° for N_3-Ala, 116.9° for N_3-Pro, and 117.0° for N_3-Nle. Therefore, if the fast anisotropy decay represents the internal rotational motion of the N_3 group around the CN bond axis, the θ_1 of the N_3-AAs studied here are expected to be around 120°. However, as shown in Table 7.2, this fast rotational diffusion undergoes within narrower angle range. Consequently, I consider that the fast decay component are not associated with the rotational motion of the N_3 group around the CN bond axis. Furthermore, as shown in Figures 7.6(a) and 7.7(a), I elucidated that the viscosity and viscosity-temperature (hereafter, simply, temperature-dependence) dependence of the T_{R1} is almost identical for the three N_3-AAs. This result suggests that the fast anisotropy decay corresponds to the local internal reorientation of the N_3 group in 1-alcohol solutions without interacting with the other intramolecular rotational

motions. It should be noted that the anisotropy decays of N_3-Ala and N_3-Pro in H_2O do not contain the sub-picosecond components (see Section 6.3.3). This is partly due to the smaller contribution of the fast decay component to the anisotropy decay in H_2O. Since the fast anisotropy decays of the N_3-AAs are expected to be strongly affected by the friction from neighboring solvents, it is important to theoretically investigate to what extent solute-solvent interactions (*e.g.* HBs) affect the fast orientational relaxation dynamics of the N_3 group in 1-alcohol solutions.

Next, the slow rotational relaxation with the time constant T_2 is discussed. Unlike the case of the T_{R1}, Figures 7.6(b) and 7.7(b) show that the viscosity- and temperature-dependence of the T_{R2} of the N_3-AAs is clearly different with each other. These results suggest that the molecular structure around the N_3 group is important for its slow reorientational motion in 1-alcohol solutions: as the structural flexibility around a vibrational probe becomes higher, the anisotropy decay proceeds on a shorter time scale, which is qualitatively in good agreement with the results for the anisotropy decays of N_3-Ala and N_3-Pro in H_2O (see Section 6.3.3). Here, by performing the polarization-controlled IR pump-probe measurements for Boc-4-azide-phenylalanine (abbreviated as N_3-Phe, Sigma Aldrich, Figure 7.1(d)) in 1-alcohol solutions, I found that the slower anisotropy decays of N_3-Phe are characterized by longer T_{R2} time constants than those of N_3-Pro (see the results for N_3-Phe in Appendix 7.E). Because both the N_3 groups of N_3-Pro and N_3-Phe are attached to ring structures (see Figure 7.1), we can expect that the degree of the structural flexibility around the N_3 group of N_3-Phe is similar to that of N_3-Pro. However, based on the fact that the T_{R2} time constants of N_3-Pro are shorter than those of N_3-Phe, I consider that the anisotropy decays of the N_3 group of N_3-Pro in 1-alcohol solutions are accelerated by the structural dynamics of the pyrrolindine ring, such as a flip-flop motion and/or the other internal rotational motions.

According to the hydrodynamic theory of the SED theory, the reorientational relaxation time constant of a solute in solution (T_R) can be described as [55-57]:

$$T_R = \frac{V_{\mathrm{eff}}\,\eta}{k_B T} C \tag{7.6}$$

where k_B and T are the Boltzmann constant and the temperature, respectively. The V_{eff} is the effective hydrodynamic volume of the solute in solution. The factor C is the friction coefficient between the solute and neighboring solvents [57]. Under the stick boundary condition where the size of the solute is much larger than that of the solvent, the friction coefficient C is unity. On the

other hand, under the slip boundary condition where the solute has comparable or smaller volume than the solvent, the C ranges between 0 and 1. By using Eq. (7.6) and the viscosity- and temperature-dependence of the rotational relaxation time T_R, we can evaluate the effective hydrodynamic volume V_{eff} of the rotating molecule in the solution. However, owing to the lack of the knowledge on the friction coefficient for the N_3-AAs in each 1-alcohol solution, only the temperature-dependence of the T_{R2} of the N_3-AAs in 1-BtOH was analyzed by the SED theory. From the linear fitting analyses for the temperature-dependence of the T_{R2}, the ratios of the V_{eff} of the N_3 group in 1-BtOH are obtained as $V_{eff,\ N3\text{-}Ala} : V_{eff,\ N3\text{-}Pro} : V_{eff,\ N3\text{-}Nle} = 0.59 : 1 : 0.46$, where the ratio for N_3-Pro is normalized to 1. Here, I assumed that the friction coefficient C was identical for the three N_3-AAs in 1-BtOH. This result indicates that the effective hydrodynamic volume of the N_3 group in 1-BtOH becomes smaller with increasing the structural flexibility around the N_3 group.

In order to discuss the relationship between the reorientational motions of the N_3 group and its adjacent alkyl chain, we consider a free energy potential surface mapped along the two dihedral angles ϕ and θ, whose definitions are given in Figure 7.8(a). Note that, although several CC single-bond rotational motions of the alkyl chain can contribute to the anisotropy decay of the N_3 group of N_3-Nle, for simplicity, we focus only on these two dihedral angles of ϕ and θ. First, we consider that N_3-Ala and N_3-Nle have an almost flat energy surface, as represented in Figure 7.8(b). On this energy surface, as indicated by the blue arrows in Figure 7.8(b), the rotational motions of N_3-Ala and N_3-Nle undergo the random walks, that is, the N_3 group and its neighboring alkyl chain reorient independently. Under such an uncorrelated reorientational motion, as the alkyl chain becomes longer, the temperature-dependence of the anisotropy decay is expected to provide larger hydrodynamic volume of the N_3 group. Moreover, the decaying behavior of the anisotropy decay on a picosecond time scale will depend on the number of the alkyl rotational motions which induce the anisotropy decay of the N_3 group.

Next, we consider the coupled rotational motions. We assume that the energy surfaces of N_3-Ala and N_3-Nle possess characteristic landscapes, as illustrated in Figure 7.8(c). In this case, the reorientational motions along ϕ and θ cannot take place freely, and the rotational dynamics will take place along a specific pathway (pink arrow in Figure 7.8(c)) as if the kinetics were one dimensional dynamics. Under such a correlated reorientational motion, the corresponding hydrodynamic volume of the N_3 group is expected to become smaller. Moreover, since the

rotational dynamics undergoes along the specific pathway, the slow anisotropy decay is characterized by one characteristic time constant of a picosecond time scale. Therefore, based on the results that the effective hydrodynamic volume of the N_3 group becomes smaller with increasing the structural flexibility around the N_3 group and that the anisotropy decays of N_3-Ala and N_3-Nle contain one picosecond decay component, I consider that the reorientational motion of the N_3 group in 1-BtOH is correlated to those of its nearby alkyl chain.

Before closing this section, I should emphasize that it is very important to investigate to what extent the rotational dynamics of a solute with multiple-bond axes are correlated to solvent motions. So far, several theoretical works examined the structural dynamics of solutes from the viewpoints of thermodynamics with free energy potential surfaces [58-60]. However, for a solution, we can expected that the solvation structure temporally evolves in accordance with the structural change of a solute. The solute must feel not only time-averaged but also time-dependent interactions from the surrounding solvents. Moreover, the time-dependent interactions influence the kinetics of the structural isomerization of the solute. Therefore, insight into such dynamical correlation between solute and solvent motions is very important for understanding structural dynamics of macromolecules, such as proteins and polymer chains, in solutions. Theoretical studies with MD simulations will provide valuable information on this question.

7.4. Conclusion

In this chapter, in order to gain insight into the relationship between the experimentally observed anisotropy decay and the structural flexibility around the vibrational probe, I performed the polarization-controlled IR pump-probe measurements for N_3-Ala, N_3-Pro, and N_3-Nle in primary 1-alcohol solutions.

From the IR pump-probe measurements, I found that the anisotropy decays of the N_3-AAs contain three decay components related to inertial motion (< 100 fs), fast (sub-picosecond time scale), and slow reorientational motions (picosecond time scale). As displayed in Figures 7.6(a) and 7.7(a), solvent- and temperature-dependence of the fast decaying time constant T_{R1} is almost identical among the three N_3-AAs. Based on the wobbling-in-a-cone model, I assign the fast relaxation component to the local internal reorientation of the N_3 group in 1-alcohol solutions without interactions from the other intramolecular rotational motions.

On the other hand, the slow time constant T_{R2} exhibits solute-dependence, as illustrated

in Figures 7.6(b) and 7.7(b). Therefore, I consider that this slow relaxation component reflects more global internal reorientation of the N_3 group with interactions from the other intramolecular rotational motions. Based on the SED theory, I estimated the effective hydrodynamic volumes of the N_3 groups of the N_3-AAs in 1-BtOH from the temperature-dependence of the T_{R2}. As a results, I found that the effective hydrodynamic volume becomes smaller with increasing the structural flexibility around the N_3 group. These experimental results indicate that structural flexibility around a vibrational probe plays a key role in the internal rotational motion of the vibrational probe. Moreover, from the discussion with the free energy potential surfaces related to the internal rotational motions of N_3 group and its neighboring alkyl chain (see Figure 7.8), I suggest that the reorientational motion of the N_3 group in 1-BtOH is correlated with that of its nearby alkyl chain.

References

1. S. Filipek, R. E. Stenkamp, D. C. Teller, and K. G. Palczewski, *Annu. Rev. Physiol.*, **65**, 851 (2003).

2. U. Haupts, J. Tittor, and D. Oesterhelt, *Annu. Rev. Biophys. Biomol. Struct.*, **28**, 367 (1999).

(3) O. P. Ernst, D. T. Lodowski, M. Elstner, P. Hegemann, L. S. Brown, H. Kandori, *Chem. Rev.*, **114**, 126 (2014).

4. J. L. Spudich, C. S. Yang, K. H. Jung, and E. N. Spudich, *Annu. Rev. Cell Dev. Biol*., **16**, 365 (2000).

5. E. Racker and W. Stoeckenius, *J. Membr. Biol*., **249**, 662 (1974).

6. B. Schobert and K. Lanyi, *J. Biol. Chem*., **257**, 10306 (1982).

7. J. L. Spudich and R. A. Bogomolni, *Nature*, **312**, 509 (1984).

8. C. Dugave and L. Demange, *Chem. Rev.*, **103**, 2475 (2003).

9. R. M. Hochstrasser, *Pure Appl. Chem.*, **52**, 2683 (1980).

10. D. H. Waldeck, *Chem. Rev.*, **91**, 415 (1991).

11. M. Sumitani, N. Nakashima, and K. Yoshihara, *Chem. Phys. Lett.*, **68**, 255 (1979).

12. S. Tahara, S. Takeuchi, R. A. Yoshizumi, K. Inoue, H. Ohtani, H. Kandori, and T. Tahara, *J. Phys. Chem. Lett.*, **6**, 4481 (2015).

13. H. Rau and E. Lueddecke, *J. Am. Chem. Soc.*, **104**, 1616 (1982).

14. T. Fujino, S. Yu, and T. Tahara, *Bull. Chem. Soc. Jpn.*, **75**, 1031 (2002).

15. Y. L. Rezus, D. Madsen, and H. J. Bakker, *J. Chem. Phys.*, **121**, 10599 (2004).

16. K. -K. Lee, K. -H. Park, C. Joo, H. -J. Kwon, H. Han, J. -H. Ha, S. Park, and M. Cho, *Chem. Phys.*, **396**, 23 (2012).

17. J. Zhang, K. Kwak, J. Xie, and M. D. Fayer, *Science*, **313**, 1951 (2006).

18. C. R. Crecca and A. E. Roitberg, *J. Phys. Chem. A*, **110**, 8188 (2006).

19. T. Cusati, G. Granucci, and M. Persico, *J. Am. Chem. Soc.*, **133**, 5109 (2011).

20. Y. Ootani, K. Satoh, A. Nakayama, T. Noro, and T. Taketsugu, *J. Chem. Phys.*, **131**, 194306 (2009).

21. J. Shao, Y. Lei, Z. Wen, Y. Dou, and Z. Wang, *J. Chem. Phys.*, **129**, 164111 (2008).

22. A. Toniolo, X. Ciminelli, M. Persico, and T. J. Martínez, *J. Chem. Phys.*, **123**, 234308 (2005).

19. G. Gershinsky and E. Pollak, *J. Chem. Phys*, **105**, 4388 (1966).

20. V. D. Vachev and J. H. Frederick, *Chem. Phys. Lett*, **215**, 306 (1993).

21. V. D. Vachev, J. H. Frederick, B. A. Grishanin, V. N. Zadkov, and N. I. Kototeev, *J. Phys. Chem.*, **99**, 5427 (1995).

22. A. J. Neukirch, L. C. Shamberger, E. Abad, B. J. Haycock, H. Wang, J. Ortega, O. V. Prezhdo, and J. P. Lewis, *J. Chem. Theory Comput.*, **10**, 14 (2014).

23. D. Chandler, *J. Chem. Phys.*, **68**, 2959 (1978).

24. T. A. Weber, *J. Chem. Phys*., **69**, 2347 (1978).

25. D. Brown and J. H. R. Clarke, *J. Chem. Phys.*, **92**, 3062 (1990).

26. R. Edberg, D. J. Evans, and G. P. Morriss, *J. Chem. Phys.*, **87**, 5700 (1987).

27. J. Ramirez and M. Laso, *J. Chem. Phys.*, **115**, 7285 (2001).

28. R. O. Rosenberg, B. J. Berne, and D. Chandler, *J. Chem. Phys. Lett.*, **75**, 162 (1980).

29. M. M. Waegele, R. M. Culik, and F. Gai, *J. Phys. Chem. Lett.*, **2**, 2598 (2011).

30. M. Cho, *J. Chem. Phys.*, **130**, 094505 (2009).

31. J. -H. Choi, K. -I. Oh, and M. Cho, *J. Chem. Phys.*, **129**, 174512 (2008).

32. K. -I. Oh, J. -H. Lee, C. Joo, H. Han, and M. Cho, *J. Phys. Chem. B*, **112**, 10352 (2008).

33.J. Tayama, A. Ishihara, M. Banno, K. Ohta, S. Saito, and K. Tominag, *J. Chem. Phys.*, **133**, 014505 (2010).

34. P. Hamm, M. Lim, and R. M. Hochstrasser, *J. Phys. Chem. B*, **102**, 6123 (1998).

35. M. P. Wolfsorndle, R. Baskin, I. Dhawan, and X.H. Londergan, *J. Phys. Chem. B*, **116**, 1172 (2012).

36. A. Morita and S. Kato, *J. Chem. Phys*. **109**, 5511 (1998).

37. S. Li, J. R. Schmidt, and J. L. Skinner, *J. Chem. Phys.*, **125**, 244507 (2006).

38. H. Son, K. -H. Park, K. -W. Kwak, S. Park, and M. Cho, *Chem. Phys.*, **422**, 37 (2013).

39. A. Nitzan, S. Mukamel, and J. Jortner, *J. Chem. Phys.*, 60, 3929 (1974).

40. D. J. Diestler, *J. Chem. Phys.*, **60**, 2692 (1974).

41. S. H. Lin, H. P. Lin, and D. Knittel, *J. Chem. Phys.*, **64**, 441 (1976).

42. S. H. Lin, *J. Chem. Phys.*, **65**, 1053 (1976).

43. A. Tokmakoff, B. Sauter, and M. D. Fayer, *J. Chem. Phys.*, **100**, 9035 (1994).

44. P. Moore, A. Tokmakoff, T. Keyes, and M. D. Fayer, *J. Chem. Phys*, **103**, 3325 (1995).

45. M. Li, J. Owrutsky, M. Sarisky, J. P. Culver, A. Yodh, and R. M. Hochstrasser, *J. Chem. Phys.*, **98**, 5499 (1993).

46. K. Ohta, J. Tayama, and K. Tominaga, *Phys. Chem. Chem. Phys.*, **14**, 10455 (2012).

47. C. Lee, H. Son, and S. Park, *J. Phys. Chem. B*, **120**, 9723 (2016).

48. S. Hirai, M. Banno, K. Ohta, D. K. Palit, and K. Tominaga, *Chem. Phys. Lett.*, **450**, 44 (2007).

49. K. J. Gaffney, I. R. Piletic, and M. D. Fayer, *J. Chem. Phys*., **118**, 2270 (2003).

50. H. -S. Tan, I. R. Piletic, and M. D. Fayer, *J. Chem. Phys*, **122**, 174501 (2005).

51. H. Son, Y. Kown, J. Kim, and S. Park, *J. Phys. Chem. B.*, **117**, 2748 (2013).

52. P. L. Kramer, C. H. Giammanco, and M. D. Fayer, *J. Chem. Phys.*, **142**, 212408 (2015).

53. H. -S. Tan, I. R. Piletic, and M. D. Fayer, *J. CHem. Phys.*, **122**, 174501 (2005).

54. M. J. Frisch *et al*., GAUSSIAN 09 (Revision B.01), Gaussian, Inc., Wallingford, CT (2009).

55. R. S. Moog, M. D. Ediger, S. G. Boxer, and M. D. Fayer, *J. Phys. Chem.*, **86**, 4694 (1982).

56. G. K. Youngren and A. Acrivos, *J. Chem. Phys.*, **63**, 3846 (1975).

57. C. -H. Hu and R. Zwanzig, *J. Chem. Phys.*, **60**, 4354 (1974).

58. C. Lv, L. Zheng, and W. Yang, *J. Chem. Phys.*, **136**, 044103 (2012).

59. C. Lu, X. Li, D. Wu, L. Zheng, And W. Yang, *J. Chem. Theory Compt*, **12**, 41 (2016).

60. Y. I. Yang, J. Zhang, X. Che, L. Yang, and Y. Q. Gai, *J. Chem. Phys.*, **144**, 094105 (2016).

61. B. González, N. Calvar, E. Gómez, and Á. Domínguez, *J. Chem. Thermodynamics*, **39**, 1578 (2007).

62. B. Mokhtarani, A. Sharifi, H. R. Mortaheb, M. Mirzaei, M. Mafi, and F. Sadeghian, *J. Chem. Thermodynamics*, **41**, 1432 (2009).

63. C. G. Bazewicz, M. T. Liskov, K. J. Hines, and S. H. Brewer, *J. Phys. Chem. B*, **117**, 8987 (2013).

Figures and Tables

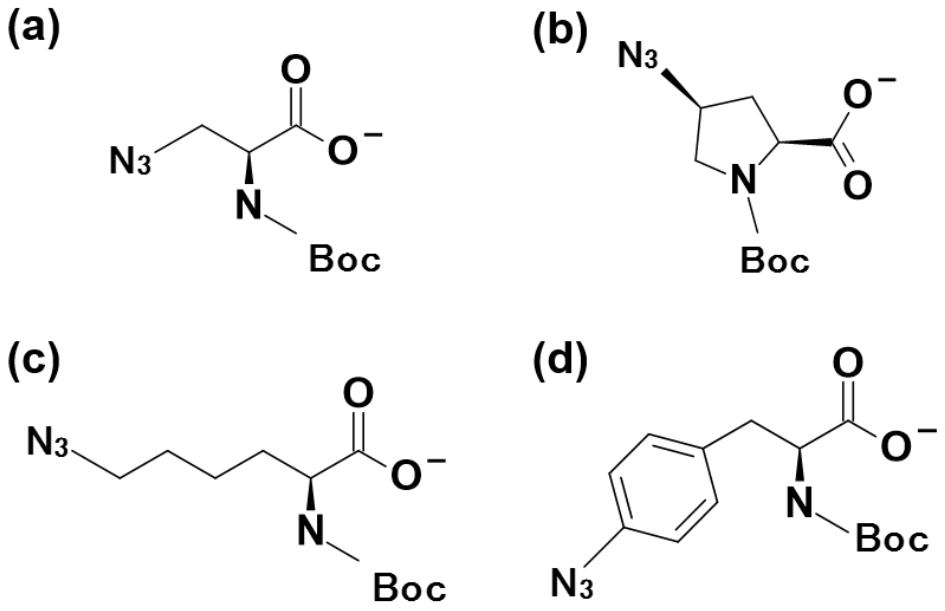

Figure 7.1. The molecular structures of (a) Boc-3-azide-Ala-OH (dicyclohexylammonium) salt and (b) *N*-Boc-cis-4-azide-L-proline **(**dicyclohexylammonium**)** salt, (c) *N*-Boc-6-azide-norleucine (dicyclohexylammonium) salt (abbreviated as N_3-Nle), (d) Boc-4-azide-phenylalanine (abbreviated as N_3-Phe).

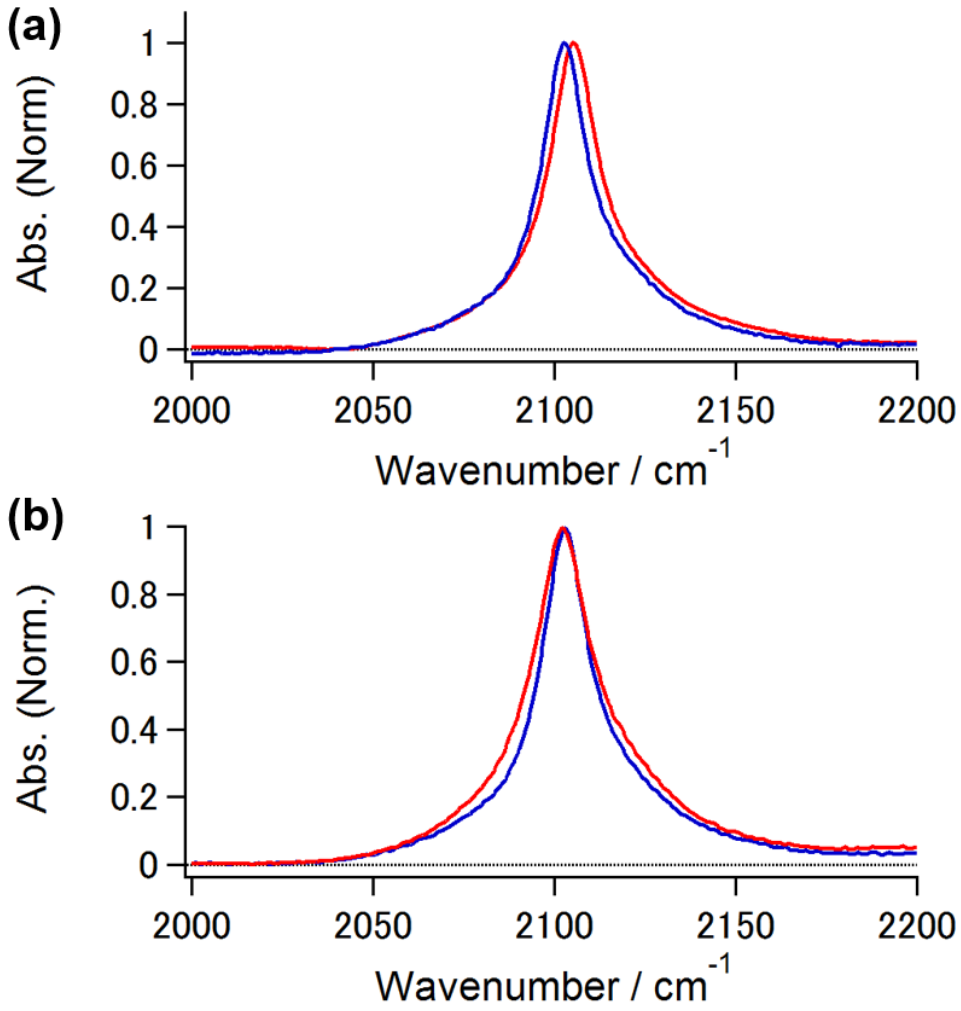

Figure 7.2. (a) IR absorption spectra of the N_3 anti-symmetric stretching mode of N_3-Pro in MeOH (red) and 1-BtOH (blue) measured at 293 K. (b) IR absorption spectra of the N_3 anti-symmetric stretching mode of N_3-Pro in 1-BtOH measured at 283 K (red) and 333 K (blue).

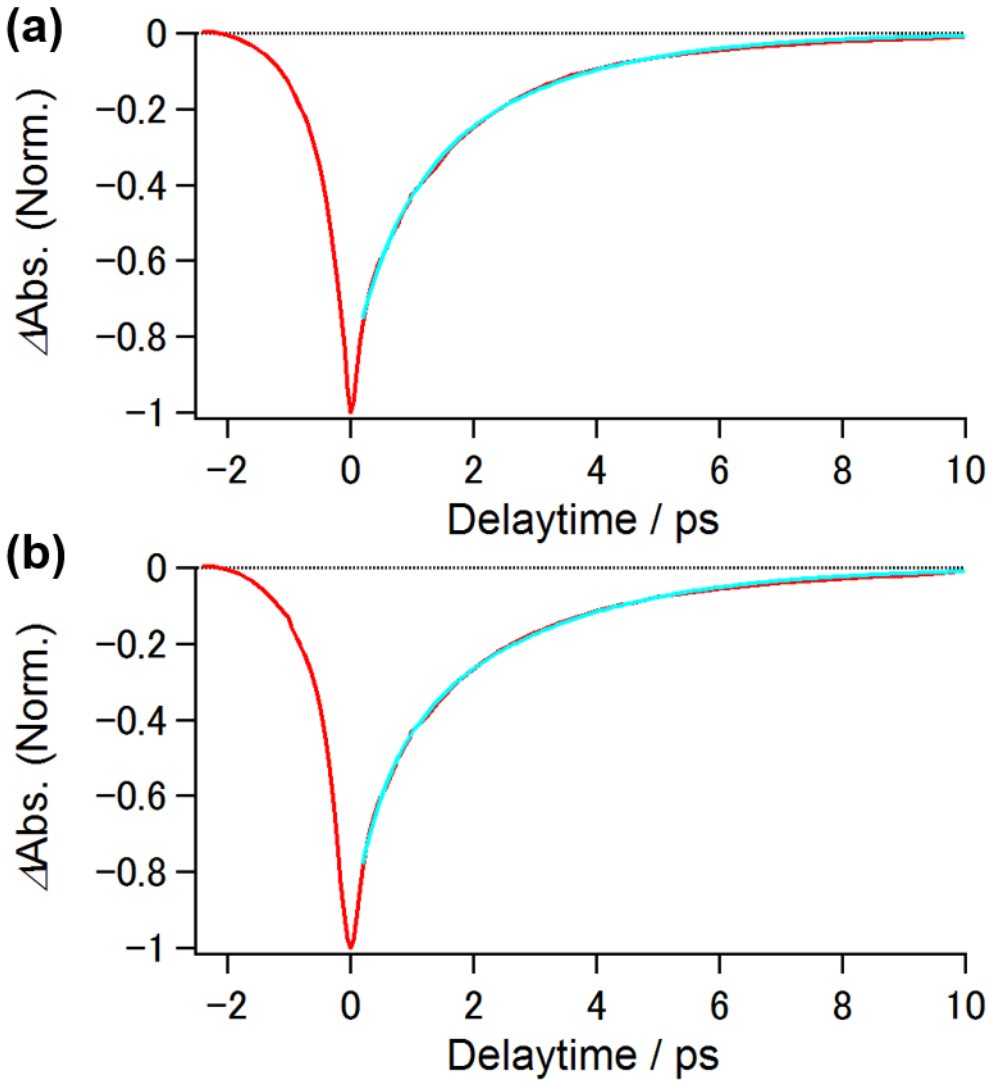

Figure 7.3. (a) Temporal profiles of the isotropic IR pump-probe signals taken from the peak wavenumber of the $\nu = 0 - 1$ vibrational transition of N_3-Pro in MeOH measured at 293 K. (b) Temporal profiles of the isotropic IR pump-probe signals taken from the peak wavenumber of the $\nu = 0 - 1$ vibrational transition of N_3-Pro in 1-BtOH measured at 283 K. The light-blue lines represent the fitting results to double exponential functions.

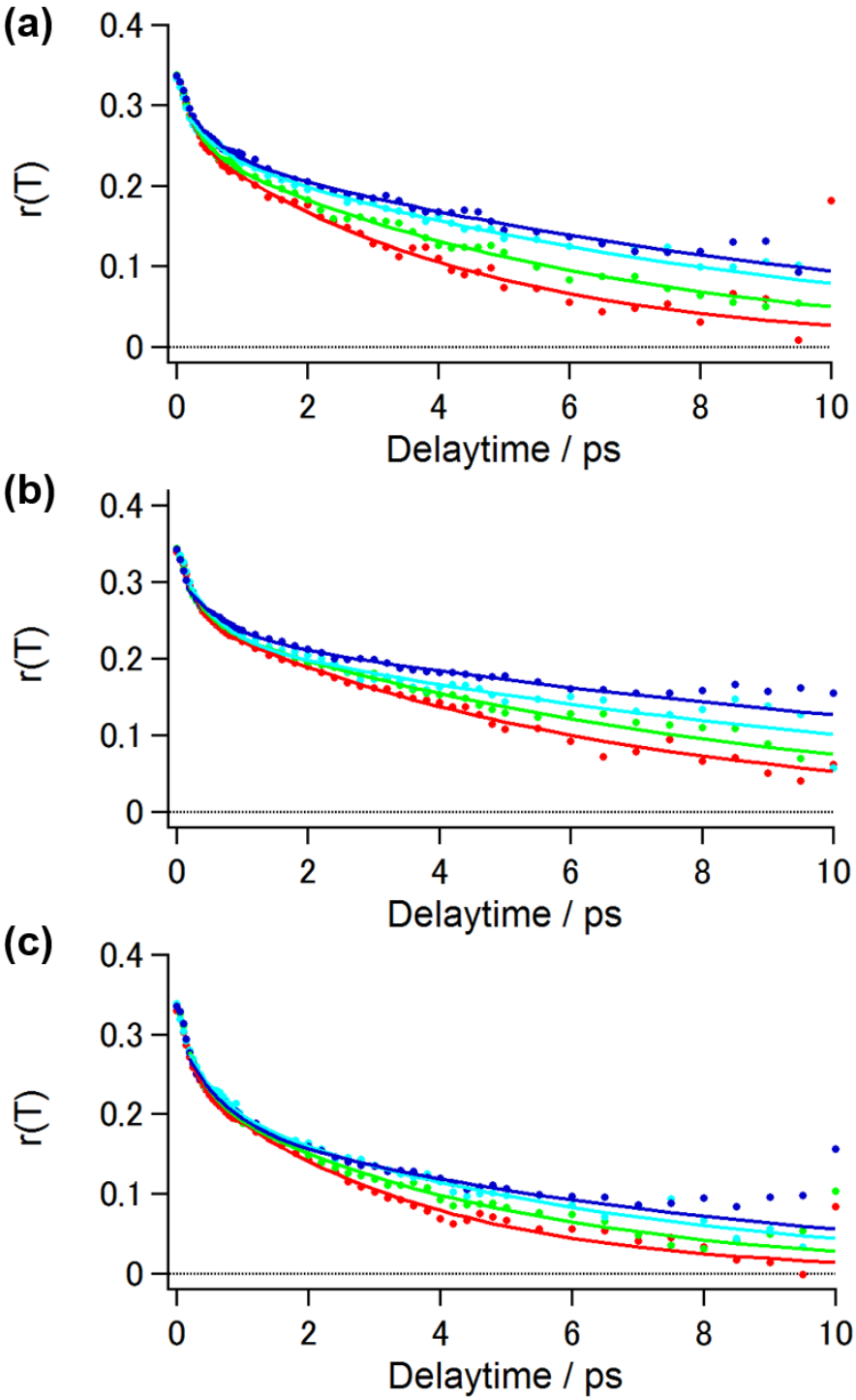

Figure 7.4. (a) Temporal profiles of solvent-dependent anisotropy decays of (a) N_3-Ala, (b) N_3-Pro, and (c) N_3-Nle measured at 293 K. MeOH (red), EtOH (green), 1-PrOH (light-blue), and 1-BtOH (blue). Close circles are the experimental results. The solid lines represent the fitting results to double exponential functions given by Eq. (7.3).

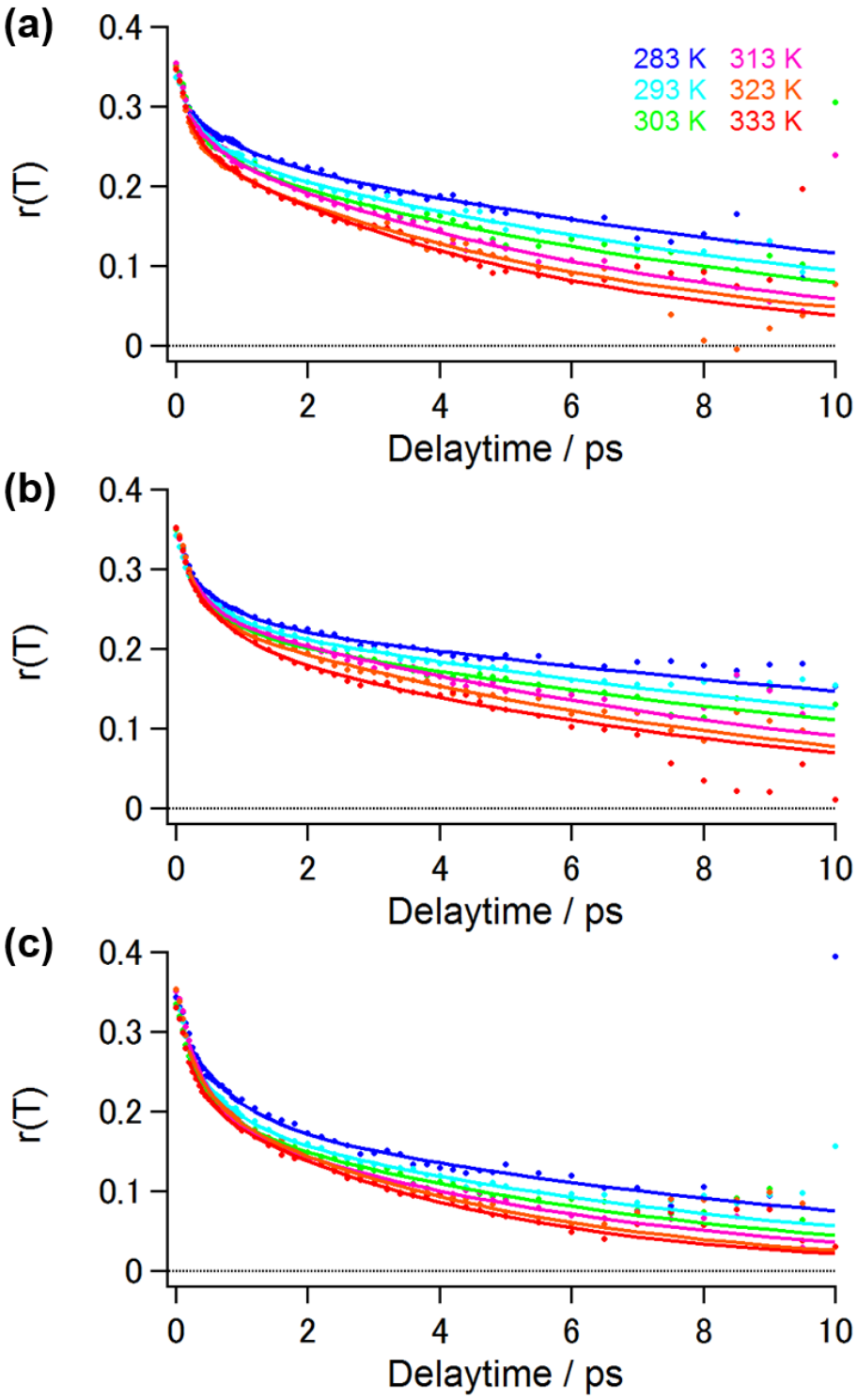

Figure 7.5. (a) Temporal profiles of temperature-dependent anisotropy decays of (a) N_3-Ala, (b) N_3-Pro, (c) N_3-Nle measured in 1-BtOH. Close circles are the experimental results. The solid lines represent the fitting results to double exponential functions given by Eq. (7.3).

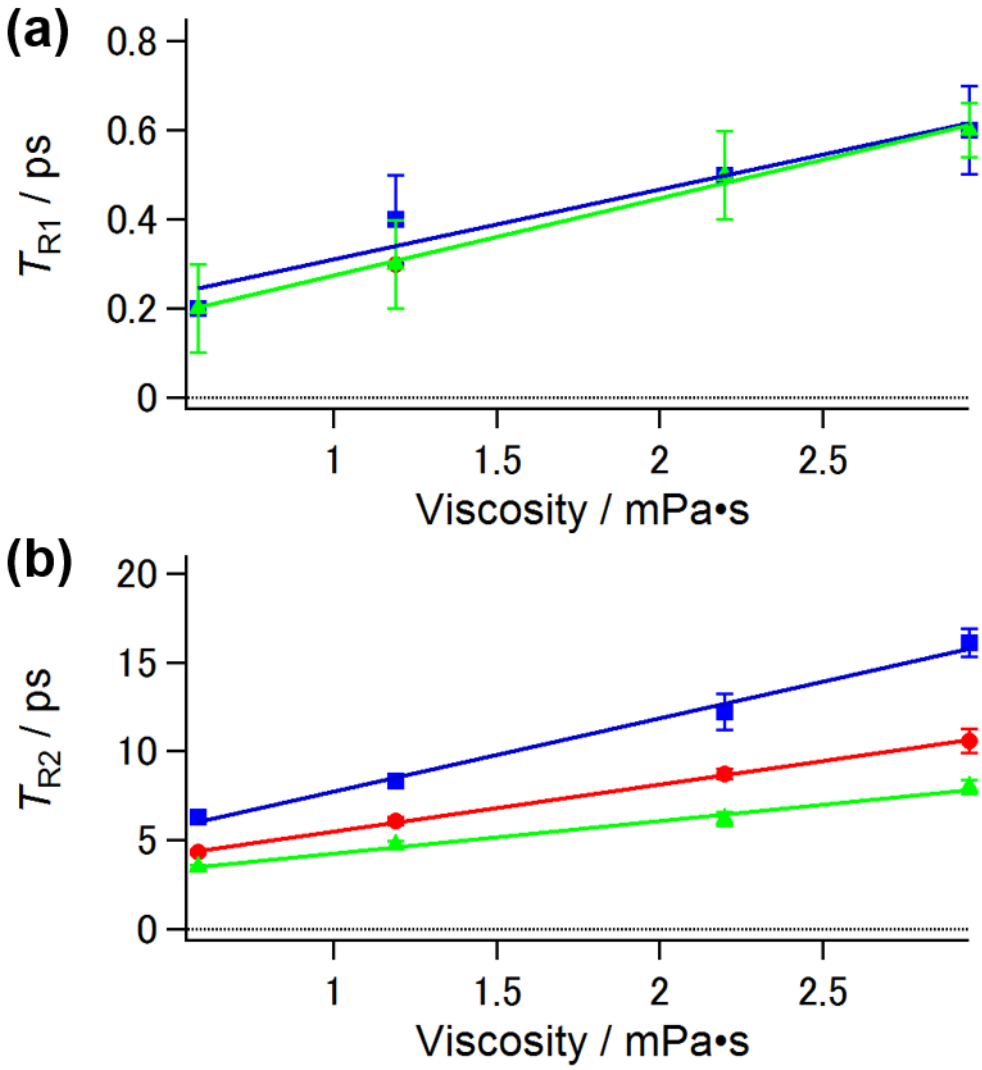

Figure 7.6. Plot of the (a) T_{R1} and (b) T_{R2} of N_3-Ala (red, ●), N_3-Pro (blue, ■), and N_3-Nle (green, ▲) as a function of viscosity of 1-alcohol solvents (η). The viscosity of each 1-alcohol solvents at 293.15 K is as follows: η_{MeOH} = 0.611 mPa・s [61], η_{EtOH} = 1.1617 mPa・s [62], $\eta_{1\text{-}PrOH}$ = 2.4104 mPa・s [62], $\eta_{1\text{-}BtOH}$ = 3.0100 mPa・s [62].

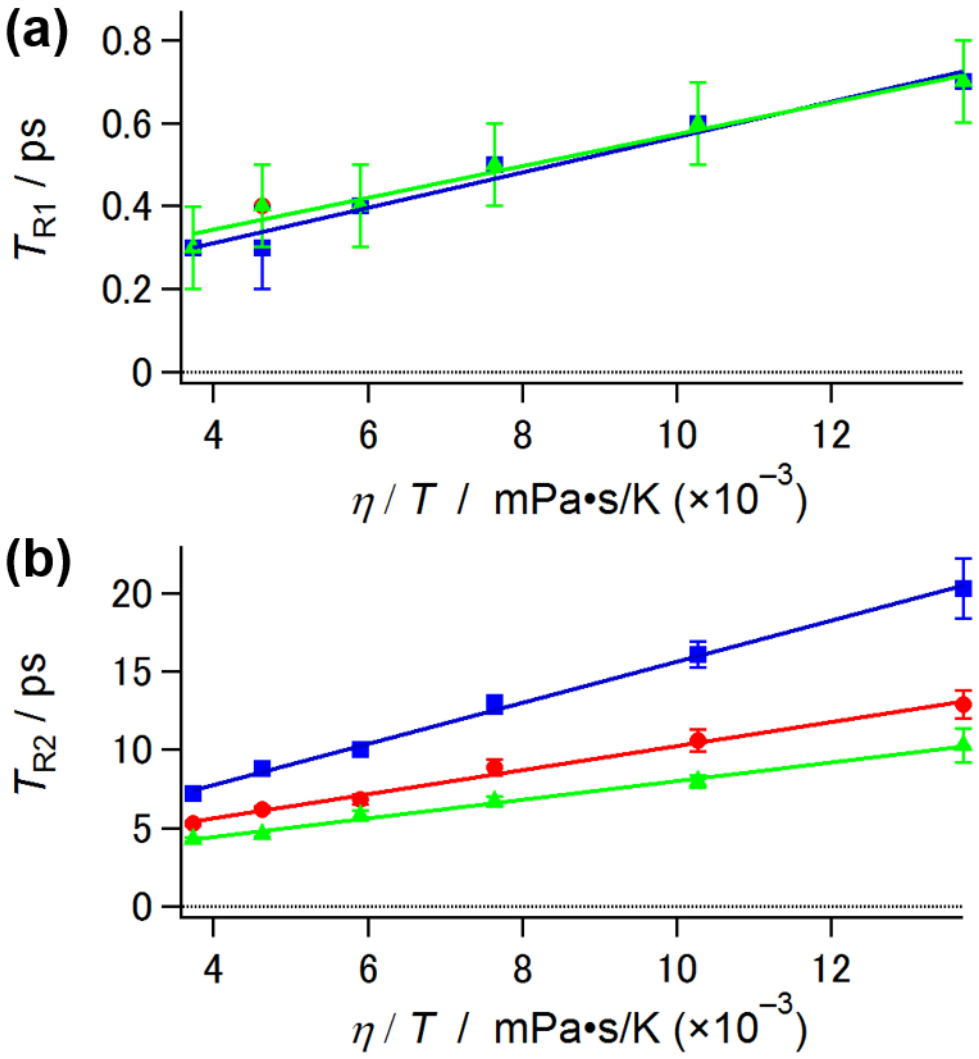

Figure 7.7 Plot of the (a) T_{R1} and (b) T_{R2} of N_3-Ala (red, ●), N_3-Pro (blue, ■), and N_3-Nle (green, ▲) as a function of viscosity over temperature (η / T). The temperature-dependence of the viscosity of 1-BtOH is as follows [62]: $\eta_{1\text{-BtOH, 283 K}}$ = 3.8794 mPa・s, $\eta_{1\text{-BtOH, 293 K}}$ = 3.0100 mPa・s, $\eta_{1\text{-BtOH, 303 K}}$ = 2.3147 mPa・s, $\eta_{1\text{-BtOH, 313 K}}$ = 1.8476 mPa・s, $\eta_{1\text{-BtOH, 323 K}}$ = 1.4952 mPa・s, and $\eta_{1\text{-BtOH, 333 K}}$ = 1.2435 mPa・s.

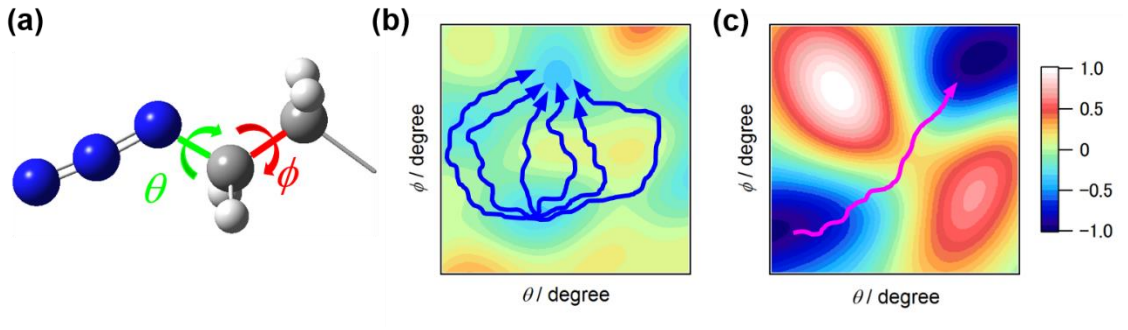

Figure 7.8. Schematic illustration of two-dimensional potential energy surface for reorientational motions of N_3-Ala and N_3-Nle mapped along the two dihedral angles ϕ (a, red) and θ (a, green). (b) Low barrier case and (c) high barrier case. Blue and pink lines represent possible pathways on the energy surface with respect to the reorientational motions around the ϕ and θ (see Section 7.3.3).

Table 7.1. Solvent- and temperature-dependence of parameters to characterize the population relaxation of N_3-Ala, N_3-Pro, and N_3-Nle in primary 1-alcohols. The uncertainty of each parameter is approximately 0.1.

Solvent	N_3-Ala			
	A_1	T_{10} / ps	A_2	T_{20} / ps
MeOH	−0.4	0.3	−0.7	2.5
EtOH	−0.4	0.2	−0.7	2.7
1-PrOH	−0.4	0.2	−0.7	3.0
1-BtOH (283 K)	−0.4	0.2	−1.1	2.7
1-BtOH (293 K)	−0.4	0.2	−0.7	2.9
1-BtOH (303 K)	−0.4	0.2	−0.8	2.6
1-BtOH (313 K)	−0.4	0.2	−0.8	2.7
1-BtOH (323 K)	−0.4	0.2	−0.6	2.7
1-BtOH (333 K)	−0.4	0.2	−0.8	2.6

Table 7.1. (continued).

Solvent	N_3-Pro			
	A_1	T_{10} / ps	A_2	T_{20} / ps
MeOH	−0.3	0.5	−0.5	2.9
EtOH	−0.4	0.5	−0.5	3.0
1-PrOH	−0.4	0.5	−0.6	2.8
1-BtOH (283 K)	−0.4	0.5	−0.5	2.8
1-BtOH (293 K)	−0.5	0.4	−0.5	2.7
1-BtOH (303 K)	−0.4	0.4	−0.5	2.6
1-BtOH (313 K)	−0.4	0.4	−0.5	2.6
1-BtOH (323 K)	−0.4	0.4	−0.7	2.6
1-BtOH (333 K)	−0.4	0.4	−0.6	2.7

Table 7.1. (continued).

Solvent	N_3-Nle			
	A_1	T_{10} / ps	A_2	T_{20} / ps
MeOH	−0.3	0.5	−0.5	2.9
EtOH	−0.4	0.5	−0.5	3.0
1-PrOH	−0.4	0.5	−0.6	2.8
1-BtOH (283 K)	−0.4	0.4	−0.5	2.8
1-BtOH (293 K)	−0.4	0.5	−0.4	3.0
1-BtOH (303 K)	−0.4	0.4	−0.5	2.6
1-BtOH (313 K)	−0.4	0.4	−0.5	2.6
1-BtOH (323 K)	−0.4	0.5	−0.6	2.8
1-BtOH (333 K)	−0.4	0.4	−0.6	2.7

A_i and T_{i0}: amplitudes and time constants in the fitting function ; $A_1\exp(-T/T_{10}) + A_2\exp(-T/T_{20})$.

Table 7.2. Solvent- and temperature-dependence of parameters to characterize the rotational relaxation of N_3-Ala, N_3-Pro, and N_3-Nle in primary 1-alcohols.

Solvent	N_3-Ala			
	T_{R1} / ps	T_{R2} / ps	θ_{in} / deg.	θ_l / deg.
MeOH	0.2 ± 0.1	4.3 ± 0.1	23.4	27.0 ± 1.8
EtOH	0.3 ± 0.1	6.1 ± 0.1	21.9	23.0 ± 1.9
1-PrOH	0.5 ± 0.1	8.7 ± 0.1	23.4	21.5 ± 2.0
1-BtOH (283 K)	0.7 ± 0.1	12.9 ± 0.9	20.4	20.8 ± 1.9
1-BtOH (293 K)	0.6 ± 0.1	10.6 ± 0.7	21.9	23.0 ± 1.9
1-BtOH (303 K)	0.5 ± 0.1	8.9 ± 0.5	20.4	24.4 ± 1.8
1-BtOH (313 K)	0.4 ± 0.1	6.8 ± 0.3	21.9	23.0 ± 1.9
1-BtOH (323 K)	0.4 ± 0.1	6.2 ± 0.2	23.4	23.4 ± 1.9
1-BtOH (333 K)	0.3 ± 0.1	5.3 ± 0.1	21.9	24.7 ± 1.8

Table 7.2. (continued).

Solvent	N_3-Pro			
	T_{R1} / ps	T_{R2} / ps	θ_{in} / deg.	θ_1 / deg.
MeOH	0.2 ± 0.1	6.3 ± 0.1	21.9	28.2 ± 1.7
EtOH	0.4 ± 0.1	8.3 ± 0.3	21.9	26.5 ± 1.7
1-PrOH	0.5 ± 0.1	12.2 ± 1.0	20.4	27.6 ± 1.6
1-BtOH (283 K)	0.7 ± 0.1	20.3 ± 1.9	20.4	22.6 ± 1.8
1-BtOH (293 K)	0.6 ± 0.1	16.1 ± 0.8	23.4	23.4 ± 1.9
1-BtOH (303 K)	0.5 ± 0.1	12.9 ± 0.6	20.4	26.0 ± 1.7
1-BtOH (313 K)	0.4 ± 0.1	10.0 ± 0.4	21.9	26.5 ± 1.7
1-BtOH (323 K)	0.3 ± 0.1	8.8 ± 0.3	21.9	29.8 ± 1.6
1-BtOH (333 K)	0.3 ± 0.1	7.2 ± 0.3	21.9	31.4 ± 1.6

Table 7.2. (continued).

Solvent	N_3-Nle			
	T_{R1} / ps	T_{R2} / ps	θ_{in} / deg.	θ_1 / deg.
MeOH	0.3 ± 0.1	3.5 ± 0.1	24.8	29.3 ± 1.8
EtOH	0.3 ± 0.1	4.7 ± 0.2	23.4	30.4 ± 1.7
1-PrOH	0.5 ± 0.1	6.2 ± 0.4	24.8	29.3 ± 1.8
1-BtOH (283 K)	0.7 ± 0.1	10.3 ± 1.1	21.9	31.4 ± 1.6
1-BtOH (293 K)	0.6 ± 0.1	8.0 ± 0.4	23.4	30.4 ± 1.6
1-BtOH (303 K)	0.5 ± 0.1	6.7 ± 0.3	24.8	31.0 ± 1.7
1-BtOH (313 K)	0.4 ± 0.1	5.8 ± 0.3	20.4	35.5 ± 1.5
1-BtOH (323 K)	0.4 ± 0.1	4.6 ± 0.1	21.9	29.8 ± 1.6
1-BtOH (333 K)	0.3 ± 0.1	4.3 ± 0.1	24.8	29.3 ± 1.8

A_i and T_{i0}: amplitudes and time constants in the fitting function ; $A_1\exp(-T/T_{10}) + A_2\exp(-T/T_{20})$.

Table 7.3. Fitting parameters and values of $r(T = 100\ \text{fs})$ for the solvent- and temperature-dependent anisotropy decays of N_3-Ala in primary 1-alcohols.

Solvent	A_1	T_{10} / ps	A_2	T_{20} / ps	$r(T = 100\ \text{fs})$
MeOH	0.1 ± 0.1	0.2 ± 0.1	0.3 ± 0.1	4.3 ± 0.1	0.31
EtOH	0.1 ± 0.1	0.3 ± 0.1	0.3 ± 0.1	6.1 ± 0.1	0.32
1-PrOH	0.1 ± 0.1	0.5 ± 0.1	0.2 ± 0.1	8.7 ± 0.1	0.31
1-BtOH (283 K)	0.1 ± 0.1	0.7 ± 0.1	0.3 ± 0.1	12.9 ± 0.9	0.33
1-BtOH (293 K)	0.1 ± 0.1	0.6 ± 0.1	0.2 ± 0.1	10.6 ± 0.7	0.32
1-BtOH (303 K)	0.1 ± 0.1	0.5 ± 0.1	0.2 ± 0.1	8.9 ± 0.5	0.33
1-BtOH (313 K)	0.1 ± 0.1	0.4 ± 0.1	0.3 ± 0.1	6.8 ± 0.3	0.32
1-BtOH (323 K)	0.1 ± 0.1	0.4 ± 0.1	0.2 ± 0.1	6.2 ± 0.2	0.31
1-BtOH (333 K)	0.1 ± 0.1	0.3 ± 0.1	0.3 ± 0.1	5.3 ± 0.1	0.32

Table 7.4. Fitting parameters and values of $r(T = 100\ \text{fs})$ for the solvent- and temperature-dependent anisotropy decays of N_3-Pro in primary 1-alcohols.

Solvent	A_1	T_{10} / ps	A_2	T_{20} / ps	$r(T = 100\ \text{fs})$
MeOH	0.1 ± 0.1	0.2 ± 0.1	0.3 ± 0.1	6.3 ± 0.1	0.32
EtOH	0.1 ± 0.1	0.4 ± 0.1	0.3 ± 0.1	8.3 ± 0.3	0.32
1-PrOH	0.1 ± 0.1	0.5 ± 0.1	0.2 ± 0.1	12.2 ± 1.0	0.33
1-BtOH (283 K)	0.1 ± 0.1	0.7 ± 0.1	0.2 ± 0.1	20.3 ± 1.9	0.33
1-BtOH (293 K)	0.1 ± 0.1	0.6 ± 0.1	0.2 ± 0.1	16.1 ± 0.8	0.31
1-BtOH (303 K)	0.1 ± 0.1	0.5 ± 0.1	0.2 ± 0.1	12.9 ± 0.6	0.33
1-BtOH (313 K)	0.2 ± 0.1	0.2 ± 0.1	0.3 ± 0.1	10.0 ± 0.4	0.32
1-BtOH (323 K)	0.1 ± 0.1	0.4 ± 0.1	0.2 ± 0.1	8.8 ± 0.3	0.33
1-BtOH (333 K)	0.1 ± 0.1	0.5 ± 0.1	0.2 ± 0.1	7.2 ± 0.3	0.32

Table 7.5. Fitting parameters and values of $r(T = 100\ \text{fs})$ for the solvent- and temperature-dependent anisotropy decays of N_3-Nle in primary 1-alcohols.

Solvent	A_1	T_{10} / ps	A_2	T_{20} / ps	$r(T = 100\ \text{fs})$
MeOH	0.1 ± 0.1	0.2 ± 0.1	0.3 ± 0.1	3.5 ± 0.1	0.30
EtOH	0.1 ± 0.1	0.3 ± 0.1	0.2 ± 0.1	4.7 ± 0.2	0.31
1-PrOH	0.1 ± 0.1	0.5 ± 0.1	0.2 ± 0.1	6.2 ± 0.4	0.30
1-BtOH (283 K)	0.1 ± 0.1	0.7 ± 0.1	0.2 ± 0.1	10.3 ± 1.1	0.32
1-BtOH (293 K)	0.1 ± 0.1	0.6 ± 0.1	0.2 ± 0.1	8.0 ± 0.4	0.31
1-BtOH (303 K)	0.1 ± 0.1	0.5 ± 0.1	0.2 ± 0.1	6.7 ± 0.3	0.30
1-BtOH (313 K)	0.2 ± 0.1	0.4 ± 0.1	0.2 ± 0.1	5.8 ± 0.3	0.33
1-BtOH (323 K)	0.1 ± 0.1	0.4 ± 0.1	0.2 ± 0.1	4.6 ± 0.1	0.32
1-BtOH (333 K)	0.1 ± 0.1	0.3 ± 0.1	0.2 ± 0.1	4.3 ± 0.1	0.30

Appendix 7.A. Solvent- and Temperature-dependent IR Absorption Measurements

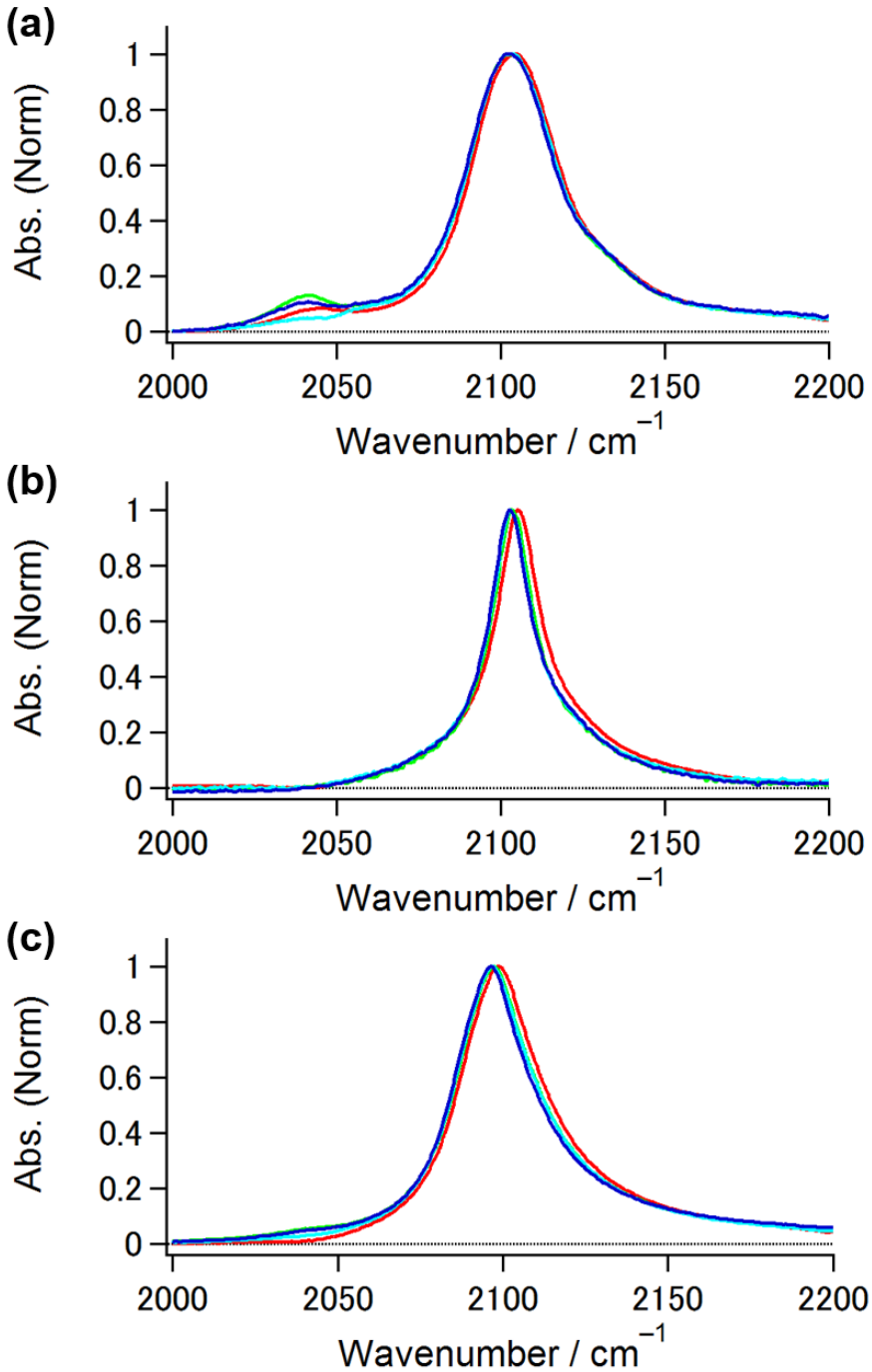

Figure 7.A.1 Solvent-dependent IR absorption spectra of the N_3 anti-symmetric stretching mode of (a) N_3-Ala, (b) N_3-Pro, and (c) N_3-Nle measured at 293 K. MeOH (red), EtOH (green), 1-PrOH (light-blue), and 1-BtOH (blue).

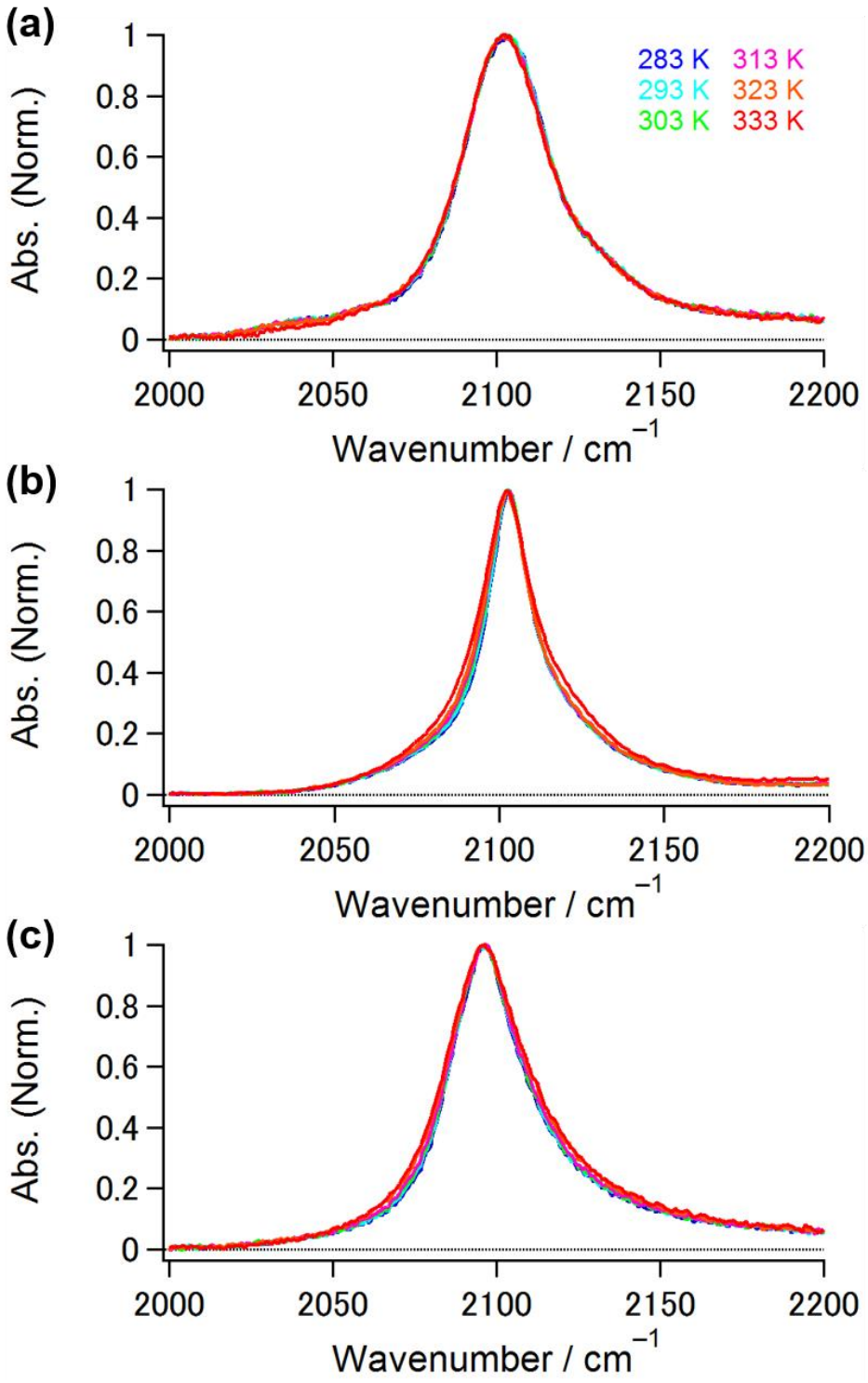

Figure 7.A.1 Temperature-dependent IR absorption spectra of the N_3 anti-symmetric stretching mode of (a) N_3-Ala, (b) N_3-Pro, and (c) N_3-Nle in 1-BtOH.

Appendix 7.B. Solvent- and Temperature-dependent Isotropic IR Pump-probe Signals

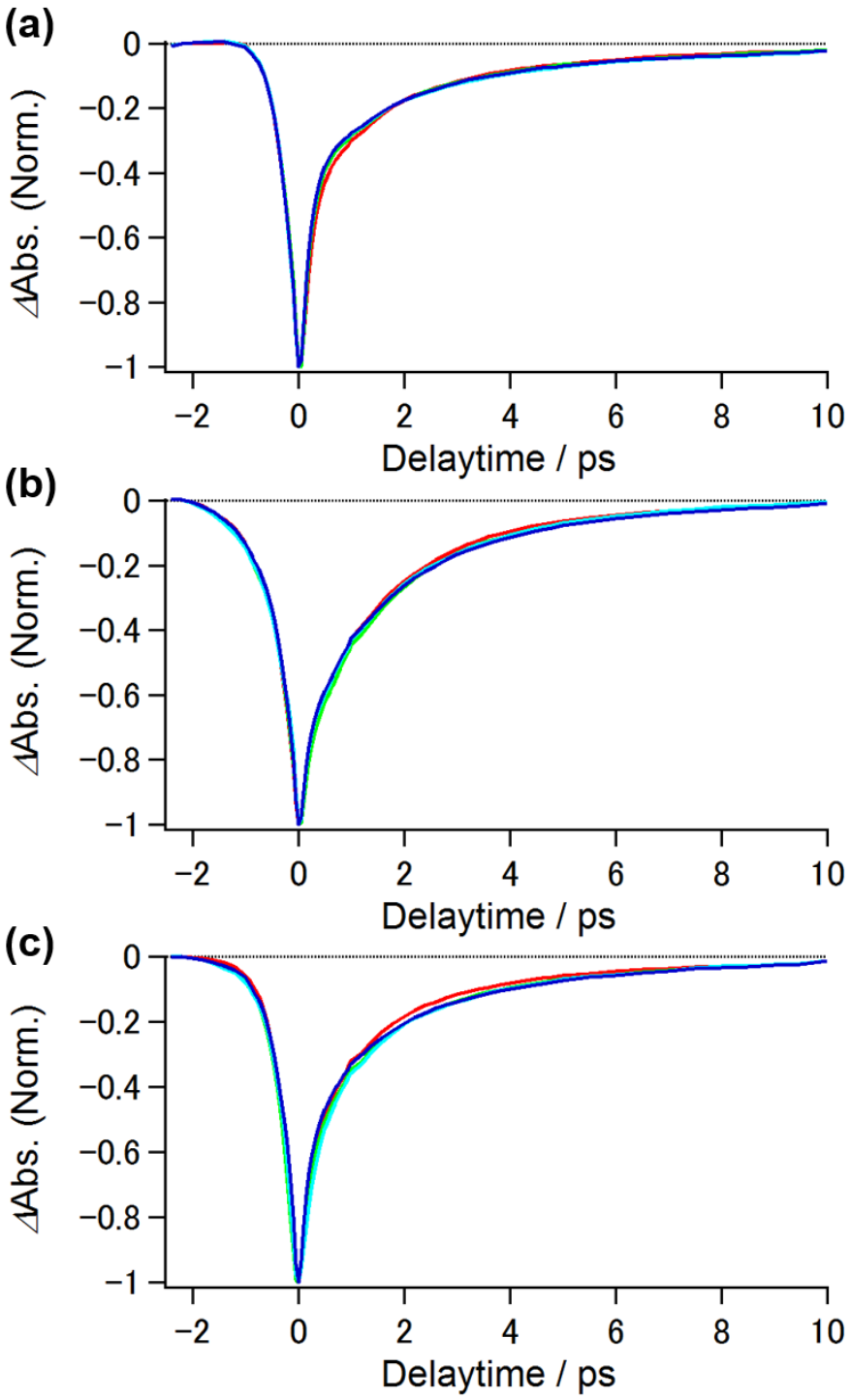

Figure 7.B.1 Solvent-dependence of the isotropic IR pump-probe of (a) N_3-Ala, (b) N_3-Pro, and (c) N_3-Nle measured at 293 K. These signals were taken from the peak wavenumber of the $\nu = 0 - 1$ vibrational transition. MeOH (red), EtOH (green), 1-PrOH (light-blue), and 1-BtOH (blue).

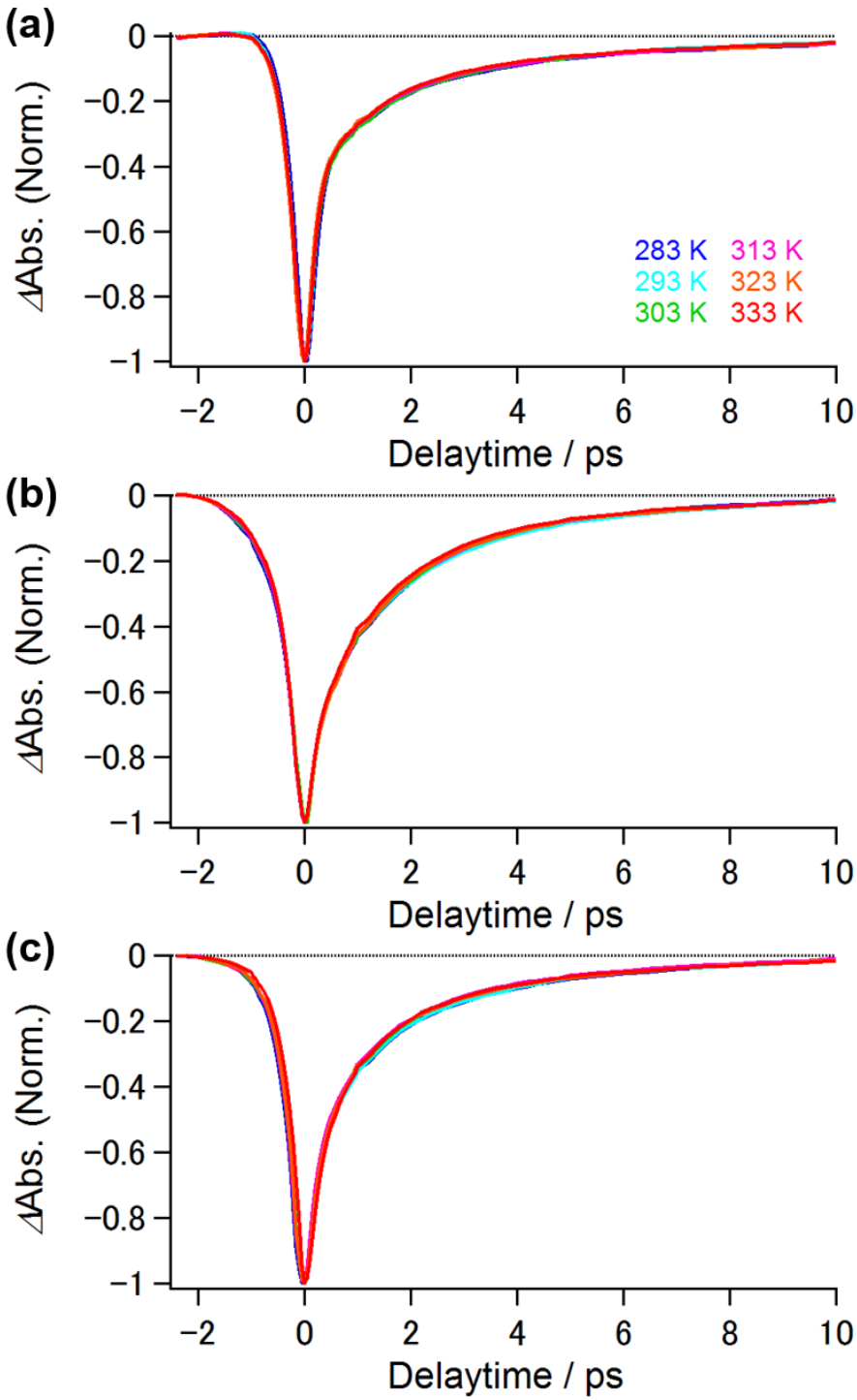

Figure 7.B.2 Temperature-dependence of the isotropic IR pump-probe of (a) N_3-Ala, (b) N_3-Pro, and (c) N_3-Nle in 1-BtOH. These signals were taken from the peak wavenumber of the $\nu = 0 - 1$ vibrational transition.

Appendix 7.C. Anisotropy Measurements for N_3-Ala and N_3-Nle in DMSO Solutions

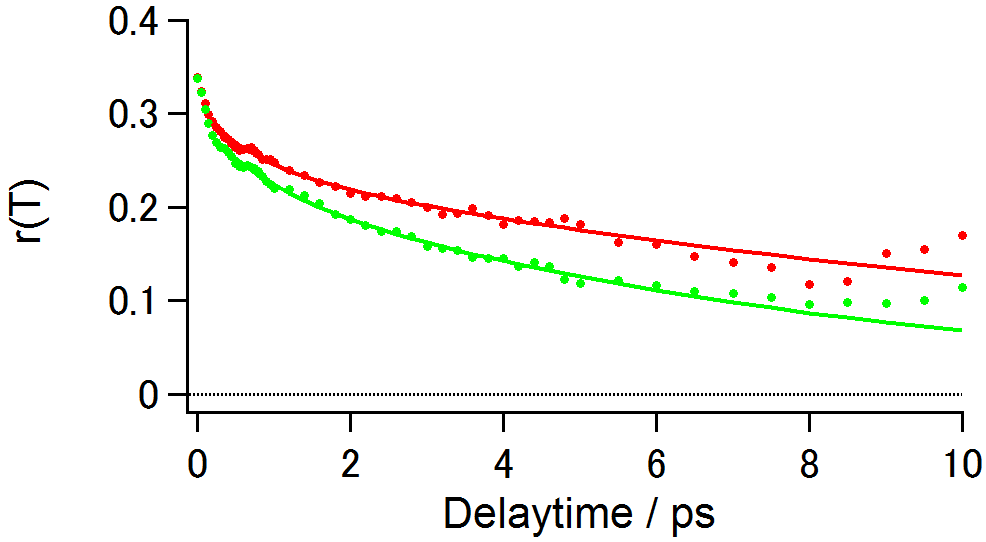

Figure 7.C.1 Temporal profiles of anisotropy decays of N_3-Ala (red) and N_3-Nle (green) in DMSO measured at 293 K. Close circles are the experimental results. The solid lines represent the fitting results to double exponential functions given by Eq. (7.3).

Appendix 7.D. Extension of the Wobbling-in-a-cone Orientational Correlation Function to Multiple-restricted Angular Motion

Suppose that three different restricted orientational diffusions are involved in the rotational relaxation process. After these relaxation processes take place, initial angular distribution is assumed to be completely randomized by unrestricted orientational diffusion process. Because these orientational diffusive processes undergo independently, the associated second-order Legendre polynomial orientational correlation function ($C_2(T)$) is given by [52]:

$$\begin{aligned} C_2(T) = &\left[P^2 + \left(1-P^2\right)\exp\left(-T/T_{\mathrm{in}}\right)\right]\left[Q^2 + \left(1-Q^2\right)\exp\left(-T/T_{\mathrm{w1}}\right)\right] \\ &\times\left[R^2 + \left(1-R^2\right)\exp\left(-T/T_{\mathrm{w2}}\right)\right]\exp\left(-T/T_m\right) \end{aligned} \tag{7.D.1}$$

where P, Q, and R are the order parameters to characterize the inertial, first diffusive, and second diffusive orientational motions, respectively. In general, the order parameter X ($X = P$, Q, or R) for the restricted orientational motion can be described as:

$$X = \frac{1}{2}\cos\theta_0\left(1+\cos\theta_0\right) \tag{7.D.2}$$

where θ_0 is the half angle of the restricted cone. The T_{in}, T_{w1}, and T_{w2} in Eq. (7.D.1) are the time constants for three restricted orientational diffusive processes. Moreover, the T_{m} is the time constant for a complete orientational randomization process due to the entire molecular rotation. Here, these time constants have the following ordering: $T_{\mathrm{in}} << T_{\mathrm{w1}} < T_{\mathrm{w2}} < T_{\mathrm{m}}$. By multiplying out Eq. (7.D.1), the orientational correlation function becomes:

$$\begin{aligned} C_2(T) = &\left(1-P^2\right)\exp\left(-T/T_{\mathrm{in}}\right) + P^2\left[R^2\left(1-Q^2\right)\exp\left(-T/T_{\mathrm{w1}}\right) + Q^2\left(1-R^2\right)\exp\left(-T/T_{\mathrm{w2}}\right)\right. \\ &\left. + \left(1-R^2\right)\left(1-Q^2\right)\exp\left\{-T\left(1/T_{\mathrm{w1}} + 1/T_{\mathrm{w2}}\right)\right\} + R^2Q^2\right]\exp\left(-T/T_m\right). \end{aligned} \tag{7.D.3}$$

Here, note that, since the inertial orientational motion occurs on much faster time scale than the other motions, the terms with the time constants of $(1/T_{\mathrm{in}} + 1/T_{\mathrm{w1}})^{-1}$ and $(1/T_{\mathrm{in}} + 1/T_{\mathrm{w2}})^{-1}$ are indistinguishable from those with the time constant of T_{in}. In this study, because T_{w1} is much shorter than T_{w2}, the term with the time constant of $(1/T_{\mathrm{w1}} + 1/T_{\mathrm{w2}})^{-1}$ is indistinguishable from the that with the time constant of T_{w1} within experimental accuracy:

$$\begin{aligned} C_2(T) = &\left(1-P^2\right)\exp\left(-T/T_{\mathrm{in}}\right) + P^2\left(1-Q^2\right)\exp\left\{-T\left(1/T_{\mathrm{w1}} + 1/T_{\mathrm{m}}\right)\right\} \\ &+ Q^2\left(1-R^2\right)\exp\left\{-T\left(1/T_{\mathrm{w2}} + 1/T_{\mathrm{m}}\right)\right\} + R^2Q^2\exp\left(-T/T_{\mathrm{m}}\right). \end{aligned} \tag{7.D.4}$$

Since the reorientational motions of the entire N_3-AAs are expected to proceed on much longer time scale than the internal rotational motion, the combinations of $(1/T_{\mathrm{w1}} + 1/T_{\mathrm{m}})^{-1}$ and $(1/T_{\mathrm{w2}} + 1/T_{\mathrm{m}})^{-1}$ are approximately equal to T_{w1} and T_{w2}, respectively:

$$C_2(T) = \left(1 - P^2\right)\exp\left(-T/T_{\mathrm{in}}\right) + P^2\left(1 - Q^2\right)\exp\left(-T/T_{\mathrm{w1}}\right) + P^2Q^2\left(1 - R^2\right)\exp\left(-T/T_{\mathrm{w2}}\right) + R^2Q^2\exp\left(-T/T_{\mathrm{m}}\right). \quad (7.D.5)$$

Moreover, by assuming that the vibrational transition dipole moments of the N_3 groups of the N_3-AAs sample the angular space through the internal rotational motions around several bond axes, R is set to 0. Therefore, finally, the orientational correlation function $C_2(T)$ can be represented as:

$$C_2(T) = \left(1 - P^2\right)\exp\left(-T/T_{\mathrm{in}}\right) + P^2\left(1 - Q^2\right)\exp\left(-T/T_{\mathrm{w1}}\right) + P^2Q^2\exp\left(-T/T_{\mathrm{w2}}\right). \quad (7.D.6)$$

This is Eq. (7.4) in the main text.

Appendix 7.E. Solvent-dependent Anisotropy Decays of N_3-Phe in 1-alcohol Solutions

Figure 7.E.1 displays the IR absorption spectra of the N_3 anti-symmetric stretching mode of N_3-Phe in 1-alcohol solutions (sample concentration: ~300 mM, optical path length: 25 μm). Compared to the other N_3-AAs, the IR absorption spectra of N_3-Phe contain at least four spectral components. This complexity of the IR absorption spectra of N_3-Phe in 1-alcohol solutions are likely due to anharmonic vibrational coupling such as accidental Fermi resonance [63]. Intense IR absorption band corresponds to the absorption of the N_3 anti-symmetric stretching mode.

Figure 7.E.2 shows the isotropic IR pump-probe signals of the N_3 anti-symmetric stretching mode of N_3-Pro in 1-alcohol solutions measured at the $\nu = 0 - 1$ vibrational transition. Based on double-exponential fits to the isotropic IR pump-probe signals after $T = 0.2$ ps, I found that the vibrational lifetimes of N_3-Phe are independent of the 1-alcohol solvents and the fast and slow VER time constants were 0.5 ± 0.1 ps and 3.5 ± 0.3 ps, respectively.

Figure 7.E.3 displays the anisotropy decays for the N_3 anti-symmetric stretching mode of N_3-Phe in 1-alcohol solutions measured at the $\nu = 0 - 1$ vibrational transition. From the fitting analyses with Eq. (7.3), the fast and slow rotational relaxation time constants (T_{R1} and T_{R2}) are obtained as follows: $T_{R1} = 0.2 \pm 0.3$ ps and $T_{R2} = 7.6 \pm 0.2$ ps for MeOH, $T_{R1} = 0.1 \pm 0.1$ ps and $T_{R2} = 9.9 \pm 0.2$ ps for EtOH, $T_{R1} = 0.3 \pm 0.2$ ps and $T_{R2} = 13.4 \pm 0.5$ ps for 1-PrOH, and $T_{R1} = 0.2 \pm 0.1$ ps and $T_{R2} = 17.3 \pm 0.5$ ps for 1-BtOH.

Figures

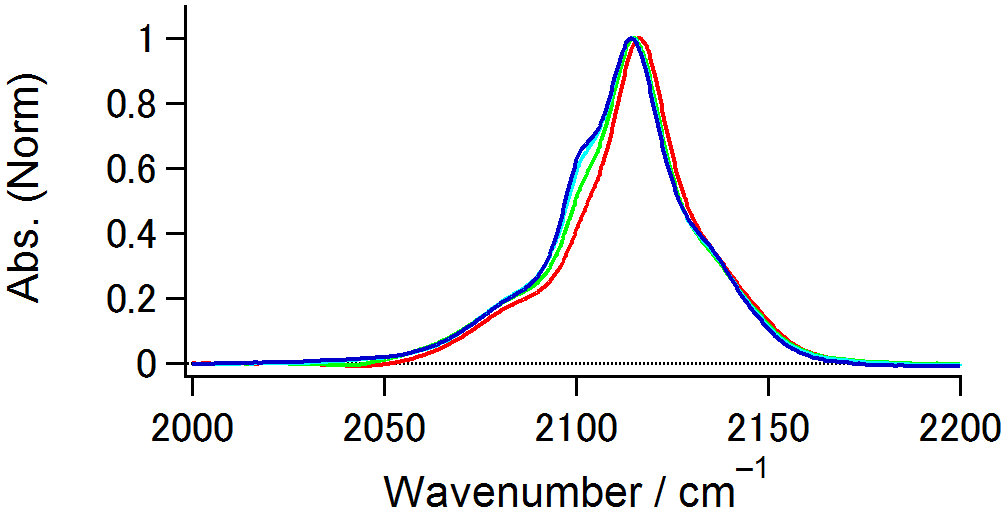

Figure 7.E.1. Solvent-dependent IR absorption spectra of the N_3 anti-symmetric stretching mode of N_3-Phe measured at 293 K. MeOH (red), EtOH (green), 1-PrOH (light-blue), and 1-BtOH (blue).

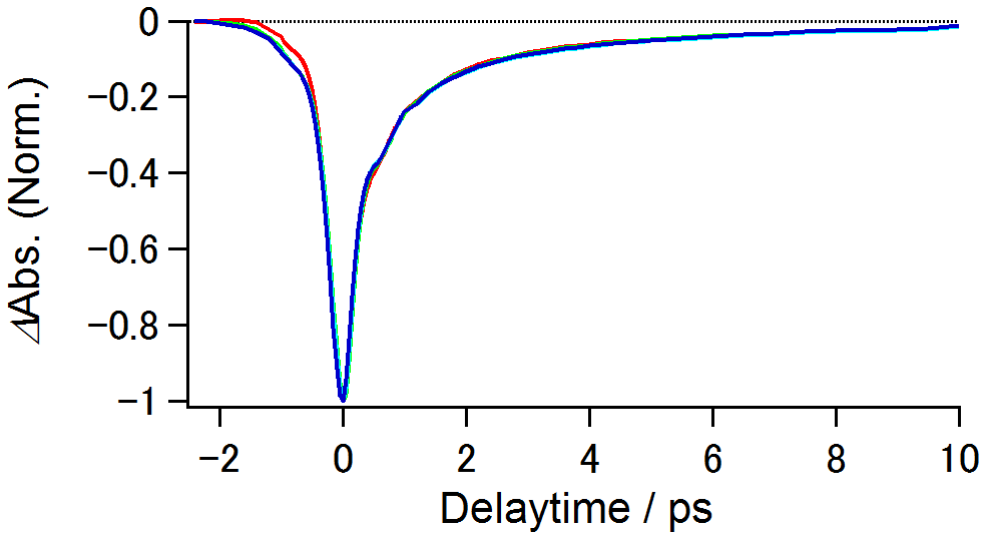

Figure 7.E.1. Solvent-dependence of the isotropic IR pump-probe of N_3-Phe measured at 293 K. These signals were taken from the peak wavenumber of the $\nu = 0 - 1$ vibrational transition. MeOH (red), EtOH (green), 1-PrOH (light-blue), and 1-BtOH (blue).

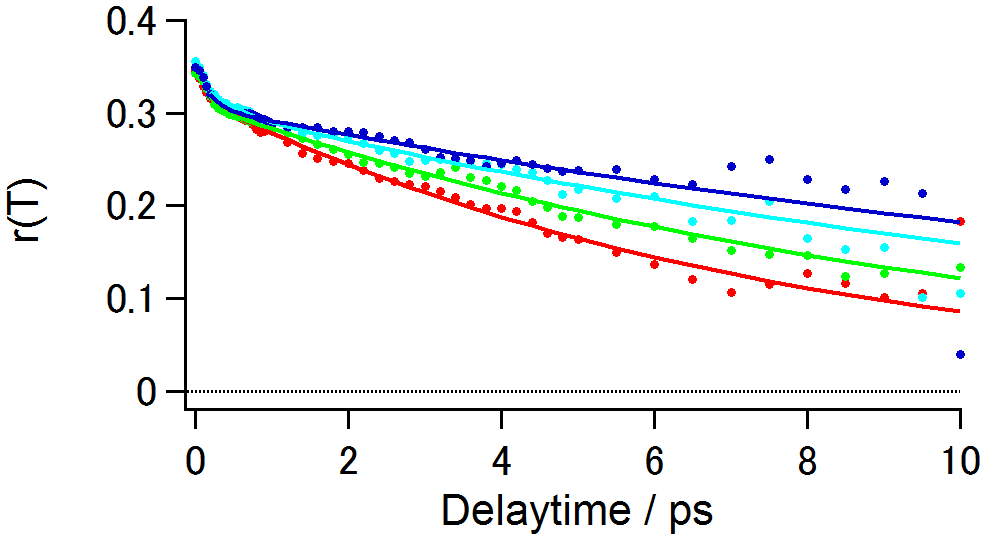

Figure 7.E.3. (a) Temporal profiles of solvent-dependent anisotropy decays of N_3-Phe measured at 293 K. MeOH (red), EtOH (green), 1-PrOH (light-blue), and 1-BtOH (blue). Close circles are the experimental results. The solid lines represent the fitting results to double exponential functions given by Eq. (7.3).

CHAPTER 8.

Hydrogen-bond Dynamics of 9-fluorenone Derivatives in Aqueous Solutions Studied by Two-dimensional Infrared Spectroscopy

8.1. Introduction

In protic liquids, hydrogen bonds (HBs) between solute and solvent molecules play a critical role in stabilizing the molecular structures and chemical activities of solutes [1-4]. Because of an intrinsically weak interaction, HBs are not permanently formed but continuously broken and formed under thermal equilibrium conditions [5]. Such HB rearrangements take place on a picosecond time scale in the condensed phase. Since vibrational frequencies are sensitive to the strength of solute-solvent interactions, we can investigate HB dynamics between solute and solvent by using three-pulse infrared (IR) photon echo method and two-dimensional infrared (2D-IR) spectroscopy. In earlier works, several groups performed these vibrational echo measurements for ions in water [6-11]. From the comparison with the experimental and theoretical investigation on the vibrational frequency fluctuations of pure water [12-18], it was suggested that the time scales of HB rearrangements around ions are almost the same as those in water. Very recently, the 2D-IR measurements are performed to examine HB dissociation and association between solute and protic solvent, such as water and alcohols [19-32].

So far, Tominaga and co-workers investigated the vibrational dynamics of the CO stretching mode of 9-FLuorenon (abbreviated as 9-FL) in protic and aprotic solvents [33, 34]. Hirai *et al*. reported that, while the IR absorption spectrum of the CO stretching modes of 9-FL in cyclohexane (*i.e.* aprotic solvent) is symmetric, that in 1-octanol (*i.e.* protic solvent) exhibits pronounced structures with two peaks at around 1713 cm^{-1} and 1721 cm^{-1}, and a shoulder at around 1700 cm^{-1} [33]. Because these three bands show different temperature dependence, they concluded the pronounced structures of the IR absorption spectrum is due to three different species at thermal equilibrium, not due to the intramolecular vibrational coupling such as a Fermi resonance. Moreover, based on the DFT calculations, they concluded that the three IR bands correspond to a non-hydrogen bonded 9-FL, a 9-FL complex with one methanol molecule (*i.e.* [9-FL:MeOH]), and a 9-FL complex with two methanol molecules (*i.e.* [9-FL:$(MeOH)_2$]) in the order of higher frequencies, respectively. Therefore, we can consider that 9-FL is good vibrational probe molecule for investigating solute-solvent HB dynamics. However, since 9-FL is not soluble in water, we cannot use this molecule to study the solute-solvent HB dynamics.

In this study, I chose two different water-soluble 9-FL derivatives as vibrational probe molecules: ionic 9-FLuorenone-2-carboxylic acid (abbreviated as 9-FL-2-COO^-, Figure 8.1(a)) and 9-oxofluorene-4-carboxylic acid (abbreviated as 9-FL-4-COO^-, Figure 8.1(b)). As shown in

Figure 8.1, since 9-FL-2-COO^- has a COO^- group closer to the CO group than 9-FL-4-COO^-, the electrostatic interactions between the COO^- group and water molecules are likely to perturb the water dynamics around the CO group of 9-FL-2-COO^- more strongly than that of 9-FL-4-COO^-. Therefore, depending on the structural difference in the position of the COO^- group, we can expect to observe different vibrational frequency fluctuations of 9-FL-2-COO^- and 9-FL-4-COO^- in water with 2D-IR spectroscopy.

8.2. Materials and Methods

An experimental setup for the 2D-IR measurements is described in Chapter 3. Briefly, an output from the Ti:sapphire regenerative amplifier is converted into a mid-IR pulse by sequential OPA and DFG processes. The pulse duration was approximately 160 fs. The bandwidth and pulse energy of the mid-IR pulses were approximately 100 cm^{-1} and 3.0 μJ, respectively. The center wavenumber of the IR pulses was tuned to approximately 1700 cm^{-1}, which corresponds to the peak vibrational frequencies of the CO stretching modes of 9-FL-2-COO^- and 9-FL-4-COO^-. In this frequency region, because water vapor shows a strong IR absorption band, the 2D-IR measurements for the 9-FL-2-COOH and 9-FL-4-COOH aqueous solutions were conducted under purging with a dry N_2 gas.

9-FL-2-COOH and 9-FL-4-COOH were purchased from Sigma-Aldrich (St. Louis, Missouri, United States of America) and used without further purification. As the solvent, D_2O was purchased from Wako (Japan, 99.9%). To dissolve 9-FL-2-COOH and 9-FL-4-COOH into water, a small amount of NaOD (Wako, Japan, 40 w/w% solution in D_2O, 99.5%) was added to the 9-FL-2-COOH and 9-FL-4-COOH aqueous solutions (pH ~ 9.0). The concentration of the samples was approximately 300 mM. Here, the amount of H atom, which comes from the carboxyl group of the solute, in the solution is considered to be negligibly small in comparison to that of D atom. In order to remove the remaining undissolved solutes, the sample solutions were filtered by using disposal membrane filters (ADVANTEC, Japan, diameter size: 0.20 μm) prior to injecting a sample cell. The sample cell consists of a pair of CaF_2 windows with the optical path length of 50 μm. All of the experiments were conducted at a room temperature (293 K), unless otherwise specified.

8.3. Results and Discussions

8.3.1. IR Absorption Spectra

Figures 8.2(a) and (b) show the IR absorption spectra of the CO stretching modes of 9-FL-2-COO^- and 9-FL-4-COO^- in D_2O, respectively. The IR absorption spectrum of 9-FL-4-COO^- is fitted by a single Gaussian function. On the other hand, as shown in Figure 8.2(b), the IR absorption spectrum of 9-FL-2-COO^- exhibits an asymmetric lineshape due to a shoulder at around 1710 cm^{-1}. Therefore, a sum of two Gaussian functions is necessary to reproduce the lineshape. The fitting results for the peak wavenumbers and full width of half maximum (FWHM) of the IR absorption spectra of 9-FL-4-COO^- and 9-FL-2-COO^- are summarized in Table 8.1. From the temperature-dependent IR absorption measurements of 9-FL-2-COO^- in D_2O, I found that two types of HB complexes between 9-FL-2-COO^- and D_2O molecules exist in the D_2O solution. Moreover, by comparing the IR absorption spectra in D_2O and THF, I assigned the absorption bands at higher and lower frequency region to a 9-FL-2-COO^- complex with one D_2O molecule (described as [9-FL-2-COO^-:D_2O]) and a 9-FL-2-COO^- complex with two D_2O molecules (described as [9-FL-2-COO^-:$(D_2O)_2$]), respectively. The results of the IR absorption measurements for 9-FL-2-COO^- in D_2O at different temperatures and in THF are summarized in Appendix 8.A.

On the other hand, as mentioned above, the IR absorption spectrum of 9-FL-4-COO^- in D_2O shows the symmetric IR absorption band. We can explain the difference in the spectral lineshapes of 9-FL-4-COO^- and 9-FL-2-COO^- in terms of the HB dynamics between the solute and water molecules. Previously, Watanabe and Hamaguchi examined the ion association dynamics of sulfate salts in aqueous solutions with Raman spectroscopy and reported that the observed Raman bands ($I(\omega)$) can be represented based on a two-exchange model as [35]:

$$I(\omega) = \frac{2W_A W_B (\omega_B - \omega_A)^2 / (W_A + W_B)}{(\omega - \omega_A)^2 (\omega - \omega_B)^2 + [W_B(\omega - \omega_A) + W_A(\omega - \omega_B)]^2} \tag{8.1}$$

where W_A and W_B are the exchange rates from the state A to the state B and *vice versa*, respectively. The ω_A and ω_B are the vibrational frequencies corresponding to the state A and B, respectively. If the two states exchange each other on a much faster time scale than their vibrational frequency difference (*i.e.* $W_A \sim W_B$ (= W_0) and $W_0 >> |\omega_A - \omega_B|$), Eq. (8.1) can be rewritten as follows:

$$I(\omega) = \frac{(\omega_B - \omega_A)^2}{4W_0(\omega - \overline{\omega})^2} \tag{8.2}$$

where $\overline{\omega}$ is the mean frequency of the ω_A and ω_B: $\overline{\omega} = (\omega_A + \omega_B) / 2$. Here, we can expect that 9-FL-4-COO^- also forms HB complexes with either one or two D_2O molecules. Therefore, based on the result that the peak wavenumber of 9-FL-4-COO^- in D_2O is approximately at the center of those of [9-FL-2-COO^-:D_2O] and [9-FL-2-COO^-:$(D_2O)_2$], I consider that the formation and dissociation of the HB occur enough rapidly to merge the IR absorption band of 9-FL-4-COO^- into one IR absorption band.

8.3.2. IR Pump-probe Experiments

By blocking the pump pulse passing thorough the moving interferometer arm (E_{pump1} in Section 3.3.1), an IR pump-probe measurement can be conducted with this 2D-IR setup. Note that, because the polarization of pump pulses is parallel to that of pump pulses, the IR pump-probe signals are measured under the parallel polarization condition. Figure 8.3 displays the IR pump-probe signals of the CO stretching modes of 9-FL-2-COO^- and 9-FL-4-COO^- in D_2O. The blue regions represent the signals originating from ground state bleaching (GSB; $\nu = 0 - 1$) and stimulated emission (SE; $\nu = 0 - 1$), and the red regions represent transient absorption (TA; $\nu = 1 - 2$). Figure 8.3 shows the IR pump-probe signals of the CO stretching modes of 9-FL-2-COO^- and 9-FL-4-COO^- in D_2O related to the GSB and SE transitions. Here, as mentioned in the previous section, I consider that 9-FL-2-COO^- forms the two kinds of HB complexes with D_2O molecules, which provide the IR absorption bands at 1694.0 cm^{-1} and 1708.0 cm^{-1}. In order to highlight these components, the IR pump-probe signals of 9-FL-2-COO^- in D_2O taken at lower (1695.1 cm^{-1}) and higher (1712.8 cm^{-1}) probe wavenumbers are represented by the pink and light-blue lines in Figure 8.3(a), respectively. The population relaxation of 9-FL-2-COO^- and 9-FL-4-COO^- in D_2O can be represented by a double exponential function, and the vibrational lifetimes of 9-FL-2-COO^- and 9-FL-4-COO^- in D_2O are summarized in Table 8.1. Here, in order to exclude the pulse overlapping effect, the IR pump-probe signals after $T = 0.2$ ps were used for the fitting analyses [36]. In earlier work, Kashid *et al*. reported that the IR absorption spectrum of the CO stretching mode of ethyl acetate (EtOAc) in D_2O also possesses the two spectral components, which are assigned to a free EtOAc and an EtOAc complex with one D_2O molecule for lower and higher frequency absorption bands, respectively. By performing the 2D-IR measurements, they

revealed that the vibrational energy relaxations (VER) of those species are characterized by time constants of 0.915 ps and 1.60 ps, respectively [30]. The time scales of the VER of 9-FL-2-COO^- and 9-FL-4-COO^- in D_2O are similar to those of EtOAc in D_2O. Note that, as shown in Table 8.1, the IR pump-probe signal of [9-FL-2-COO^-:$(D_2O)_2$] decays faster than that of [9-FL-2-COO^-:D_2O]. As mentioned in Ref. 33, based on the Fermi's golden rule, we can consider that this acceleration results from the increase of the vibrational density of states of energy accepting modes due to the formation of the HB with a D_2O molecule.

8.3.3. 2D-IR Experiment for 9-FL-2-COO^- in D_2O

The 2D-IR spectra of 9-FL-2-COO^- in D_2O were measured at different t_2 times ranging from 0 to 4 ps. Figure 8.4(a) displays the 2D-IR spectra of 9-FL-2-COO^- at four t_2 times. As mentioned in Section 8.3.1, based on the asymmetrical lineshape of IR absorption spectrum for 9-FL-2-COO^- in D_2O, I consider that the two types of 9-FL-2-COO^- HB complexes with D_2O molecules (*i.e.* [9-FL-2-COO^-:D_2O] and [9-FL-2-COO^-:$(D_2O)_2$]) exist in the aqueous solution and formation and breaking of HB takes place on a picosecond time scale. We can obtain insight into such chemical exchange processes from the t_2-dependence of 2D-IR spectra [37].

Here, suppose that two different states A and B, which are characterized by the vibrational frequencies ω_A and ω_B, are equilibrated in the solution. When molecules are in the population states created by the interaction with the second pump pulse, those can undergo the chemical exchange, that is, state A interconverts into state B and *vice versa*. Figure 8.5 schematically illustrates the temporal change of the 2D-IR spectrum corresponding to the chemical exchange process. As shown in Figure 8.5(a), at early t_2 times, we can observe two peaks along the diagonal direction of the 2D-IR spectrum, which represents that the states A and B are independently excited and no chemical change occurs between these two states during the t_2 period. On the other hand, as the t_2 time increases, the signals due to the interconversion between states A and B will gradually appear in the off-diagonal regions of the 2D-IR spectrum (see Figure 8.5(b)), which are referred to as cross-peak signals. Therefore, t_2-dependence of the cross-peak signals provides information on the exchange dynamics in solutions. Hereafter, the HB complexes of [9-FL-2-COO^-:$(D_2O)_2$] and [9-FL-2-COO^-:D_2O] are regarded as states A and B, respectively.

Figure 8.6 displays the slice of the 2D-IR spectra taken along the ω_3 axis at ω_1 = 1693.8 cm^{-1}, which corresponds to the peak wavenumber of the IR absorption band of state A. Due to

the cross-peak signal reflecting the interconversion of state A into state B, the slice spectra exhibit the more distinctive shoulder at around ω_3 frequency of 1710 cm^{-1} at longer t_2 times. Therefore, I used the ratio of the cross-peak signal (S_{AB}) to the diagonal peak signal at lower frequency (S_{AA}) to track the growth kinetics of the cross-peak signal. Figure 8.7 shows the ratio of S_{AB} / S_{AA} as a function of the t_2 time. It should be noted that, to remove the contribution from the experimental noise, the S_{AB} and S_{AA} are determined by averaging the signal intensities over a small area of the 2D-IR spectrum, which is displayed in Figure 8.4(a) [18]. Moreover, because the IR absorption bands of states A and B overlap to some extent (see Figure 8.2(b)), the S_{AB} is obtained from the signals in the slight higher ω_3 frequency regions with respect to the absorption peak position of [9-FL-2-COO^-:D_2O].

For the two-state exchange process between states A and B, the S_{AB} / S_{AA} can be represented as [23, 31]:

$$S(t_2) \equiv \frac{S_{AB}(t_2)}{S_{AA}(t_2)} = \frac{\mu_A^2 \mu_B^2 c_A P_{AB}(t_2)}{\mu_A^4 c_A P_{BB}(t_2)} = \frac{\mu_B^2 P_{AB}(t_2)}{\mu_A^2 P_{BB}(t_2)} \tag{8.3}$$

where μ_i and c_i are the vibrational transition dipole moment and mole fraction of states i, respectively. The P_{AA} and P_{AB} represent the condition probabilities:

$$P_{AA}(t_2) = \Omega \cosh\left(\frac{\Omega T}{2}\right) + (K - 2k_A)\sinh\left(\frac{\Omega T}{2}\right) \tag{8.4}$$

$$P_{AB}(t_2) = 2k_{AB} \sinh\left(\frac{\Omega T}{2}\right) \tag{8.5}$$

, respectively, and the Ω and K are defined as:

$$K = k_A + k_B \tag{8.6}$$

$$\Omega = \left[(k_A - k_B)^2 + 4k_{AB}k_{BA}\right]^{1/2} \tag{8.7}$$

respectively. Here, the k_i is the total decay rate constant for the states i, which corresponds to the sum of the VER and exchange rates, and the k_{ij} is the exchange rates from state i to state j. Furthermore, by assuming that the VER rates of states A and B are the same (which may be reasonable, based on the VER times listed in Table 8.1), the Ω given by Eq. (8.7) becomes k_{AB} + k_{BA}. Consequently, finally, the $S(t_2)$ in Eq. (8.3) can be written as:

$$S(t_2) = \frac{\mu_A^2}{\mu_B^2} \frac{1 - \exp(-k_{ex} t_2)}{K_{eq} + \exp(-k_{ex} t_2)} \tag{8.8}$$

where K_{eq} and k_{ex} are the equilibrium constant and energy transfer rate between states A and B, which are defined as $K_{eq} = k_{BA} / k_{AB}$ and $k_{ex} = (k_{AB} + k_{BA}) / 2$, respectively. By using the model function given by Eq. (8.8), I conducted the fitting analysis of the cross-peak evolution obtained from the 2D-IR spectra of 9-FL-2-COO^- in D_2O. In order to consider only the t_2-dependence of the S_{AB} / S_{AA}, the initial value was subtracted from the data (the residual signal will be discussed later):

$$\Delta S(t_2) \equiv \frac{S_{AB}(t_2)}{S_{AA}(t_2)} - \frac{S_{AB}(0)}{S_{AA}(0)}. \tag{8.9}$$

Here, the area ratio of the IR absorption bands of states A and B can provide the constrain to the equilibrium constant of K_{eq} as: $K_{eq} = A_{int}\mu_A^2 / B_{int}\mu_B^2$ where A_{int} and B_{int} represents the areas of the IR absorption spectra of the states A and B, which are obtained from the fitting analysis for that of 9-FL-2-COO^- in D_2O. By calculating the integral of the IR absorption bands, the A_{int}/B_{int} is found to be about 1.9. Therefore, by assuming that the relative strength of the vibrational transition dipole moments of the states A and B does not significantly depend on the solute-solvent HB [30], the K_{eq} is set to 1.9 during the fitting analysis. From the fitting analysis, I found that the k^{-1}_{AB} and k^{-1}_{BA} are approximately 2.0 ps and 1.0 ps, respectively, whose time scale are in good agreement with the results of the 2D-IR experiments for EtOAc in D_2O done by Kim and co-workers [30]. Therefore, based on the result of the 2D-IR measurement for 9-FL-2-COO^- in D_2O, I consider that the formation and dissociation of HBs between the CO group of 9-FL-4-COO^- and surrounding D_2O molecules undergo within 1 ps. As mentioned in Section 8.1, this difference in solute-solvent HB dynamics may be due to the interaction between the COO^- group and D_2O molecules. If a D_2O molecule simultaneously forms HBs with both CO group and COO^- group, we can expect that the HBs between 9-FL-2-COO^- and the bridging D_2O molecule continue on longer time scale than that between 9-FL-4-COO^- and a D_2O molecule. With respect to the HB dynamics in the vicinity of 9-FL-2-COO^-, MD simulations will provide more detailed information at a molecular-level [37].

According to the theoretical description of the S_{AB} / S_{AA} given by Eq. (8.8), the initial value of the growth curve $S(t_2)$ should be zero. However, as mentioned above, the experimentally obtained $S(t_2)$ starts with the value of approximately 0.135. The pulse duration of min-IR pulses

used for the 2D-IR experiment was about 100 fs, so interconversion processes cannot occur during pulse overlap regime. Therefore, the observation of the cross-peak signal at t_2 = 0 ps suggests that the vibrational coherence jumping between states A and B takes place when the solutes are in the coherent state. In order to obtain accurate time constant for the interconversion rate between states A and B, it is necessary to perform more detailed analyses for the t_2-dependent cross-peak signal with including the effects of the coherence jumping on the lineshape of the 2D-IR spectrum [26, 30].

8.3.4. 2D-IR Experiments for 9-FL-4-COO$^-$ in D_2O

The 2D-IR spectra of 9-FL-4-COO$^-$ in D_2O were measured at different population times (t_2) ranging from 0 to 4 ps. Figure 8.4(b) represents the 2D-IR spectra of 9-FL-4-COO$^-$ at several t_2 times. Red and blue regions indicate the GSB + SE signals and the TA signal, respectively. The red lines represent the diagonal directions of the 2D-IR spectra ($\omega_1 = \omega_3$). Reflecting the result that the IR absorption spectrum of 9-FL-4-COO$^-$ in D_2O can be represented by a Gaussian function, the 2D-IR spectrum at the population time of 0.2 ps is elongated along the diagonal direction, which indicates that there is a strong correlation between the ω_1 and ω_3 vibrational frequencies. At longer population times, the lineshape of the 2D-IR spectrum becomes round, which is attributed to the loss of the correlation with evolution of the local environment around 9-FL-4-COO$^-$. Therefore, same as in Section 4.3.4 and Section 6.3.4, I conducted a center line slope (CLS) analysis to obtain information on the frequency fluctuations of 9-FL-4-COO$^-$ in D_2O [39, 40].

The green lines in Figure 8.4(b) are the center lines of the 2D-IR spectra. The CLS is obtained from the slope of these lines with respect to the ω_1 axis at each population time. As shown in Figure 8.8(a), the CLS of 9-FL-4-COO$^-$ has the initial value of approximately 0.43, which indicates that 9-FL-4-COO$^-$ in D_2O shows the frequency fluctuations in the fast modulation limit. Moreover, the CLS of 9-FL-4-COO$^-$ exhibits the decay due to the slower frequency fluctuations. Consequently, in order to represent these behaviors of the CLS curve, I assumed the FFTCF of 9-FL-4-COO$^-$ as:

$$C_\omega(t_2) = \delta(t_2)/T_2^* + \Delta_C^2 \exp\left(-t_2/\tau_C\right) + \Delta_0^2 \tag{8.10}$$

where T_2^* is the pure dephasing time constant to characterize the homogeneous broadening of the IR absorption spectrum. The Δ_C^2 and τ_C are the amplitude and correlation time of the frequency

fluctuations, respectively, which reflect the spectral diffusion process. Δ_0^2 is the static inhomogeneous component. Note that, due to the lack of polarization-controlled IR pump-probe experiment for 9-FL-4-COO^- in D_2O, there are no data on the vibrational energy relaxation (VER) and rotational relaxation time constants of the solute. In earlier work, Spears and Steinmetz investigated the rotational dynamics of resorufin, which is considered to have approximately the same volume as 9-FL-4-COO^-, in various kind of solvents, and reported that the anisotropy of fluorescence depolarization of the solute in H_2O at 19.2 °C and D_2O at 17.6 °C decays with time constants of 94 ps and 107 ps, respectively [41]. Moreover, different from NTBA (in Chapter 4), N_3-Ala and N_3-Pro (in Chapter 6), 9-FL-4-COO^- in D_2O can lead the anisotropy decay of the CO stretching mode by the whole molecular reorientation. Therefore, in this study, by assuming that the reorientation of 9-FL-4-COO^- in D_2O occurs on much longer time scale than the VER and spectral diffusion processes, I neglected the contribution from the rotational dynamics to the lineshape broadening. By fitting the CLS curve after $T = 0.2$ ps with a single exponential function, the τ_C is obtained. Furthermore, similar to Chapters 4 and 6, the T_2^*, Δ_C^2, and Δ_0^2 values of the FFTCF in Eq. (8.10) were determined by a numerical calculation to reproduce the experimentally obtained IR spectrum and the CLS [38, 39]. Here, by using the relative amplitude a_i shown in Table 8.1, the amplitude-averaged VER time constant (*i.e.* $a_1T_{10} + a_2T_{20}$) was used for the calculation of the vibrational broadening function. The obtained FFTCF parameters are summarized in Table 8.1. With respect to the IR absorption spectrum and CLS curve, the results of the CLS analysis for 9-FL-4-COO^- in D_2O are displayed in Figures 8.9(a) and (b), respectively. Here, as shown in Table 8.1, the contribution from the quasi-static frequency fluctuations (Δ_0) to the FFTCF of 9-FL-4-COO^- is much smaller than the other components. Therefore, I consider that the water dynamics around 9-FL-4-COO^-, which are characterized by the T_2^* and τ_C, dominates the frequency fluctuations of the CO stretching mode of the solute in D_2O.

Previously, the frequency fluctuations of *N*-methylacetamide (NMA) in D_2O were studied experimentally and theoretically. Woutersen *et al*. performed the 2D-IR measurement for NMA in D_2O and found that the frequency fluctuations are characterized by a correlation time constant of 1.6 ps [42]. By performing the molecular dynamics simulation for this system, they concluded that the frequency fluctuations arise from the HB dynamics between the solute and water molecules. Here, as mentioned in Chapters 4 and 6, I found that the FFTCFs of ions in water contain the decaying component with the solute-independent time constant of

approximately 1 ps, which is considered to result from the collective motion of the HB network [14, 17]. From the comparison with these previous works, this result for 9-FL-4-COO^- in D_2O suggests that different kind of hydration dynamics and/or solute-solvent interactions cause the slower frequency fluctuations of the solute (*i.e.* τ_C = 2.8 ps, see Table 8.1).

One possible origin of the slower frequency fluctuations of 9-FL-4-COO^- in D_2O is hydrophobic hydration dynamics. As displayed in Figure 8.1(b), the CO group of 9-FL-4-COO^- is neighboring to the large hydrophobic group, that is, fluorene ring with two benzene rings and one cyclopentadiene. Therefore, we can expect that the fluorene ring strongly affects the water structure and dynamics around the CO group. In order to support this possibility, I performed the 2D-IR measurement for acetone in D_2O. Although an acetone molecule has two methyl groups around the CO group, the hydrophobic effect of the groups is considered to be weaker than that of the fluorene ring of 9-FL-4-COO^-. The result of the 2D-IR experiment for acetone in D_2O is summarized in Appendix 8.B. Figure 8.B.3 shows the CLS curve of acetone in D_2O. The decay can be fitted by a single exponential function, which provides a correlation time constant of 1.6 ± 0.2 ps. Hence, by comparing the 2D-IR results of 9-FL-4-COO^- and acetone in D_2O, I consider that the fluorene ring of 9-FL-4-COO^- likely provides the hydrophobic effect on surrounding water molecules and the interactions with water molecules in the vicinity of the fluorene ring leads the slow frequency fluctuations to the CO stretching mode of 9-FL-4-COO^-.

Another possible origin of the slow frequency fluctuations is associated with the lower relative dielectric constant around 9-FL-4-COO^-. As mentioned in Chapter 5, by calculating the radial-dependence of the electrostatic potential on NTBA and SCN^- (see Figure 5.10), I found that the effective distance of the electrostatic potential on NTBA is longer than that on SCN^-. Based on these results, I consider that the relative dielectric constant around NTBA is lower than that around SCN^-, which may be due to the existence of a non-polar group (*i.e.* aromatic ring) in NTBA. If this mechanism can be also applied to 9-FL-4-COO^-/water system, since the size of a non-polar group (*i.e.* fluorene ring) of 9-FL-4-COO^- is larger than that of NTBA, the relative dielectric constant around 9-FL-4-COO^- is much lower than that in bulk. Therefore, one can expect that the contribution of the electrostatic interactions from water molecules further away from the first (or second) hydration shell of the solute becomes more important. Here, as shown in Figure 8.C, the decay of the total dipole moment time correlation function for water molecules with larger cutoff distance *r* becomes slower and getting closer to that of bulk water. This means

that the total dipole moment time correlation function gets to reflect the collective reorientational motions of water molecules with increasing the cutoff distance. Consequently, by reflecting such slower collective water dynamics, the CO vibrational frequency fluctuations of 9-FL-4-COO^- would undergo on a slower time scale than 1 ps. A theoretical study based on the MD simulation will help to provide more detailed insight into the vibrational frequency fluctuations of the CO stretching mode of 9-FL-4-COO^- in D_2O.

8.4. Conclusion

In this chapter, by using two different 9-FL derivatives, 9-FL-2-COO^- and 9-FL-4-COO^-, effects of the COO^- group on the CO vibrational frequency fluctuations in D_2O were investigated by 2D-IR spectroscopy.

As expected, depending on the molecular structure, 9-FL-2-COO^- and 9-FL-4-COO^- exhibited different lineshapes of the IR absorption spectra (see Figure 8.2): while the IR absorption spectrum of 9-FL-4-COO^- is characterized by a single Gaussian function, that of 9-FL-2-COO^- is characterized by a sum of two Gaussian functions. Based on the IR absorption measurements at different temperature and in THF solvent, I consider that the asymmetric spectral lineshape of 9-FL-2-COO^- results from two types of HB complexes between 9-FL-2-COO^- and D_2O molecules (*i.e.* [9-FL-2-COO^-:D_2O] and [9-FL-2-COO^-:$(D_2O)_2$]). On the other hand, from the result that the peak wavenumber of the IR absorption band of 9-FL-4-COO^- is approximately located at the center of those of 9-FL-2-COO^-, I consider that the IR absorption spectrum of 9-FL-4-COO^- in D_2O is merged into one absorption band due to the rapid formation and dissociation of the HB.

The 2D-IR measurement for 9-FL-2-COO^- in D_2O revealed that the 2D-IR spectra exhibit more distinctive cross peak signal with population time t_2 increasing, which is attributed to the chemical exchange process between [9-FL-2-COO^-:D_2O] and [9-FL-2-COO^-:$(D_2O)_2$] (see Figure 8.7). From the fitting analysis with the model function given by Eq. (8.8) [23, 31], I found that the interconversion rates of [9-FL-2-COO^-:$(D_2O)_2$] into [9-FL-2-COO^-:D_2O] (*i.e.* HB dissociation) and *vice versa* (*i.e.* HB formation) are 2.0 ps and 1.0 ps, respectively. Different from 9-FL-4-COO^-, a water molecule can form two HBs with CO group and COO^- group of 9-FL-2-COO^- simultaneously. Therefore, it can be suggested that this bridged-type HB plays an important role in the vibrational frequency fluctuations of 9-FL-2-COO^- in D_2O.

On the other hand, the temporal evolution of the 2D-IR spectrum of 9-FL-4-COO^- in D_2O was analyzed by the center line slope (CLS) method [39, 40]. From the CLS analysis, I found that the FFTCF of 9-FL-4-COO^- can be characterized by Eq. (8.10) with parameters listed in Table 8.1. Although the FFTCFs of ions in water have been found to exhibit the solute-independent decays on approximately 1 ps time scale [6-11], the CO vibrational frequency fluctuations of 9-FL-4-COO^- in D_2O are characterized slower time constant of 2.8 ps than that in the previous studies (see τ_C in Table 8.1). Based on the fact that the FFTFC of acetone in D_2O possesses the decay component with the time constant of 1.6 ps (see Appendix 8.B), I conclude that the slower CO vibrational frequency fluctuations of 9-FL-4-COO^- in D_2O may reflect the dynamics of surrounding water molecules, which are affected by the hydrophobic effect from the fluorene ring of 9-FL-4-COO^-.

References

1. R. M. Stratt and M. Maroncelli, *J. Phys. Chem.*, **100**, 12981 (1996).

2. G. A. Voth and R. M. Hochstrasser, *J. Phys. Chem.*, **100**, 13034 (1996).

3. C. L. Perrin and J.B. Nielson, *Annu. Rev. Phys. Chem.*, **48**, 511 (1997).

4. G. R. Desiraju and T. Steiner, "*The Weak Hydrogen Bond, in: Structural Chemistry and Biology"*, New York, Oxford University Press (1999).

5. I. Ohmine and H. Tanaka, *Chem. Rev.*, **93**, 2545 (1993).

6. K. Ohta, H. Maekawa, and K. Tominaga, *J. Phys. Chem. A*, **108**, 1333 (2004).

7. K. Ohta, J. Tayama, S. Saito, and K. Tominaga, *Acc. Chem. Res,*, **45**, 1982 (2012).

8. P. Hamm, M. Lim, R. M. Hochstrasser, *Phys. Chem. Lett*, **81**, 5326 (1998).

9. M. Kozinski, S. Garrett-Roe, and P. Hamm, *Chem. Phys.*, **341**, 5 (2007).

10. J. F. Brookes, K. M. Slenkamp, M. S. Lynch, and M. Khalil, *J. Phys. Chem. A*, **177**, 6234 (2013).

11. K. M. Slenkamp, M. S. Lynch, J. F. Brookes, C. C. Bannan, S. L. Daifuku, and M. Khalil, *Structural Dynamics*, **3**, 023609 (2016).

12. J. Stenger, D. Madsen, P. Hamm, E.T.J. Nibbering, and T. Elesaesser, *Phys. Rev. Lett.*, **87**, 027401 (2001).

13. J. Stenger, D. Madsen, P. Hamm, E.T.J. Nibbering, and T. Elesaesser, *J. Phys. Chem. A*, **106**, 2341 (2002).

14. C. J. Fecko, J. D. Eaves, J. J. Loparo, A. Tokmakoff and P. L. Geissler, *Science*, **301**, 1698 (2003).

15. S. Yeremenko, M. S. Pshenichnikov, and D. A. Wiersma, *Chem. Phys. Lett.*, **369**, 107 (2003).

16. J. B. Asbury, T. Steinel, C. Stromberg, S. A. Corcelli, C. P. Lawrence, J. L. Skinner, and M. D. Fayer, *J. Phys. Chem. A*, **108**, 1107 (2004).

17. C. J. Fecko, J. J. Loparo, S. T. Loberts, and A. Tokmakoff, *J. Chem. Phys.*, **122**, 054506 (2005).

18. J. J. Loparo, S. T. Roberts, and A. Tokmakoff, *J. Chem Phys.*, **125**, 194521 (2006).

19. S. Woutersen, Y. Mu, G. Stock, and P. Hamm, *Chem. Phys.*, **137**, 266 (2001).

20. H. Son, D. Nam, and S. Park, *J. Phys. Chem. B*, **117**, 13604 (2013).

21. A. Ghosh, A. Remorino, M. J. Tucker, and R. M. Hochstrasser, *Chem. Phys. Lett.*, **469**, 325

(2009).

22. D. E. Moilanen, D. Wong, D. E. Rosenfeld, E. E. Fenn, and M. D. Fayer, *Proc. Natl. Acad. Sci. USA*, **106**, 375 (2009).

23. Y. S. Kim and R. M. Hochstrasser, *Proc. Natl. Acad. Sci. USA*, **102**, 11185 (2005).

24. M. Candelaresi, M. Pagliai, M. Lima, and R. Righini, *J. Phys. Chem. A*, **113**, 12783 (2009).

25. K. Kwak, J. Zheng, H. Cang, and M. D. Fayer, *J. Phys. Chem. B*, **110**, 19998 (2006).

26. Y. S. Kim and R. M. Hochstrasser, *J. Phys. Chem. B*, **110**, 8531 (2006).

27. S. Park and M. D. Fayer, *Proc. Natl. Acad. Sci. USA*, **104**, 16731 (2007).

28. S. Park, D. E. Moilanen, and M. D. Fayer, *J. Phys. Chem. B*, **102**, 5279 (2008).

29. S. Park, M. Odelius, and K. J. Gaffney, *J. Phys. Chem. B*, **113**, 7825 (2009).

30. S. M. Kashid, G Y. Jin, S. Bagchi, and Y. S. Kim, *J. Phys. Chem. B*, **119**, 15334 (2015).

31. Y. S. Kim and R. M. Hochstrasser, *J. Phys. Chem. B*, **113**, 8231 (2009).

32. L. Chuntonov, I. M. Pazos, J. Ma, and F. Gai, *J. Phys. Chem. B*, **119**, 4512 (2015).

33. H. Hirai, M. Banno, K. Ohta, D. K. Palit, and K. Tominaga, *Chem. Phys. Lett.*, **450**, 44 (2007).

34. Y. Fukui, K. Ohta, and K. Tominaga, *Faraday Discuss.*, **177**, 65 (2015).

35. D. Watanabe and H. Hamaguchi, *J. Chem. Phys.*, **123**, 034508 (2005).

36. P. Hamm, M. Lim, R. M. Hochstrasser, *J. Phys. Chem. B*, **102**, 6123 (1998).

37. M. D. Fayer, *Annu. Rev. Phys. Chem.*, **60**, 21 (2009).

38. K. Kwak, H. Lee, and M. Cho, *J. Chem. Phys.*, **120**, 1477 (2004).

39. K. Kwak, S. Park, I. J. Finkelstein, and M. D. Fayer, *J. Chem. Phys.*, **127**, 124503 (2007).

40. K. Kwak, D. E. Rosenfeld, and M. D. Fayer, *J. Chem. Phys.*, **128**, 204505 (2008).

41. K. G. Spears and K. M. Steinmetz, *J. Phys. Chem.*, **89**, 3623 (1985).

42. S. Woutersen, R. Pfister, P. Hamm, Y. Mu, D. S. Kosov, and G. Stock, *J. Chem. Phys.*, **117**, 6833 (2002).

Figures and Table

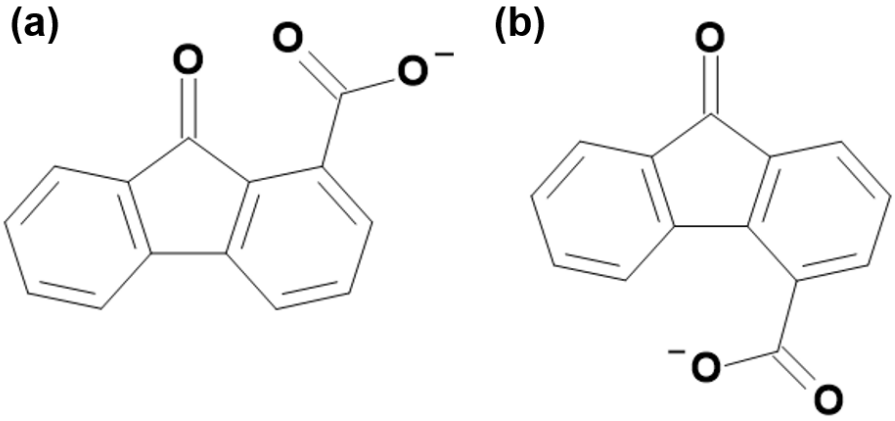

Figure 8.1. Molecular structure of (a) 9-fluorenone-2-carboxylic acid (abbreviated as 9-FL-2-COO^-) and (b) 9-Oxofluorene-4-carboxylic acid (abbreviated as 9-FL-4-COO^-).

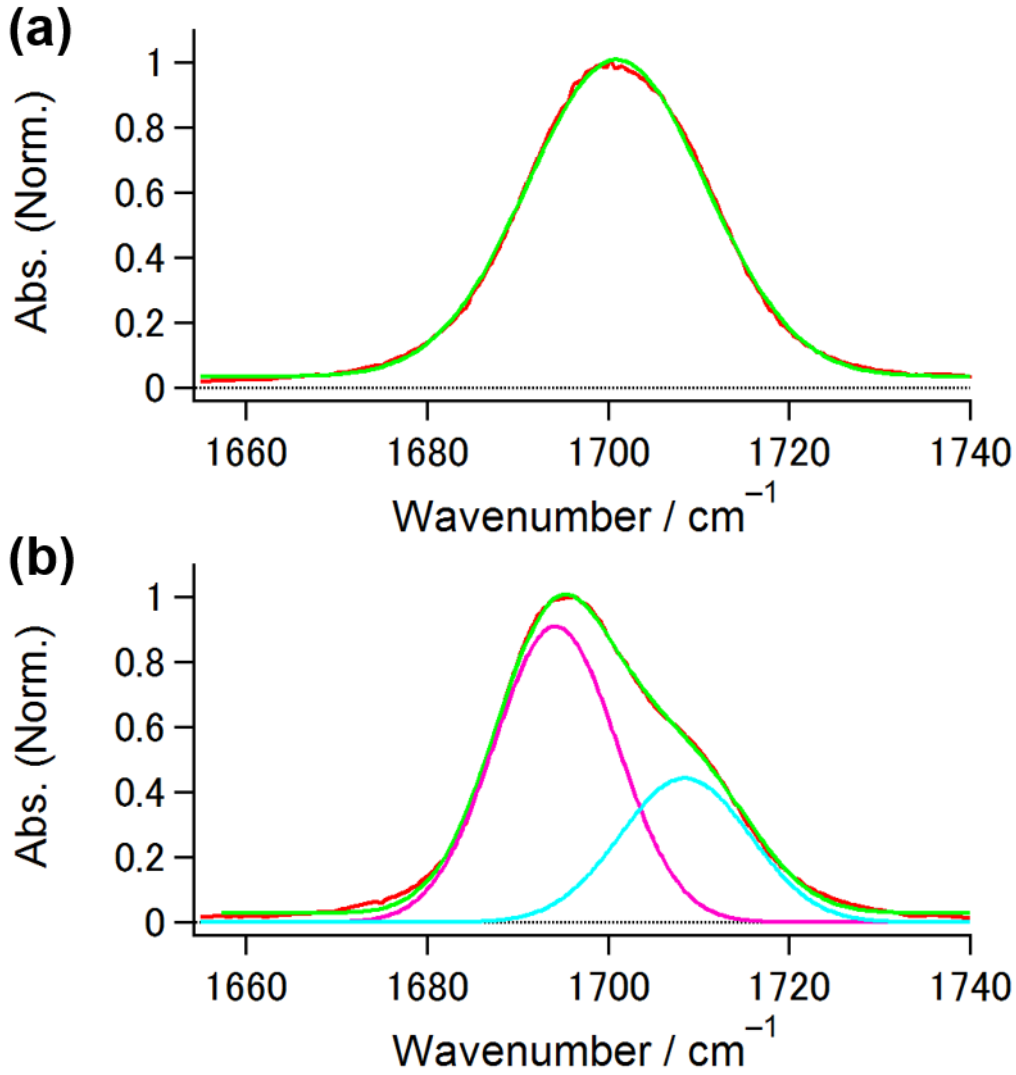

Figure 8.2. IR absorption spectra of the CO stretching modes of (a) 9-FL-4-COO$^-$ and (b) 9-FL-2-COO$^-$ in D_2O measured at 293 K. The green line represents the fitting result with a Gaussian function for 9-FL-4-COO$^-$ and a sum of two Gaussian functions for 9-FL-2-COO$^-$. The pink and light-blue lines are the IR absorption bands related to [9-FL-2-COO$^-$:$(D_2O)_2$] and [9-FL-2-COO$^-$:D_2O], respectively.

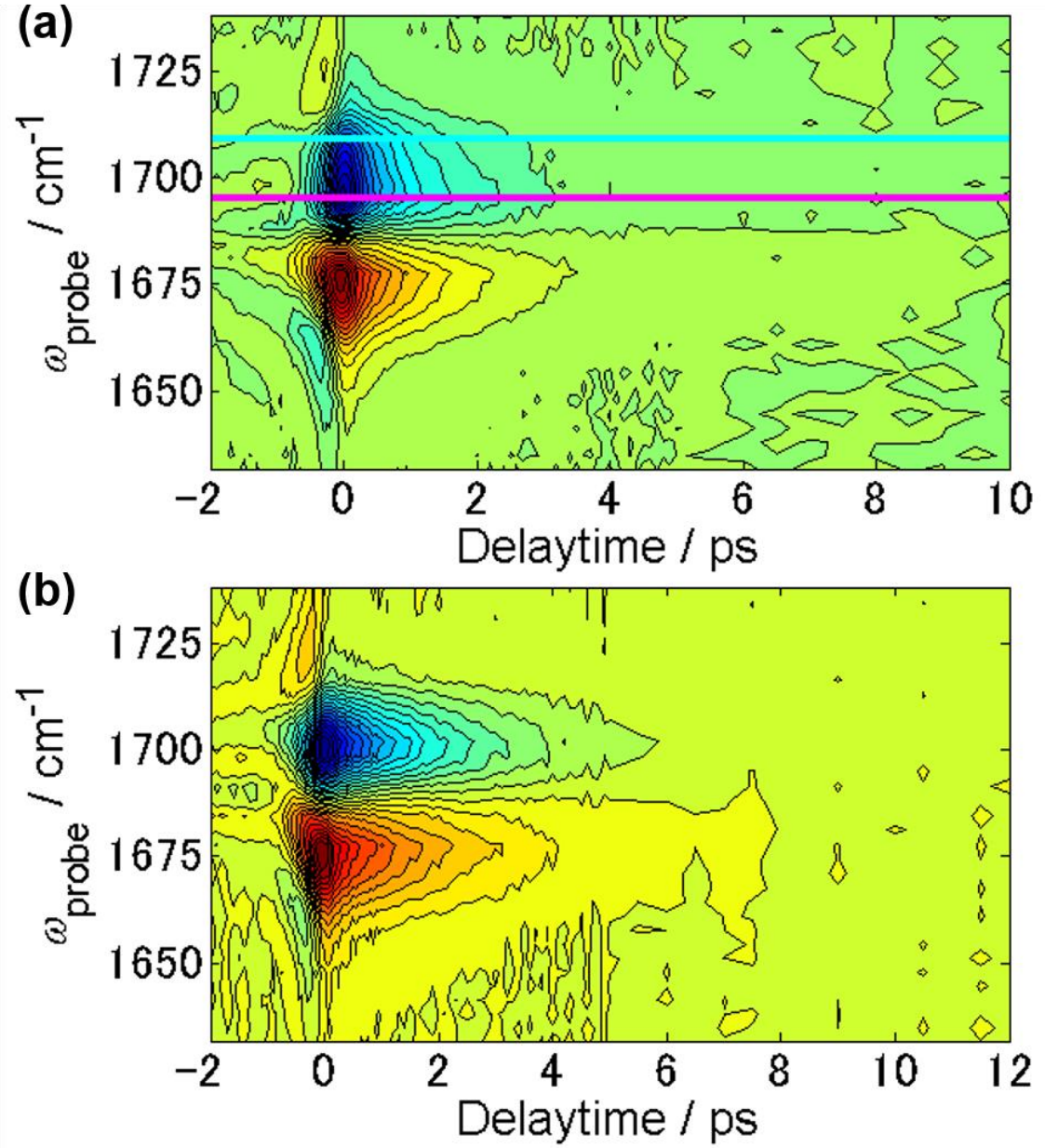

Figure 8.3. Frequency resolved IR pump-probe signals of the CO stretching modes of (a) 9-FL-2-COO^- and (b) 9-FL-4-COO^- in D_2O measured at 293 K. The temporal profiles of IR pump-probe signals due to the GSB + SE of [9-FL-2-COO^-:$(D_2O)_2$] and [9-FL-2-COO^-:D_2O] are taken from the slice of the frequency resolved IR pump-probe signal along pink and light-blue lines, respectively (see Figure 8.4).

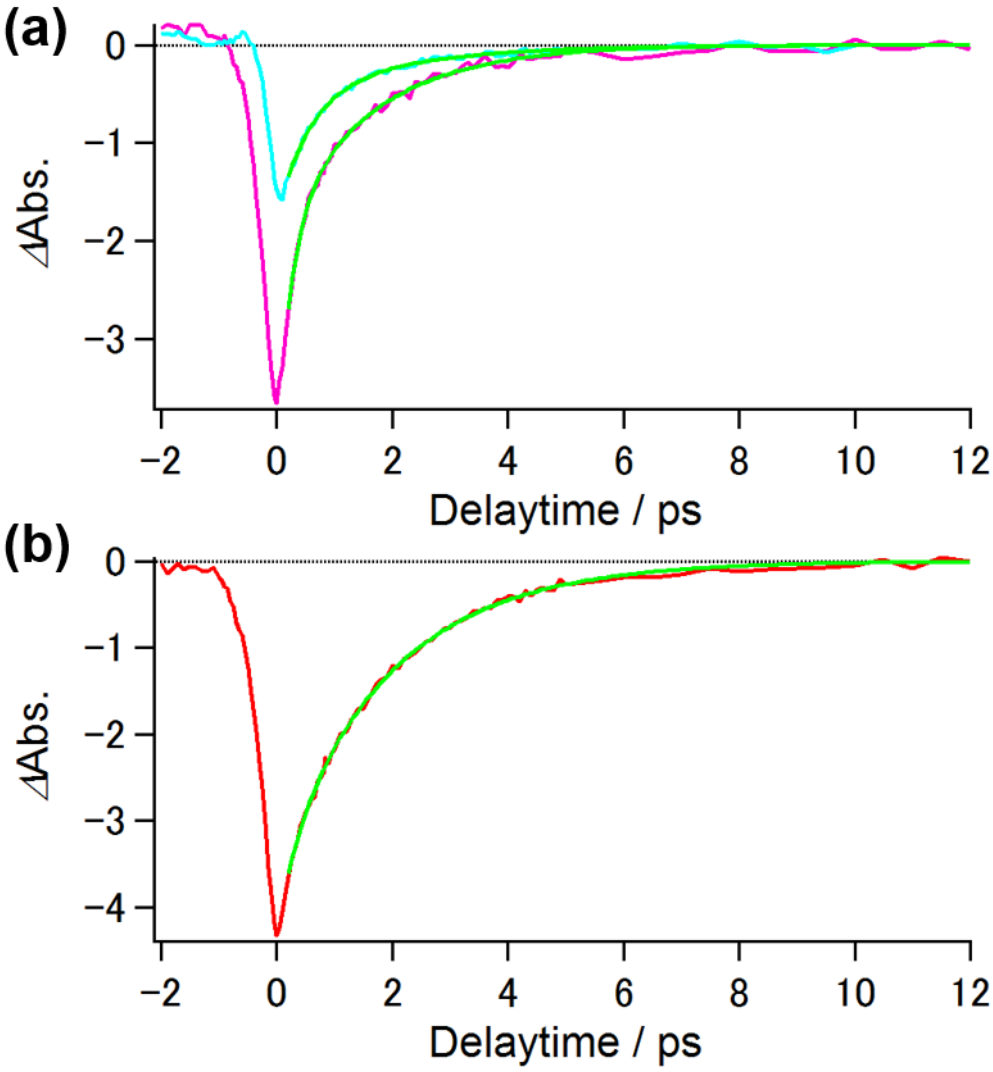

Figure 8.4. Temporal profiles of IR pump-probe signals of the CO stretching modes of (a) 9-FL-2-COO^- and (b) 9-FL-4-COO^- in D_2O. The temporal profiles of IR pump-probe signals of [9-FL-2-COO^-:$(D_2O)_2$] (pink), [9-FL-2-COO^-:D_2O] (light-blue) are taken from the peak wavenumbers of the GSB + SE signals at 1695.1 cm^{-1} and 1712.8 cm^{-1}, respectively, and that of 9-FL-4-COO^- (red) is taken at 1702.1 cm^{-1}. The green lines represent the fits to the IR pump-probe signals with a double-exponential function.

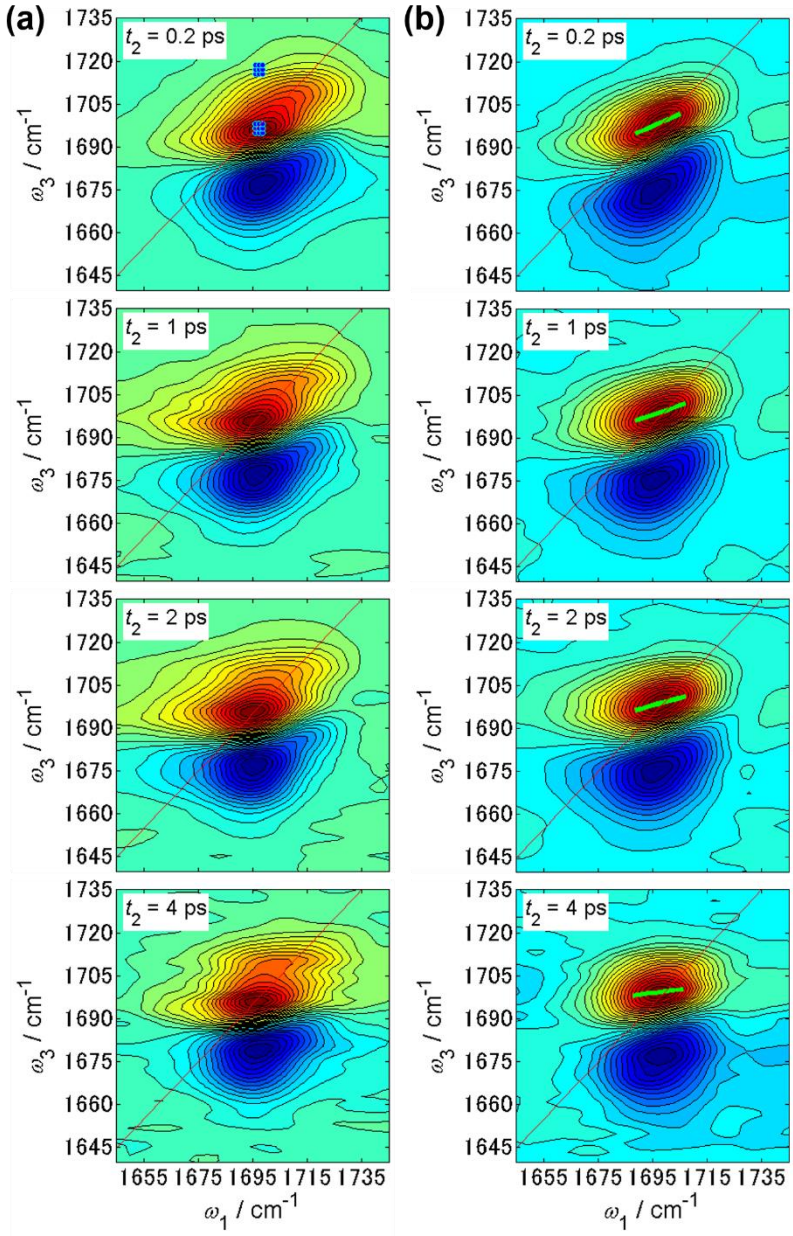

Figure 8.5. 2D-IR spectra of the CO stretching mode of (a) 9-FL-2-COO$^-$ and (b) 9-FL-4-COO$^-$ in D_2O at t_2 times of 0.2 ps, 1 ps, 2 ps, and 4 ps. The red lines indicate where the pump frequency (ω_1) is equal to the probe frequency (ω_3). The close circles in the 2D-IR spectra of 9-FL-2-COO$^-$ represent the frequency range to calculate of the S_{AA} and S_{AB} (see Section 8.3.3); ω_1 = 1695.8 − 1698.6 cm^{-1} and ω_3 = 1694.8 − 1698.0 cm^{-1} for the S_{AA}, and ω_1 = 1695.8 − 1698.6 cm^{-1} and ω_3 = 1715.6 − 1718.8 cm^{-1} for the S_{AB}. The green lines in the 2D-IR spectra of 9-FL-4-COO$^-$ indicate the center lines of the 2D-IR signals originated from the $\nu = 0 - 1$ vibrational transition.

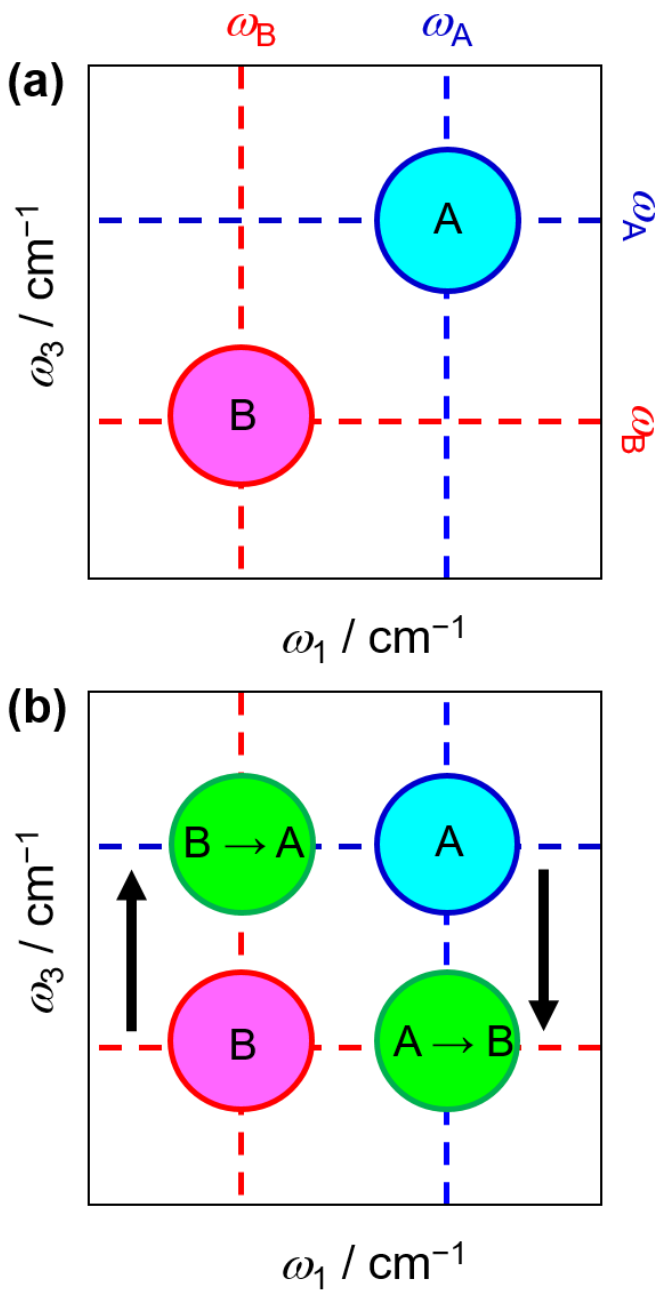

Figure 8.6. Schematic illustration of the influence of chemical exchange process on the 2D-IR spectrum between states A and B in chemical equilibrium. (a) At shorter t_2 time when no exchange dynamics occurs, two 2D-IR signals are observed along the diagonal direction peaks: (ω_1, ω_3) = (ω_A, ω_A) and (ω_B, ω_B) for states A and B, respectively. (b) At sufficiently longer t_2 time, 2D-IR signals due to the chemical exchange are growing in the off-diagonal regions: cross-peak signals at (ω_1, ω_3) = (ω_A, ω_B) and (ω_B, ω_A) are related to the interconversion of states A into B and *vice versa*, respectively.

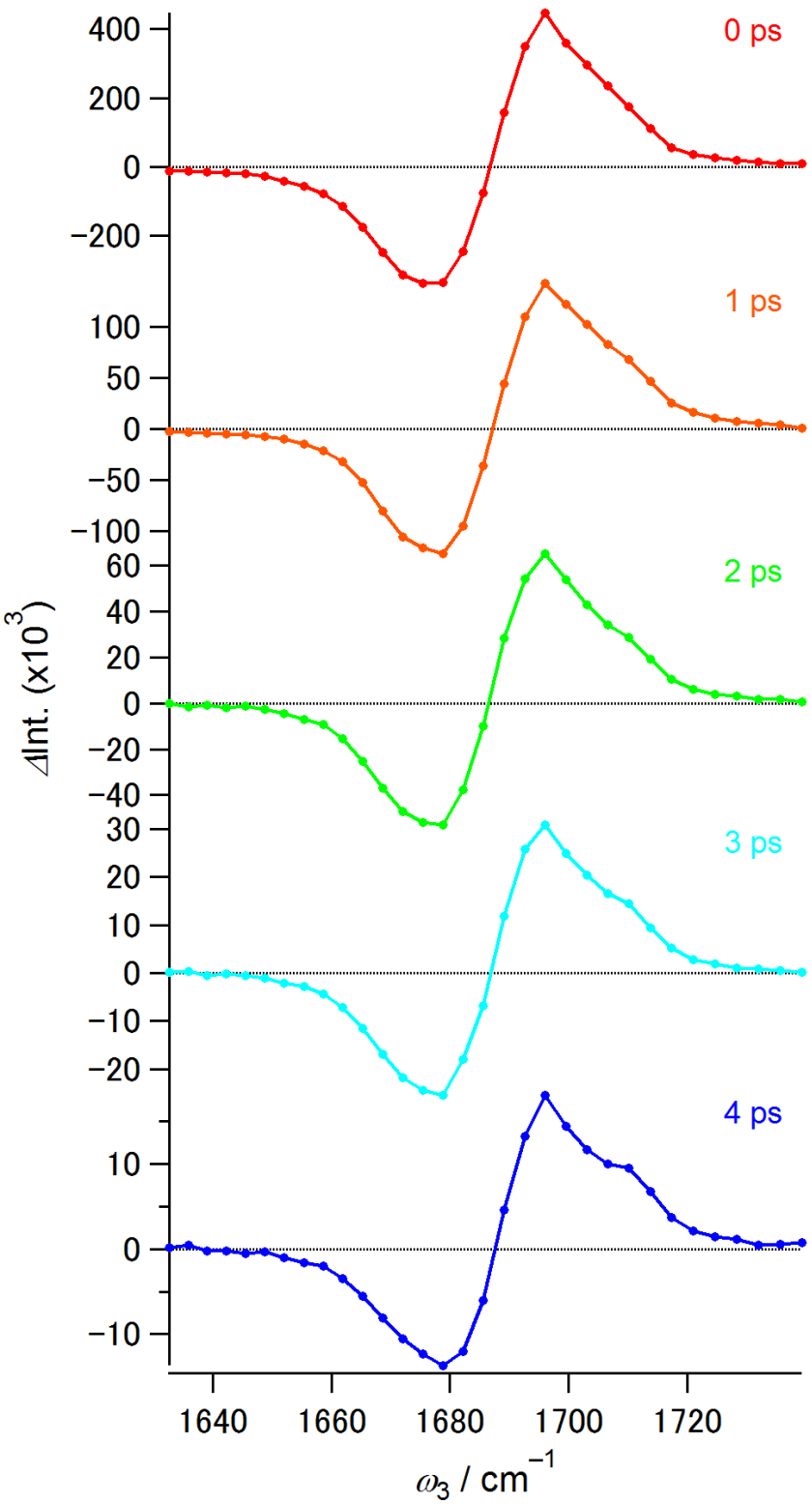

Figure 8.7. Slices taken from the 2D-IR spectra of 9-FL-2-COO^- in D_2O at ω_1 = 1697.1 cm^{-1} for several t_2 times. The population time t_2 flows from the top to bottom.

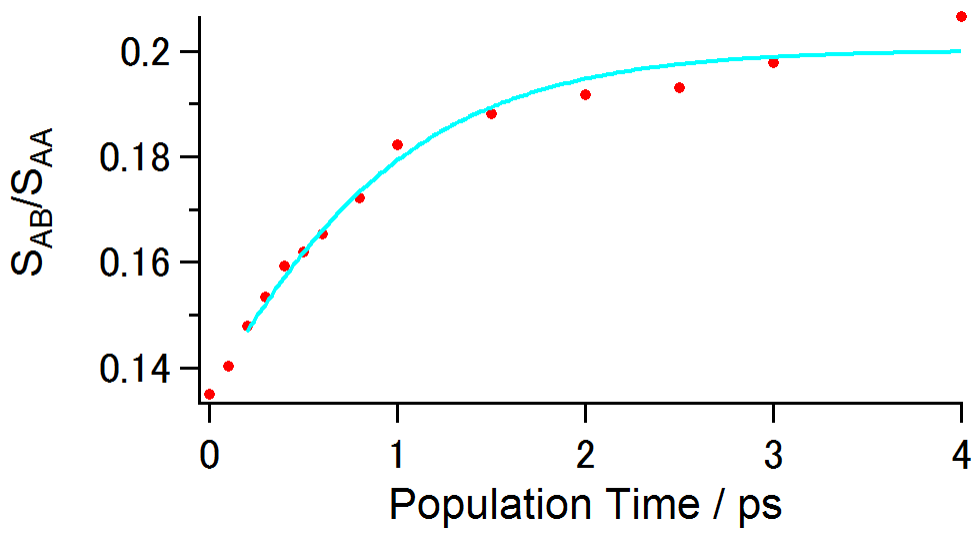

Figure 8.8. Temporal evolution of the ratio of the cross-peak signal (S_{AB}) to diagonal peak (S_{AA}). Closed circles are the experimental data and the light-blue line represents the fitting result with the two-state exchange model function given by Eq. (8.8).

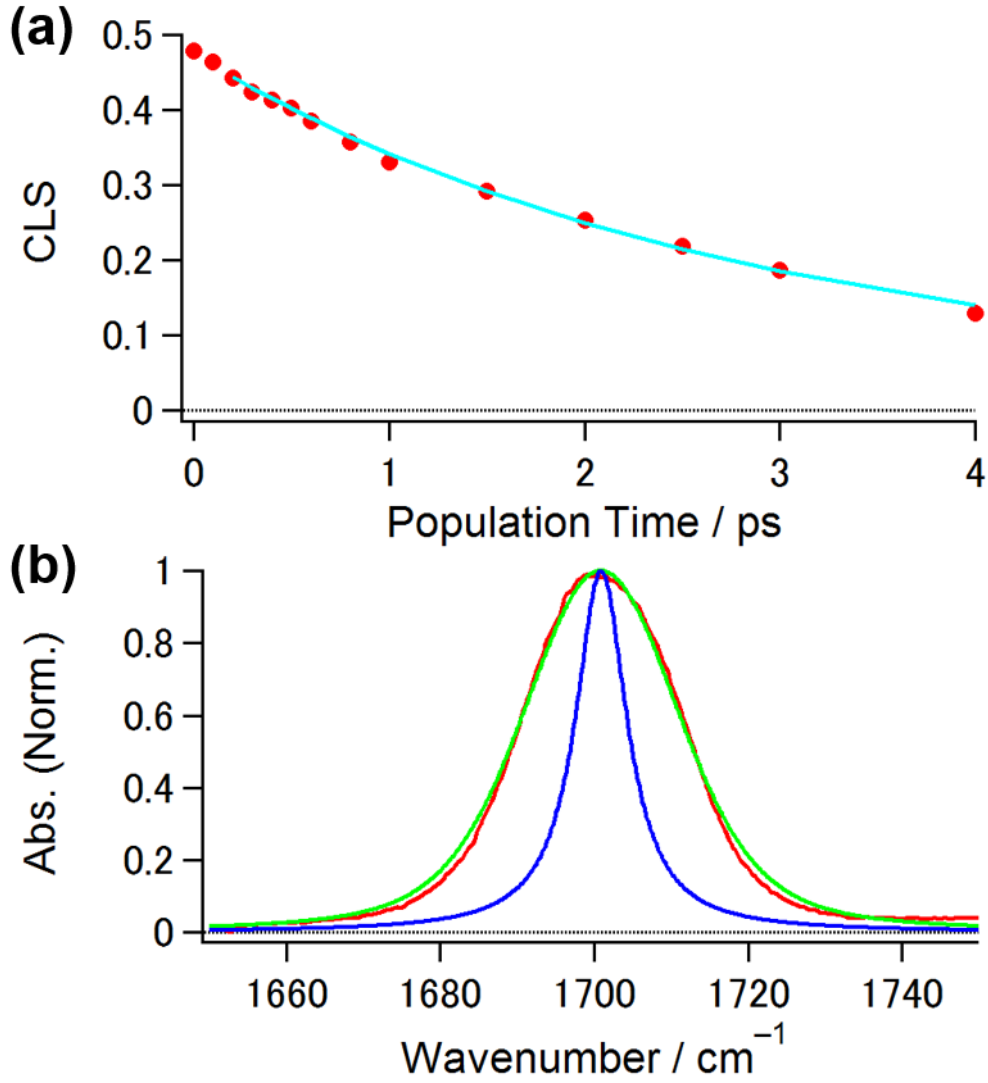

Figure 8.9. (a) CLS decay curve of 9-FL-4-COO$^-$ in D_2O. The closed circles and light-blue line indicate experimentally and numerically obtained CLSs, respectively. (b) Comparison of the experimental and simulated FT-IR spectra of 9-FL-4-COO$^-$ in D_2O. The red line indicates the experimental FT-IR spectra, and the green and blue lines correspond to the simulated ones with and without the slow decaying components in the FFTCF, respectively.

Table 8.1. Parameters that characterize the normalized IR absorption spectra of the CO stretching mode of 9-FL-2-COO^- and 9-FL-4-COO^- in D_2O as well as the vibrational dynamics of them, which were obtained from nonlinear IR experiments.

Solute	Linear Absorption Spectrum[a]		Population Relaxation[b]				Spectral Diffusion			
	ω_0 / cm^{-1}	FWHM / cm^{-1}	a_1	T_{10} / ps	a_2	T_{20} / ps	T_2^* / ps	Δ_C / ps^{-1}	τ_C / ps	Δ_0 / ps^{-1}
9-FL-2-COO^- (Lower freq.)	1694.0	15.9	0.5 ± 0.1	0.3 ± 0.1	0.5 ± 0.1	1.6 ± 0.1	–	–	–	–
9-FL-2-COO^- (Higher freq.)	1708.0	15.5	0.7 ± 0.1	0.6 ± 0.1	0.3 ± 0.1	2.0 ± 0.2	–	–	–	–
9-FL-4-COO^-	1701.3	22.9	0.2 ± 0.1	0.4 ± 0.1	0.8 ± 0.1	1.9 ± 0.1	2.2	1.6	2.8	0.4

(a) ω_0: wavenumber at band peak, FWHM: full width at half maximum.

(b) a_i and T_{i0}: relative amplitude and decay time constant of ith component in the fitting function; $a_1\exp(-T/T_{10}) + a_2\exp(-T/T_{20})$.

Appendix 8.A. IR Absorption Measurements for 9-FL-2-COO^- in D_2O at Different Temperature and in THF

Figure 8.A.1 displays the IR absorption spectra of the CO stretching mode of 9-FL-2-COO^- in D_2O measured at different temperature ranging from 283 K to 313 K. As shown in Figure 8.A.1, I found that the intensities of the higher and lower frequency bands of 9-FL-2-COO^- increase and decrease by increasing temperature, respectively. Therefore, from the similarity to the temperature dependence of the IR absorption spectrum of 9-FL in 1-octanol, I consider that the asymmetric IR band of 9-FL-2-COO^- is considered to reflect two types of HB complexes between 9-FL-2-COO^- and D_2O molecules in the D_2O solution. Moreover, Figure 8.A.2 shows the IR absorption spectrum of the CO stretching mode of 9-FL-2-COO^- in tetrahydrofuran (THF), which is an aprotic solvent. As displayed in Figure 8.A.2, 9-FL-2-COO^- in THF exhibits the sharper absorption at around 1724 cm^{-1}, which is likely due to the IR absorption of a non-hydrogen bonded 9-FL-2-COO^-. Note that, because the carboxyl group of 9-FL-2-COO^- is protonated in THF solution, the CO absorption spectrum of the carboxyl group might appear at around 1700 cm^{-1}. However, because no distinctive absorption bands is observed in this frequency region except for the absorption band shown in Figure 8.A.2, I assign the absorption spectrum to the non-hydrogen bonded 9-FL-2-COO^-. Therefore, based on the results that the IR absorption spectrum in D_2O is observed in the lower frequency side than that in THF, I assign the higher and lower frequency absorption bands in D_2O to a 9-FL-2-COO^- complex with one D_2O molecule (described as [9-FL-2-COO^-:D_2O]), and a 9-FL-2-COO^- complex with two methanol molecules (described as [9-FL-2-COO^-:$(D_2O)_2$]), respectively.

Figures

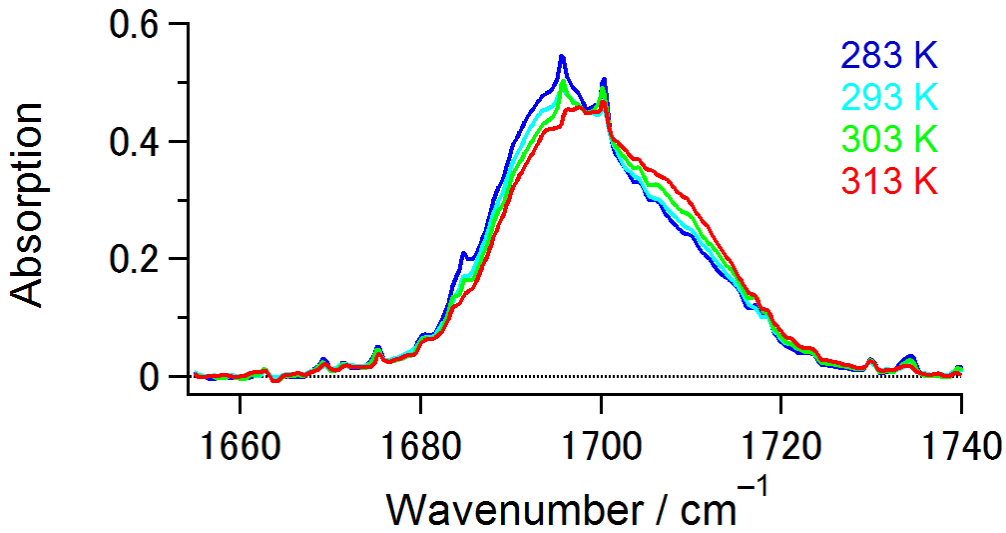

Figure 8.A.1. Temperature-dependence of the IR absorption spectrum of 9-FL-2-COO$^-$ in D_2O. As the temperature increases, the IR absorption at around 1695 cm^{-1} and 1710 cm^{-1} are decreasing and increasing, respectively.

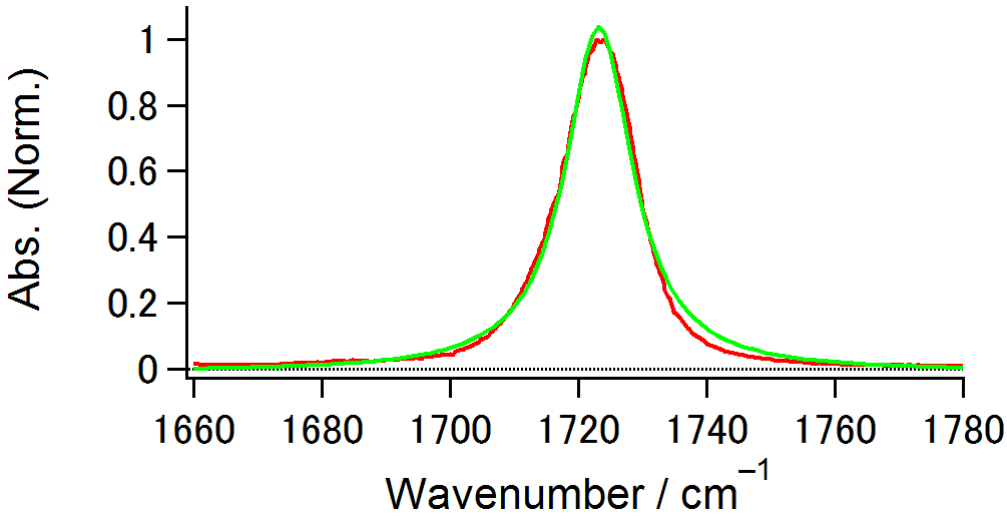

Figure 8.A.2. IR absorption spectrum of the CO stretching mode of 9-FL-2-COO$^-$ in THF. The red and green lines represent the experimental data and fitting result with a single Lorentzian function, respectively.

Appendix 8.B. 2D-IR Measurements for Acetone in D_2O

Figure 8.B.1 displays the IR absorption spectra of the CO stretching mode of acetone in D_2O (sample concentration: ~300 mM, optical path length: 50 μm). The IR absorption band can be fitted by a Lorentzian function, and the peak wavenumber and FWHM are found to be 1697.5 cm^{-1} and 14.8 cm^{-1}, respectively.

The 2D-IR spectra of acetone in D_2O were measured at different t_2 times ranging from 0 ps to 4 ps. Figure 8.B.2 displays the 2D-IR spectra of acetone in D_2O at different population times. Same as 9-FL-4-COO^- in D_2O, the CLS of acetone was determined by the slope of the green lines with respect to the ω_1 axis (see Figure 8.B.2). The obtained CLS of acetone is presented in Figure 8.B.3 as a function of the t_2. By fitting the CLS curve after t_2 = 0.2 ps with a single exponential function, I revealed that the correlation time (τ_C in Eq. (8.3.9)) of acetone in D_2O is 1.6 ± 0.2 ps.

Figures

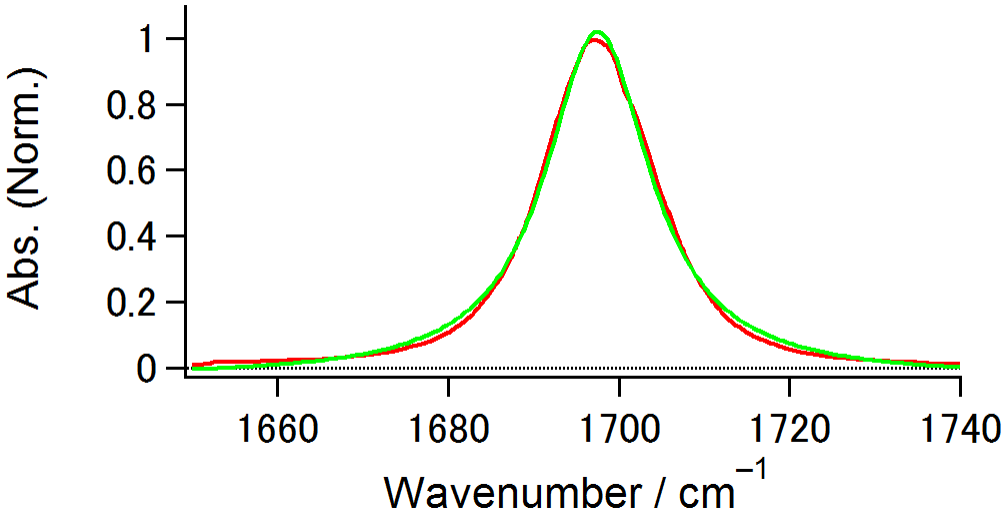

Figure 8.B.1. IR absorption spectrum of the CO stretching mode of acetone in D_2O. The red and green lines represent the experimental data and fitting result with a single Lorentzian function, respectively.

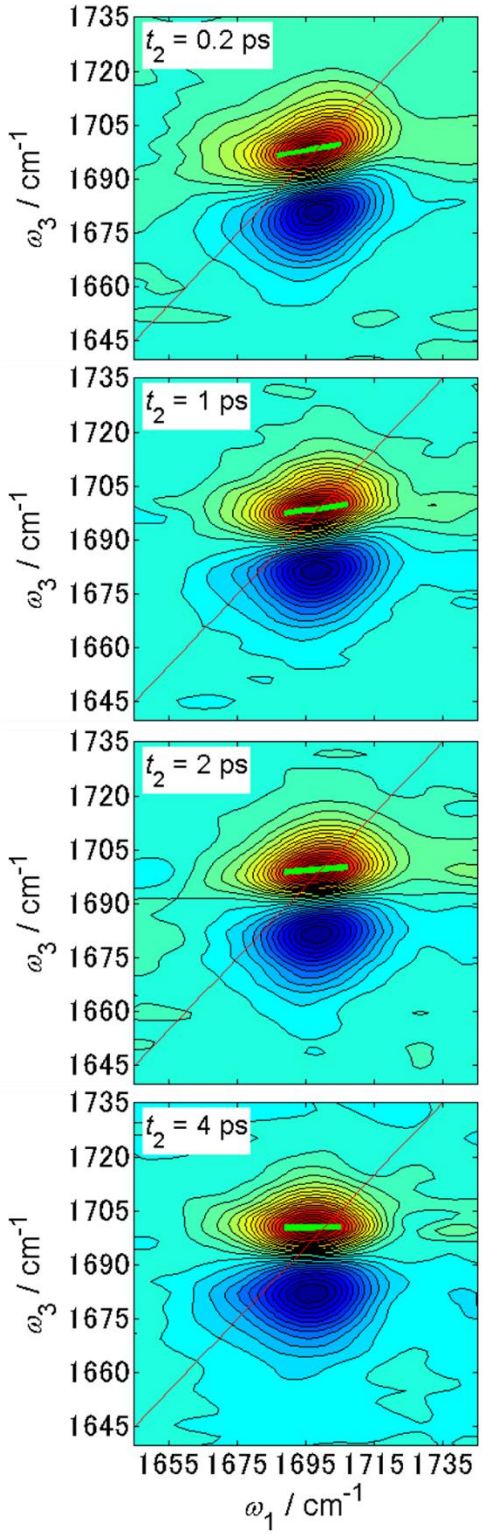

Figure 8.B.2. 2D-IR spectra of the CO stretching mode of acetone in D_2O at t_2 times of 0.2 ps, 1 ps, 2 ps, and 4 ps. The red lines represent the diagonal direction of the 2D-IR spectra. The green lines in the 2D-IR spectra indicate the center lines of the 2D-IR signals related to the GSB + SE signals.

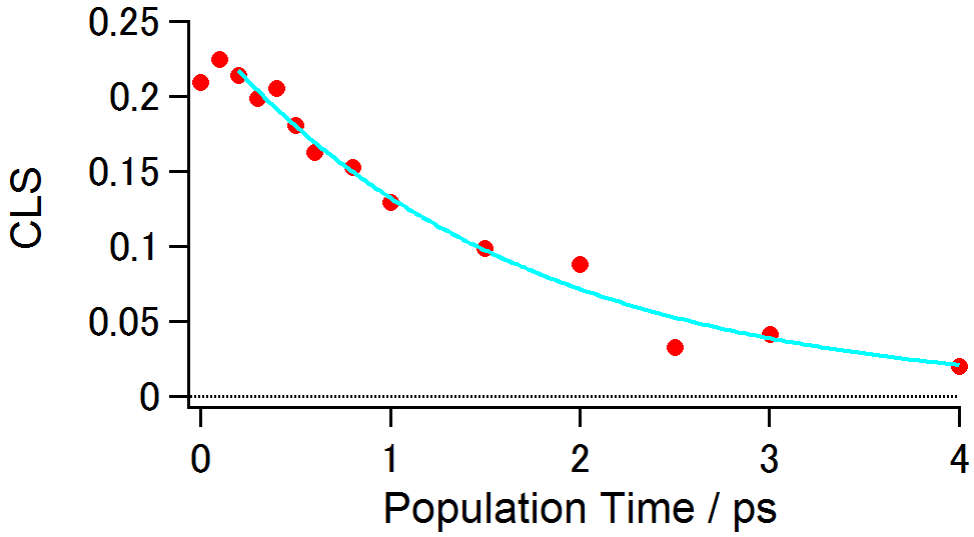

Figure 8.B.3. CLS decay curve of acetone in D_2O. The closed circles are the experimentally obtained CLS. The light-blue line represents the fitting result with a single exponential function, which provides the correlation time τ_C in Eq. (8.10)

Appendix 8.C. Radial-dependence of Collective Reorientatioanl Motions of Water Molecules

In order to investigate the radial-dependence of the collective water dynamics, by using the classical MD simulations for the bulk water system performed in Chapter 5, I calculated the normalized total dipole moment time correlation function for water molecules in bulk water system as follows:

$$C_{\mathrm{TDP,water}}(T,r) \equiv \frac{\left\langle \left(\sum_{i=1}^{N_{\mathrm{H_2O}}} \boldsymbol{\mu}_i(T) f_i(T,r) \right) \cdot \left(\sum_{j=1}^{N_{\mathrm{H_2O}}} \boldsymbol{\mu}_j(0) f_j(0,r) \right) \right\rangle}{\left\langle \left| \sum_{i=1}^{N_{\mathrm{H_2O}}} \boldsymbol{\mu}_i(0) f_i(0,r) \right|^2 \right\rangle} \tag{8.C.1}$$

where $\boldsymbol{\mu}_i(T)$ is the dipole moment vector of the ith water molecule, and N_{H2O} is the number of water molecules in the bulk water system (*i.e.* N_{H2O} = 1118). In order to characterize the radial-dependence of $C_{\mathrm{TDP,water}}(T, r)$, I defined the filtering function $f_i(T, r)$ as:

$$f_i(T,r) \equiv \frac{1}{2}\left(1 - \tanh\left[\gamma\left(\left|\mathbf{r}_C(T) - \mathbf{r}_i(T)\right| - r\right)\right]\right) \tag{8.C.2}$$

where γ is the damping constant (set to 10 Å^{-1}), and $\mathbf{r}_{\mathrm{C}}$ and $\mathbf{r}_j$ are the coordinates of the oxygen atoms of a central and ith water molecules, respectively. The r is a given cutoff distance, which is varied from 3.5 Å to 11.5 Å with a 2.0 Å step. Figures 8.C shows the series of the $C_{\mathrm{TDP,water}}(T, r)$ obtained from the bulk water system.

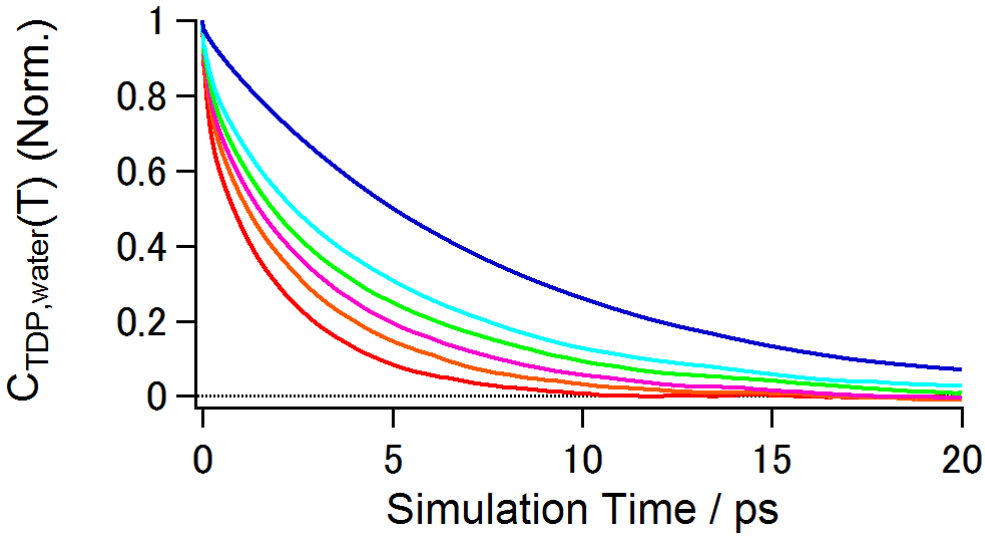

Figure 8.C. Radial-dependence of the $C_{\mathrm{TDP,water}}(T)$ for water molecules in bulk water system calculated by Eqs. (8.C.1) and (8.C.2). The cutoff distance r for each profile is as follows: r = 3.5 Å (red), 5.5 Å (orange), 7.5 Å (pink), 9.5 Å (green), 11.5 Å (light-blue), and no filtering (blue). The characteristic time constant $\tau_{1/e}$, which is defined as $C_{\mathrm{TDP,water}}(\tau_{1/e}) = e^{-1}C_{\mathrm{TDP,water}}(0)$, for each profile is as follows: 1.46 ps (red), 2.07 ps (orange), 2.52 ps (pink), 3.13 ps (green), 4.02 ps (right-blue), and 7.37 ps (blue).

Concluding Remarks

In this thesis, I experimentally and theoretically investigated the vibrational dynamics of the solutes in the hydrogen-bonding liquids.

In Chapter 2, as a theoretical background of 2D-IR spectroscopy, I derived the 3rd-order nonlinear response function and associated line broadening functions based on the time-dependent perturbation theory with appropriate assumptions. In Chapter 3, as an experimental background of 2D-IR spectroscopy, I summarized the method of generating ultrashort mid-IR pulses and optical setup for 2D-IR spectroscopy with 32-channel multi-channel MCT array detectors.

In Chapter 4, I examined the vibrational dynamics of SCN anti-symmetric stretching modes of NTBA and SCN^- in H_2O by using polarization-controlled IR pump-probe and 2D-IR spectroscopies with a 64-channel multi-channel MCT array detector. From the 2D-IR measurements for NTBA and SCN^- in H_2O, I elucidated that both the FFTCFs of the solutes are characterized by similar time constants of approximately 1 ps. In Chapter 5, to understand the molecular origin of these slow decay components (*i.e.* 1-ps decay components) of the FFTCFs of NTBA and SCN^- in H_2O, I performed the theoretical investigation on the SCN vibrational frequency fluctuations with the classical MD simulations for NTBA/water and SCN^-/water systems. By investigating the solute-solvent interactions which cause the SCN vibrational frequency fluctuations in detail, I elucidated that the radial-dependence of the electrostatic interactions for NTBA and SCN^- are distinctively different. While NTBA can feel electrostatic interactions induced by water molecules relatively apart from the solute (approximately up to 7 Å from the solute), those for SCN^- are almost dominated by the contribution from water molecules within the second hydration shell of the ion (< 5 Å from the solute). Therefore, in the case of NTBA/water system, I consider that the SCN vibrational frequency fluctuations on the 1 ps time scale reflect the collective water dynamics in bulk through the electrostatic interactions with such “bulk-like” water molecules. On the other hand, in the case of SCN^-/water system, based on the result that the hydrogen bond dynamics between water molecules in the vicinity of SCN^- is similar to that between water molecules in bulk, I consider that the 1-ps SCN vibrational frequency of SCN^- reflect the structural fluctuations of the hydrogen bond network through water molecules directly hydrogen-bonded to the ion.

In Chapter 6, by performing the polarization-controlled IR pump-probe and 2D-IR

measurements, I examined the vibrational dynamics of the N_3 anti-symmetric stretching mode of N_3-Ala, N_3-Pro, and N_3^- in H_2O. Similar to NTBA and SCN^- in H_2O, the CLS analyses for the experimentally observed 2D-IR spectra revealed that the FFTCFs of N_3-Ala, N_3-Pro, and N_3^- in H_2O possess the decay components with the time constants of about 1 ps. Moreover, from the anisotropy decay measurements for N_3-Ala and N_3-Pro in H_2O, I found that the structural degrees of freedom (*i.e.* structural flexibility around the N_3 group may influence the reorientational relaxation of the solutes. In Chapter 7, by using different three N_3-derivatized amino acids (*i.e.* N_3-Ala, N_3-Pro, and N_3-Nle) I examined the rotational dynamics of the N_3 groups of the vibrational probe molecules on a picosecond time scale in detail with polarization-controlled IR pump-probe spectroscopy. From the comparison among the rotational relaxation of the N_3 groups of N_3-Ala, N_3-Pro, and N_3-Nle in primary 1-alcohol solutions, I elucidated that the anisotropy decay of the N_3 group becomes faster with increasing the structural flexibility around the vibrational probe. Form the temperature-dependent anisotropy decay measurements, I revealed that the internal rotational motion of the N_3 groups of N_3-Ala and N_3-Nle are correlated with those of the neighboring alkyl chain.

In Chapter 8, I investigated the vibrational frequency fluctuations of the CO stretching modes of 9-FL-2-COO^- and 9-FL-4-COO^- in D_2O by using 2D-IR spectroscopy. From the comparison between the 2D-IR spectra of 9-FL-2-COO^- and 9-FL-4-COO^- in D_2O, I found that the hydrogen bond dynamics between the CO group of 9-FL-2-COO^- and surrounding water molecules is more suppressed than that of 9-FL-4-COO^-. I consider that the difference in the solute-solvent hydrogen bond dynamics likely results from the formation of bridged-type hydrogen bond between 9-FL-2-COO^- and a water molecule. From this result, it is suggested that water dynamics in the vicinity of a solute is determined by the delicate balance of solute-solvent interactions (*i.e.* combination of hydrophobic and hydrophilic interactions). On the other hand, from the 2D-IR experiment for 9-FL-4-COO^- in D_2O, I found that the FFTCF of the solute contains the decay component with a time constant of 2.8 ps, which is relatively slower than the slow decay component of the FFTCF of ions in water (*i.e.* 1-ps decay component). As a possible origin of the slow decay component of 9-FL-4-COO^- in D_2O, I consider that the CO vibrational frequency fluctuations may be affected by the dynamics of surrounding water molecules, which are affected by the hydrophobic effect from the fluorene ring of 9-FL-4-COO^-.

Ultimately, it is found from the experimental and theoretical works in this doctoral thesis

that vibrational dynamics of a solute in hydrogen-bonding liquids strongly depends on the molecular properties of the vibrational probe molecule. Based on the detailed analysis, all the results obtained in this thesis are very helpful for understanding of molecular dynamics and microscopic environment in solution. For example, the experimental findings on the reorientational dynamics around multiple-bond axes, which were obtained in Chapter 7, are indispensable for understanding the structural dynamics of macromolecules. Based on the results that the effective distance of the electrostatic interaction from water molecules is different between NTBA and SCN^- in H_2O (in Chapter 5), I found that a relative dielectric constant around a solute depends on the molecular properties (*i.e.* molecular structure, charge distribution, hydrophobic/hydrophilic group, and so on). From the results discussed in Chapter 8, I revealed that the size of the hydrophobic group strongly influences the vibrational frequency fluctuation of the vibrational probes in water. In this case, the relative dielectric constant around the vibrational probe molecule with the larger hydrophobic group would be much smaller. Therefore, one can expect that this solute-dependent relative dielectric constant plays an important role for the vibrational frequency fluctuations. I conclude that the methodology associated with the radial-dependent electrostatic potential and spatially-resolved vibrational frequency fluctuation calculations, which I developed in Chapter 5, is powerful tool to obtain deeper understanding on molecular dynamics of complex systems, such as biomolecules in solution, revealed in 2D-IR spectra.

Publication List

1. Masaki Okuda, K. Ohta, and K. Tominaga, "Vibrational dynamics of azide-derivatized amino acids studied by nonlinear infrared spectroscopy", *J. Chem. Phys.*, **142**, 212418 (2015).

2. Masaki Okuda, K. Ohta, and K. Tominaga, "Comparison of vibrational dynamics between non-ionic and ionic vibrational probes in water: Experimental study with two-dimensional infrared and infrared pump-probe spectroscopies", *J. Chem. Phys.*, **145**, 114503 (2016).

3. Masaki Okuda, M. Higashi, K. Ohta, S. Saito, and K. Tominaga, "Vibrational frequency fluctuations of ionic vibrational probe in water: theoretical study with molecular dynamics simulation", *Chem. Phys. Lett.*, submitted.

Acknowledgements

The work reported in this doctoral dissertation has been carried out in Department of Chemistry, Graduate school of Science in Kobe University under the direction of Professor Keisuke Tominaga from April 2014 to January 2017.

First of all, I am profoundly grateful to Professor Keisuke Tominaga for giving me opportunity to study really interesting and challenging subjects. He gave me much discussion time and pertinent suggestions which I could not think of by myself as my supervisor. He also gave me many opportunities to attend conferences at various places including foreign countries. Thanks to his tremendous support, I could spend fruitful days for six years in his laboratory and improve my skills as a scientist.

Regarding the experimental studies with nonlinear IR spectroscopies, I would like to express my deep gratitude to Dr. Kaoru Ohta. For all the nonlinear IR experiments which I conducted in the Tominaga laboratory, he gave me considerable help. Generally speaking, it is quite difficult for beginners to perform and master nonlinear IR spectroscopies, especially 2D-IR spectroscopy. However, since he kindly gave me a lot of knowledge on these experiments in detail, I could conduct nonlinear IR measurements without any serious accidents and, finally, understand the principle of nonlinear IR spectroscopies deeply. He also gave me much precise advice which is based on his prominent insight not only into experimental but also into theoretical studies.

Regarding the theoretical studies based on molecular dynamics simulations, I sincerely appreciate Professor Shinji Saito in Institute of Molecular Science. He always readily gave me discussion time and many meaningful suggestions based on his outstanding knowledge on theoretical works. I also would like to thank assistant Professor Masahiro Higashi in University of the Ryukyus. He kindly taught me how to perform MD simulations from the beginning. Additionally, whenever I was in trouble with the theoretical calculations including the MD simulations, he thoughtfully gave me appropriate solution with detailed explanation.

I would like to express my thanks to associate Professor Seiji Akimoto in Kobe University. He also gave me meaningful comments in the progress report meetings of the Tominaga and Akimoto laboratory. And, thanks to Tominaga and Akimoto group members, I could spend the wonderful days here. I also would like to recognize all of the group members. Moreover, I would like to appreciate my dear classmates, especially, Yuki Fukui, Kenta Niki, and Ami Ohta (Yamamoto), for encouraging me. With their warm cheer, I could overcome my tough times during this period and, finally, accomplished my doctoral work.

Theoretical calculations were performed using the Research Center for Computational Science, Okazaki, Japan. This research was supported by Joint Research by Institutes for Molecular Science (IMS program No. 201 in 2016, No. 224 and 612 in 2015) and a Grant-in-Aid for JSPS Research Fellow (16J05643).

Finally, I would like to express deepest appreciation to my family for continuous supports in everything and warm cheering me up at all times.

January 2017, in Kobe

MASAKI OKUDA